Demagnetizing and hardening mechanisms in Nd-Fe-B and Sr-hexaferrite permanent magnets

---

Entmagnetisierungs- und Härtungsmechanismen in Nd-Fe-B und Sr-Hexaferrit Permanentmagneten

Dissertation genehmigt zur Erlangung des akademischen Grades Doktoringenieur
(Dr. Ing.)

vorgelegt dem Fachbereich Material- und Geowissenschaften der Technischen Universität
Darmstadt

von Tim Oliver Helbig M. Sc.
Geboren am 07.03.1987 in Goslar

Erstgutachter: Prof. Dr. Oliver Gutfleisch
Zweitgutachter: Prof. Dr. Thomas Schrefl

Darmstadt 2018

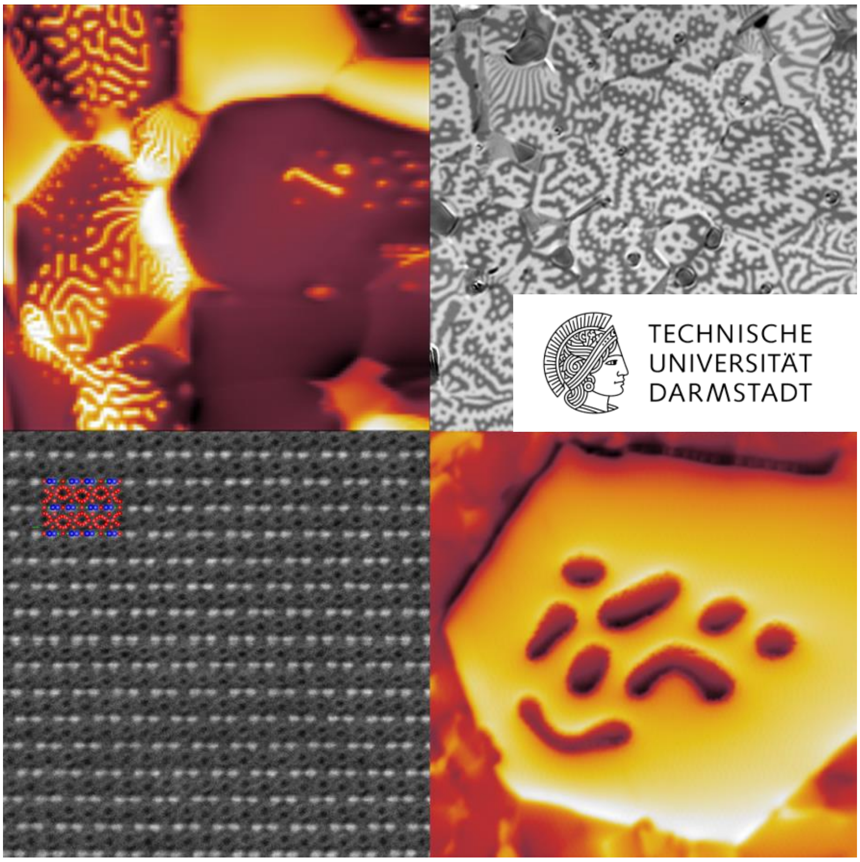

TECHNISCHE
UNIVERSITÄT
DARMSTADT

Helbig, Tim Oliver: Demagnetizing and hardening mechanisms in Nd-Fe-B and
Sr-hexaferrite permanent magnets
Darmstadt, Technische Universität Darmstadt,
Jahr der Veröffentlichung der Dissertation auf TUprints: 2018
Tag der mündlichen Prüfung: 26.10.18

"Science is a cooperative enterprise, spanning the generations. It's the passing of a torch from teacher, to student, to teacher. A community of minds reaching back to antiquity and forward to the stars."

-Neil deGrasse Tyson

Erklärung zur Dissertation

Hiermit erkläre ich, Tim Oliver Helbig, dass ich die vorliegende Dissertation selbstständig verfasst habe und keine anderen als die angegebenen Hilfsmittel verwendet habe. Alle wörtlich oder inhaltliche übernommenen Stellen sind als solche gekennzeichnet.

Ich versichere zudem, dass diese Arbeit in gleicher oder ähnlicher Form keiner anderen Prüfungsbehörde vorgelegt wurde.

Darmstadt den 13.08.2018

Tim Oliver Helbig

Abstract

In the first part of this work, the microstructural influence on magnetic properties Sr-hexaferrites is investigated. Using a Magnetic Force Microscope (MFM) the domain evolution during magnetization from the Thermally Demagnetized State (TDS) and DC field Demagnetized State (DCD) and during demagnetization was investigated *in-situ*. A surface magnetization was determined from the MFM contrast that quantitatively matched the bulk magnetization determined by Superconducting Quantum Interface Device (SQUID). For the surface magnetization it was found that smaller grains below the critical single domain size reversed their magnetization from Single Domain State (SDS) to the reversed SDS, while larger grains form an intermediate Multi Domain State (MDS). Using a series of minor loops it was determined that the presence of MDS in the bulk is neglectable.

An in-depth analysis of core-shell structured Nd-Fe-B grains was carried out using Scanning Electron Microscopy (SEM), Transmission Electron Microscopy (TEM), optical Kerr microscopy and MFM. While the core consisted of pure $Nd_2Fe_{14}B$ the shell, the composition of the shell was $(Nd_{1-x}Dy_x)_2Fe_{14}B$. The composition and morphology of the grain boundary was analyzed using TEM. Using MFM the magnetic contrast of core and shell due to the lower saturation magnetization of the Dy substituted species could be correlated to the chemical contrast observed by SEM. The demagnetization of core and shell was observed under *in-situ* condition using MFM and Kerr microscopy. The results show a uniform demagnetization across core and shell. The time resolution of the Kerr microscope of 43 frames per second is not large enough to resolve an intermediate domain state between SDS and stable MDS within the 23 ms between two frames. In a subsequent micromagnetic simulation the nucleation site was shown to lie either at the grain boundary or in the core depending on the magnetocrystalline anisotropy at the grain boundary defect layer.

The texture dependency of the Grain Boundary Diffusion Process (GBDP) in sintered and hot-deformed Nd-Fe-B magnets was analyzed by creating a global and a local coercivity profile of the diffused samples. While the former method allows a conclusion on how the magnet acts as a whole, the latter allows a more precise resolution of local coercivity. In sintered magnets a slightly higher coercivity improvement was observed for the diffusion perpendicular to the texture axis. A pole hardening effect was observed for diffusion parallel to the texture axis that compensated the higher coercivity improvement for parallel diffusion. In hot-deformed magnets on the other hand, no pole hardening effect was observed and a higher coercivity improvement was observed for parallel diffusion. A microstructural investigation showed that this effect could be attributed to the platelet shaped grains in hot-deformed magnets. The *in-situ* demagnetization of hot-deformed magnets was analyzed for different Dy contents.

The composition of different pilot batch Nd-Fe-B magnets by VACUUMSCHMELZE GmbH & Co. KG was determined by Inductively Coupled Plasma – Optical Emission Spectroscopy (ICP-OES). The grain size distribution and orientation was determined using Electron Back Scattered Diffraction (EBSD). The influence of Heavy Rare Earth Elements (HRE) and microstructure engineering on the intrinsic and extrinsic magnetic properties was investigated. A similar minor loop investigation was also done for Nd-Fe-B sintered magnets showing that the vast majority of grains display a single domain like behavior despite being approximately one order of magnitude larger than the critical single domain size. Furthermore the amount of MDS during the demagnetization could be reduced by the addition of HRE.

Kurzfassung

Im ersten Teil dieser Dissertation wurde eine detaillierte Analyse des Gefüges und dessen Einfluss auf magnetische Eigenschaften in Sr-Hexaferrit Magneten durchgeführt. Mittels Magnet Kraft Mikroskopie (MFM) wurde die Domänenentwicklung in Sr-Hexaferrit Sintermagneten während der Aufmagnetisierung aus dem thermisch entmagnetisierten Zustand (Thermally Demagnetized State, TDS) und vom DC Feld demagnetisierten Zustand (DC Demagnetized State, DCD) wurde mittels Magnet-Kraftmikroskopie (MFM) unter *in-situ* Bedingungen untersucht. Aus dem MFM Kontrast wurde eine Magnetisierung der Oberfläche bestimmt, welche quantitativ der Magnetisierung des Volumenmagnets entspricht, welche mittels Superconducting Quantum Interface Device (SQUID) bestimmt wurde. Für die Oberflächenmagnetisierung wurde festgestellt, dass die Ummagnetisierung kleinerer Körner von einem Eindomänenzustand (Single Domain State, SDS) zum jeweils entgegengesetzten SDS geschieht, während größere Körner einen intermediären Multidomänenzustand (Multi Domain State, MDS) aufweisen. Durch die Messung sog. innerer Hystereseschleifen konnte hingegen gezeigt werden, dass MDS im Volumenmagnet weitestgehend nicht auftreten.
Eine eingehende Untersuchung von „Core-Shell“ strukturierten Nd-Fe-B Körnern mittels Rasterelektronenmikroskopie (SEM), Transmissionselektronenmikroskopie (TEM), optische Kerr Mikroskopie und MFM wurde durchgeführt. Während der „Core“ aus reinem $Nd_2Fe_{14}B$ bestand, entsprach die Zusammensetzung „Shell“ $(Nd_{1-x}Dy_x)Fe_{14}B$. Die Zusammensetzung und Morphologie der Korngrenze wurde mittels TEM untersucht. Ein magnetischer Kontrast zwischen „Core“ und „Shell“ konnte im MFM festgestellt werden, aufgrund der geringeren Sättigungsmagnetisierung der Dy substituierten Spezies, welcher mit dem chemischen Kontrast des SEMs korreliert werden konnte. Die Entmagnetisierung von „Core“ und „Shell“ wurde mittels MFM und Kerr Mikroskopie unter *in-situ* Bedingungen untersucht. Es konnte eine einheitliche Ummagnetisierung von „Core“ und „Shell“ mit beiden Methoden beobachtet werden. Die zeitliche Auflösung des Kerr Mikroskops von 43 Bildern pro Sekunde war nicht ausreichend, um einen Domänenzustand zwischen SDS und stabilem MDS innerhalb der 23 ms zwischen zwei Bildern. In einer anschließenden mikromagnetischen Simulation konnte gezeigt werden, dass der Nukleationspunkt der entgegengesetzten Domäne entweder an der Korngrenze oder im „Core“ liegt, abhängig von der Magnetokristallinen Anisotropie der Defektschicht an der Korngrenze.
Die Texturabhängigkeit der Korngrenzendiffusion wurde anhand globaler und lokaler Koerzivitätsprofile in Sinter- und heißumgeformten Nd-Fe-B Magneten untersucht. Während erstere Methode Schlussfolgerungen über das Verhalten als Magnet im Ganzen erlaubt, kann mit zweiterer Methode die Koerzivität lokal aufgelöst werden. In Sintermagneten konnte eine geringfügig höhere Verbesserung der Koerzivität für die Diffusion senkrecht zur Texturachse festgestellt werden. Ein Polhärtungseffekt wurde für die Diffusion parallel zur Texturachse beobachtet, welcher den Effekt der stärker erhöhten Koerzivität für senkrechte Diffusion kompensiert. In heißumgeformten Magneten wurde kein Polhärtungseffekt beobachtet sowie eine größere Erhöhung der Koerzivität für parallele Diffusion. Eine Untersuchung des Gefüges zeigte, dass dieser Effekt vermutlich auf die plättchenartige Form der Körner zurückzuführen ist. Eine in-situ Untersuchung der Entmagnetisierung für unterschiedliche Dy Konzentrationen wurde an heißumgeformten Magneten durchgeführt.

In Nd-Fe-B Sintermagneten wurden Korngröße, Textur und Korngrößenverteilung durch „Electron Back Scattered Diffraction” (EBSD) bestimmt. Die Zusammensetzung von verschiedenen Nd-Fe-B Magneten der VACUUMSCHMELZE GmbH & Co. KG wurde mittels

Inductively Coupled Plasma – Optical Emission Spectroscopy (ICP-OES) bestimmt. Der Einfluss der Schweren Seltene Erden, den sog. „Heavy Rare Earths“ (HRE), in Kombination mit einer Gefügeoptimierung wurde bezüglich intrinsischer und extrinsischer magnetischen Eigenschaften untersucht. Eine Untersuchung von inneren Hystereseschleifen wurde ebenfalls an Nd-Fe-B Sintermagneten durchgeführt, wodurch gezeigt werden konnte, dass der Großteil der Körner ein ein-domänenartiges Verhalten zeigen, obwohl die Korngröße ca. eine Größenordnung über der kritischen Eindomänengröße liegt. Darüber hinaus konnte festgestellt werden, dass der Anteil der MDS durch die Zugabe von HRE reduziert werden konnte.

Inhalt

List of abbreviations

AFM	Atomic Force Microscopy
APT	Atom Probe Tomography
BSE	Back Scattered Electrons
EBSD	Electron Back Scatted Diffraction
EDX	Energy Dispersive X-Ray Spectroscopy
FIB	Focused Ion Beam
GBDP	Grain Boundary Diffusion Process
GBP	Grain Boundary Phase
HAADF	High Angle Annular Dark Field
HDDR	Hydrogen-Disproportionation–Desorption-Recombination
HRE	Heavy Rare Earth, Singular Or Plural
ICP	Inductively Coupled Plasma
LRE	Light Rare Earth , Singular Or Plural
MDS	Multi Domain State
MFM	Magnetic Force Microscopy
OES	Optical Emission Spectroscopy
SDS	Single Domain State
SE	Secondary Electron
SEM	Scanning Electron Microscopy
SQUID	Superconducting Quantum Interference Device
STEM	Scanning Transmission Electron Microscopy
TEM	Transmission Electron Microscopy
VSM	Vibrating Sample Magnetometer

List of symbols

$(BH)_{max}$	maximum energy product
A	exchange constant
B	magnetic flux density
D	grain boundary diffusion coefficient
d_c	critical single domain size
d_{final}	final sample diameter
D_{krit}	critical particle diameter
d_o	initial sample diameter
e_A	anisotropy energy density
E_{ex}	exchange energy
E_{ms}	magnetostriction energy
E_{Str}	stray field energy
E_Z	Zeeman energy
e_Z	Zeeman energy density
H	magnetic field
H_a	anisotropy field
H_c	coercivity
$H_{c,B}$	coercivity with respect to flux density
$H_{c,bulk}$	coercivity in the bulk
$H_{c,M}$	coercivity with respect to magnetization
$H_{c,surf}$	coercivity at the hre source
H_d	demagnetization field
H_{ext}	external magnetic field
h_{final}	final sample height
H_n	nucleation field
$H_{pass,}$, H_{expans}	passage field, expansion field
h_o	initial sample height
H_{Str}	magnetic stray field
J_{ex}	exchange integral
J_s	saturation magnetization
$K_{1,2}$	anisotropy constant
l_{ex}	exchange length
M	magnetization
M_s	saturation magnetization
N	demagnetization factor
N_{eff}	effective demagnetizing factor
S_i,S_j	localized spin states
T_C	Curie temperature
V	volume
v_n	volume of nucleus of a reversed domain
α_H	angle between the easy axis and external field
α_K, α_Ψ	Kronmüller parameter
γ_{DW}	180° Bloch domain wall energy
$\gamma_{DW,n}$	180° Bloch domain wall energy of a nucleus
δ_{DW}	180° Bloch domain wall width
ΔJ_{irr}	irreversible magnetization
ΔJ_{rev}	reversible magnetization
θ	angle between external field and magnetization
Φ	angle between spins
φ	degree of deformation
χ	magnetic susceptibility
μ_0	permeability constant of the vacuum

List of figures

List of Tables

1. Introduction

Despite the considerable number of ferro- and ferrimagnetic materials, the global permanent magnet market is dominated by only two material systems, the so-called ferrites and Nd-Fe-B magnets [Gutfleisch2011]. Ferrites still make up around 80 % of the market by volume, due to low price and abundant raw materials, despite being one of the oldest permanent magnet material system [Gutfleisch2011, Grand View Research2016]. The most common hard magnetic ferrites are M-type hexaferrites e.g. $SrFe_{12}O_{19}$ or $BaFe_{12}O_{19}$. They are used in a variety of applications, from speakers to small electronic motors but are always operating under a low price low performance premise. Since their discovery in the 1950s, the magnetic properties of hexaferrites, such as coercivity and remanence, have been improved significantly, but do not compare to high performance magnets like Nd-Fe-B or Sm-Co [Kools2003]. The advantage of this material system is the high abundance of raw material, making it a perfect low cost mass product. Nd-Fe-B magnets on the other hand represent the "high-end" material system, for high performance applications that require low weight and/or volume. They belong to the material class of the so-called rare earth magnets. They were discovered in 1984 (arguably 1983) by three different groups almost simultaneously [Hadjipanayis1983, Croat1984, Sagawa1984]. The reasons why this material system provides excellent properties for the manufacturing of hard magnets can be attributed to the strong Spin-Orbit Coupling of the localized 4f electrons of the rare earth element Nd. At the same time, however, the usage of Nd drastically increases the production costs due to the high raw material prices. Other elements like Dy and Tb belong to the group of heavy rare earth elements (HRE) that are often added in small quantities to improve magnetic properties, especially for high temperatures applications. The addition of HRE, however, increases the costs even further due to the raw material prices of Dy and Tb.

The use of rare earth elements as a raw material on an industrial scale also poses several environmental, ecological and economic problems: As a result of their chemical similarity, rare earth elements naturally do not occur in pure form but are always bound in complex minerals comprised of multiple rare earth elements [Bauer2010]. As a consequence the desired rare earth elements, such as Nd or Dy, cannot be mined individually, but have to be extracted from the so-called "rare earth basket". Another consequence of their chemical similarity is that the pure elements are extracted by the using strong and/or toxic acids and solvents, resulting in serious environmental consequences if not managed appropriately [Izatt2016]. Due to their chemical nature, rare earth ores often contain radioactive elements such as Th and U that occur as a waste product of the production and refining process [Kanazawa and Kamitani2006]. Nowadays approximately 95 % of all rare earths worldwide are mined and produced in China [EUROPEAN COMMISSION2017], resulting in a monopolistic market situation that has led to the so-called rare earth crisis in 2011. During this crisis the cost for rare earth elements increased by a factor of 10 within a few months [Widmer2015]. The current market situation is the same as prior to the rare earth crisis if not worse since rare earth elements today pose an even larger key role in many branches of industries such as electro mobility and renewable energies [Gutfleisch2011].

As a consequence of the criticality of rare earth elements and the rare earth crisis, a considerable amount of research was undertaken, from academia and industry, in order to improve the situation. The different approaches can be divided into 4 main categories:

1. The substitution of Nd in Nd-Fe-B magnets by other RE elements such as La and Ce. Since rare earths are always obtained together as part of the rare earth basket, a surplus of these elements is produced as waste product of the separation process[Binnemans2018]. This problem is often referred to as the “rare-earth balance”, while stockpiled rare earth elements are the so often referred to as “free rare earths”.
2. The search for new magnetic compounds in order to substitute ferrites in the low performance-, or Nd-Fe-B in the high performance sector. This approach aims to find new phases with sufficiently high intrinsic properties that consist of either non-rare earth elements or free rare earth elements. The challenge of this approach also lies in transferring these intrinsic properties to extrinsic ones through appropriate microstructure engineering.
3. The third approach is focused on improving magnetic properties mainly in Nd-Fe-B magnets while minimizing the amount of used rare earth elements, especially HRE elements. This is obtained by careful microstructural engineering e.g. through grain refinement or elements like Ga or Cu to optimize the translation of intrinsic to extrinsic properties.
4. Further optimization of ferrite magnets. Despite their “age”, ferrites still spark the interest of researchers for further optimization [Pullar2012]. The approaches range from elemental substitution to microstructure engineering and exchange coupled spring magnets.

The last two approaches are the main focus points of this PhD thesis analyzing the Sr-hexaferrite and Nd-Fe-B systems. From a theoretical point of view neither of those systems has reached its intrinsic upper limit in current industrial or research state of the art magnets. The challenge of this PhD work is the analysis of the demagnetizing processes and hardening mechanisms in Nd-Fe-B and hexaferrite magnets in order to derive improvement strategies. An important factor to be determined is the influence of the microstructure on the magnetization and demagnetization behavior. From an understanding of the demagnetization processes, some approaches are derived to improve hard magnetic properties that are specific to the ferrite and/or Nd-Fe-B system. A detailed overview over the principle demagnetization processes and hardening mechanisms is given in chapter 2.1.2. One of the difficulties of this task is the actual experimental observation and quantification of magnetization and demagnetization. Magnetization is a bulk phenomenon and can be easily measured globally as an average over the entire sample. The demagnetization, however, occurs via processes on a micro- and nanoscopic scale that requires a respective local resolution to be analyzed. A variety of different techniques have been employed during the course of this work to connect local and global demagnetization behavior.

2 Basics

2.1 Magnetism of permanent magnets

Several quantum mechanical and semi classical models have been developed to describe the magnetism in various materials. Each model often describes a specific type of magnetism in a specific type of material class. The two types of magnetism that create a net magnetic moment and are thus of interest for permanent magnets are ferro- and ferrimagnetism. In order to form ferro- or ferrimagnetic interactions, an interatomic interaction between electrons is required that leads to a parallel alignment of magnetic moments. One model that explains the parallel (or antiparallel) orientation of neighboring atoms was developed by Heisenberg in 1928. It describes the energy of two atoms *i* and *j* that possess a spin angular momentum $S_i \hbar$ and $S_j \hbar$ (with $\hbar$ being Planck´s constant divided by 2 π) as:

$$E_{ex} = -2J_{ex}S_iS_j = -2JS_iS_j \cos\Phi \tag{2.1}$$

In this equation, J_{ex} is the exchange integral that occurs in the calculation when the respective electrons are treated as quantum mechanical objects that can be exchanged. The angle Φ describes the angle between the two spins. If J_{ex} is positive the resulting exchange energy E_{ex} has a minimum if the spins are aligned parallel ($\cos \Phi = 1$) thus forming a ferromagnetic order. To calculate the energy of a continuum instead of individual atoms and assuming identical spins *S*, the equation can be expressed as:

$$E_{ex} = -2A \cos\left(\frac{d\Phi}{dx}\right) \tag{2.2}$$

Where $A = (nJS^2 / a)$ is called the material specific exchange stiffness or exchange constant that can be calculated from the number of atoms per unit cell *n* and the lattice parameter a and has the unit J/m. The elegance of the model is that it only relies on the Coulomb interaction and the Pauli Exclusion Principle. The weakness of the model lies therein that equation 2.1 is only considering the interaction of adjacent hydrogen atoms. It is therefore not suited to describe the ferromagnetism in transition metals e.g. Fe, Ni, Co, where the 3d-electrons are delocalized. Here the Stoner model can be applied, which describes the spin dependency of the band structure. In the Stoner model the resulting magnetic moment arises from a difference in the density of states near the Fermi level. The Heisenberg model, however, can be used to derive several interesting quantities as will be shown later.

The exchange interaction that occurs between electrons can be considered as spin - spin coupling that is isotropic. The spins are, however, also coupling to the orbital momentum (spin – orbit coupling) that itself is coupling to the lattice (orbit – lattice coupling). While the orbit – lattice coupling is very strong, the spin – orbit coupling is relatively weak. Nevertheless the result is a preferred orientation of electrons i.e. their magnetic moment with respect to specific crystallographic axis or planes (orbit – lattice coupling). A preferred crystallographic orientation is referred to as an easy axis, while a non-preferred axis is called a hard axis. In order to rotate the magnetic moment away from the easy axis to the hard axis the energy of the spin – orbit coupling has to be overcome which is also-called the anisotropy energy or magnetocrystalline anisotropy energy. The anisotropy energy density of a uniaxial system can be described with the following equation:

$$e_A = K_0 + K_1 sin^2\theta + K_2 sin^4\theta + \cdots \tag{2.3}$$

Here K_0, K_1, K_2 are material and temperature dependent constants that can be expressed in J/m³, while θ describes the angle between the easy axis and the magnetization direction. Hard magnetic materials typically exhibit uniaxial magnetocrystalline anisotropy along the c-axis of an anisotropic (i.e. hexagonal, tetragonal or rhombohedral) crystal structure. For uniaxial systems K_0 *and* K_2 are often neglected, since K_0 is not angular dependent and K_2, which describes the planar component, is typically quite small.

If the magnetic moments inside a given material are aligned due to the described mechanisms, the resulting dipole – dipole interaction generates a magnetic stray field H_{Str}. In comparison to the exchange interaction the dipole – dipole interaction is relatively weak but is acting on a larger range. The magnetic stray field is forming on the surface of a homogenously magnetic volume, where all magnetic moments are aligned parallel. The energy of H_{Str}, which is also-called magnetostatic energy, is given as:

$$E_{Str} = \frac{1}{2}\mu_0 \int_{space} H_{Str}^2 \, dV = -\frac{1}{2}\mu_0 \int_{sample} H_d M \, dV \tag{2.4}$$

The stray field can either be described by integrating over the entire volume outside the sample or by integrating the demagnetization field H_d and the magnetization M over the volume of the sample.

Magnetic domains

From the previously introduced concepts, one can derive another fundamental approach called the domain concept that applies to all ferro- and ferrimagnetic materials. The domain concept was first introduced by Pierre-Ernest Weiss in the beginning of the 20th century to explain the behavior of ferromagnetic materials. It assumes that a certain volume referred to as a “domain” inside a magnetic sample is uniformly magnetized, in the case of permanent magnets, along the easy axis. From such a uniformly magnetized domain follows a respective stray field energy E_{str} that has to be “spent”. Since thermodynamics always favors the energetically lower state, the system is striving to minimize the stray field energy by forming an antiparallel magnetized domain of equal volume. In principle this process can be repeated to reduce the stray field energy even further, but each time a domain is divided a domain wall i.e. a gradual rotation of magnetization has to be introduced as depicted in Figure 2.1.

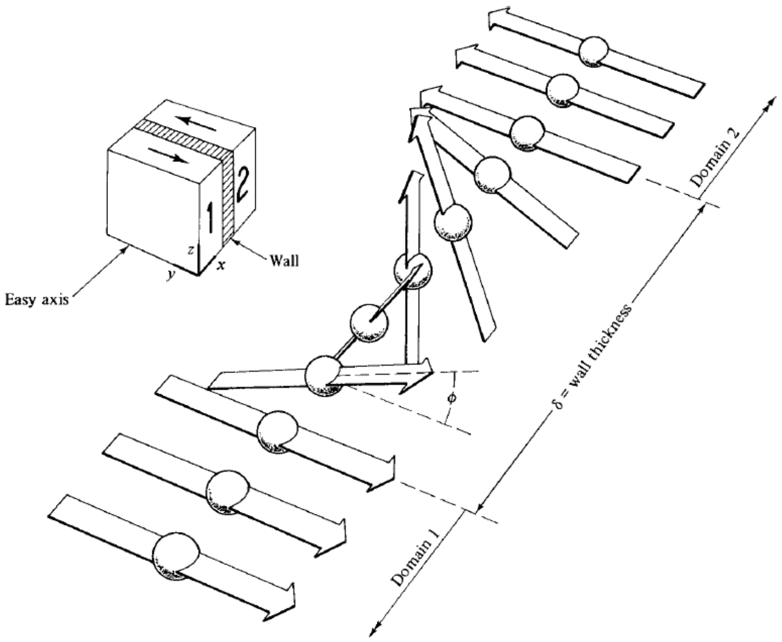

Figure 2.1 Depiction of a 180° Bloch wall [Cullity and Graham2008].

The gradual rotation of magnetization means that magnetic moments deviate from a parallel alignment as well as the easy axis. The rotation of the magnetic moment can either be parallel to the domain wall (Bloch wall) or perpendicular to the domain wall (Néel-wall). The energy that is required to form a 180° Bloch domain wall must therefore be proportional to the A as well as the K_1 and can be calculated as:

$$\gamma_{DW} = 4\sqrt{AK_1} \tag{2.5}$$

In order to minimize the exchange energy, the system is inclined to form infinitely large domain walls, where the rotation of magnetic moments against each other becomes minimal. The anisotropy energy on the other hand is driving the system towards infinitely thin domain walls in order to minimize the angle between magnetization and easy axis. Thus the width of a 180° (Bloch) domain wall is given as a result of the competition of the two energies as:

$$\delta_{DW} = \pi\sqrt{\frac{A}{K_1}} \tag{2.6}$$

Since a Bloch wall (shown in Figure 2.1) does not create any stray fields within the wall, they are generally the energetically preferred domain wall in bulk materials. Néel walls on the other hand become energetically favorable to Bloch walls if the sample thickness becomes comparable to the thickness of the domain wall e.g. in thin films. Closely related to the domain wall width (eq. 2.6) is the so-called exchange length given by:

$$l_{ex} = \sqrt{\frac{A}{K_1}} \tag{2.7}$$

It also arises from the competition of stray field minimization and exchange energy and describes the shortest length that the magnetic moments can be rotated in order to minimize the stray field. In other words, if two magnetic moments are further apart than the *exchange* *length*, the minimization of stray field energy by aligning antiparallel becomes favorable meaning that no exchange coupling is occurring and the magnetic moments can be considered as decoupled. This definition, however, is only true, if the anisotropy constant K_1 maintains the same over the entire length. This means that this definition works in a specific material, however, losses its validity if other phases e.g. at the grain boundary are involved.

From the concept that each introduced domain reduces the stray field energy, but each domain wall formation requires a domain wall energy it follows that under ideal condition an optimum domain width can be calculated. Assuming an isolated spherical particle with a uniaxial anisotropy one can calculate the critical radius r_c at which the stray field energy of a single domain is equal to the energy required to form a domain wall. This consideration also makes the assumption that the stray field energy of the two-domain-state is half the energy of the single-domain-state and gives the critical-single-domain size as [Kittel1949]:

$$d_c = 2 \times r_c = 2 \times \frac{9\gamma_{DW}}{\mu_0 M_S^2} = 72\frac{\sqrt{AK_1}}{\mu_0 M_S^2} \tag{2.8}$$

This means that particles with a larger radius are energetically favored to form multi-domain-states (MDS) while smaller particles form Single Domain States (SDS). In reality, however, the assumption of a spherical, isolated particle is usually not valid. Furthermore additional energy terms such as magnetostriction energy E_{ms} *and Zeeman energy* E_Z are coming into play. The Zeeman energy describes the potential energy of a magnetized sample in an external magnetic field as:

$$E_Z = -\mu_0 \int_{Sample} M H_{ext} dV \tag{2.9}$$

Where H_{ext} is the external magnetic field and M the local magnetization. According to the Stoner-Wohlfarth-Model that assumes a uniaxial ellipsoid particle with the easy axis along the longitudinal axis, the Zeeman energy is the energy that is necessary to rotate the magnetization perpendicular to the easy axis. The energy density of the respective moment is given as:

$$e_Z = -\mu_0 M H_{ext} \cos(\alpha_H - \theta) \tag{2.10}$$

With α_H and θ as the angles between the easy axis and the external field and as the angle between external field and magnetization respectively.

The magnetic field energy that is necessary to saturate the magnetization of a uniaxial magnetic system along the hard direction is given by:

$$E = K_1 \sin^2(\theta) + K_2 \sin^4(\theta) - \mu_0 M_s H_{ext} \cos\left(\frac{\pi}{2} - 0\right) \tag{2.11}$$

By minimizing E according to $\partial E/\partial\theta = 0$ and setting $\theta = \pi/2,$ the anisotropy field H_a, which is the field necessary to align the magnetization along the hard axis, for a uniaxial system can be calculated as:

$$H_a = \frac{2K_1 + 4K_2}{\mu_0 M_s} \approx \frac{2K_1}{\mu_0 M_s} \tag{2.12}$$

As mentioned before, the parameter K_2 is often neglected for uniaxial systems since it is in general quite small [Livingston1987]. H_a is an experimentally well accessible quantity that can be used to quantify the obtainable magnetic hardness of a particular material. It is an intrinsic property that is often used as a reference point to evaluate the extrinsic coercivity of a particular magnet, since the anisotropy field is the theoretical maximum obtainable coercivity. It takes into account that the obtainable coercivity is not only a function of anisotropy energy but also of the saturation magnetization of the respective material.

2.1.1 Magnetization processes

The in the previous paragraph introduced domain concept has major implications for the magnetization and demagnetization behavior of permanent magnets. Depending on the sample geometry, microstructure, intrinsic properties and magnetic history, the magnetic domains form a specific pattern. Most often, the so-called Thermally Demagnetized State (TDS) is considered as the “ground state” of the domain structure. This domain structure forms if the magnet is cooled down below the Curie temperature T_C. A few examples of domain structures are depicted in Figure 2.2. The magnetic easy axis or texture axis respectively is pointing out of the image plane in all images. Figure 2.2 (a) displays a Nd-Fe-B film with an increasing thickness from 1 µm (left) to 14 µm (right). The domain pattern changes gradually from a stripe-like structure to a maze-like structure to a “ribbon-like” structure. In bulk samples, such as sintered magnets, the domains form the typical star-like patterns as shown in Figure 2.2 (b). The pattern of the individual grain, however, also depends on its specific orientation. The typically round domain in the center of a star-like domain is sometimes also referred to as a closure-type domain [Goll2014].

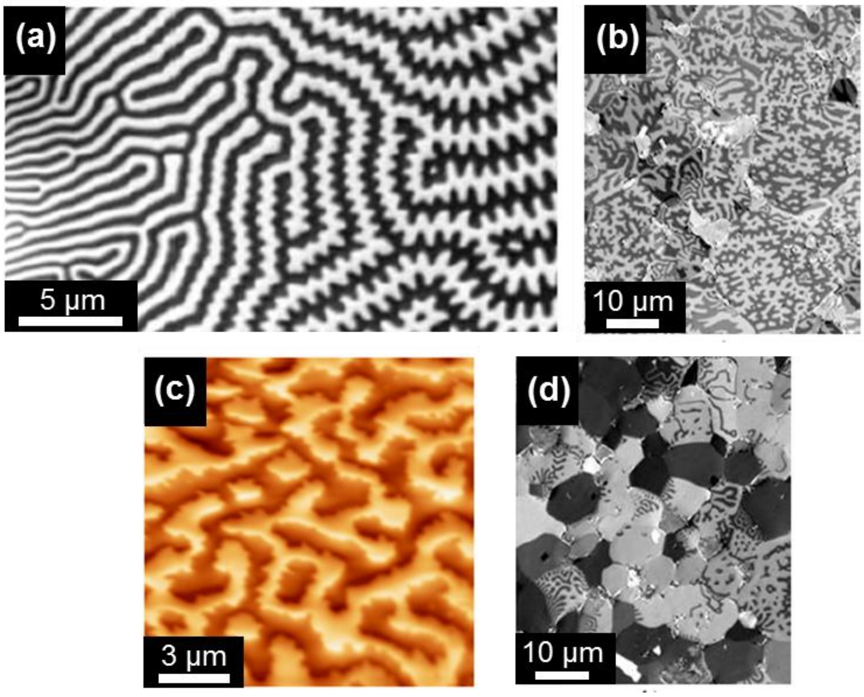

Figure 2.2 Domain images of different Nd-Fe-B magnets (a) Kerr microscopy of a film with increasing thickness from 1 µm to 14 µm [Hubert and Schäfer1998], (b) Kerr microscopy image of a sintered Nd-Fe-B magnet [Hubert and Schäfer1998], (c) Magnetic Force Microscopy image of hot-deformed Nd-Fe-B [Thielsch2012] and (d) Kerr microscopy image of a Nd-Fe-B sintered magnet that was demagnetized by applying a magnetic field slightly larger than the coercivity [Hubert and Schäfer1998]. The nominal magnetic easy axis i.e. the c-axis of the tetragonal $Nd_2Fe_{14}B$ is pointing out of the image plane in all images.

In hot-deformed Nd-Fe-B magnets (Figure 2.2 (c)), where the grain size is below or comparable to the critical single domain size, so-called interaction domains are forming that extend over multiple grains. Figure 2.2 (d) shows a picture of a Nd-Fe-B sintered magnet that was exposed to a magnetic field slightly larger than the coercivity. The end result is a domain pattern that differs significantly from the TDS. Here many grains are in a SDS that can point either out of the image plane or into the image plane.

Under the influence of an external magnetic field, the domains that have a parallel magnetization with respect to the external field start to grow at the expense of antiparallel magnetized domains. Here two fundamental types of magnets have to be distinguished: i) nucleation type and ii) pinning type magnets. In pinning type magnets the movement of domain walls is “hindered” by so-called pinning centers that consist of chemical inhomogeneities or defects that make it energetically favorable to form a domain wall at the pinning center. In order to overcome a pinning center a higher magnetic field has to be applied in order to “unpin” a domain wall. In nucleation type magnets on the other hand, domain walls can be moved quite easily up to the point where all domain walls are driven out of a specific grain. In textured magnets, the two mechanisms can usually be discernable by the shape of the initial magnetization curve from the TDS as depicted in Figure 2.3.

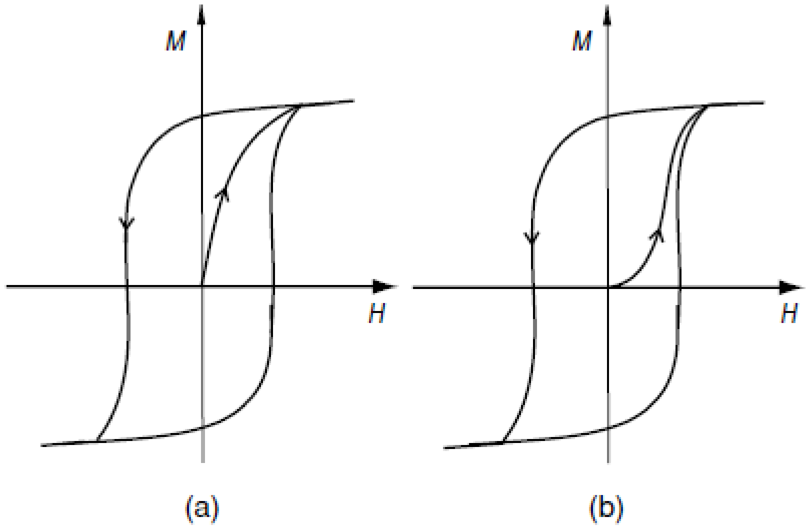

Figure 2.3 Schematic of the initial magnetization curve of a nucleation dominated permanent magnet (a) and a pinning dominated permanent magnet (b) [Coey2010].

Nucleation dominated magnets display a high initial susceptibility ($\chi = \partial M/\partial H$) since domain walls can be moved easily and require very low fields. Pinning dominated magnets on the other hand display a very low initial susceptibility since the domain walls have to be unpinned from the pinning centers. Furthermore the domain walls are constantly “trapped” by pinning centers over the cause of the initial magnetization resulting in a low susceptibility at low fields [Coey2010]. The two processes of nucleation and pinning type magnets, however, become indistinguishable or rather not defined if the grain size lies in the range of the critical single domain size as in the case of hot-deformed Nd-Fe-B magnets. Here the concept of classical domain formation does not apply, hence classical domains do not exist and the two types actually merge at this scale [Gutfleisch2000a].

If the magnetization by domain growth is completed i.e. all domain walls have been driven out and all grains are in a SDS, a further magnetization can only be achieved by spin rotation processes of misaligned grains. This means that in grains where the easy axis is not aligned with the texture axis or rather external field, the magnetization is rotated away from the easy axis to align with the external field. Due to the high anisotropy field and degree of texture in permanent magnets, this process typically occurs only at very high fields and increases magnetization only slightly.

2.1.2 Demagnetization and magnetic hardening mechanisms

Most of the parameters that have been discussed so far are *intrinsic* parameters, in order to create a good permanent magnet those parameters have to be transferred to *extrinsic* parameters. The extrinsic parameters can be determined by measuring the "response" of a magnetic sample to an external magnetic field which is usually referred to a M-H loop or hysteresis loop. An exemplary curve showing the magnetization of a textured magnet as a function of the external field that is applied along the texture axis is depicted in Figure 2.4. In a sufficiently high external field all magnetic moments are aligned along the external field, resulting in the saturation magnetization J_s. Upon removal of the field, the magnet is in the remanent state or remanence with the magnetization J_r. At negative i.e. demagnetizing fields, the magnets maintains a (positive) magnetization until the coercive field or coercivity H_c is reached which is a measure for the magnets ability to withstand the demagnetization by a magnetic field. The coercivity H_c can be defined with respect to the magnetization $H_{c,M}$ or the flux density $H_{c,B}$. In this work the term coercivity, coercive field and H_c always referrer to $H_{c,M}$. From the B-H curve the so-called *Energy Product* $(BH)_{max}$ can be determined as the maximum of B multiplied by H. It can be considered as the "magnetic energy" that is being stored in a permanent magnet, typically measured in kJ/m³.

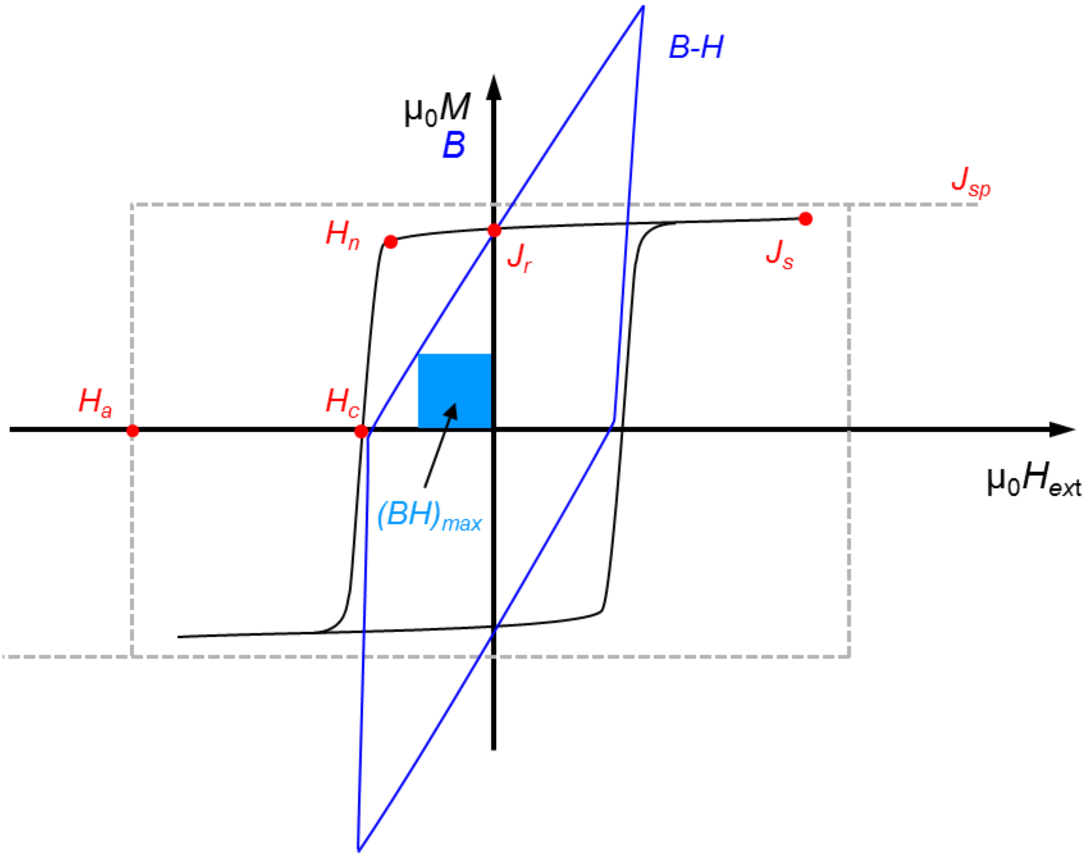

Figure 2.4 Exemplary hysteresis curve of a textured hard magnetic material with the external field applied along the texture axis, displaying the spontaneous magnetization J_{sp}, the saturation magnetization J_s, remanent magnetization J_r, coercivity H_c, nucleation field H_n and anisotropy field H_a.

It is noteworthy that the coercivity H_c in permanent magnets is typically only 20 – 30 % of the respective anisotropy field H_a despite the fact that H_a is the field that is theoretically necessary to rotate and thus reverse the magnetization. This phenomenon i.e. the discrepancy between anisotropy field and coercivity is known as *Brown´s paradox* [Brown1945], which can also be expressed as:

$$H_c \leq \frac{2K_1}{\mu_0 M_s} - NM_s \tag{2.13}$$

In this inequality the first term describes the anisotropy field, while the second one describes the demagnetizing field.

The demagnetization of a uniaxial, ellipsoid particle can be described using the Stoner-Wohlfarth model, despite its limited quantitative accuracy due to Brown´s paradox. In this model the demagnetization occurs via a coherent rotation. Depending on the angle α between external magnetic field and easy axis, the coercivity of the particle is either equal to the anisotropy field at $\alpha = 0°$ or equal to 0 at $\alpha = 90°$.

The reason why the Stoner-Wohlfarth model does not describe the hysteresis curve of real magnets correctly (Brown´s paradox) is that the assumption of the model i.e. a homogeneous, magnetized material does not exist in reality. Real magnets always possess defects and inhomogeneities such as grain boundaries, secondary phases, point defects etc. that locally reduce the magnetocrystalline anisotropy and allow the nucleation of an initial reversed domain [Coey2010, Woodcock2012]. The respective field where reversed domains start to nucleate is usually referred to as the nucleation field H_n. Since the nucleation field is different for each grain, a smaller grain size statistically leads to a higher coercivity. For practical applications the nucleation field should be as close to the coercivity as possible to avoid demagnetization during operation.

An empirical model that describes the experimentally obtainable coercivity of real magnets was formulated by Kronmüller [Kronmüller1985, Kronmüller1987, Kronmüller1988]:

$$H_c = \alpha_K \alpha_\psi \frac{2K_1}{\mu_0 M_s} - N_{eff} M_s \tag{2.14}$$

In this equation, α_K describes the pinning or nucleation effects that arrives from defect induced locally reduction of anisotropy, α_Ψ describes the effects of misaligned grains and N_{eff} describes an effective demagnetizing factor that also takes grain size and shape, as well as non-magnetic phases into account. By determining the temperature dependency of the anisotropy field, the saturation magnetization and the coercivity the parameter α_K can be linked to the size of the critical nucleation diameter, which was determined to range from 0.8 nm to 2.4 nm for Nd-Fe-B sintered magnets.

A similar model to explain Brown´s paradox, called the “global-model”, was formulated by Givord et al. [Givord1988] to describe the temperature dependence of the coercivity. Instead of a locally reduced anisotropy, the model assumes a thermally excitation of a so-called *activation volume* in which the initial nucleus of a reversed domain is forming and expanding under the applied magnetic field. The dependency of the coercivity can be expressed as:

$$H_c = \frac{\alpha' \gamma_{DW,n}}{\mu_0 {v_n}^{1/3} M_s} - N_{eff} M_s \tag{215}$$

Where $\underline{\gamma_{DW,n}}$ relates to the domain wall energy inside the nucleus, v_n to the volume of the respective nucleus and α' is a phenomenological parameter similar to α_K in the Kronmüller equation. The idea of the thermal activation volume is based on the *magnetic viscosity* also-called the “after effect” that was described by Street and Woolley [Street and Woolley1949]. This effect describes the time dependency of magnetization processes usually under constant field. The respective factors in the global model can be determined by magnetic viscosity measurements. For Nd-Fe-B the activation volume was determined to be approximately 512 nm³, which corresponds to a nucleation diameter of 4.96 nm assuming a spherical nucleus [Givord1987a]. In this study, Givord *et al.* also found that the global model is not applicable to nanocrystalline Nd-Fe-B magnets. Furthermore it could be shown that the activation volume v_n is proportional to the third power of domain wall width δ_{DM} $(v_n \sim \delta_{DM}^3)$. Using this phenomenological equation, the global model can be converted into the Kronmüller model. According to Givord *et al.* the nucleation of a reversed domain at a defect at the applied field H_n is followed by the growth of the nucleus and entering the main phase at the respective fields H_{pass} and H_{expans} [Givord2003]. However the separation between passage and expansion is an artificial one, since both mechanisms are likely to intimately associated

From the described demagnetization models a few strategies can be derived to increase magnetic hardness in permanent magnets:

i) Substitution of elements to increase the *anisotropy field* either to obtain higher values of K_1 or to obtain lower values of J_s.
ii) Optimizing grain misalignment results in a higher H_c according to the and the Kronmüller equation.

iii) Grain size reduction to statistically mediate the effects of the nucleation field.
iv) Reducing the defect density to reduce the nucleation of a reversed domain. This becomes especially relevant for the grain boundary interfaces, since each grain boundary poses a two dimensional defect with lattice distortions vacancies etc.
v) Depending on the material system, pinning centers can be introduced that hinder the domain wall propagation once a nucleus is formed.

2.2 The M-Type hexaferrite system

Historically hexaferrites are one of the oldest materials that were used for permanent magnets. Although a similar magnetic M-type structure, called “*magento-plumbite*”, was known before, the main introduction of M-type hexaferrites into the permanent magnet market occurred in the early 1950s [Kools2003]. Unlike most other permanent magnet material systems, hexaferrites are ferrimagnetic i.e. have two antiparallel magnetic sub-lattices with a resulting net magnetic moment. Also untypical for magnets is that ferrites are oxides, which means that they are quite resistant against corrosion and oxidation. Furthermore they are electric insulators at room temperature, what makes them an interesting material for applications that produce a lot of eddy currents inside the magnet. The raw materials are quite abundant and of low price, making ferrites the most used material (by volume) for permanent magnets [Gutfleisch2011]. They are used for all kinds of applications that do not require a low volume or weight and where the price should be as low as possible e.g. low cost electro motors, loudspeakers etc. The term “*M-type hexaferrite*” usually referrers to magnets with $BaFe_{12}O_{19}$ or $SrFe_{12}O_{19}$ as the main magnetic phase. Since in this work only the latter is analyzed, all following discussions referrer to the M-type Sr-hexaferrite ($SrFe_{12}O_{19}$) system as ferrite or hexaferrite. The synthesis of the main phase occurs according to reaction:

$$SrCO_3 + 6Fe_2O_3 \rightarrow SrO + CO_2 + 6Fe_2O_3 \rightarrow SrFe_{12}O_{19} + CO_2 \qquad (2.16)$$

At calcination temperatures above 1206°C the M-type hexaferrite main phase is formed according to the phase diagram [Langhof2008]. The $SrFe_{12}O_{19}$ main phase particles are milled to a fine powder that is typically wet-pressed in a magnetic field to align the particles along their easy axis to produce textured magnets. Prior to the pressing sinter additives such as CaO and SiO_2 are added to control the grain growth during the sintering. The additives are liquid at the respective sintering temperature of about 1200°C, enwrapping the grains of the $SrFe_{12}O_{19}$ main phase. The addition of CaO suppresses grain growth along the basal plane, leading to a more cubical grain growth that is not only beneficial to obtain higher coercivity, but also leads to a higher density and thus better remanence. SiO_2 on the other hand suppresses the gain growth according to Kools *et al.* by the so-called *Reaction Induced Grain Growth Inhibition (RIGGI)* mechanism [Kools2003]. A precise control of the microstructure, especially grain size is essential to obtain good hard magnetic properties.
The hexagonal crystal structure of the $SrFe_{12}O_{19}$ main phase with the space group P6₃/mmc with the lattice parameters a = 5.884 Å (in the hexagonal lattice plain) and c = 23.06 Å is depicted in Figure 2.5.

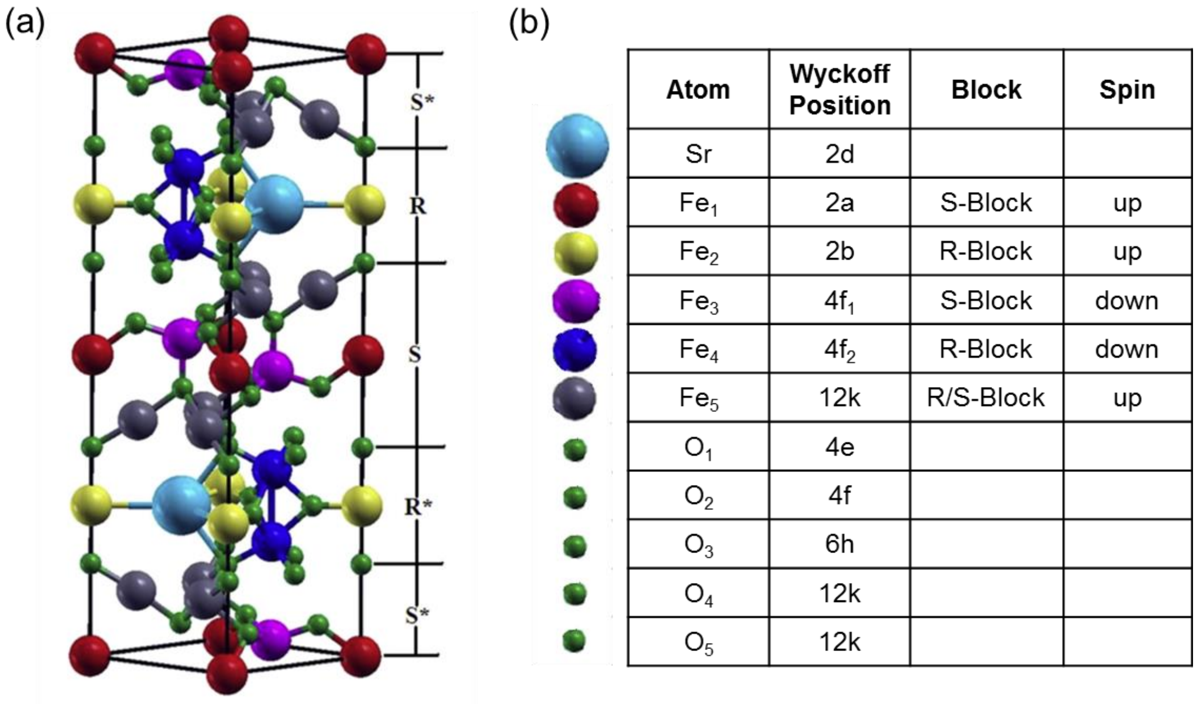

	Atom	Wyckoff Position	Block	Spin
●	Sr	2d		
●	Fe_1	2a	S-Block	up
●	Fe_2	2b	R-Block	up
●	Fe_3	$4f_1$	S-Block	down
●	Fe_4	$4f_2$	R-Block	down
●	Fe_5	12k	R/S-Block	up
●	O_1	4e		
●	O_2	4f		
●	O_3	6h		
●	O_4	12k		
●	O_5	12k		

Figure 2.5 (a) Crystal structure of the M-type Sr-hexaferrite [Moitra2014] and (b) atomic lattice positions and spin direction of the Fe atoms.

The unit cell of the M-type hexaferrite can be divided into an S- and an R- block. The S-block denotes a two-layer block that contains two O_4 with the composition $Fe_6^{3+}O_8^{2-}$ with Fe on the 2a, $4f_1$ and 12k positions [Moitra2014], while the R-block denotes a three-layer block containing two O_4 and one SrO_3 with the composition $Sr^{2+}Fe_6^{3+}O_{11}^{2-}$ with Fe on the 2b, $4f_2$ and 12k positions. The asterisk denotes the rotation of the corresponding block by 180° around the c-axis. The only magnetic ions in the Sr-hexaferrite are the Fe^{3+} ions that contribute 5 μ_B each due to their 5d orbital´s electron configuration and Hund´s rule. The Fe^{3+} ions occupy three different kinds of sites: tetragonal, octahedral and hexahedral. Each Fe^{3+} coordinated by several O^{2-} ions that allow their spins to interact with the respective “next” Fe^{3+} ion via a process called *superexchange*. Despite O^{2-} not having a net spin moment, it can act as a mediator when it comes to the *“*exchange*”* interaction between ions, hence the term superexchange. By applying this principle to the hexaferrite unit cell, one can arrive at the conclusion that 16 Fe^{3+} ions display an “up” magnetic moment, while 8 display a “down” magnetic moment. With 5 μ_B per Fe^{3+} ion this results in 40 μ_B per unit cell or 20 μ_B per formula unit i.e. ($SrFe_{12}O_{19}$). This corresponds for Ba-hexaferrite to approximately 100 Am^2/kg, which agrees exactly with the measured value of the saturation magnetization at 0 K [Cullity and Graham2008].

The saturation magnetization in hexaferrites can be increased by substituting the “spin-down” Fe atoms on the $4f_1$ and $4f_2$ position by elements of lower magnet moments i.e. less unpaired electron in the d-orbitals. Such a substitution can be done with Co^{2+} ($3d^9$ with 1 μ_B), with Zn^{2+} ($3d^{10}$ with 0 μ_B) or with Co^{2+} ($3d^7$ with 3 μ_B) [Carey1994, Bai2002]. Another way to increase the resulting magnetic moment is by reducing Fe^{3+} to Fe^{2+} hence having a $3d^6$ with 6 μ_B configuration, which can be achieved by substituting Sr^{2+} with La^{3+} [Dung1997, Grossinger2003, Wang2004]. The substitution also leads to a reduced c-lattice parameter, which reduces the antiferromagnetic coupling between the Fe^{3+} ions.

In this work the influence of the partial substitution of Fe^{3+} by Al^{3+} on the magnetization behavior is analyzed. The Al substitution is mainly performed to increase the anisotropy field and coercivity. The general relation between the involved parameters is given in equation 2.12 and 2.14. In $SrFe_{12}O_{19}$ K_1 is approximately 0.357 MJ/m³, which results in an anisotropy field of 1.9 T for the unsubstituted main phase [Kools2003]. According to Nga *et al.* the substitution of Fe^{3+} by Al^{3+} slight reduction of K_1 depending on the Al content x per formula unit [Nga2012]:

$$K_1(x) = \frac{K_1(0) \cdot (24 - 4x)}{24} \tag{2.17}$$

Despite the fact that K_1 is reduced by the Al substitution, the process still results in a higher anisotropy field due to the fact that the Al^{3+} ions primarily substitute Fe^{3+} ions on the position 2a and 12k, thus reducing the saturation magnetization per unit cell [Kazin2008]. The reduction of saturation magnetization can also be approximated to be a function of the Al substitution per formula unit for $x < 6$ [Nga2012]:

$$M_s(x) = \frac{M_s(0) \cdot (12 - 3x)}{12} \tag{2.18}$$

With $M_s(0) = 0.478$ T for the unsubstituted $SrFe_{12}O_{19}$ compound. The strong reduction of saturation magnetization is the reason, why the Al substitution leads to an overall higher anisotropy field and coercivity. Other factors like grain shape and grain size also play an important role, which is why the microstructure in ferrites is very carefully engineered by using the appropriate sinter profile, sinter additive, milling procedure etc. Ferrites are generally regarded to be nucleation dominated magnets. However, several authors have argued that pinning processes might also play a role in this material system [Welte Mahltechnik1995, Taguchi1998, Kools2003, Nishio2009, Alsmadi2013].

2.3 The Nd-Fe-B system

The discovery of the Nd-Fe-B permanent magnet 1984 was the result of intense research to find a substitution for the then widely used Sm-Co magnets. Due to the scarcity of Co originating from the political unrest in the Congo, the efforts were focused to find a Co-free alternative to the *then* most powerful permanent magnet system. As a result the discovery was made by three different groups almost simultaneously: by using a powder metallurgical route by Sagawa *et al.* [Sagawa1984] and via rapid solidification by Croat *et al.* [Croat1984]. Hadjipanayis *et al.* also used rapid solidification, however, with Pr instead of Nd (which is nowadays a typical additive in industrial production) as well as additional Si [Hadjipanayis1983]. Immediately after their discovery till today, Nd-Fe-B permanent magnets are the permanent magnets with the highest energy product making it the material of choice for all kinds of high performance application that either require low volume, low weight or high magnetic properties. The downside is that they are also one of the most expansive permanent magnets due to their rare earth component. Commercial Nd-Fe-B magnets are produced by two separate routes: either i) powder metallurgical to produce sintered magnets (see chapter 2.3.1) or ii) by hot deformation to produce hot-deformed magnets (see chapter 2.3.3).

The magnetic phase that most of the Nd-Fe-B excellent magnetic properties are attributed to is the so-called Φ-(rarely also τ1) phase with the composition $Nd_2Fe_{14}B$, which is also referred to as 2-14-1 or 2-14-B. However, to obtain the extrinsic hard magnetic properties (i.e. high coercivity), other secondary phases are essential. For the production of permanent magnets the phase formation is obtained by producing a pre-alloy i.e. by melting the respective elemental composition. It is of vital importance to suppress the formation of soft magnetic phases, especially α-Fe during the cooling down process and any following heat treatment e.g. sintering. The respective isothermal phase diagram of the ternary composition at the approximate sintering temperature of 1000°C is depicted in Figure 2.6 [Malfliet2008]. The composition and temperature treatment (cooling down, sintering etc.) should to be chosen to take place in the “Φ + L” regime. Through compositional shifts, i.e. due to oxidation, evaporation, insufficient mixing etc., a variety of other phases can form such as $N_{1.1}Fe_4B_4$ (also-called η or τ2), γ-Fe, Fe_2B, and Nd_2Fe_{17}. While paramagnetic phases like $N_{1.1}Fe_4B_4$ “only” lead to a slight reduction in saturation/remanent magnetization, at room temperature soft-ferromagnetic phases like γ-Fe, Fe_2B, and Nd_2Fe_{17} have a detrimental effect on the coercivity since they lead to a magnetic coupling of the 2-14-1 grains [Schneider1990]. Since they are soft magnetic these phases also pose nucleation sites for reversed domains, thereby decreasing coercivity.

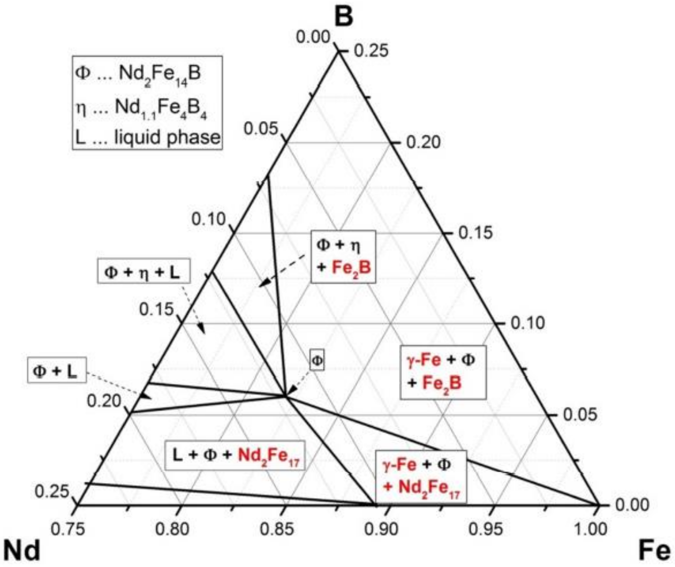

Figure 2.6 Isothermal section of the ternary Nd-Fe-B phase diagram near the iron rich region at 1000°C [Malfliet2008, Löwe2016].

In the “quasi binary” phase diagram displayed in Figure 2.7 it can be seen, that for Fe concentrations larger than 77 at.%, elemental Fe is formed during the cooling process from the liquid phase. This formation can be suppressed by choosing a composition close to the peritectic point with a slight surplus of Nd and B, by rapid cooling or by a subsequent homogenization annealing step.

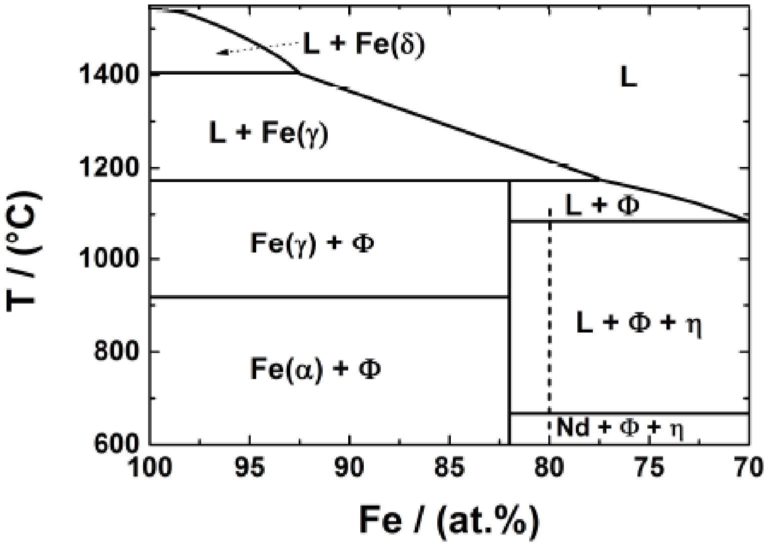

Figure 2.7 Quasi binary phase diagram of Nd-Fe-B with a fixed ratio of Nd:B of 2:1 after Schneider *et al.* [Schneider1986]. The composition of a sintered magnet is indicated by the dashed line.

For permanent magnet production off-stoichiometric compositions are used to obtain good magnetic properties. The stoichiometric composition of the $N_2Fe_{14}B$ phase corresponds to a Nd content of 11.76 at.% and a total composition of $Nd_{11.76}Fe_{82.35}B_{5.88}$ at.% or $Nd_{26.68}Fe_{72.32}B_{1.00}$ wt.%. To this ratio a surplus of Nd is added for several reason: As can be seen in the phase diagram in Figure 2.7 a higher Nd ratio at the sintering (or hot deformation temperature) of approximately 1000°C (or 750°C) results in the formation of a liquid (L) phase, which is essential to create dense magnets. The secondary phases that are forming as a result are also responsible for the coercivity mechanism in Nd-Fe-B magnets, which are usually referred to as Nd-rich or grain boundary phase. Furthermore a surplus of Nd and B is also essential to “bind” impurities of C, O or N that are picked up during the process, by forming secondary Nd- or Nd-boride phases. A typical value to form the Nd-rich grain boundary phase is ideally at least 2 wt.% of additional Nd [Rodewald2002]. Assuming e.g. for a sintered magnet, the amount of impurities of O, N, and C [Li2009] and the formation of their respective compounds (Nd_2O_3, NdN and NdC Sasaki [Sasaki2015]) an additional 2.89 wt.% of Nd has to be accounted for [Löwe2016]. Assuming also a Fe to B ratio of 14 to 1.05 at.% (i.e. a surplus of 5 at.% B) the final composition would be $Nd_{31.57}Fe_{67.45}B_{0.98}$ wt.% or $Nd_{14.43}Fe_{79.60}B_{5.97}$ at.%. Additional of elements such as refractory metals like Ti, Nb, Mo, Zr, can be added in small concentrations to influence and suppress the grain growth during the production, while elements like Cu, Ga, Sn, Al are typically added to form low meting eutectics which are beneficial to obtain a high amount of liquid phase during the sintering or hot-deformation. Elements like Co, Pr, Dy, Tb, are often added to the composition in low quantities to improve the intrinsic parameters of the 2-14-1 phase such as anisotropy field H_a or Curie temperature T_c [Herbst1991].

The secondary phases agglomerate at the grain boundary in the final magnet and are thus usually referred to as “Grain Boundary Phase” (GBP) or “Nd-rich phase”. However, they actually consist of multiple phases that have been reported to be metallic, oxidic, crystalline, amorphous, ferromagnetic and paramagnetic [Fidler and Knoch1989, Mo2008, Sepehri-Amin2011, Woodcock and Gutfleisch2011, Sepehri-Amin2012, Woodcock2012]. In other words, it is not easy to derive any definitive conclusion concerning the working mechanism of the GBP. Most important to understand the coercivity mechanism is probably the distinction whether the GBP is ferro- or paramagnetic. A paramagnetic GBP (as generally assumed) would result in a magnetic decoupling of the grains from each other [Gutfleisch2000a] meaning that the demagnetizing mechanism would be purely nucleation dominated. In the case of a ferromagnetic GBP, as suggested by Sepehri Amin *et al*. [Sepehri-Amin2011], the demagnetizing process might also include pinning effects of domain walls at the grain boundary. Since the magnetic properties of the GBP is experimentally not accessible, the claims regarding their magnetic properties are generally made by quantifying the amount of ferromagnetic elements i.e. Fe or Co in the GBP by local probing techniques like TEM or Atom Probe Tomography (APT). An insight into the magnetic behavior can be gained from the initial magnetization curve from the TDS as done by Sepehri-Amin *et al*. [Sepehri-Amin2011].

Concerning the chemical composition and morphology of the GBP it was reported that large, usually round grains, showing a bright contrast in the Scanning Electron Microscope (SEM) by Back Scattered Electron (BSE) imaging mode, usually consist of oxide phases, while angular shaped grains as well as the thin grain boundary layer is usually metallic [Woodcock and Gutfleisch2011, Sepehri-Amin2012]. The oxidic phases consist of fcc-NdO, hcp-Nd_2O_3 or c-Nd_2O_3, depending on the heat treatment that the magnet has undergone [Kim2011, Woodcock and Gutfleisch2011]. Metallic phases are fcc-Nd as well as a Ia-3 phase and $Nd_{1.1}Fe_4B_4$ [Sasaki2016]. If the grain boundary is thinner than 1 nm, the GBP has a tendency to become amorphous as reported by Shinba *et al.* [Shinba2005].

Beyond the magnetic decoupling of the grains (assuming a paramagnetic behavior), the secondary phases are also widely assumed to reduce stress in the $Nd_2Fe_{14}B$ phase and a recovery in the intergranular region [Szymura1999, Shinba2005] as well as reducing and/or removing defects at the $Nd_2Fe_{14}B$ grain surfaces [Woodcock2012].

Additionally the GBP takes part in the Grain Boundary Diffusion Process (GBDP, see 2.3.4), by supplying a diffusion pathway for the HRE. At the temperature the GBDP is performed, the GBP is considered to be liquid [Seelam2014, Loewe2015] enabling the HRE diffusion along the grain boundaries into the magnet, where it substitutes Nd in the 2-14-1 phase.

One part of the excellent hard magnetic properties of Nd-Fe-B magnets lies in the careful engineering of the microstructure and grain boundaries, the other part lies in the close to perfect crystal structure of the $Nd_2Fe_{14}B$ main phase depicted in Figure 2.8.

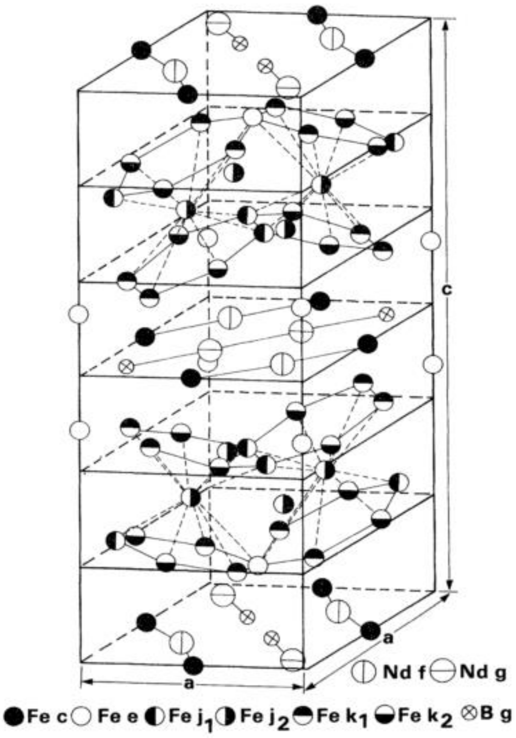

Figure 2.8 Crystal structure of the $Nd_2Fe_{14}B$ main phase (Φ-phase) [Herbst1991].

The unit cell crystallizes in a tetragonal symmetry containing 68 atoms corresponding to 4 formula units and the $P4_2/mnm$ space group [Herbst1991]. Within the unit cell with the lattice constants a = 8.80 Å and c = 12.19 Å, are 6 different Fe, 2 Nd and 1 B lattice positions. Very characteristic is that the Fe atoms are arranged into rings with Nd atoms lying between them. In this constellation Fe is responsible for the large magnetic moment and high Curie temperature of the phase, while Nd with its localized 4f electron is responsible for the high magnetocrystalline anisotropy [Fahnle1993]. B does not contribute magnetically, however, is responsible for the thermodynamic phase stability [Herbst1991]. Below the temperature of 135 K the phase undergoes a spin reorientation and changes from an easy axis anisotropy to an easy cone anisotropy [Herbst1991]. At higher temperatures the magnetization and anisotropy reduces with increasing temperature. To compensate this effect, commercial magnets are often substituted with HRE like Dy and Tb. For low concentrations Dy and Tb substitute Nd without causing a significant change in the crystal structure or phase composition. In this range, the respective properties scale linearly with the replacement ratio [Hirosawa1986]. The anisotropy fields of the fully substituted compounds are approximately two to three times larger than the unsubstituted $Nd_2Fe_{14}B$ compound as shown in Table 1.

	$\mu_0 J_s$ (T)	$\mu_0 H_a$ (T)	T_c (K)
$Nd_2Fe_{14}B$	1.60	7.30	585
$Dy_2Fe_{14}B$	0.71	≈15	598
$Tb_2Fe_{14}B$	0.70	≈22	620

Table 1 Intrinsic magnetic properties of $Nd_2Fe_{14}B$, $Dy_2Fe_{14}B$ and $Tb_2Fe_{14}B$ [Herbst1991].

For $Dy_2Fe_{14}B$ and $Tb_2Fe_{14}B$ the significantly lower saturation magnetization in comparison to $Nd_2Fe_{14}B$ is the result of antiferromagnetic coupling the HRE magnetic moments with the Fe sub-lattice [Boltich1985, Herbst1991]. In $Dy_2Fe_{14}B$ the higher anisotropy field can be largely be attributed to the lower saturation magnetization according to equation 2.12, since the K_1

values of the two compounds ($Nd_2Fe_{14}B$ and $Dy_2Fe_{14}B$) are almost identical [Herbst1991]. For $Tb_2Fe_{14}B$ on the other hand the 3 times higher anisotropy field (with respect to $Nd_2Fe_{14}B$) of 22 T is the result of the lower saturation magnetization and a higher K_1 value combined. A partial substitution of Dy or Tb in $Nd_2Fe_{14}B$ also slightly increases the Curie temperature due to the higher T_C of the $Dy_2Fe_{14}B$ and $Tb_2Fe_{14}B$ (see Table 1). A higher T_C can also be obtained by substituting Fe by Co or Ni [Herbst1991]. While the former can also result in a higher saturation magnetization and is done for commercial magnet, the latter drastically reduces the saturation magnetization [Herbst1991]. As a result of the different anisotropy constants the substitution of Dy and Tb also alters the characteristic values involved in the domain formation process. A comparison of the micromagnetic parameters for the components $Nd_2Fe_{14}B$, $Dy_2Fe_{14}B$ and $Tb_2Fe_{14}B$ is summarized in Table 2.

	$Nd_2Fe_{14}B$	$Dy_2Fe_{14}B$	$Tb_2Fe_{14}B$
A (pJ/m)	$8^{(6)}$; $7.3\text{-}8.4^{(5)}$	(8*)	(8*)
K_1 (MJ/m³)	$4.9^{(6,*)}$; $4.3^{(5)}$; $4.5^{(2)}$	$4.2^{(4)}$; $4.0^{(2)}$	$6.2^{(4)}$; $6.7^{(2)}$
K_2 (MJ/m³)	$0.65^{(5)}$	-	-
l_{ex} (nm)	1.28*	1.37*	1.13*
δ_{DW} (nm)	4.02*	4.30*	3.56*
γ_{DW} (mJ/m²)	25.04*	23.32*	28.20*
d_c (nm)	218*	1044*	1625*

Table 2 Comparison of intrinsic and micromagnetic parameters of different $RE_2Fe_{14}B$ compounds: Exchange constant A, anisotropy constants K_1, and K_2, exchange length l_{ex}, domain wall width δ_{DW}, domain wall energy γ_{DW}, and critical single domain size d_c according to [Hirosawa1986(1), Sagawa1987(2), Herbst1991(3), Lee1999(4), Kronmüller2007(5), Coey2010(6), Sawatzki2015] values marked * are calculated from the values given in literature according to equation 2.12 assuming the same exchange constant A.

2.3.1 Sintered magnets

Sintered magnets are the classical powder metallurgical approach to produce Nd-Fe-B magnets. An advantage of this production method is that for simple shapes, near net shaped magnet geometries can be realized (depending on the used pressing/alignment procedure). The pre-alloy of the desired composition is crushed and milled down to the desired particle size. This process is the most critical and most defining step since it largely defines the grain size of the sintered magnet. As mentioned before, smaller grains statistically result in a higher coercivity since they possess a lower demagnetized volume per surface defects i.e. nucleation sites for reversed domains [Uestuener2006, Li2009]. At the same time smaller particles have a higher tendency to pick up impurities, mainly O, during the process. Thus for a given milling process, powder composition and oxygen content result in a critical particle diameter D_{crit} below which the coercivity deteriorates drastically [Nothnagel1991]. The technical difficulties that come with the additional processing steps for the grain size reduction also make the whole procedure economically less feasible, to the point where a HRE substitution becomes the better alternative. The partial substitution of Nd with HRE like Dy or Tb changes the intrinsic properties of the 2-14-1 phase, most importantly for most applications are anisotropy field H_a and Curie temperature T_C [Herbst1991]. A lower particle size also means that the particles are harder to align in a magnetic field to induce texture in the subsequent step since the friction between individual grains increases. A typical particle size of commercial sintered magnets is around 5 µm even though smaller particles in the range of 1 µm can also be obtained [Goto2011]. Since the grain size in Nd-Fe-B sintered magnets is generally larger than the critical single domain size (see Table 2) sintered magnets are largely considered to be nucleation dominated [Kronmüller1985, Givord1988, Schrefl1993, Li2009, Woodcock2012, Bance2015a, Sepehri-Amin2016] however, for fine grained magnets a pinning mechanism has also been proposed [Sepehri-Amin2011].

The powder particles are aligned in a magnetic field to induce texture and consolidated into a green body, at pressures around 200 MPa. As already mentioned smaller grains generally lead to a higher average misalignment since the grains exhibit a higher internal friction due to the larger surface area. Depending on the respective pressing technique different properties can be obtained that also result in the corresponding processing cost [Hilzinger and Rodewald2013]. Most importantly has to be differentiated between uniaxial and isostatic pressing. Isostatic pressing typically results in a low grain misalignment during the process and hence a high remanence. Uniaxial pressing can be further divided into transversal- (TP) and axial field pressing (AP). While TP results in a lower grain misalignment close to isostatic pressing, AP enables a better net shape magnet production [Hilzinger and Rodewald2013].

The sintering temperature is usually around 1000°C, allowing the formation of a liquid phase depending on the composition. To avoid oxidation and the agglomeration of impurities, it is essential that the manufacturing process from milling to sintering is performed under protective gas atmosphere or vacuum. During the sintering step a fully dense magnet should be obtained to achieve a maximum saturation/remanent magnetization and coercivity. At the same time the sintering parameters i.e. sintering temperature and duration have to be low enough to suppress abnormal grain growth. Finer powders generally require lower sintering temperatures but are also more likely to undergo abnormal grain growth if the sintering temperature is too high [Uestuener2006]. Under optimal sintering conditions the grain size of the final magnet is approximately double the initial particle size [Uestuener2006].

To obtain maximum coercivity it is essential that a so-called *Post Sinter Annealing* (PSA) is carried out after the sintering process. The ideal PSA temperature highly depends on the respective composition e.g. in the original work by Sagawa *et al.* the PSA was performed at 610°C [Sagawa1984], while other authors found the optimum temperatures to be as low as 480°C [Yan2006]. The addition of Cu in low concentrations typically decreases the optimum PSA temperature. A typical PSA duration is about 2 h. It has also been reported by Shinba *et al.* that a two-stage PSA at 800°C and 500°C was used to fine tune the magnetic properties.

Most theories regarding the processes that are occurring during the PSA are centered around the grain boundaries: Schneider *et al.* proposed the presence of a metastable magnetically soft phase, which is dissolved during the PSA thus decoupling the grains and reducing internal demagnetization fields [Schneider1990]. Another theory, suggested by Shinba *et al*. states that the formation of small amounts of liquid phase (above the eutectic temperature of 665°C) causes a more uniform distribution of the GBP and a uniform grain boundary thickness of a few nm [Shinba2005]. A second PSA at 500°C below the eutectic point is supposed to decrease the defect density at the grain boundaries, which are assumed to be act as nucleation sites of reversed domains. Kim *et al.* also found a change in crystal structure of Nd_2O_3 from hexagonal to cubic during the PSA [Kim2012]. This transition is supposed to reduce the stress at the $Nd_2Fe_{14}B$ and grain boundary interface by reducing the lattice misfit. The authors also concluded that the enrichment of Cu at the grain boundary plays a significant role during the process to reduce stress at the interfaces to the amorphous grain boundaries. The same Cu segregation at the grain boundary was also confirmed by Sepehri-Amin *et al.* using APT. In atomistic structure modeling (based on TEM investigations) done by Hrkac *et al.* [Hrkac2014b] the authors confirmed that the “depth” of the distortion of the $Nd_2Fe_{14}B$ crystal structure depends in the crystal structure of the GBP and can reduce the magnetocrystalline anisotropy. In a study done by Woodcock *et al.*

[Woodcock2014a] in Cu lean magnets, it was shown that the process was fully reversible (for at least 3 times) and was completed after only 5 minutes suggesting that the process is not based on long-range diffusion as proposed by Kim *et al.* [Kim2012]. The mechanism proposed by Woodcock *et al.* suggests that the PSA results in an overall better coverage of the 2-14-1 grains by the GBP. The role of a low-melting Nd-Cu eutectic could also be largely ruled out due to the low Cu content leading the authors to the conclusion that a low melting Nd-rich phase penetrates the gaps between $Nd_2Fe_{14}B$ grains resulting in an ideal distribution of the Nd-rich phase.

As an overall conclusion it can be said that the precise role of the PSA is not completely understood, but is most likely linked to the defect density at the grain boundary.

2.3.2 Demagnetization observation in Nd-Fe-B sintered magnets

In order to provide some basic understanding for the results discussed in chapter 5 and chapter 7.1, the *in-situ* demagnetization under external magnetic field of an exemplary Nd-Fe-B sintered magnet is shown in Figure 2.9. To observe magnetic domains in sintered magnets e.g. by Kerr microscopy (see chapter 3.2.3) or magnetic force microscopy (MFM see chapter 3.2.5) the surface has to be polished using standard metallographic methods. As a result of the polishing procedure, the surface grains are not covered by the GBP anymore and the highly reactive surface is exposed to oxidation by ambient oxygen. The respective exposure to air has to be minimized in order to minimize oxidation. As a results of the polishing procedure the coercivity of the respective surface grains is drastically reduced [Hirosawa1987, Fukagawa and Hirosawa2008, Nakamura2012, Kobayashi2015]. While some authors have claimed that this is a result of the mechanical deformation of the surface [Hirosawa1987], others have attributed it to a combination of surface deformation and oxidation [Pastushenkov1994]. Surface grains typically show a coercivity of approximately 0.2 T to 0.6 T (depending on the composition) which means that, depending on the sample geometry, in the remanent state the self-demonization can already suffice to demagnetize a large portion of the surface grains. This is shown in in Figure 2.9, where the first image shows the saturated state at 10 T where all grains are in a SDS. The grain boundaries can be seen as a slightly bright contrast between the grains as well as secondary i.e. non-magnetic phases that also show a bright contrast. In the remanent state at 0 T, a large fraction of the previously SDS grain collapse to a MDS due to the above mentioned reduced coercivity of surface grains and the demagnetizing field of the sample. The MDS in the remanent state show star-like, bubble-like and stripe-like domains. Which type of domain structure forms depends not only on the grain orientation and “thickness” which is latitude in z direction, but also on the domain structure of the surrounding grains. A few grains in the upper part marked 1, 2, 3, 4 and 5 in the first images maintain their SDS at 0 T and also maintain their SDS at low demagnetizing fields. At a demagnetizing field of -0.09 T and -0.8 T, the grains 1 and 3 collapse to a MDS.

At the same time, the domain structure of the MDS grains gradually alter their shape and show an increasing amount of dark domains. At a field of -1.34 T, the grains marked 1 and 4 form a SDS again, at least within the limited area of the grains which is depicted. While those grains have reversed their magnetization state by forming an intermediate MDS, the grains marked 2, 4 and 5 seem to reverse their magnetization state from -1.34 T, -1.46 T and -1.8 T SDS to the reversed SDS within a rather small field range. Of course it cannot be excluded that the observed grains form a MDS between the respective two observed external fields. However, the images allow the conclusion that some grains might change their magnetization by a single domain like behavior despite being far larger than the cirtical single domain size. It is noteworthy that each grain requires different external fields to expel the domain walls and reach a SDS, for instance the grain marked 6 is in a MDS at 0 T and reobtains a SDS at -1.34 T. The grain marked 7 on the other hand is already in a SDS at -0.8 T, while the grain marked 8 requires a field of -2.0 T to expel domain walls. The different magnetization behavior might be caused by slightly different orientation of each grain (as assumed by the Stoner-Wohlfarth model), but it is more likely that the magnetic surrounding of each individual grain is responsible as well as statistical effects, meaning that only a limited amount of grains can be observed at the same time. Since the influence of these factors is hard to exclude or to verify, a quantitative comparison of nucleation or saturation fields cannot be performed in this kind of analysis. Furthermore, the size of the depicted area is with 30 x 30 µm² close to the maximum scanning range of the MFM (35 x 35 µm²) used in this PhD thesis. Due to the large grain size of sintered magnets, only a few grains can be depicted at the same time, limiting the statistic of the measurement. An alternative technique could be Kerr microscopy, however for Kerr microscopy the maximum applicable field is lower and far more inhomogeneous, which makes quantification very hard.

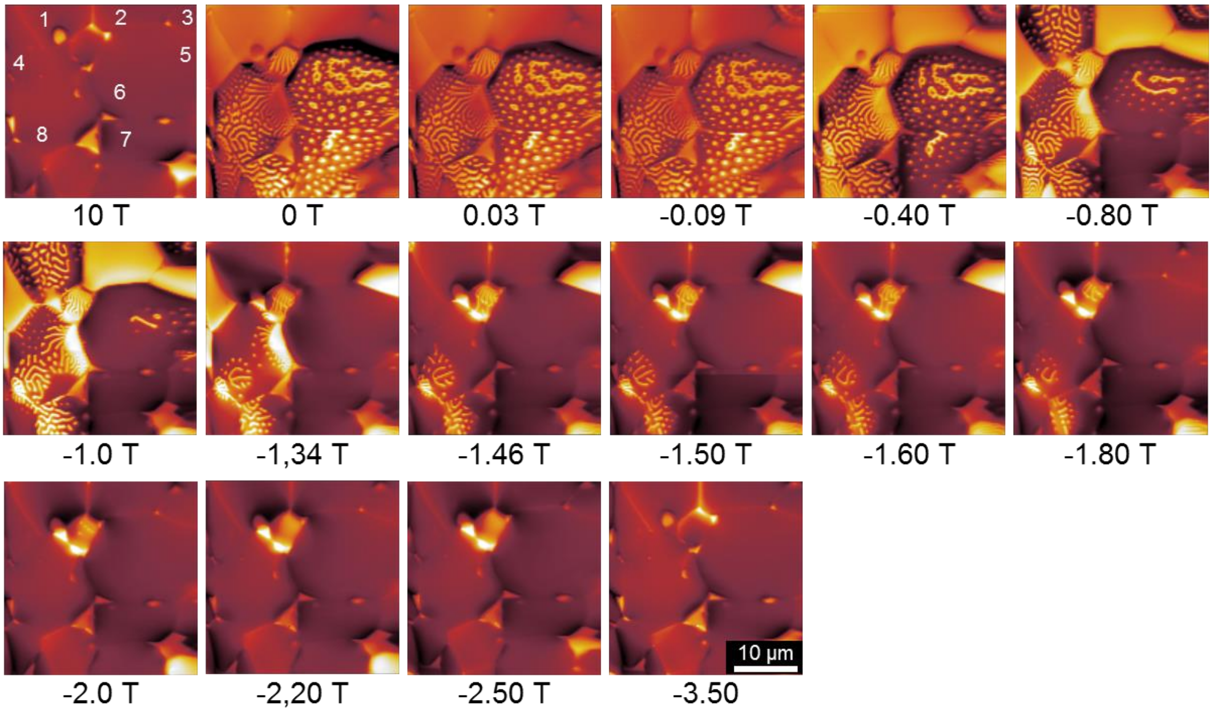

10 T 0 T 0.03 T -0.09 T -0.40 T -0.80 T

-1.0 T -1,34 T -1.46 T -1.50 T -1.60 T -1.80 T

-2.0 T -2,20 T -2.50 T -3.50

Figure 2.9 Domain evolution in Nd-Fe-B sintered magnets during demagnetization.

2.3.3 Hot-deformed magnets

The hot-deforming process in Nd-Fe-B magnets in used to induce a texture into the magnet, while maintaining a nanocrystalline microstructure. Essential for the hot-deformation and texturing process is the production of a powder with a polycrystalline, nanocrystalline or amorphous microstructure. This can be obtained by mechanical alloying and solid state reaction [Schultz1987], the so-called "Hydrogen–Disproportionation–Desorption–Recombination" HDDR-process [Harris1985, Gutfleisch1998, Gutfleisch1998b, Gutfleisch2000a, Gutfleisch2013] or by rapid solidification [Hadjipanayis1983, Croat1984].

The process is typically separated into a consolidation and a deformation process. During the consolidation, which is done at temperature above the melting point of the Nd-rich phase, a compact body is formed. During the subsequent deformation process, which is also performed above the melting point of the Nd-rich phase, the texture along the c -axis is induced. Essential for the texturing process is the material transport within the liquid grain boundary phase. However, a low texture can also be induced at temperature of 600°C. According to Grünberger *et al.* this can be attributed to a grain-rotation through a gliding of the grains along the grain boundaries [Grünberger1997]. A few different approaches have been developed to explain the texturing process in nanocrystalline magnets [Lee1985, Mishra and Lee1986, Tenaud1987, Graham and Li1989, Li and Graham1990]. A well accepted concept is the so-called "Solution-Precipitation-Creep-Model, which was adapted to Nd-Fe-B magnets by Grünberger *et al.* [Grünberger1997]. The model is based on the anisotropic elastic properties of the tetragonal $Nd_2Fe_{14}B$ unit cell. This concludes that under uniaxial pressure the grain growth along the a-b-plane is favored in comparison to the c-axis. Assuming a material transport through the liquid GBP this results in a larger growth of grains that have a c axis parallel to the pressing direction. The resulting final microstructure consists of platelet shaped grains typically in the range of a few hundred nm.

Using different geometries, this process can be adapted to a variety of hot deformation techniques. In comparison to sintered magnets, hot-deformed magnets have a higher temperature- [Brown2014] and corrosion-stability [Grieb1997]. Hot-deformed magnets are known to form interaction domains (described in chapter 2.1.1) due to their nanocrystalline grain size and texture [Khlopkov2007]. Most importantly this means that the demagnetization mechanism cannot be categorized as nucleation or pinning.

2.3.4 The Grain Boundary Diffusion Process (GBDP) and core-shell-approach

As mentioned in the previous chapters, one of the main areas of application for Nd-Fe-B permanent magnets are high performance motors and generators that operate at temperature of 150 - 200°C [Gutfleisch2011, Brown2014]. As a result of the temperature dependence of the magnetocrystalline anisotropy and magnetization, Nd-Fe-B magnets suffer from poor temperature stability and display a significantly lower $(BH)_{max}$ at these elevated temperatures. This is especially critical for the coercivity since the magnets can self-demagnetize depending on the respective magnet geometry. As mentioned previously these effects can be compensated by the substitution of HRE such as Dy or Tb for Nd which results in a higher anisotropy field and slightly higher Curie temperature [Herbst1991]. This simultaneously lowers the obtained saturation and remanent magnetization and also drastically increases the production cost due to the high raw materials price of Dy and Tb. A solution to the problem was introduced to sintered Nd-Fe-B magnets by Park *et al.* [Park2000] by forming a core-shell structure in each grains consisting of a thin HRE substituted shell and a "pure" Nd-Fe-B core. This idea is based on the widely assumed theory that the demagnetization process starts at the grain boundary by the nucleation of a reversed domain. By substituting only the shell, the "weakest link" i.e. the defect dense regions close to the grain boundary are magnetically hardened using a minimum amount of HRE, while simultaneously maintaining the high magnetization of the unsubstituted $Nd_2Fe_{14}B$ core. Since the total volume of the shell is small in comparison to the core the loss in volume magnetization due to the substitution is minimal. Most theories regarding the nucleation of a reversed domain at the grain boundary [Kronmüller1985, Kronmüller1987, Givord1988, Kronmüller1988, Hrkac2014a] assume that the nucleation diameter or respective defect layer (due to lattice distortion) is in the range of a few nm. A magnetic hardening should be obtained if the shell is covering this range, meaning that shell only needs to be a few nm thick [Bance2015a, Bance2015b]. The industrially applied method to obtain such core-shell structured magnets is the so-called Grain Boundary Diffusion Process (GBDP). For this procedure a magnet is covered with a HRE or HRE compound and subjugated to a heat treatment. The respective HRE concentration gradient causes the diffusion into the magnet in accordance with Fick´s law. Due to the fact that the grain boundary is liquid during the heat treatment, the diffusion along the grain boundary occurs much faster than the bulk diffusion [Seelam2014, Loewe2015]. The HRE accordingly diffuses primarily along the grain boundaries, forming thin HRE rich regions (shell) in each grain near the grain boundary, while the grain center remains HRE free. While other authors have implied that the shell formation occurs via solid state diffusion from the liquid grain boundary into the $Nd_2Fe_{14}B$ main phase, others have claimed that the shell forms due to the (re-)solidification of the HRE-rich grain boundary phase [Sepehri-Amin2010, Seelam2014, Loewe2015]. Sepehri-Amin *et al.* could show that the process forms a uniform Dy concentration across the $(Nd,Dy)_2Fe_{14}B$ phase and the adjacent grain boundary phase [Sepehri-Amin2010]. As a result of the HRE substitution for Nd, the excess Nd is ejected from the 2-14-1 main phase and segregated at the grain boundary.

Löwe *et al.* assumed proportionality between HRE concentration and *coercivity* and used the following equation to describe the GBDP for a constant source [Loewe2017]:

$$H_c(x,t) = H_{c,surf} - (H_{c,surf} - H_{c,bulk}) \cdot \mathrm{erf}(\frac{x}{\sqrt{4Dt}}) \tag{2.19}$$

With $H_{c,surf/bulk}$ as the respective coercivity for the magnetic layer closest to the HRE source ($H_{c,surf}$) and the layer that was far enough from the Dy source to be unaffected by the GBDP ($H_{c,bulk}$). Here x is the distance from the HRE source and D the diffusion coefficient, which was determined to be $8.45 \pm 1.10 \cdot 10^{-7}$ cm²/s for Dy and $1.23 \pm 0.84 \cdot 10^{-6}$ cm²/s for Tb at 900°C for a HRE lean Nd-Fe-B magnet. Depending on the diffusant, diffusion temperature and duration, a magnetic hardening effect can be observed at diffusion depths of several mm [Loewe2017]. Sepheri-Amin *et al.* could show an enhanced Dy concentration at the grain boundary using APT by investigating a spot approximately 2.7 mm deep into the magnet [Sepehri-Amin2013b].

The GBDP can be done using the pure metallic Dy or Tb [Park2000, Sepehri-Amin2010, Loewe2017] using the respective fluorites [Komuro2010, Nakamura2011] as well as low-melting-eutectics such as Dy-Ni-Al [Oono2011, Liang2014]. While the GBDP was initially applied to sintered Nd-Fe-B magnets, in recent years it was also applied to hot-deformed Nd-Fe-B Magnets [Sepehri-Amin2013a, Akiya2014, Liu2016, Sawatzki2016]. In hot-deformed magnets the GBDP is usually carried out at lower temperatures (around 600°C) in comparison to sintered magnets (around 900°C) to minimize grain growth. To ensure sufficient wettability at these temperatures, a low melting binary or ternary eutectic is typically used [Liang2014, Sawatzki2014b].

The maximum diffusion length of a few mm is limiting the size of the magnet to be in the same range in at least one dimension and cannot be up-scaled. In order to adapt the process to bulk samples, several authors used a powder-metallurgical approach to obtain core-shell structured grains. The procedure involves the blending of a Nd-Fe-B “base-powder” with a HRE containing “anisotropy-powder” prior to the aligning, pressing and subsequent annealing. Ideally the “anisotropy-powder” has a significantly lower particle size than the “base-powder” in order to “encapsulate” the latter. During the sintering process the “anisotropy-powder” melts partially forming a HRE rich shell around the “base-powder” grains. Therefore the melting point of the “anisotropy-powder” should ideally be lower than the melting point of the “base-powder”. This procedure has been done using $Dy_{40}Al_{30}Cu_{30}$ [Itou1995], DyH_x [Yan2010], Dy_2O_3 [Ghandehari1986, Doser and Keeler1988], $(Nd,Dy)_3Co_x$ [Velicescu1995], DyGa [De Groot1998] DyF_3 [Xu2011] and Dy_2S_3 [Gabay2011]. However, these approaches require very high sintering temperatures and times (resulting in a strong grain growth) or suffer from the introduction of unwanted impurities, which are detrimental to the coercivity. Löwe used the approach of introducing Dy in the form of $(Nd,Dy)_2Fe_{14}B$ powder, to overcome these problems [Löwe2016]. One such sample is analyzed in later chapters.

3 Experimental

3.1 Sample preparation

3.1.1 Sr-hexaferrite sintered magnets

The sample preparation of Sr-hexaferrite magnets was performed by Dr.-Ing. Fabian Rhein in the framework of his doctoral thesis. A detailed description of the sample preparation and synthesis can be found in his doctoral thesis [Rhein2018] as well as the publication by the same author [Rhein2018].

The commercial Sr-hexaferrite powder M884 by Tridelta Hartferrite GmbH was mixed at the ration 80 wt.% : 20 wt.% with an Al substituted Sr-hexaferrite powder $SrFe_{10}Al_2O_{19}$ using a roller mill. The later powder was developed and produces by Fabian Rhein within the framework of his doctoral thesis. A polyamide grinding jar was used with isopropanol and two agate balls with a diameter of 30 mm and five balls with a diameter of 20 mm for 24 h. Cylindrical green bodies were formed using a commercial prototype press by Tridelta Hartferrite GmbH with a diameter of 50 mm. During the uniaxial pressing process an axial magnetic field of 0.9 T was applied to induce the texture as well as 40 kN of force.
The green body was then cut into pieces that were sintered for 1.5 h at different temperatures ranging from 1160°C to 1280°C. The heating rate was adjusted in order to achieve the respective sintering temperature within 6 h, while the cooling rate was approximately 1200 K/h. After sintering cuboids of approximately 5 x 5 x 3 mm³ were cut for magnetic characterization using a Hystograph (HG 200 by Brockhaus Messtechnik GmbH). For MFM and SQUID measurement the samples were cut in half along the texture axis. For the MFM measurement the surface perpendicular to texture axis was polished using different diamond suspensions with particle sizes ranging from 6 µm to 0.01 µm. After the MFM measurements the samples were thermally etched 100°C below the respective sintering temperature for 5 minutes using a heating rate of 300 K/h and a cooling rate of 1200 K/h for the microstructural analysis by SEM.

3.1.2 Preparation of sintered magnets

Sintered magnets were obtained from VACUUMSCHMELZE GmbH. For microstructural characterization, the samples were polished using standard metallographic procedures. For magnetic characterization the sample surfaces were polished using abrasive paper in order to remove oxides from the surface. The samples were characterized using Vibrating Sample Magnetometry (VSM) as well as pulsed field magnetometry.

3.1.3 Preparation of hot-deformed Nd-Fe-B magnets

The starting material for the synthesis of hot-deformed Nd-Fe-B magnets is the commercial powder MQU-F by Molycorp Magnetquench. The powder is obtained by rapid solidification of a liquid smelter with the composition $Nd_{13.6}Fe_{73.6}Co_{6.6}Ga_{0.6}B_{5.6}$ (at.%) respectively $Nd_{26.6}Fe_{62.57}Co_{5.88}Ga_{0.6}B_{0.92}$ (wt.%) and is ground to a fine powder with a particle size of approximately 440 µm. The magnet preparation itself is divided into a hot-compaction and a hot-deformation process. In the former 9 g of MQU-F powder are compacted at 725°C to an isotropic hot-pressed magnet using a hydraulic 500 kN press by Weber. The powder is filled into a steel matrix with an inner diameter of 13.5 mm, made from a highly heat resisting nickel based alloy. To avoid the sample sticking to the matrix all metal parts were covered with a thin graphite layer. The process itself is done under vacuum at a pressure of 10^{-2} - 10^{-3} mbar. Using an optical heater, the respective temperature was achieved within 6 - 7 minutes and a pressure of 90 MPa corresponding to 13 kN of force is applied at 725°C for 1.5 minutes. After cooling down the sample surface was polished using abrasive paper to remove excess graphite powder.

The hot-deformation process was carried out at 750°C using a matrix with a diameter of 22.5 mm. The deformation temperature was reached within 8 minutes of optical heating and the deformation process took about 450 s in total. The *degree of deformation*, which can be calculated according to equation 3.20 (with h_0, h_{final} d_0 and d_{final} referring to initial and final sample height and diameter) was $\varphi = 1$ and deformation speed of $\dot{\varphi} = 2 \cdot 10^{-3}\ \mathrm{s}^{-1}$ in all deformation experiments.

$$\varphi = \ln\left(\frac{h_0}{h_{final}}\right) = \ln\left(\frac{d_{final}^2}{d_0^2}\right) \tag{3.20}$$

Respectively the final sample height was calculated according to equation 3.21 with d_{final} being the matrix diameter of 22.5 mm.

$$h_{final} = \frac{h_0 \cdot d_0^2}{d_{final}^2} \tag{3.21}$$

The maximum force used in the deformation process was 40 kN.

3.1.4 Diffusion in Nd-Fe-B sintered and hot-deformed magnets

For Diffusion experiments sintered magnets provided by VACUUMSCHMELZE GmbH and Co. KG. were used as well as hot-deformed magnets. The sintered magnets were a pilot batch with an initial Dy content of 0.06 %. All diffusion experiments of Dy and Dy-Nd-Cu in sintered and hot-deformed Nd-Fe-b magnets were carried out in a Carbolite furnace under 1.15 – 1.50 bar Ar atmosphere. The preparation of hot-deformed magnets is described in the previous chapter. The respective magnets were cut into cuboid shapes of approximately 10 x 4 x 4 mm³ using a WS-22 High Precision Wire Saw by Princeton Scientific Corp. Commercial Dy-foil by Alfa Aesar (25 µm thickness, purity 99.9 %) as well as approximately 0.5 – 1 mm thick slices of a low melting $Dy_{20}Nd_{50}Cu_{30}$ alloy was used for the diffusion. The $Dy_{20}Nd_{50}Cu_{30}$ alloy was produced from Cu (99.9 % purity), Nd (99.27 % purity) and Dy (99.27 % purity) by ChemPur using a Reitel induction melter. The diffusant was placed between the two cuboids and wrapped with Mo or Ta foil. The texture direction was arranged in such a way that parallel and perpendicular diffusion was carried out in the same experiment as depicted in Figure 3.1. For the magnetic and microstructural characterization smaller cuboids were cut from the diffused samples. For magnetic characterization the samples were cut perpendicular to the diffusion direction into thin slices of approximately 0.5 mm using a wire saw. For microstructural characterization the samples were cut parallel to the diffusion direction. The diffusion experiments and analysis on Nd-Fe-B magnets were partially performed by Andreas Abel in the framework of his master thesis.

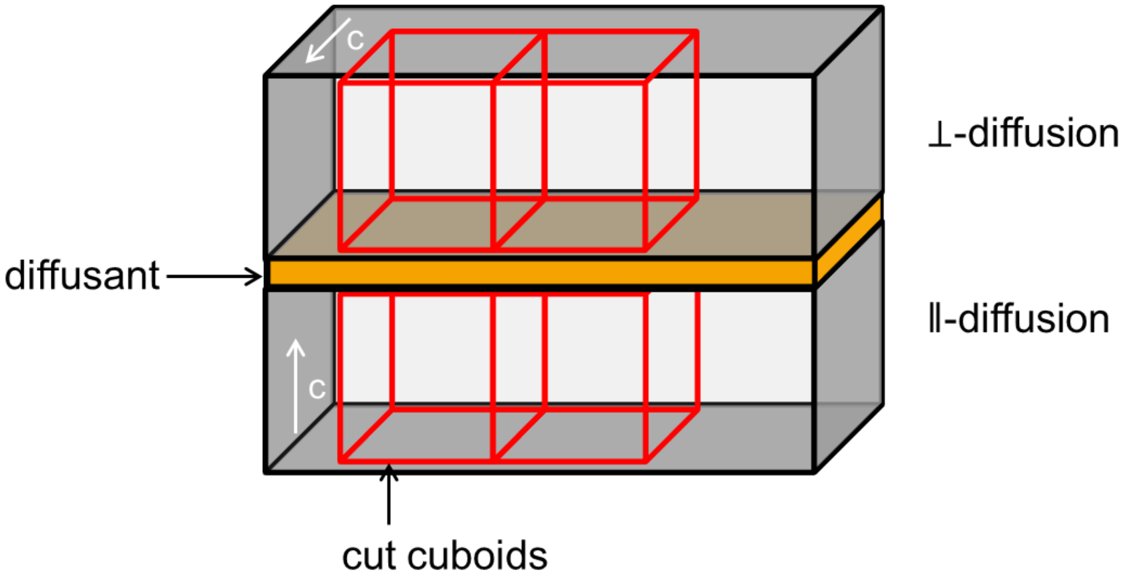

Figure 3.1 Experimental setup for the texture dependent diffusion in Nd-Fe-B magnets, with the texture axis lying along the c-axis.

In sintered magnets Dy and $Dy_{20}Nd_{50}Cu_{30}$ were used as diffusants. The diffusion in sintered magnets was done at 900°C for 4 h, followed by a PSA at 500°C. The diffusion in hot-deformed magnets was done at 650°C for 2 h without a PSA.

3.1.5 Preparation of core-shell structured sintered magnets

The core-shell structured sintered magnet analyzed in chapter 5 was prepared by Dr.-Ing. Konrad Löwe within the framework of his doctoral thesis and a detailed description of the procedure can be found there [Löwe2016] .

The method is based on the blending of two powders referred to as “base-powder” and “anisotropy powder” produced from 99.9 % pure Fe, Fe_2B and Dy provided by ChemPur. The pre-alloys were produced using an induction melter (Reitel), subsequently homogenized at 1120°C for 24 h and hydrogen decrepitated. Both powders were milled using a planetary ball mill (Fritsch Pulverisette 6) with heptane down to a particle size of approximately 5 – 10 µm. The base-powder was unsubstituted Nd-Fe-B powder with the composition $Nd_{15}Fe_{79}B_6$. The “anisotropy powder” was partially substituted with Dy with a composition of $(Nd_{0.725}Dy_{0.275})_{15}Fe_{79}B_6$ which is milled down to a slightly smaller grain size than the “base-powder”. The two powders are mixed, resulting in an overall composition of $(Nd_{0.9}Dy_{0.1})_{15}Fe_{79}B_6$ which is a Dy concentration of 4 at.% (10 wt.%) which means that statistically every 10th Nd atom is replaced by Dy. The powder blends are aligned in a magnetic field of approximately 1.77 T, pressed at 10 MPa and sintered at 1050°C for 1.5 h followed by a two-step low temperature annealing at 750°C for 2 h and subsequently at 500°C for 2 h.

3.2 Analysis methods

3.2.1 Scanning Electron Microscopy (SEM)

Scanning Electron Microscopy (SEM) was used for microstructural analysis. For the presented results in this work five different devices were uses: (i) a Philips XL30 FEG high resolution SEM, (ii) a Tescan VEGA3-SBH SEM (iii) a Tescan MIRA3-XM SEM and (iv) a Phillips/FEI XL-30 SEM. Acceleration voltages between 15 kV and 20 kV were used.
Depending on model and installed detectors, different imaging and analysis techniques can be used:

- **Secondary Electrons (SE):** The primary electron beam causes secondary electron to be emitted from the sample, which have a lower in kinetic energy than the primary electrons and can be collected towards the detector by a biased grid. Secondary Electron images typically display the topography information through a three dimensional appearance.

- **Back Scattered Electrons (BSE):** These electrons are elastically scattered from the sample and picked up at the detector. Since elements with a higher atomic number have a higher scattering index, elements with higher atomic number appear brighter. In Nd-Fe-B magnets this imaging mode allows the distinction of different phases. This is especially important in order to differentiate between individual grains separated by the grain boundary phase.

- **Energy Dispersive X-Ray Spectroscopy (EDX):** The primary electron beam causes electrons from lower atomic energy levels to be expelled from the sample atoms. The resulting vacancy is “filled-up” by electrons from a higher energy level. The energetic loss of these electrons during this process is emitted as an x-ray photon, which is characteristic for the respective element. Using an appropriate detector, the elemental composition of a sample or a specific spot can be quantified according to the x-ray emission spectrum. Typically elements emit the highest x-ray intensity for the transition from the L-shell to the K-shell, the so-called K_α line, which is usually used to quantify the elemental concentration. In some cases, as in this work for i.e. Dy and Fe, the respective K_α line of one element overlaps with another line. Thus a different line (with a lower intensity) has to be used for quantification, which reduces the accuracy of the measurement. In the case of Dy, the M_α line is used for quantification in this work. For precise quantification the absorption rate of the respective x-ray photons also has to be taken into account, which is done according to a database of the Backscatter Absorption Fluorescence (ZAF). The limiting factors for EDX are the lateral resolution of the primary electron beam, which is typically in the range of a few micrometers, and energetic resolution of the detector. EDX results displayed in this work were mostly obtained using a TESCAN VEGA3-SBH SEM with a tungsten filament and mainly carried out by Andreas Abel.

- **Electron Backscatter Diffraction (EBSD):** In this experimental setup, the sample is tilted by approximately 70° with respect to the primary electron beam source. The detector is placed at approximately 90° with respect to the electron beam. The primary electrons that are hitting the sample are diffracted according to *Bragg´s-law* depending on the crystallographic orientation of the respective grain. The diffraction pattern, also-called Kikuchi-pattern, is projected onto the detector, which can then be used to index the crystallographic orientation of a specific phase (e.g. $Nd_2Fe_{14}B$) according to a database. The main limiting factors for this measurement method are the quality of the surface polishing and the lateral resolution of the primary electron beam. The EBSD results presented in this work were obtained using a TESCAN MIRA 3 high resolution SEM with an EDAX-EBSD detector and carried out by Thorsten Gröb.

3.2.2 Transmission Electron Microscopy (TEM)

In Transmission Electron Microscopy (TEM) a primary electron beam is transmitted through a sample and its interaction with the sample is used to obtain an image. In order to do this the sample has to be *electron-transparent*, which can only be obtained if the sample material is very thin, ideally below 100 nm. In this work such thin samples are obtained by cutting thin lamellas (or needles) using a Focused Ion Beam (FIB) that evaporates material using accelerated Ga-Ions. The FIB-cutting was performed by Dr Urban Rohrmann at the Fraunhofer Projektgruppe IWKS Alzenau. The imaging process can be done using a parallel beam setup to obtain an overview image of the entire sample (TEM), or by a focused electron beam that is used to scan the sample to obtain a higher resolution (STEM). The TEM images in this work were taken together with Dr. Michael Dürrschnabel using a JEOL ARM-200F (120 kV acceleration voltage), as well as a JEOL 2100F (with 200 kV acceleration voltage). Several different imaging modes can be used in TEM:

- **High Angle Annular Dark Field (HAADF) - STEM:** This imaging method detects electrons that have large scattering angles. The dominating process at such angles is the *Rutherford-scattering*, which depends on the atomic number of the respective element, which is why the contrast of this method allows elemental discrimination similar to BSE. A higher atomic number Z corresponds to a higher signal intensity.

- **STEM - EDX:** The generation and detection of characteristic x-ray photons is analogous to the SEM-EDX. The focused electron beam and thin TEM lamella allow a higher lateral resolution below 1 nm. The same problem concerning the overlapping of EDX lines applies here too. The resolution and signal to noise ratio strongly depend on the geometry i.e. thickness of the lamella, since thick lamellas result in a large signal but also result in a larger active volume, limiting the resolution.

- **Atomic Resolution STEM - HAADF:** Atomic resolution can be obtained if a crystallographic zone axis of the sample is aligned parallel to the electron beam. By Fourier-transformation of the resulting images, a diffractogram can be obtained to extract the lattice parameters and crystal orientation.

3.2.3 Kerr Microscopy

The Magneto – Optic Kerr Effect (MOKE) is a phenomenon based on the rotation of the polarization plane of a polarized light beam, which can be made visible using a polarization microscope [Kerr1877]. If the sample material is non transparent i.e. the incident beam is reflected, it is referred to as the Kerr-effect [Hubert and Schäfer1998]. By tilting polarizer and analyzer against each other an optical contrast can be observed between individual domains. This effect is typically very small, but can be enhanced by digitally subtracting the contrast of the background (e.g. differing grain orientation) from the magnetic contrast. Both methods were used in this work. In this way the magnetic domains in most permanent magnetic materials can be visualized. The effect can be applied to polar Kerr microscopy (magnetization direction pointing out of the image plane) and longitudinal Kerr microscopy (magnetization lying in the image plane). The samples presented in this work were carefully polished and analyzed within few hours or stored under protective atmosphere to minimize surface oxidation. The device used was an envico magnetics GmbH Kerr microscope using a 100x oil immersion objective. The limiting factor of this method is the optical resolution limit of about 300 nm.

3.2.4 Inductively Coupled Plasma (ICP) – Optical Emission Spectroscopy (OES)

For this measurement method, the sample is dissolved in an acidic solution. The solution is then dispersed as an aerosol into an Inductively Coupled Plasma (ICP) Ar-plasma. The high temperature of the plasma of about 6500 K causes the dissolved elements to be atomized and eventually ionized. This results in the emission of a characteristic emission spectrum that can be detected. The intensity of the respective spectrum is proportional to the concentration of the element in the initial solution and hence the sample. The here analyzed elements were Al, B, Co, Cu, Dy, Fe, Ga, Ho, Nd, Pr and Tb. The sample size was approximately 100 mg, prior to the measurement the samples were polished smooth to minimize oxidation. The ICP experiments were performed by Dr. Alexander Ländner at the IWKS, Alzenau using an Optima 8300 by PerkinElmer.

3.2.5 Magnetic Force Microscopy (MFM)

Magnetic Force Microscopy (MFM) is a scanning probe microscopy technique, derived from the Atomic Force Microscopy (AFM), used to image magnetic domains. A silicon cantilever is excited to its resonance frequency using a piezo-electric element. The backside of the cantilever is coated with a thin reflective Al layer, which allows measuring the position and respectively the amplitude of the cantilever tip via a laser. The MFM used in this work (attoAFM/MFM Ixs by attocube systems) uses an infrared laser ($\lambda = 1330$ nm) and an interferometer. The oscillating end of the cantilever is equipped with a pointed tip, which is coated with a ferromagnetic layer. The imaging process is divided into steps: During the so called “first pass” a line is scanned (trace and re-trace) using the AFM “tapping-mode” the topography is obtained. In a second step called “second pass” the same line is scanned again at a constant distance from the surface by adding a certain “lift height” to the previously obtained topography as depicted in Figure 3.2.

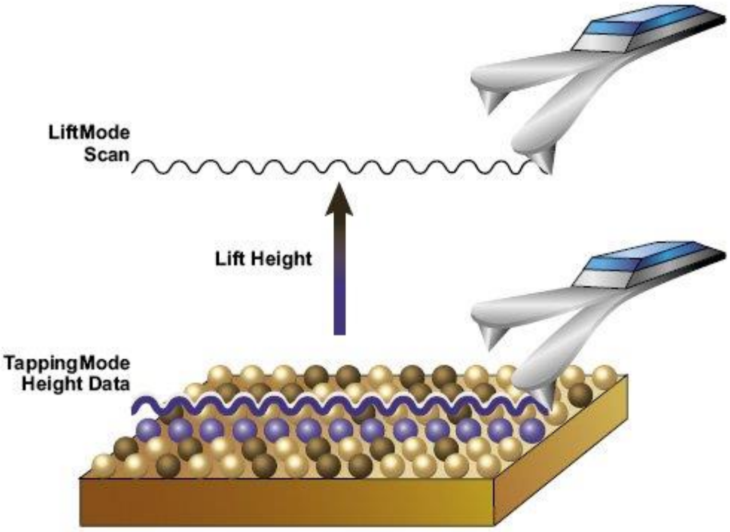

Figure 3.2 Working principle of an Magnetic Force Microscope using the tapping mode to obtain the topography information and scanning at a constant lift height to obtain the magnetic information[1].

During the second scan, typically 30 – 50 nm above the surface, the magnetic information is obtained. This procedure exploids that that, that magnetic interaction act on a longer range than Van der Waals forces and Pauli repulsion, that occure during the “first pass” (i.e. AFM tapping mode). In this work a special procedure was used that increases spatial resolution by minimizing the lift height to the lowest possible value: During the first pass the “normal” excitation voltage is applied to the. For the second pass the excitation voltage is reduced to 25 % of the “normal” value used in the first pass. But before a scan can be initialized, the minimal lift height for the second pass has to be determined. In the first step the “normal” excitation amplitude is applied to the freely oscillating cantilever, which corresponds to an amplitude of approximately 100 nm (Figure 3.3 (a)). Afterwards the “tapping mode” is initialized by activating a feedback loop that controls the z position of the cantilever by based on the oscillation amplitude. This means that the cantilever is brought closer to the sample, until the tip – sample interaction reduces the oscillation amplitude to approximately 80 % (Figure 3.3 (b)). The z-feedback loop adjusts the cantilever height to maintain a constant distance between cantilever and surface. In the second step the z-feedback loop is deactivated, without changing the distance between sample surface and cantilever. In the third step the excitation voltage (and hence amplitude) of the cantilever is reduced to 25 %, meaning that the new amplitude is no longer dampened by the tapping mode (Figure 3.3 (c)). In the fourth and final step the distance between surface and cantilever is manually reduced (in 10 nm steps), until the amplitude reduces due to the tip surface interaction. The last point at which the cantilever is still oscillating freely marks the lowest possible lift height. With this approach the lift height can actually be negative, meaning that the cantilever is actually closer to the sample when measuring the domain structure than when measuring the topography.

---

[1] https://blog.brukerafmprobes.com/guide-to-spm-and-afm-modes/magnetic-force-microscopy-mfm/ (10.08.18)

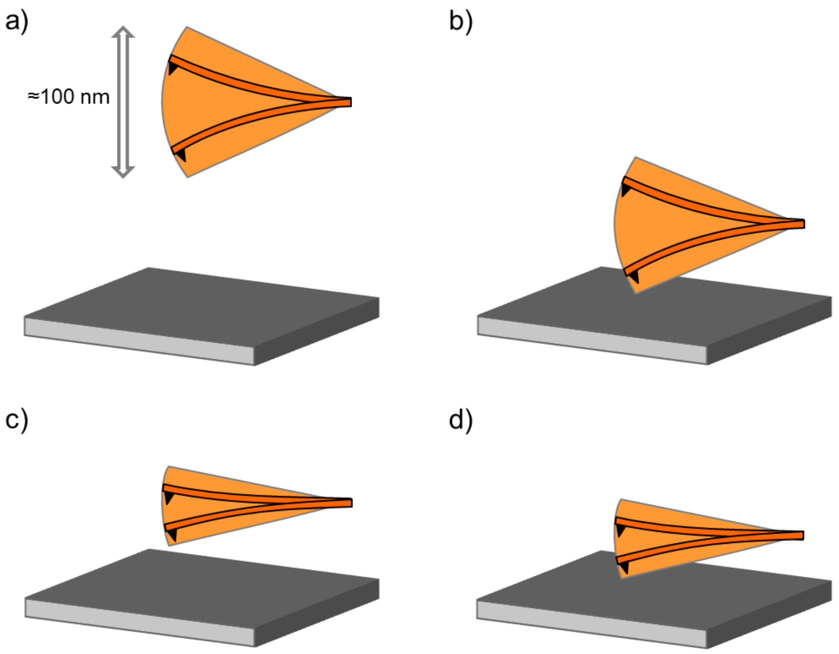

Figure 3.3 Schematic illustration to minimize the lift height using an alternative excitation amplitude (a) freely oscillating cantilever, (b) active z-feedback loop "tapping mode", (c) freely oscillating cantilever with alternative excitation amplitude and (d) manual approach using an alternative excitation amplitude.

Due to the magnetostatic interaction of the magnetic tip with the underlying domains, the resonance frequency and therefore phase of the cantilever shifts slightly depending on the magnetization direction of the respective domain. For measurements under ambient pressure a constant excitation frequency can be used i.e. the resonance frequency of the cantilever, and the resulting phase shift is used to depict the domain structure. For field dependent measurements, an exchange gas atmosphere (of approximately 20 mbar He) was established. Under these conditions the resonance peak of the cantilever becomes so sharp that the slight changes in resonance frequency caused by the domain structure are enough to destroy the resonance condition. For such measurements the excitation frequency has to be adjusted dynamically (to ensure resonance condition) using a phase-lock-loop (PLL). The PLL is a feedback loop that keeps the phase shift between excitation oscillation and cantilever oscillation constant. The respective shift in resonance frequency is plotted to display the contrast between different domains.

The physical reason for the contrast formation arises from the convolution of the magnetic stray field of the MFM tip with the magnetic stray field of the sample. Since the magnetization direction of the MFM tip is along the z-direction i.e. normal to the sample surface, only the z-component of the sample stray field takes part in the contrast formation. To obtain a correct depiction of the domain structure it is of vital importance that the magnetization state of the MFM tip does not change during the scanning process. A magnetization "flip" can occur, if the coercivity of the tip is too low, and it changes its magnetization depending on the underlying domain [Vock2014]. For most results shown in this PhD thesis high coercivity cantilever ASYMFMHC by Asylum Research were used that are coated with a CoPt/FePt layer with a coercivity of 0.5 T. The coercivity of these cantilevers was sufficient to maintain a stable magnetization. The integrity of the tip has to be maintained during the scanning procedure, if the tip gets damaged, i.e. by crashing into topography features, the magnetic layer can be damaged. This can result in a less defined magnetic moment causing a blurry domain image. A similar problem occurred if the tip picks up a "dirt" particle during the scanning process. Besides causing artifacts in the topography, such particles (especially magnetic ones) alter the magnetic stray field of the tip and interfere with the domain imaging. If the dirt particle is magnetic it can also reverse its magnetization causing a similar effect as a tip “flip”. To avoid this, great care has to be taken during the surface preparation, sample handling and scanning procedure (to avoid crashing the tip into the sample).

The MFM used in this PhD thesis is a special construction in the form of an insert, which allows it to be operated inside a Physical Property Measurement System (PPMS) by LOT Quantum Design. All field dependent measurements were performed at 300 K under a He exchange gas atmosphere. In order to suppress unintended heating of the sample or the MFM insert, the field was changed at a maximum rate of 50 Oe/min. In order to fit into the PPMS the core components of the MFM (scanning unit, positioning unit etc.) are designed very small. As a consequence of this minimalistic design the total scan time had to be lower than 1.5 h (per image) in order to minimize linear drifts that occur in the piezo-electric elements. Another consequence of the special design was the comparable low scanning speed which could be used. The maximum scanning speed used was 7 µm/s, for higher scanning speeds the z position feedback loop would be to slow resulting in frequent tip crashes with the topography features.

3.2.6 Vibrating Sample Magnetometer (VSM)

In a Vibrating Sample Magnetometer (VSM) the sample is attached to a rod and placed between two oppositely wound pic up coils. The sample is vibrating during the measurement with an amplitude in the tenth on millimeter range, typically at a frequency of 10 – 100 Hz. The resulting time dependent change in magnetic flux induces a voltage into the pic up coils, which is proportional to the magnetic moment of the sample. The VSM is calibrated using a Ni sphere of known dimensions. By applying a homogenous external magnetic field and external temperature control, the magnetization can be measured as a function of external field and/or temperature. The sample is measured under “open circuit conditions” meaning that the sample is subjugated to a geometry dependent demagnetization field which needs to be corrected to obtain sample independent material properties. The limiting factor with this method is that only very small sample sizes can be measured below 150 mg for Nd-Fe-B.

In this work two different VSMs were used: (i) a Lake Shore Cryogenics, Inc. with water cooled Cu coils around tapered Fe/Fe-Co pole shoes generating a maximum field of 2 T, which was operated inside an oven to obtain the magnetization as a function of temperature. And (ii) a Quantum-design VSM system operated inside a PPMS using a superconducting solenoid to generate magnetic field up to 14 T. The later measurements were performed at 300 K to obtain the magnetization as a function of external field.

3.2.7 Superconducting Quantum Interface Device (SQUID) Magnetometry

In the Superconducting Quantum Interference Device (SQUID) Magnetometer the magnetization can be measured as a function of the external field and temperature: The sample is moved between two superconducting pick up coils, inducing a current. In a separate input coil this current generates a magnetic field, which is then measures using the actual SQUID. The SQUID itself consist of two superconducting semi-rings that are connected by two tunneling contacts also known as Josephson-contact. A DC voltage is applied between the two half rings. If a magnetic field is generated an additional current is induced into the SQUID, which causes a periodic voltage change which can be used to determine differences in flux density of the input coil very precisely. This allows the calculation of the magnetization of the sample.

The SQUID magnetometry measurements in this work were performed by Fabian Rhein using a MPMS XL device by LOT-Quantum-Design GmbH. With the system it is possible to measure the magnetization under “open-circuit” conditions up to an external field of 7 T.

3.2.8 Pulsed Field Magnetometry

The Pulsed Field Magnetometer uses the discharge of a capacitor bank to generate a pulsed field of 7 T via a coil to magnetize the sample. The sample is then turned around and demagnetized by using a second pulse. The magnetization reversal in the sample along with the external magnetic field is measured using a double Helmholtz coil. Prior to the measurement, a reference is recorded without any sample to subtract the background resulting from the external field and the sample holder to obtain the sample properties. This method also uses “open-circuit” conditions, meaning that an appropriate demagnetization factor has to be used to correct the resulting curve. This is done automatically by the software of the system, which calculates the demagnetization factor N from the geometry of the sample. Large samples sometimes require to additionally measure the influence caused by eddy-current induction, which can be subtracted from the measurement. As a consequence of the complicated internal correction algorithm of the device (due to demagnetization factor, eddy current induction, surface grains etc.) the measured remanence only provides a limited accuracy, which has to be kept in mind for the data analysis. A limitation of this method is also that only the second and third quadrant i.e. the demagnetization can be measured.

In this work, a magnetometer by Metis Instruments was used for magnetic characterization at room temperature. Some of the shown measurements were performed by Andreas Abel within the framework of his master thesis.

3.2.9 Hystograph

A Hystograph uses two primary coils and pole shoes to generate a magnetic field with a constant field rate $d\Phi/dt$ to avoid a phase shift caused by eddy currents between the field strength and the magnetization measurement. The magnetization of the sample is measured via a J-compensated secondary coil according to the induced voltage. Unlike the so far presented magnetic characterization techniques, this method uses closed circuit conditions where the magnetic flux is “closed” by the pole shoes. This means that the influence of the stray field and self-demagnetization is lower and the measurements do not have to be corrected. In this work a Hystograph HG 200 by Brockhaus Messtechnik GmbH was used which can generate an external field between -1500 kA/m and 1500 kA/m (ca. 1.88 T). The experiments were carried out by Fabian Rhein within the framework of his doctoral thesis.

4 Magnetization and demagnetization behavior in Sr-hexaferrite sintered magnets

The following chapter will describe the different effects of microstructural factors on magnetic properties in Sr-hexaferrite sintered magnets as well as the formation and behavior of magnetic domains. Further information on the theoretical background and the concept of magnetic domains can be found in chapter 2.1. Most micromagnetic models assume a strong connection between domains and microstructure. This means that the domain structure is described using the microstructure as reference e.g. a grain is either in a Multi Domain State (MDS) or a Single Domain State (SDS). When it comes to the description of magnetic domains, it is also important to differentiate between surface domains and bulk domains. Surface domains are always exposed to a distortion by the magnetic stray field. This becomes especially important if the magnetic easy axis and magnetization direction is perpendicular to the surface. In this case the magnetic stray field has a destabilizing influence on the SDS, and a stabilizing effect on the MDS by reducing the stray field energy. While the structure and evolution of surface domains can experimentally be directly measured by e.g. Kerr- or Magnetic Force Microscopy (MFM), bulk domains are usually measured indirectly e.g. by determining the susceptibility. The sample preparation, microstructural characterization and SQUID measurements in this chapter were performed by Dr. Fabian Rhein, and a more detailed description of the preparation can be found in his doctoral thesis “Nanoskalige Magnete und Magnetkomposite auf Ferritbasis” [Rhein2018].

The analyzed samples were prepared by blending a commercial Sr-hexaferrite powder (M884 Tridelta Hartferrite GmbH®) that also contained $CaSiO_3$ and Al_2O_3 with an Al rich Sr-hexaferrite ($SrFe_{10}Al_2O_{19}$) powder, using ratio of 80 wt.% to 20 wt.%. A detailed description of the preparation of the Al rich powder can be found in [Rhein2017]. The substitution of Fe by Al in the hexaferrite increases the anisotropy field, thus resulting in a higher coercivity (see also chapter 2.2). After blending, the powder was aligned in an external magnetic field and pressed to obtain textured green bodies. Different sintering temperatures ranging from 1180°C to 1280°C were employed to obtain different microstructures. The resulting microstructures obtained at sintering temperatures of 1180°C (M 1180), 1240°C (M 1240) and 1280°C (M 1280) are depicted in Figure 4.1.

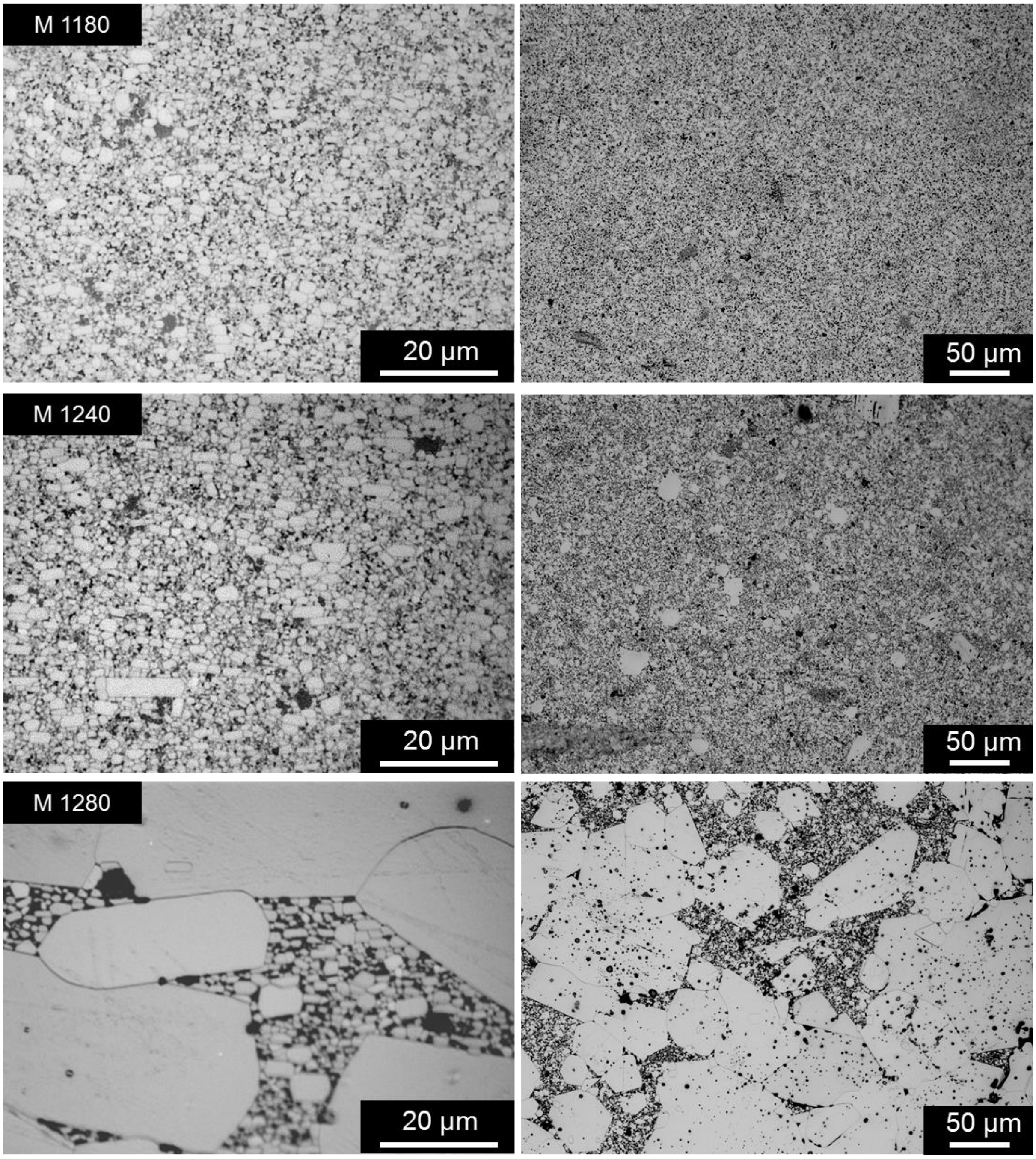

Figure 4.1 Light microscopy images depicting the microstructure of the thermally etched hexaferrite samples sintered at 1180°C, 1240°C and 1280°C, showing the cross section where the texture axis lies in the image plane (left) and top view where the texture axis points out of the image plane (right).

Sample M 1180 displays the smallest grain size out of the here analyzed samples, revealing a fine microstructure with grain sizes ranging from approximately 500 nm to 4 µm. The cross section shows that the sample contains a large amount of 500 nm to 2 µm large spherically shaped grains; grains that are larger than 2 µm tend to grow preferably within the basal plane. Due to the low sintering temperature, the sample also contains a large quantity of pores. A slightly higher sintering temperature of 1240°C (M 1240) leads to the formation of a more heterogeneous microstructure with the grain size ranging from 500 nm to 20 µm, showing a higher amount of larger grains that become more and more platelet shaped with increasing size. The same trend continues at a sintering temperature of 1280°C where the microstructure becomes even more heterogeneous with the grain size ranging from few micrometers up to more than 100 µm. It is well known that in this system the growth of well oriented grains during sintering is preferred at the expense of worse oriented grains [Esper1977], as can be seen in sample M 1240 and M 1280. This sample was intentionally over processed to serve as a reference sample too observe magnetization processes in very large grains. The sample M 1280 has a density of 4.8 g/cm^3, which is close to 100 % of the expected theoretical density of approximately 5.0 g/cm^3.

The initial magnetization curves of the samples M 1180, M 1240 and M 1280 are depicted in Figure 4.2 (a). All three samples show a high initial slope i.e. high susceptibility at lower fields below 200 mT, which is typical for nucleation dominated magnets [Coey2010] and a magnetization by domain growth from a MDS. At higher fields, however, sample M 1180 and M 1240 show a lower slope and almost form a plateau. At higher fields of ca. 400 mT the slope i.e. susceptibility increases again. Sample M 1280 on the other hand only shows a barely noticeable slight plateau like behavior, here the major part of the magnetization occurs below 200 mT.

Sample M 1180 and M 1240 differ from the typical nucleation dominated magnet behavior; this could either be caused by domain wall pinning or by a single domain like behavior [Gutfleisch2000b, Coey2010]. The here analyzed ferrite system is widely assumed to be nucleation dominated, however, pinning mechanism were also discussed in literature [Nishio2009, Alsmadi2013]. On the other hand, a certain amount of grains depicted in Figure 4.1 might also be below the critical single domain size of approximately 740 nm and are therefore expected to show single domain like behavior [Dahal2014].

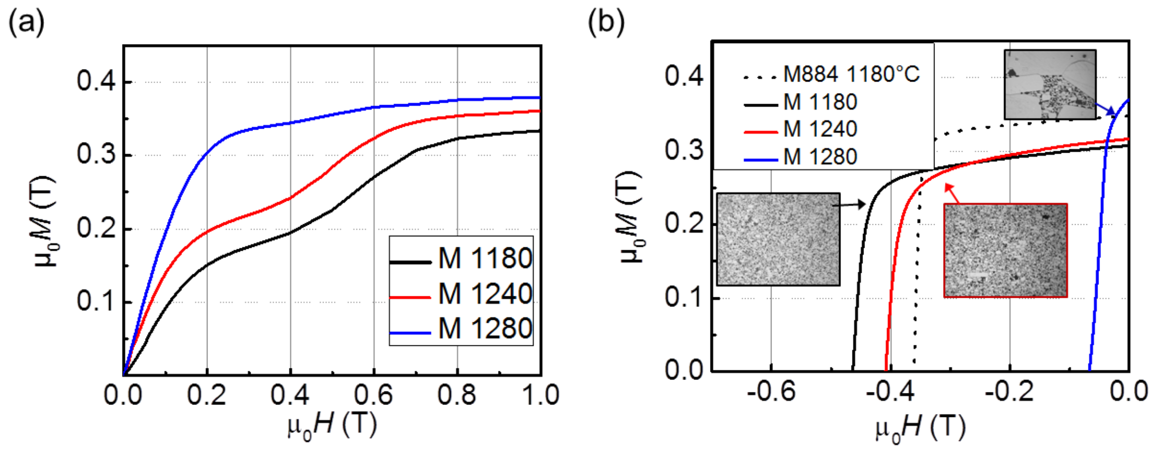

Figure 4.2 (a) Initial magnetization curves of the samples M 1180, M 1240 and M 1280 from the thermally demagnetized state, measured by hystograph and (b) the demagnetization curves and respective microstructures.

Figure 4.2 (b) shows the demagnetization curves of the analyzed samples M 1180 – M 1280 as well as the pure commercial powder M884 sintered at 1180°C as a reference. The image also shows the respective microstructure of the samples. As can be seen, the addition of the Al rich $SrFe_{10}Al_2O_{19}$ powder increases coercivity significantly, the highest coercivity can be achieved for M 1180 with the smallest grain size. At the same time M 1180 and M 1240 samples also show a lower remanence in comparison to pure M884. Only sample M 1280 shows a higher remanence than M884 but also shows the lowest coercivity. All samples show a single step demagnetization behavior, considering that these samples were prepared from a powder blend with different magnetic properties, this is not self-evident. In terms of hard magnetic properties, sample M 1180 shows the best overall values in this study. Its lower remanence in comparison to pure M884 can be attributed to the i) lower saturation magnetization of $SrFe_{10}Al_2O_{19}$ due to the Al substitution and ii) overall lower grain size of the $SrFe_{10}Al_2O_{19}$ powder, as well as a higher porosity. The increasing remanence with higher annealing temperature can be attributed to a reduction of porosity i.e. higher density as well the before mentioned preferred growth of well oriented grains during the sintering process.

A more detailed depiction of the microstructure of sample M 1180 is shown in Figure 4.3 (a) as well as a correlation with the chemical composition (b). The images were obtained by SEM, while the chemical composition was obtained by EDX. Later in this chapter the same area will be discussed, showing the domain evolution under applied magnetic field. The here depicted surface was obtained by thermally etching the sample. This process was done after the MFM measurements (later in this chapter) were performed in order to exclude an influence of the thermal etching process on the magnetic behavior.

The SEM image confirms the presence of grains in the range of 500 nm in size that are stacked in between larger grains. The presence of such grains is significant because, as mentioned above, the critical single domain size in this system was reported to be in the range of approximately 740 nm depending on the Al concentration [Dahal2014]. In order to gain some insight into the Al distribution in the sample after the sintering process, an EDX map was recorded as well as an EDX point analysis on a large grain (4 µm) and smaller grains (~ 500 nm). The EDX map shows that Al, depicted as orange, has a tendency to coincide with smaller grain sizes. This result is confirmed by EDX point analysis that shows low Al concentration in the center of the ca. 4 µm large grain (red dot in Figure 4.3 (a)) but shows a large Al concentration in the smaller grains (blue dot in Figure 4.3 (a)). As reported by Dahal *et al.* a Al substitution also increases the critical single domain size (D_c) to up to 5.7 µm for a composition of $SrFe_{10}Al_2O_{19}$ [Dahal2014]. However, since the EDX analysis shows higher concentrations of Al only in smaller grains and larger grains to be quite Al poor, it has to be assumed that larger grains in the range of 4 µm are larger than D_c, while smaller grains are below D_c. This means that based on the grain size and composition, one would expect a single domain like behavior in smaller grains, while larger grains should act as multi domain grains, as will be discussed later.

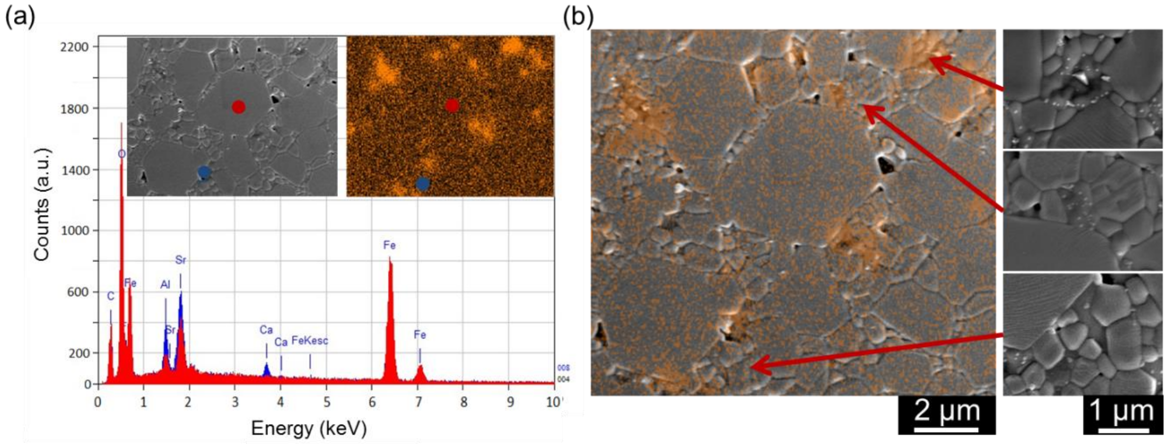

Figure 4.3 Microstructure and chemical composition determined by SEM and EDX, EDX point analysis spectra and EDX map of a large and smaller grain(s) (a) superposition of microstructure and EDX map of Al distribution (b).

In addition to the Al signal, the EDX point analysis also shows a clear Ca signal that is present in smaller grains but absent in larger ones. This signal is originating from the $CaSiO_3$ that is added as a sinter additive to the mixture. As shown by Töpfer *et al.* [Töpfer2005] and Kools et al. [Kools2003] the addition of CaO and SiO_2 suppresses grain growth and aids to the formation of spherical grains, which is both beneficial for the magnetic properties (see also chapter 2.2). Since the sinter additives are assumed to be liquid during the sintering process, thereby encapsulating the grains, the respective EDX Ca signal shows only in smaller grains when picking up the signal from the grain boundaries. The EDX Si-K_α peak overlaps with the Sr-K_α and Sr-K_β signal, therefore cannot be detected explicitly but is presumably the reason for the increased signal in Figure 4.3.

The same detailed microstructure analysis was performed for sample M 1240 shown in Figure 4.4. The investigation also reveals that a significant amount of the depicted grains are in the submicron regime, meaning that they are below the critical single domain size of approximately 740 nm [Dahal2014] depending on composition i.e. local Al concentration. The EDX analysis revealed (data not shown) that the same principles concerning the distribution of Al, Ca and supposedly Si apply for this sample as they do for sample M 1180.

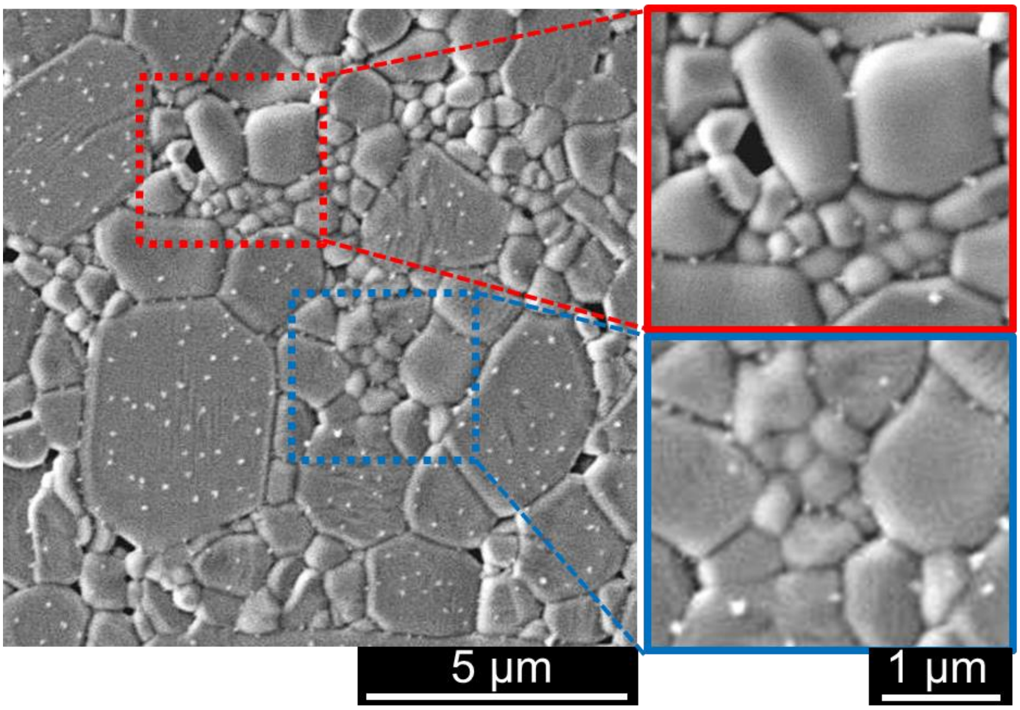

Figure 4.4 Microstructure of sample M 1240 obtained by SEM after thermally etching the surface.

The same area shown in Figure 4.4 will also be discussed later in this chapter showing the domain evolution under applied magnetic field. In Comparison to sample M 1180, sample M 1240 shows a slightly lower amount of small grains and a larger amount of large grains, going back to the higher sintering temperature leading to a higher grain growth.

The domain structure obtained by MFM of the Thermally Demagnetized State (TDS) of the samples M 1180, M 1240 and M 1280 are depicted in the left column of Figure 4.5. The respective microstructure of each sample is shown in the middle column of Figure 4.5, while the right column shows the superposition of the domain- and microstructure. From the images it becomes evident that there are three different domain-grain combinations preset: Large grains (exemplary marked A in Figure 4.5) in the range of approximately 2 – 4 µm in size that consist of multiple magnetic domains i.e. are in the MDS. Such grains can be found in all three samples, as well as even larger MDS grains especially in M 1280. Here the grains are so large that the domains even form star-like structures similar to Nd-Fe-B that were also reported in Ba-ferrite single crystals [Jalli2011]. The second category (marked B) are smaller grains, approximately 1 – 2 µm that are occupied by a single domain i.e. are in the SDS. Similar grain/domain structures were also observed by Pang *et al.* [Pang2010]. Such grains are primarily found in M 1180 and M 1240 rather than M 1280 due to the large grain size in the later. Based on the size and singe domain character, these grains might presumably show a single domain like behavior during the magnetization and demagnetization process. The third category (marked C) are grains that are in the submicron range in terms of size, in these grains the respective magnetic domain extends over more than one grain. A similar kind of domain type is known to form in nanocrystalline Nd-Fe-B [Khlopkov2007, Thielsch2012] and Sm-Co [Gutfleisch2006] magnets and is referred to as interaction domains. This means that the underlying microstructure is smaller than the domain structure i.e. domains are spanning across many grains. Such domain structures form if the grain size of a (usually textured) magnet is smaller than the critical single domain size [Khlopkov2006]. The here presented grains do not quite match the definition of interaction domains since they are embedded in a matrix of larger grains that are above the critical single domains size. Furthermore it has to be taken into consideration that the smaller grains might not share the same orientation since small grains tend to be harder to orientate. Therefore it could be an alternative explanation that the presented domain structure forms as a result of overlapping stray fields, which is also supported by fact that the domain shapes seem to resemble the underlying grain structure.

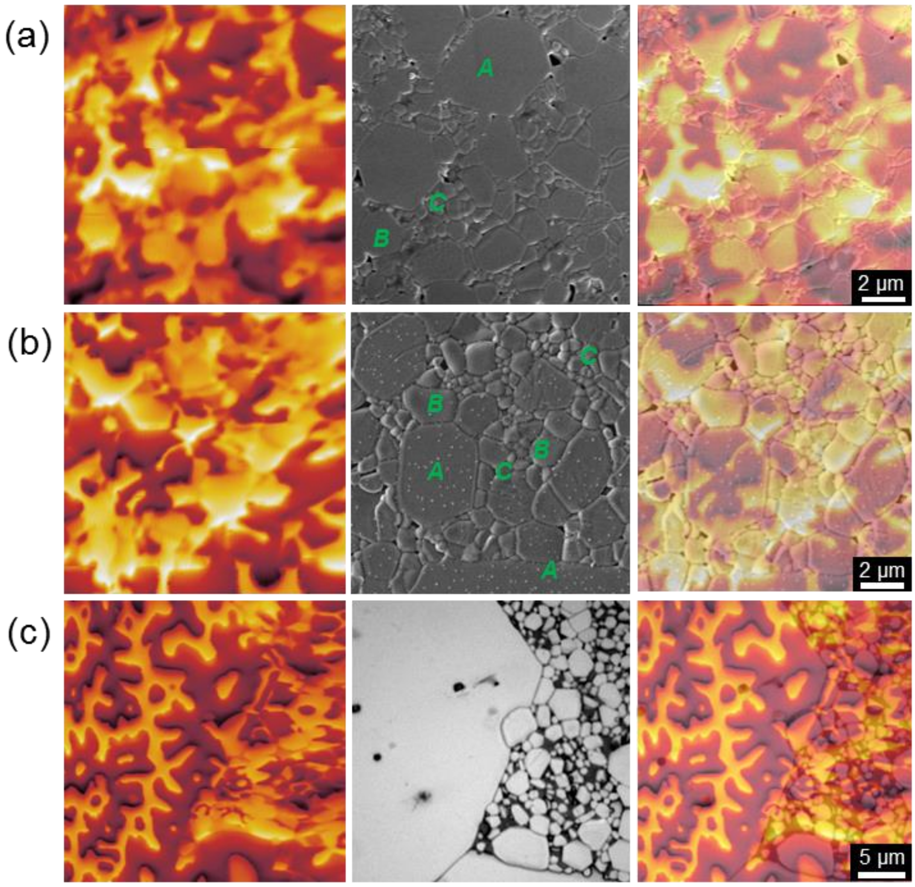

Figure 4.5 Domain structures of Thermally Demagnetized State (TDS) (left), microstructures (middle) of the same area depicted by SEM and light microscopy and superposition (right) of the domain structures onto the microstructures of M 1180 (row a), M 1240 (row b) and M 1280 (row c).

In the following the magnetization and demagnetization by an external magnetic field is recorded by *in-situ* MFM. The external magnetic field is always applied perpendicular to the image plane, the same as the texture axis of the depicted sample. A dark contrast corresponds to an attractive interaction i.e. a parallel magnetization of domain and MFM tip. The coercivity of the magnetically coated tip is approximately 0.5 T meaning that at larger fields, the magnetization direction of the tip is reversed (depending on the previous magnetization direction) thus leading to an inversion of contrast in the image. In the following chapters the contrast is therefore digitally inverted if such a re-magnetization of the tip occurs during the measurement.

In-situ magnetization of M 1180

In order to understand the magnetization behavior of the described grain types, an *in-situ* analysis was carried out showing the magnetization process from the TDS in sample M 1180 depicted in Figure 4.6. The depicted area is the sample that was already shown in Figure 4.3 and Figure 4.5 (a). In the first picture at 0 T the microstructure is super-positioned with the domain structure allowing a direct comparison.

The application of a small magnetic field of 0.1 T causes a growth of the dark contrasted domains. This growth occurs primarily in larger grains (2 – 4 µm) that were initially in a MDS. At an applied field of 0.4 T the domain growth in these larger grains has led to a complete saturation resulting in a SDS. A contrast i.e. magnetization inversion can also be observed in smaller grains that change from SDS to the respective reversed SDS. This behavior can be caused by i) magnetization changes in deeper lying grains, ii) magnetostatic interactions of the domains with the MFM tip and iii) statistics, meaning that not all grains have identical magnetic properties due to local differences like local defects, stress etc.. At 0.4 T the external magnetic field is close to reversing the magnetization direction of the MFM tip, as a result the magnetization of the tip is destabilized slightly canted with respect to the z-direction, which causes the image to be slightly blurry.

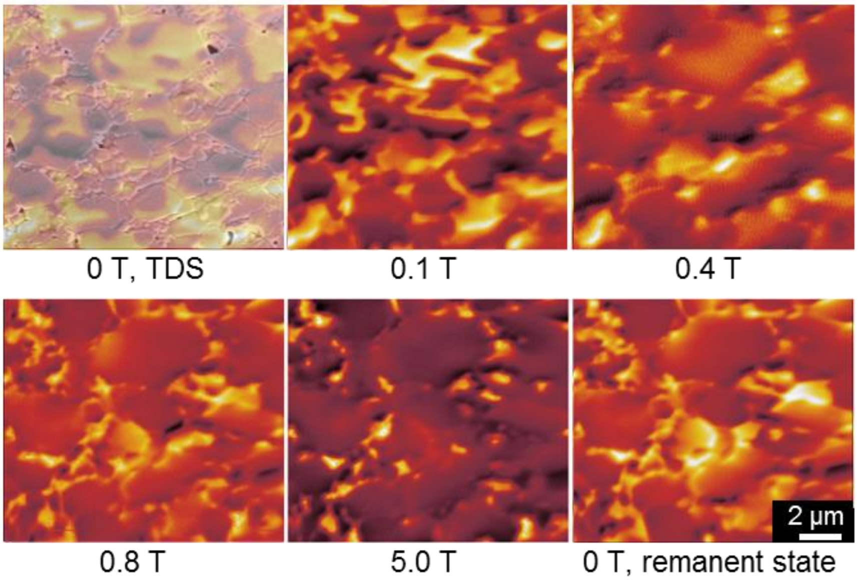

Figure 4.6 Magnetization process of sample M 1180 under external magnetic field recorded by MFM under *in-situ* conditions.

At 0.8 T almost all grains have changed to a dark contrast, with respect to the domain configuration at 0.4 T. A large amount of smaller grains, i.e. smaller than the critical single domain size D_c, have reversed their magnetization state. At an applied field of 5 T all grains have changed their magnetization direction to dark contrast i.e. parallel to the applied field direction. The remaining bright contrast corresponds either to pores in the sample surface or to a lower magnetic moment caused by local compositional changes either at the grain boundaries as a result of the sinter additives (i.e. paramagnetic phases) or as a result of the higher Al content and hence lower magnetization. This optical impression is amplified by the elimination of the previously bright domain contrast. Upon removal of the external field (remanent state) most of the grain maintain their magnetization and contrast, however, some grains revert to a bright contrast again. This behavior might be caused by misaligned grains that revert to their easy axis magnetization direction, resulting in a locally altered stray field.

In order to draw a complete picture of the magnetization processes in M 1180, the initial magnetization data in Figure 4.2 (a) have to be cross referenced to the microstructural and magnetic data in Figure 4.5 and Figure 4.6. In order to do this the contrast that was obtained by MFM was converted into a magnetization value. Each image was first converted to a black and white contrast using the public domain software ImageJ, by applying a threshold value. The magnetization was then calculated according to the formula:

$$\mu_0 M_{MFM} = \frac{A_{black} - A_{white}}{A_{total}} \cdot J_S$$

Where A_{black} and A_{white} correspond to the amount black/white area, while A_{total} corresponds to the total image area. By using this method, a respective magnetization value was obtained from each image depicted in Figure 4.6. By manually adjusting the threshold value to fit the MFM image, an error for each point was estimated.

The two datasets i.e. the global magnetization obtained by SQUID magnetometry and the calculated surface magnetization values obtained by MFM are compared in Figure 4.7. In the TDS a large part of the grains, i.e. 2 – 4 µm large ones, are in a MDS as depicted in Figure 4.5 and Figure 4.6. This observation matches the results obtained by SQUID magnetometry in the sense that the initial magnetization increases strongly at lower fields indicating a magnetization by domain growth i.e. domain wall movement. This process can be observed in Figure 4.6, since only larger grains are in a MDS, the domain growth only occurs in larger grains, while smaller grains maintain their magnetization. The results obtained from MFM also match the results obtained by SQUID magnetometry quantitatively in terms of magnetization (see Figure 4.7). At larger fields around 0.4 T the magnetization curve obtained by SQUID magnetometry flattens and forms a plateau at the same field the domain growth in larger grains observed by MFM comes to an end since the larger grains are in a saturated SDS. A further increase of magnetization at fields larger than 0.4 T can then be correlated to the magnetization of smaller grains below the critical single domain size requiring larger fields to get magnetized which can be observed in Figure 4.6. Unlike larger grains that are in a MDS in the TDS, smaller grains require a certain nucleation field in order to reverse their magnetization.

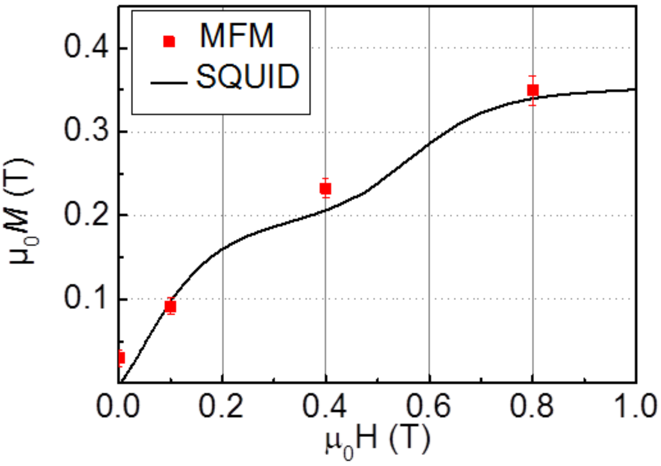

Figure 4.7 Magnetization of M 1180 from the TDS measured by SQUID magnetometry correlated with the magnetization extracted from MFM images.

The magnetization obtained from the MFM images matches the magnetization obtained by SQUID magnetometry almost exactly in Figure 4.7. Small deviations are most likely the result of the limited statistic of the observed area. The fact that the two methods produce quantitatively the same result is not self-evident considering that SQUID magnetometry is a bulk measurement method and MFM only considers surface magnetization. The fact that surface and bulk magnetization match so well might be connected to the fact that the observed grains are close to the critical single domain size and the demagnetizing influence of the stray field is not large enough to form MDS at the surface. As will be shown in the following the quantitative correlation of magnetization works less well if larger grains are involved.

The *in-situ* demagnetization from the remanent state of M 1180 observed by MFM is depicted in Figure 4.8. In the remanent state all grains are saturated, the remaining contrast originates either from pores or from compositional changes. It is also likely that misaligned grains are the reason, but this can only be estimated based on the size of the grains and the known difficulty to orientate smaller grains. At an applied field of -0.1 T the domain configuration maintains largely the same indicating no magnetization reversal. Increasing the external field to -0.2 T results in the magnetic reversal of approximately 4 small grains with a grains size well below 1 µm (see Figure 4.5). Based on the previous results this behavior appears surprising, however, it might be the result of the surrounding grains that show a bright contrast in the remanent state and might therefore be misaligned.

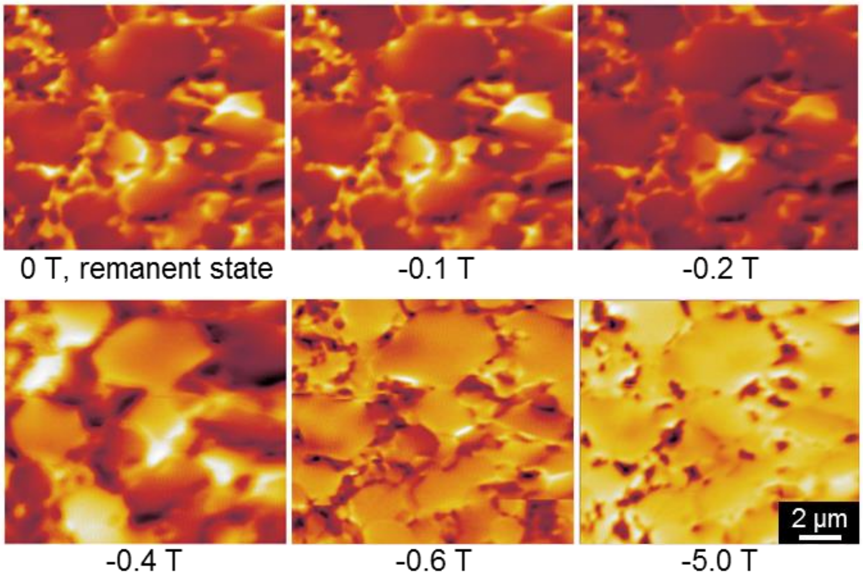

Figure 4.8 Demagnetization under external magnetic field of M 1180 observed by MFM.

At a field of -0.4 T a significant amount of the grains show a bright contrast i.e. have changed their magnetization state. The magnetization change mainly occurs by forming reversed SDS, which happens mainly in larger grains, nevertheless some smaller grains also have reversed their magnetization. The fact that the reversed larger grains reverse their magnetization from a SDS to the reversed SDS in Figure 4.8 is most likely an effect of the relatively large field steps during the experiment. Since the grains are in principle large enough to allow the formation of a MDS (at the surface) it is likely that they form an intermediate MDS during the demagnetization. As was shown in Figure 4.6 an external field of 0.4 T is large enough to form a SDS in larger grains that were initially in a MDS. The application of an external field of -0.6 T causes most of the remaining, mostly smaller, grains to reverse their magnetization. A comparison between -0.6 T and -5.0 T shows that only a small amount of very small grains have not reversed their magnetization at -0.6 T. This may be due to statistical effects, but might also be because very small grains possess a larger coercivity due to their size as well as high Al content.

The same procedure described above was used to extract the magnetization values from the MFM images of the demagnetization. The correlation with the SQUID data is depicted in Figure 4.9. Similar to the initial magnetization curve in Figure 4.7, the results obtained from the global SQUID measurement and the local MFM measurement also match very well. This allows the assumption that the processes regarding the domain evolution that are observed by MFM are also, to some degree, representative for the bulk.

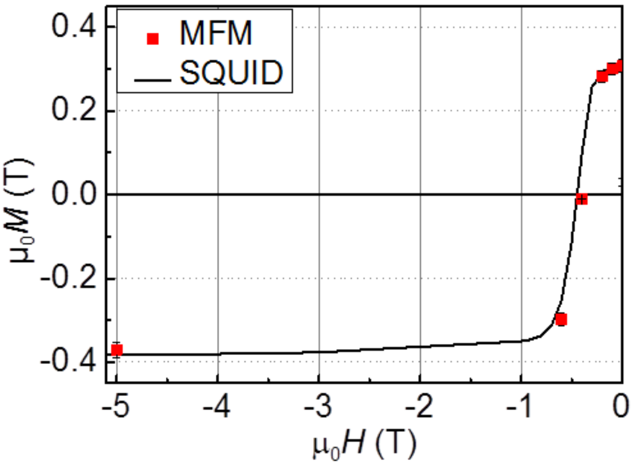

Figure 4.9 Demagnetization of M 1180 from the saturated state measured by SQUID magnetometry correlated with the magnetization extracted from MFM images.

This behavior i.e. a matching surface and bulk magnetic behavior is rather extraordinary and is not found in e.g. rare earth containing magnets [Hubert and Schäfer1998, Kobayashi2015]. It should be mentioned however, that in a recent publication by Soderžnik *et al.[Soderžnik2017]* the authors were able to achieve an almost quantitative agreement between bulk and surface by analyzing the domain structure perpendicular to the pole surface. Nevertheless a considerable difference between bulk and surface magnetization still remained. One of the reasons for this is, as described in previous chapters that in rare earth magnets such as Nd-Fe-B the coercivity is highly dependent on the presence of secondary phases (see also chapter 2.3). If these secondary phases are removed by the polishing, the highly reactive surface is exposed to oxidation by ambient air, resulting in a drastically altered magnetic behavior of surface grains. Ferrites (as stable oxides) do not show such a mechanism and do not oxidize under ambient air, meaning that surface and bulk grains behave more alike. In addition to this, the magnetization and therefore the stray field energy, which can lead to a self-demagnetizing of surface grains, is lower in ferrites. Another factor that comes into play here is the relatively small grain size close to or below the critical single domain size that is causing the grains to act as- or close to- single domain like behavior.

In-situ magnetization of M 1240

In comparison to M 1180, sample M 1240 exhibits a more inhomogeneous microstructure. Here the grain size distribution spreads from sub-micron grains up to grains in the range of 20 – 30 µm. The magnetization from the TDS is shown in Figure 4.10. In the depicted area the grain size is largely comparable to M 1180, however, most of the bottom part of the depicted area shows a fraction of a single grain with a diameter of approximately 18 µm. The same grain will also be discussed later in this chapter.

In the TDS, most of the larger grains, including the very large grain at the bottom are in a MDS. The application of a small magnetic field of 0.1 T leads to a clear growth of the dark contrasted domains but is not large enough to expel the bright domains from the respective grains. Also here the sporadic magnetization reversal of small single domain grains (< 2 µm) can be observed. At larger fields of 0.4 T essentially all of the larger grains are in a SDS i.e.

have been fully magnetized by the external magnetic field. In comparison to 0.1 T, a larger amount of smaller SDS grains have also reversed their magnetization. Nevertheless a significant number of primarily smaller grains (< 2 µm) are not yet magnetized along the external field direction.

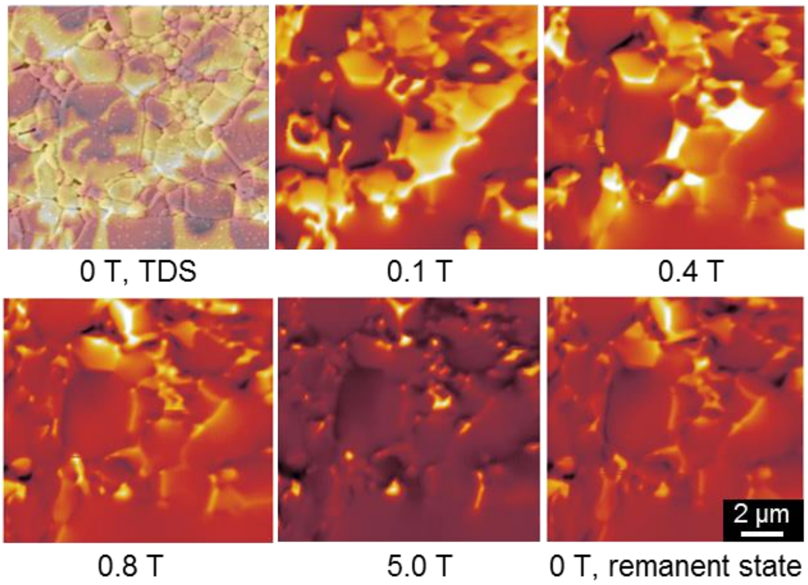

Figure 4.10 Magnetization process of sample M 1240 under external magnetic field recorded by *in-situ* MFM.

If the external field is increased to 0.8 T almost the entire sample is magnetized with the exception of a few small grains. The only remaining bright contrast in a larger grain is coming from a grain in the upper middle part of the image, which is most likely originating from a misaligned grain as the respective pictures at 5.0 T and in the remanent state indicate. At 5.0 T the entire area is magnetized, with the remaining contrast originating from pores and compositional changes. In the remanent state the grains maintain their magnetization.

The *in-situ* demagnetization of M 1240 is depicted in Figure 4.11. At an applied field of -0.1 T the domain structure does not show any change, the only difference is that the bright contrast of supposedly misaligned grain increases slightly. Applying a field of -0.2 T causes the very large grain at the bottom of the image to change its magnetization state to a bright contrast. Since only a small part of the grain is visible in the depicted area, it is not possible to say whether the grain is forming a MDS or a SDS.

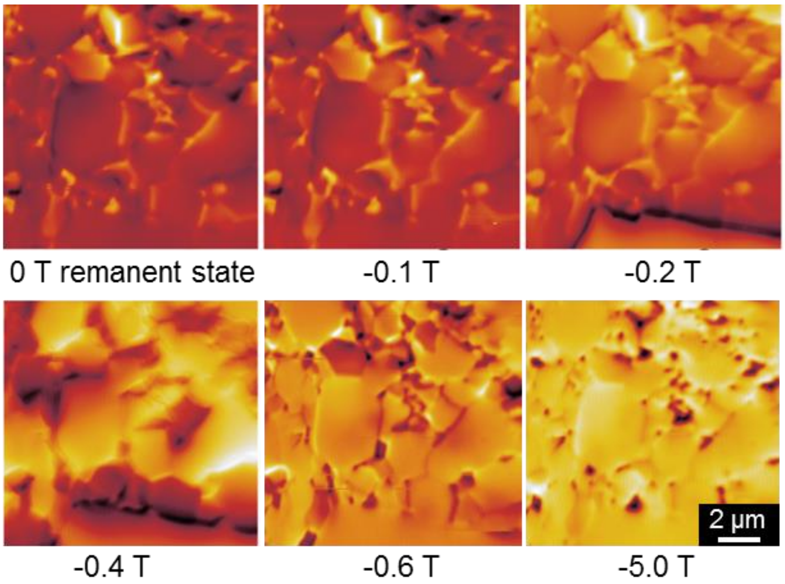

Figure 4.11 Demagnetization under external magnetic field of M 1240 observed by MFM.

At a demagnetization field of -0.4 T the larger grains in range of 2 – 4 µm have reversed their magnetization accompanied by the sporadic reversal of smaller grains. The contrast in this picture is slightly blurry due to the magnetic instability of the tip in the external field. Matching the previous observation in M 1180, the larger grains form reversed SDS, while smaller grains largely maintain their initial magnetization. Increasing the demagnetizing field to -0.6 T results in a magnetic reversal most of the remaining smaller grains. At -5 T magnetization of the remaining small grains is also oriented along the external field, with the only contrast originating from pores and/or compositional changes.

Depicted in Figure 4.12 are the comparisons for the initial magnetization and demagnetization of M 1140 determined by SQUID magnetometry and MFM. The magnetization of SQUID and MFM follow the same trend as M 1180. At low fields, the magnetization increases quite rapidly due to the magnetization by domain wall motion. Since the domain walls can be moved easily, the magnetization of MDS grain does not require large fields, which is typical for nucleation dominated magnets [Coey2010]. As can be seen in the MFM images in Figure 4.10 the larger grains that are in a MDS in the TDS, have saturated to a SDS at approximately 0.4 T resulting in a plateau in the magnetization curve. Smaller grains, below the critical single domain size are in the SDS and require a nucleation field larger than 0.4 T to reverse their magnetization state from SDS to the reversed SDS. The curves determined by SQUID magnetometry match the MFM measurements similarly well as previously for M 1180.

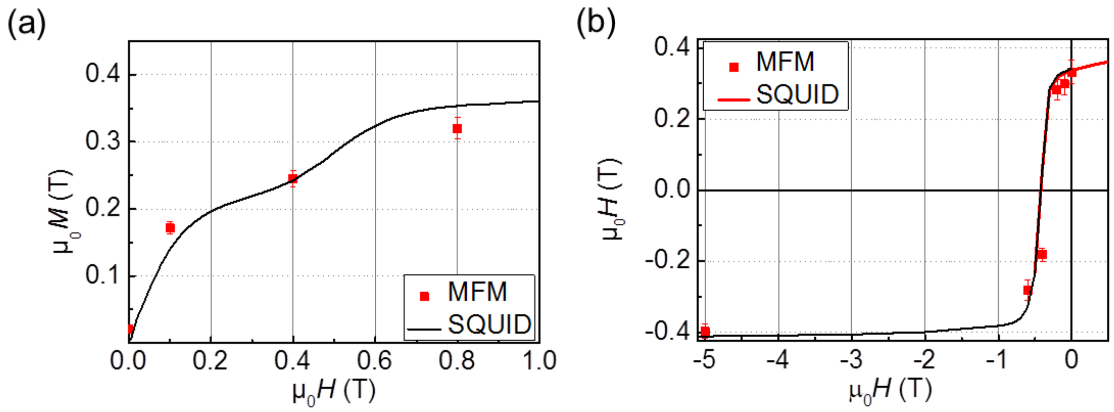

Figure 4.12 Initial magnetization from the TDS and demagnetization of M 1240 by SQUID magnetometry and MFM.

During the demagnetization, a similar behavior as in M 1180 can be observed in Figure 4.11 i.e. larger grains reverse their magnetization at lower fields than smaller ones. The formation of MDS is not observed during the demagnetization, which is presumably a result of the “large” magnetic field steps i.e. the MDS occurs but grains are re-saturated within the field interval. The demagnetization determined by MFM and SQUID magnetometry match quite well, however, slightly worse in comparison to M 1180 (Figure 4.9). This is most likely due to the slightly larger average grain size of M 1240, which will be shown in the following. The analyzed area also includes the fraction of a very large grain which can be seen at the bottom right hand and middle of each picture. As will be shown later, the magnetic properties change drastically with grain size. This means that the involvement of this grain is not necessarily representative for the entire sample. Nevertheless, the agreement between MFM and SQUID magnetometry is very good considering that the MFM image only depicts a limited sample size with a limited statistic. Experiments with Kerr microscopy (that would offer a better statistic) showed insufficient Kerr contrast on these samples.

In order to check the existence of intermediate MDS during the demagnetization, a particularly large grain of approximately 18 µm in diameter was analyzed in M 1240. Larger grains have a higher tendency to form MDS since the stray field energy is larger and the formation of domain walls to minimize stray field energy is thermodynamically favored. The probability to find a MDS in a large grain that exceeds the critical single domain size by approximately one order of magnitude is therefore very high. The observed grain is depicted in Figure 4.13 and it is the same grain that was already displayed in the bottom right and middle in Figure 4.10 and Figure 4.11.
Prior to the measurement, the grain was magnetized using an external magnetic field of 5 T, resulting in a SDS at remanence as shown in the first picture of Figure 4.13. Applying a small demagnetizing field of -0.1 T does not result in a significant change in magnetization, meaning that all depicted grains maintain their SDS. The same magnetic configuration could be observed at a field up to -0.16 T (not shown in Figure 4.13) before the depicted large grain collapsed from a SDS to a MDS at an applied field of -0.18 T. The resulting domain structure shows a large reversed domain (bright contrast) with a few remaining circular or elongated domains showing the dark contrast as in the remanent state. The domains that maintained their magnetization direction (with respect to the remanence) are located in the center of the grain. By gradually increasing the external field, the remaining dark domains are shrinking to small circles, before they disappear.

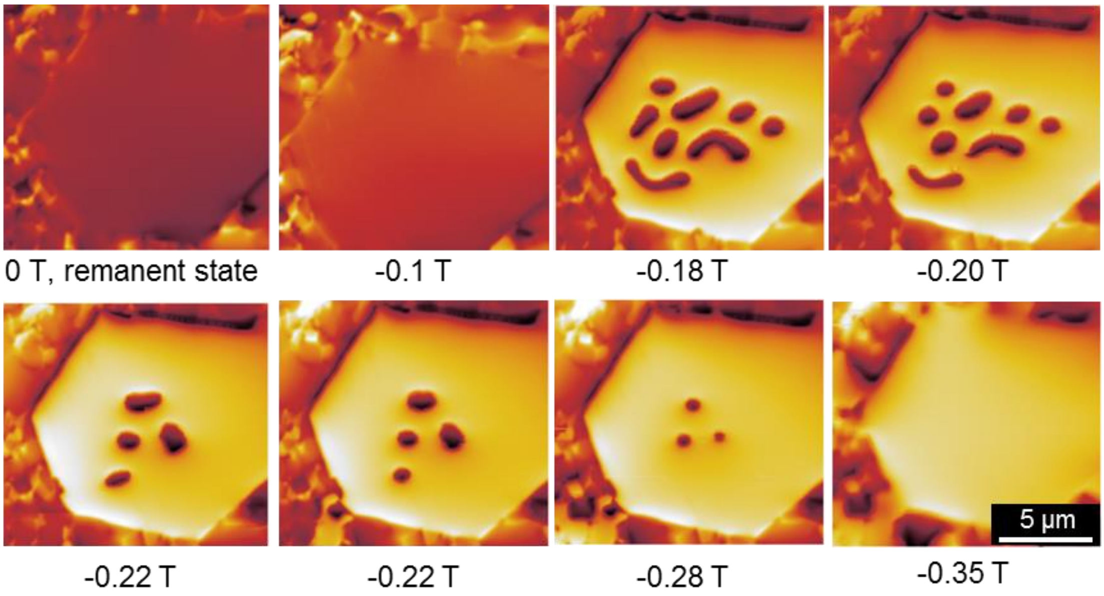

Figure 4.13 Demagnetization of a very large grain far above the critical single domain size in sample M 1240.

The final result is a re-saturated SDS at an applied field of -0.35 T where all the bubble like domains have disappeared. Most of the surrounding smaller grains maintain their magnetization state, but a few, mostly adjacent, also change their magnetization during the demagnetization and re-magnetization process. It is noticeable that the remaining dark domains that form at -0.18 T maintain largely stationary with respect to their position during the demagnetization process. The center of each domain seems to be fixed to a specific location, while the shape of the domain changes with increasing field. The larger domains change their form from a “boomerang” shape gradually to a spherical shape. The diameter of spherical domains decreases with increasing field, before they disappear completely. This phenomenon might be an indication for pinning effects that fix the domains to the specific locations on surface observed in Figure 4.13. Though hexaferrites are considered nucleation type magnets the possibility of a pinning mechanism was pointed out by Kools *et al.* [Kools2003] and other authors [Tabatabaie2009]. The extent of this possible mechanism will be discussed in the further course.

4.1.1 Domain formation and evolution after field demagnetization

The quantitative agreement between surface and bulk magnetization during the magnetization from the TDS indicated that the processes that are observed by MFM at the surface are also representative for the bulk. However, so far the correlation was only carried out for comparably small grains. Since large gains have been shown to demagnetize at smaller fields than smaller grains, the role of larger grains is especially important for the demagnetization process. From the demagnetization of an 18 µm large grain in Figure 4.13 the presence of MDS during the process becomes evident, as does the importance of field step size for the observation of MDS. To capture the role that MDS play during the demagnetization a different measurement procedure was applied in the following paragraph. The samples were magnetized in an external field of 5 T, before a demagnetizing field was applied that was large enough to obtain a remaining magnetization of 0.0 T. This demagnetizing field is typically slightly larger than the coercivity of the respective sample.

The resulting magnetic state is the DC-demagnetized state (DCD) that is typically different than the TDS. From the DCD the samples were re-magnetized and the respective re-magnetization curve was recorded by SQUID magnetometry to obtain the bulk magnetization behavior. This procedure was applied to sample M 1180, M 1240 and M 1280 as shown in Figure 4.14 (a).
For the domain observation by MFM, sample M 1240 was chosen for these measurements, since the grain size distribution allows the observation of a very fine microstructure that is comparable to the optimized sample M 1180, but also shows the processes that occur in larger grains. A larger surface area was chosen in order to observe small and large grains simultaneously. The domain configuration in the DCD is depicted in Figure 4.14 (b).

The DCD can be understood as a “snapshot” of the domain structure that forms during the demagnetization by external magnetic field, allowing an insight into domain evolution during this process. By defining the DCD by zero remaining magnetization it can be assumed that close to 50 % of the magnetic domains have changed their magnetization in this state. As shown in Figure 4.14, the re-magnetization curve from the DCD differs from the initial magnetization curve shown in Figure 4.2 (a) for the samples M 1180 and M 1240. The magnetization curve from the TDS and DCD of M 1280 are almost identical. This behavior can be understood based on the domain structure of the DCD depicted in Figure 4.14 (b). Most large (2 – 4 µm) grains form a SDS in the DCD unlike in the TDS, where they form MDS (see Figure 4.5). This shows that these grains are large enough to from MDS, but the DC demagnetization does not form this domain configuration. Small grains below 2 µm that are close to the critical single domain size also form SDS in the DCD as they do in the TDS. The only MDS grain that can be observed in the DCD is the approximately 18 µm large grain. Based on the previous observations such grains are expected to have the lowest coercivity and the largest demagnetizing i.e. stray field, which is presumably the reason why the observed grain collapses to a MDS.

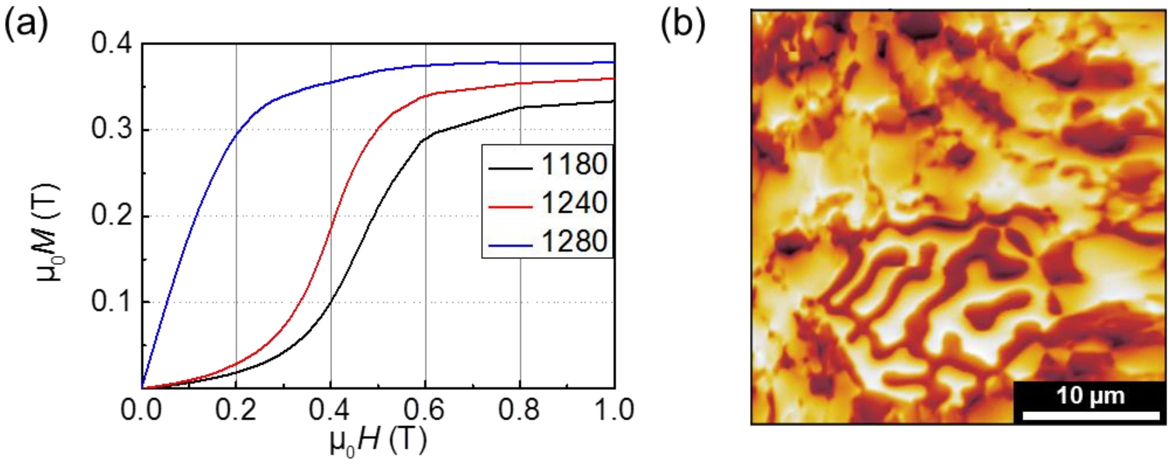

Figure 4.14 (a) Re-magnetization from the DC-demagnetized state (DCD) for sample M 1180, M 1240 and M 1280 determined by SQUID magnetometry and (b) the DCD domain configuration of sample M 1240 determined by MFM.

Sample M 1280 was intentionally over processed to form especially large, low coercivity grains that form MDS in the TDS and the DCD as a reference. The large initial magnetization increase of M 1280 can therefore be attributed to the magnetization via domain wall movement in large grain as was previously observed for the TDS indicating that the domain configuration in the TDS and DCD differs only marginally. M 1180 and M 1240 on the other hand, do not show the high magnetization increase at low fields that was present in the initial magnetization from the TDS. In the TDS this was attributed to the presence of MDS in larger grains, since these grains do not show a MDS in the DCD in Figure 4.14 (b) the observed re-magnetization agrees with the expected behavior bases on the domain configuration observed by MFM. The large increase of magnetization of M 1180 and M 1240 at larger fields of about 0.4 T is a result of the SDS grains reaching their nucleation field and reversing their magnetization.

The re-magnetization process from the DCD observed by MFM is depicted in Figure 4.15 as well as the saturated state at 5 T, the remanent state and the domain configuration at the demagnetizing field of -0.426 T that was used to obtain the DCD. As is to be expected, the saturated and remanent state differ very little from each other. Under the applied demagnetization field of -0.426 T the contrast formation becomes slightly blurry since the applied field is close to the coercivity of the MFM tip. Noteworthy is here that the very large grain in the bottom center part of each image, as well as a few 2 – 4 µm large grains, are in a reversed SDS, but collapse to a MDS upon removal of the field.

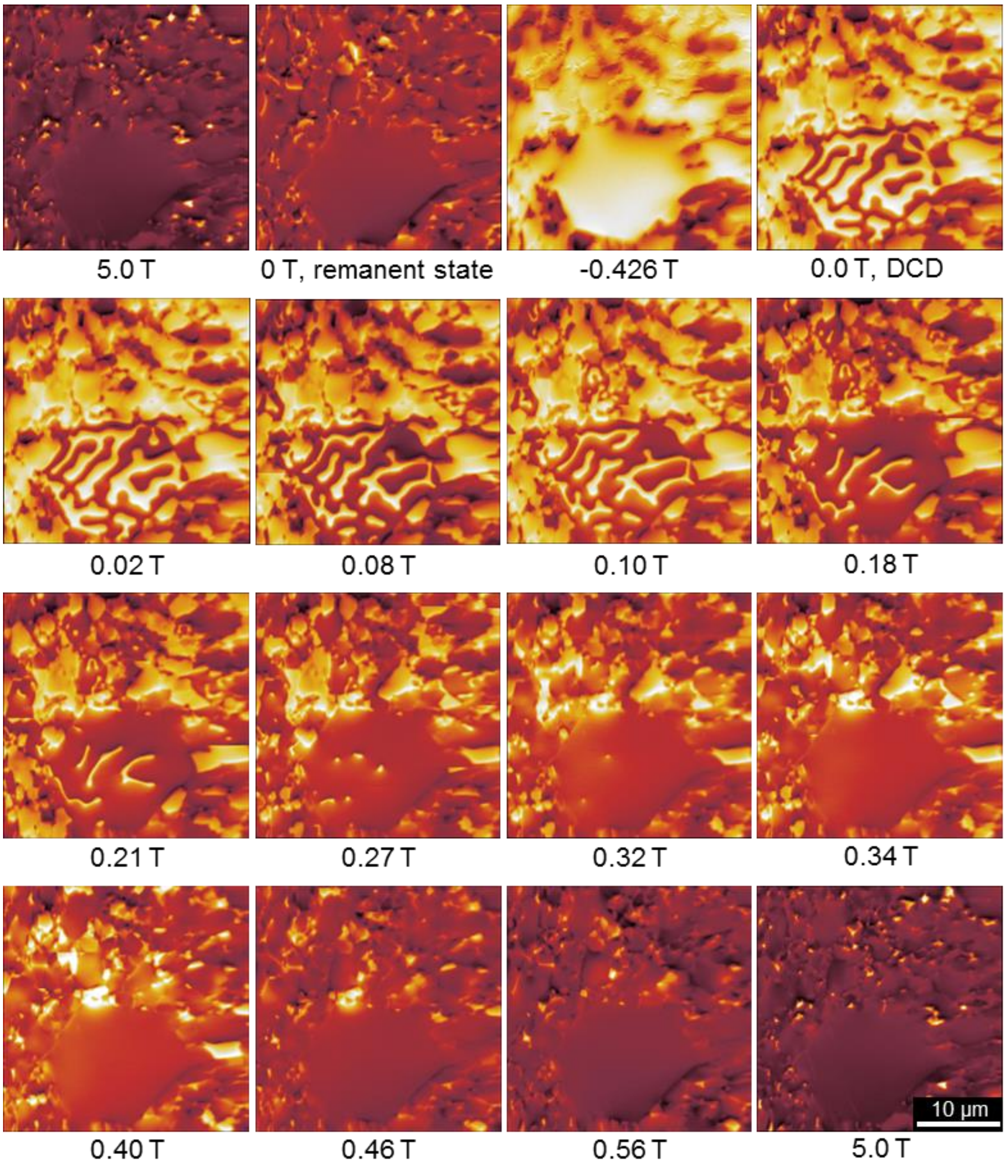
5.0 T
0 T, remanent state
-0.426 T
0.0 T, DCD
0.02 T
0.08 T
0.10 T
0.18 T
0.21 T
0.27 T
0.32 T
0.34 T
0.40 T
0.46 T
0.56 T
5.0 T

Figure 4.15 Saturation, demagnetization and re-magnetization process of M 1240 after DC-demagnetization observed by MFM.

Gradually increasing the magnetic field in the same direction as the initial magnetization, leads to a step wise collapse of 2 – 4 µm large grains from SDS to MDS. Grains that have collapsed to a MDS gradually re-magnetize by domain wall movement i.e. a growth of dark depicted domains until all domain walls are driven out of the respective grain and it forms a SDS. The process of domain wall motion and expulsion is completed at 0.4 T, where all observed grains are in a SDS with their magnetization either parallel or antiparallel with respect to the external field. Smaller grains <2 µm reverse their magnetization by a coherent spin rotation where no intermediate MDS can be observed. These processes start at a field of approximately 0.32 T and are the only magnetization processes occurring above 0.4 T until saturation.

An interesting feature of the measurement technique MFM can be observed i.e. at 0.18 T or 0.21 T where individual grains change their magnetization state from one scan line to the next. This is an effect of the magnetic moment of the MFM tip that is large enough to change the magnetic state of a respective grain, typically in combination with an external magnetic field.

The before mentioned method to extract the magnetization value from MFM images was applied here as well and compared to the SQUID magnetometry measurements (Figure 4.16). Here the MFM magnetization at lower fields diverges from the SQUID data, however, for external fields larger than 0.4 T, the two data sets match quantitatively very well. The disagreement between MFM and SQUID at low fields is presumably a result of the contribution of multi domain grains, keeping in mind that approximately quarter of the total area is occupied by the very large multi domain grain.

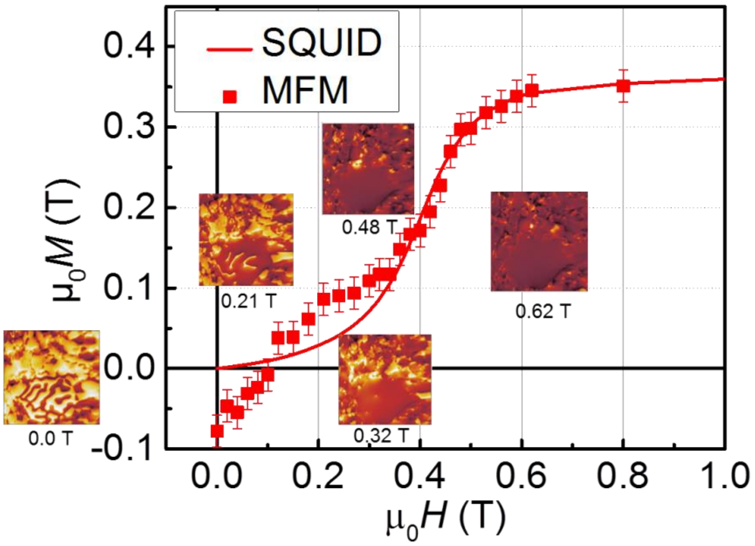

Figure 4.16 Correlation of MFM and SQUID magnetometry magnetization for the re-magnetization from the DC demagnetized state (DCD).

At the surface the formation of MDS is caused by the minimization of stray field energy, the larger a grain, the higher the probability to form a MDS. The domain walls in MDS on the surface can be moved quite easily, and are harder to correlate with the processes in the bulk, as the discrepancy at lower fields between MFM and SQUID shows. At higher fields, when all domain walls are expelled from the grains, the processes observed on the surface seem to describe the bulk behavior as well.

Since the formation of MDS during the de- and re-magnetization has been shown so far, and the involvement of large MDS shows significant discrepancy regarding the magnetization of bulk and surface by MFM and SQUID, the question arises if and how MDS form in the bulk. Since the domain structure in the bulk is not easy to access experimentally the analysis and quantification of MDS can only be performed indirectly. In order to do this, the following assumptions were made: i) domain walls can be moved by applying an external magnetic field, ii) if the antiparallel oriented domains are not entirely driven out of the respective grain, the magnetization will return to a certain degree to its initial MDS to minimize stray fields. Assuming this, it can be concluded that minor loops at sufficiently small fields should display a certain amount of reversible magnetization, and thus reversible susceptibility, if multi domains are present. For this chapter a minor loop or minor loops will be considered as the application of a small magnetic field resulting in a partial magnetization $J_{\mu0Hi}$, followed by the reduction of the magnetic field to zero resulting in the partial remanence $J_{r,\mu0Hi}$. The average reversible susceptibility (χ_{Rev}) is given by the difference of $J_{r,\mu 0Hi}$ and $J_{\mu 0Hi}$ divided by the applied field H_i i.e. as the slope of the line connecting the partial magnetization $J_{\mu 0Hi}$ with the partial remanence $J_{r,\mu 0Hi}$. The minor loop analysis was performed for the magnetization from the TDS and the DCD for all samples as depicted in Figure 4.17. The average reversible susceptibility is a representation of reversible magnetization processes via domain wall motion in multi domain grains while irreversible magnetization processes correspond to coherent spin rotations that mainly occur in smaller grains [Kobayashi2013]. This means that the amount of reversible susceptibility is proportional to the amount of MDS involved in the minor loop.

As shown before, the magnetization curves from the TDS and the DCD for M 1280 are almost identical, which is also the case for the minor loop analysis (Figure 4.17 (a) and (b)). The involved magnetization processes are largely reversible Figure 4.17 (c) and (d)) confirming the previous conclusion of MDS in the bulk due to the large amount of several 100 µm large grains.

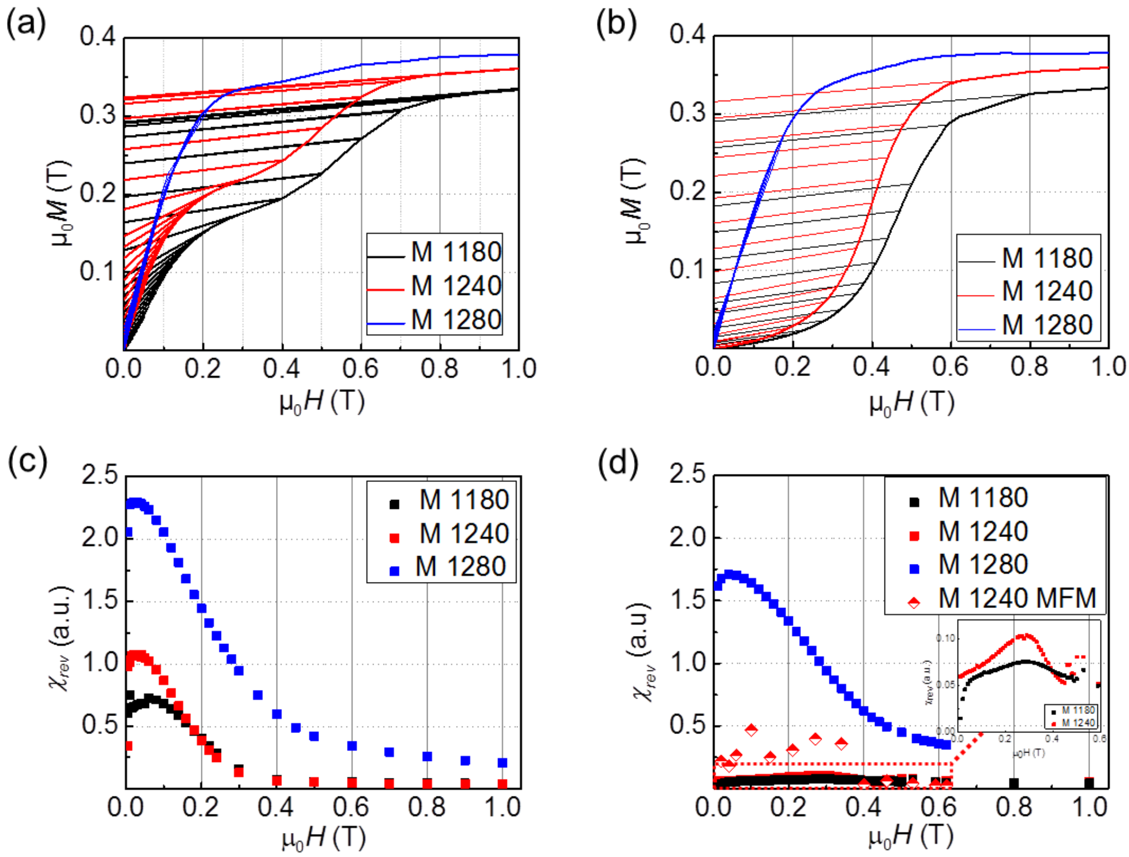

Figure 4.17 Minor loops of the magnetization from TDS (a) and the DCD (b) of sample M 1180, M 1240 and M 1280. (c) χ_{rev} determined from minor loops shown in (a) and (d) χ_{rev} determined from minor loops after DCD shown in (b) as well as χ_{rev} of minor loops after DCD determined from MFM measurements of sample M 1240.

The maximum reversible magnetization processes occur at approximately 0.05 T and are decreasing with larger fields, indicating that domain walls indeed require only small fields to be moved. Due to the gradual saturation of multi domain grains to the SDS, the amount of reversible susceptibility decreases at larger fields. At larger fields, the reversible susceptibility does not drop to zero due to rotation processes in misaligned grains and the self-demagnetization of large grains in the sample. The particular high amount of reversible magnetization processes at higher fields of M 1280 is a result of the low coercivity and thus large magnetization change by self-demagnetization. Since there is only a small quantitative difference between the magnetization from the TDS and DCD in M 1280, both states contain large amounts of MDS and presumably differ very little from each other. From the TDS the samples M 1180 and M 1240 show the same maximum at 0.05 T but their reversible susceptibility decreases to almost zero at higher fields. This is in line with the previous conclusions that the magnetization processes via domain wall motion are almost finished at a field of 0.4 T and further magnetization occurs mainly through irreversible processes i.e. coherent spin rotation. From the DCD, on the other hand, the samples M 1180 and M 1240 display a comparably small amount of reversible processes. A detailed depiction of the respective curves can be seen in the inset, showing that the two curves form a maximum at approximately 0.3 T. The results show that neither in the DCD nor during the re-magnetization from the DCD a significant amount of MDS are involved or present in the bulk (unlike in M 1280). The results are consistent in the sense that there is a tendency towards larger portions of reversible magnetization from M 1180 to M 1280 in accordance with the microstructure [Maki1989, Schrefl1993]

By applying the minor loop technique, the processes regarding SDS and MDS in the bulk can be understood. However, as already established, surface domains especially of larger grains can differ from the bulk behavior. The question arises therefore, how surface domains behave if subjugated to the minor loop technique. In an attempt to validate the assumptions made previously regarding the reversible magnetization of minor loops, the same magnetic field steps as used in the minor loop bulk analysis were applied to M 1240 and analyzed by MFM, starting from the DCD. The domain structure was determined by MFM of every respective partial magnetization $J_{\mu 0Hi}$ and the partial remanence $J_{r,\mu 0Hi}$. The result is shown in Figure 4.18 starting with the domain state of the DCD.

The ca. 18 µm large grain is initially forming a MDS in the DCD. The application of a small magnetic field during the first minor loops causes the antiparallel i.e. bright domain to shrink. The shrinkage of the antiparallel domain is proportional to the external field. However, upon removal of the field, the domain structure returns to the almost identical configuration as in the DCD for fields smaller than 0.15 T. At a field of 0.34 T, the grain forms a SDS, upon removal of the magnetic field the SDS collapses to a different MDS than the previous. The SDS maintains stable at zero field, if the external field is increased to 0.4 T and the grain remains fully magnetized. These measurements confirm that domain walls can be moved quite easily; however, in a nucleation dominated magnet where domain walls can move freely and do not require much energy to do so, the domains should form circular shapes to minimize domain surface energy. By applying a magnetic field, those domains should shrink and disappear. The domains in the depicted large grain, however, form elongated shapes, creating a lot of surface energy. From an optical impression one could conclude that the domain is pinned to certain points on the surface that hinder a free domain wall motion. Based on the amount of reversible susceptibility displayed in Figure 4.17 (c) and (d) a pinning mechanism in the bulk is neglectable and does not contribute to the coercivity mechanism.

Grains in the range of 2 – 4 µm show similar behavior; the only difference is that most of them are in a SDS in the initial DCD and collapse to a MDS during the re-magnetization. Once in the MDS they follow the same behavior as the 18 µm large grain.

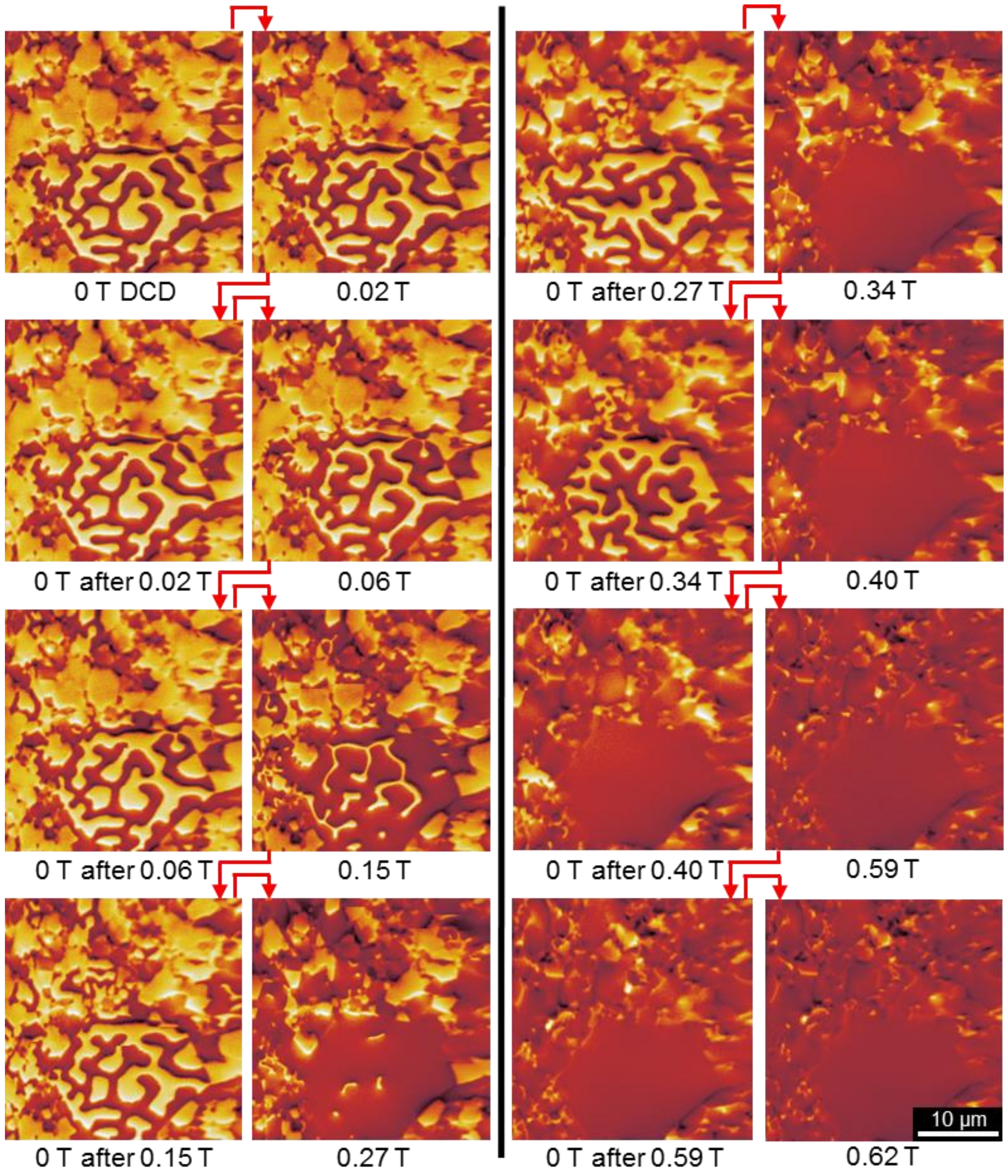

Figure 4.18 Domain evolution during the application of minor loops of M 1240. The initial field was applied from the DCD.

Small grains below 2 µm do not form MDS and do not reverse or change their magnetization if the magnetic field is reduced to zero. Above a field of ca 0.4 T, no MDS can be identified and the further magnetization occurs by coherent spin rotation.

In conclusion, regarding the minor loops of surface domains, it can be said that they behave qualitatively according to the previously made assumptions that were used for the bulk investigations, thus validating the conclusions drawn from Figure 4.17.

Concerning the quantitative agreement between surface and bulk, a comparison was drawn by extracting the magnetization values from Figure 4.18 and comparing them to the bulk values, as depicted in Figure 4.19. The magnetization behavior at low fields is depicted in Figure 4.19 (a) while Figure 4.19 (b) shows the entire measurement range. From each MFM image in Figure 4.18, a respective magnetization value for $J_{\mu 0Hi}$ and $J_{r,\mu 0Hi}$ was determined, which are connected by a solid line in Figure 4.19. The respective magnetization values under applied field $J_{\mu 0Hi}$ were fitted by a sigmoidal curve as the solid red curve. The same procedure is applied to the SQUID measurements, using the same minor loop fields as in the

MFM measurement which is depicted as the dotted red line (fit of the partial magnetizations $J_{\mu 0Hi}$) while the dotted straight lines connect partial magnetization and partial remanence of each loop.

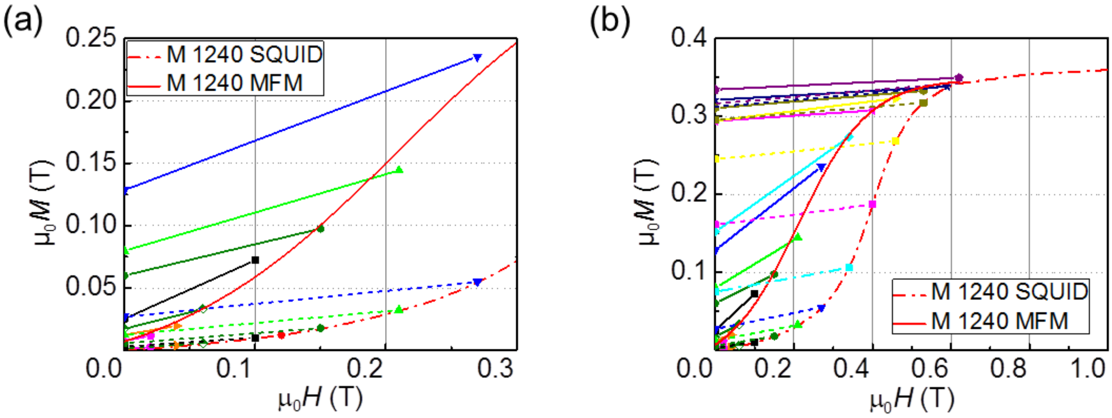

Figure 4.19 Minor loop magnetizations from DCD extracted from MFM and measured by SQUID magnetometry.

The two fitted magnetization curves from MFM and SQUID magnetometry display qualitatively the same behavior i.e. both fitted curves show a sigmoidal shape. The values/curve determined by MFM however is strongly shifted towards lower fields as a result of the discrepancy of surface and bulk in large grains. Another difference between MFM and SQUID is the slope of the solid- and respective dotted lines connecting the partial magnetization and partial remanence of each minor loop. The slope of these lines corresponds to the reversible susceptibility χ_{rev} that is also depicted in Figure 4.17. Lines of the same color refer to the same magnetizing field ($\mu_0 H_i$) of the respective minor loop in Figure 4.19. At lower fields i.e. below 0.3 T the reversible susceptibility by MFM is clearly larger than the one determined by SQUID magnetometry (see Figure 4.17 and Figure 4.19). Once the field exceeds 0.34 T, where most of the domain walls are expelled from the grains, the reversible susceptibility of MFM and SQUID are almost identical.

This means essentially that if MDS are involved, the larger the grain size, the less and less representative the surface domains become for the bulk. This applies to the absolute magnetization as well as the reversibility of magnetization processes. To be more precise, the size of the grains here becomes important if it is above the critical single domain size and the respective grain differs from a single domain like behavior. In order to minimize stray field energy, the MDS in large grains is the energetically stable state. The larger the grain is, the larger the stray field in the SDS and the more energetically favorable is the MDS. On the surface, the ratio of the two opposing domains in a MDS can be shifted to either side by applying a magnetic field. However, once the field is removed, the ratio becomes close to 50:50. If present, MDS in the bulk behave in the same way, showing a high amount of reversible magnetization. An interesting side note is that the 18 µm large grain in Figure 4.13 demagnetizes at an external field of -0.18 T but requires a field of 0.4 T to expel all domain walls and maintain a stable SDS at zero field.

From the presented results, the following approach to improve magnetic hardness can be derived: large grains at the surface have been shown to be magnetically less stable i.e. they collapse from the saturated SDS to a MDS at lower fields than smaller grains. Such MDS do not only reduce the magnetization, but can also act as nucleation sites for deeper lying grains thus trigger their demagnetization. Consequently, an improved coercivity should be achievable if the magnet surface is free of such large grains that form even under optimized sintering conditions. Experimentally, this could be realized by covering the magnet surface, especially the pole surfaces, with a layer of high coercivity, single domain grains e.g. by using Al substituted hexaferrite phase of $SrFe_{10}Al_2O_{19}$ with a particle size below the critical single domain size. The similar sintering parameters make this phase a promising candidate for this procedure. Nevertheless, preliminary experiments showed that an elaborate parameter optimization is necessary that could not be included in the frame of this work. The fundamental process of selectively hardening the pole surface by using high coercivity single domain grains should be adaptable to any type of ferrite magnet and can therefore be expanded to a large range of substitution elements, synthesis- and processing methods.

5 *In-Situ* demagnetization of core shell Nd-Fe-B grains

The following chapter is a study of the demagnetization process in (Nd,Dy)-Fe-B core-shell structured magnets on a microscopic level. The strategy behind the core-shell approach was already introduced in chapter 2.3.4. Core-shell structured magnets can be obtained via the Grain Boundary Diffusion Process (GBDP), which was discussed in chapter 2.3.4. As will be shown later in chapter 6.1 the formation of core-shell structures is only distinguishable by SEM at a very narrow diffusion depth from the surface (see e.g. Figure 6.5). Beyond the diffusion depth of a few hundred micrometers, the thickness of the Heavy Rare Earth (HRE) rich shell is in the sub-micron range making it inaccessible to most microscopic methods. It was been reported that for the shell to maintain its effectiveness i.e. to compensate the coercivity loss due to grain boundary related defects, a shell thickness of 4 nm is sufficient to obtain magnetic hardening [Bance2015a, Bance2015b]. Such shell thicknesses are too thin to be observed by domain imaging methods such as Kerr- or Magnetic Force Microscopy (MFM). For the analysis presented in this chapter, a preparation method was therefore chosen that allows the formation of HRE rich shells with a thickness of 1 – 10 µm. The magnet sample was produced by Dr. Konrad Löwe in the framework of his doctoral thesis [Löwe2016]. The patented preparation procedure involved the blending of two powders with different chemical composition [Loewe2016]: The “base-powder” consisted of “normal” milled Nd-Fe-B particles that are suitable for the preparation of sintered magnets. The second powder was partially substituted by about 4 at.% (10 wt.%) Dy resulting in a (Nd,Dy)-Fe-B powder. The latter one exhibited a slightly lower grain size in order to dissolve and then to “surround” the base-powder particles. The detailed procedure can be found in the doctoral thesis of Löwe [Löwe2016]. The resulting microstructure is depicted in Figure 5.1 (a) displaying approximately 10 – 20 µm large grains that appear as grey contrast and are separated by a thin white grain boundary layer. Other secondary phases as described in previous chapters are also displayed in white. Many of the grains show two separate contrasts from a light grey to a darker gray within the same grain. It was shown in previous publications by Löwe *et al.* that this contrast arises from the different atomic number Z in the Dy substituted $(Nd,Dy)_2Fe_{14}B$ phase [Loewe2015]. The Dy substituted shell appears slightly brighter than the pure $Nd_2Fe_{14}B$ core.

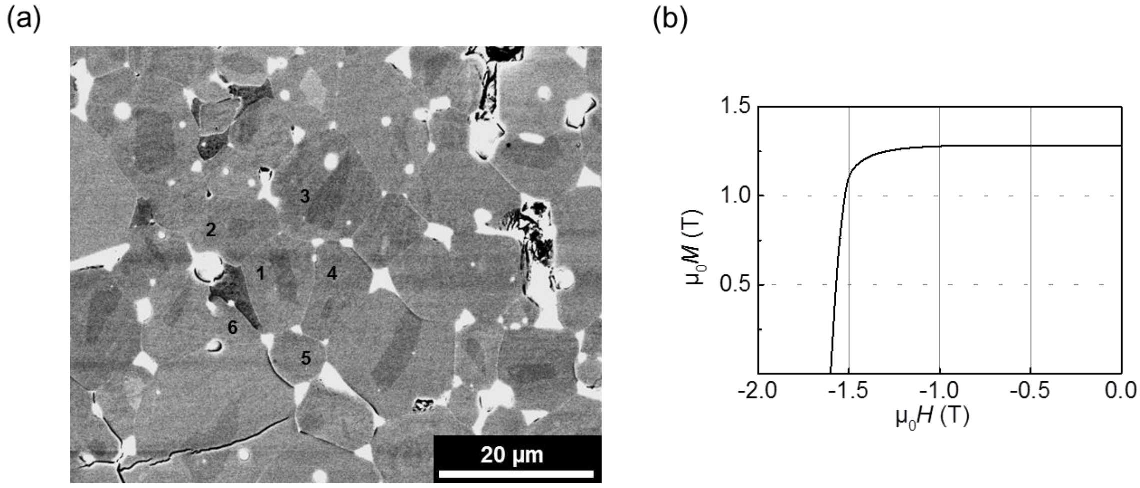

Figure 5.1 a) resulting microstructure after blending of a Dy substituted and a pure Nd-Fe-B powder to obtain a core-shell structure, b) demagnetization curve of the magnet shown in a).

The demagnetization curve in Figure 5.1 (b) measured by Dr. Konrad Löwe shows a reasonable remanence, coercivity and nucleation field, indicating that the sample used in the further cause of this chapter is qualitatively comparable to industrial standard magnets. A closer analysis of the core-shell microstructure is shown in Figure 5.2 showing a lamella that was cut from the same sample using a Focused Ion Beam (FIB) across a core-shell grain. The core-shell interfaces can be seen in an SEM image in Figure 5.2 (a) as light grey (shell) and dark grey (core). The arrow indicates the EDX line profile position and direction. Figure 5.2 (b) shows an EDX line profile across core and shell. As expected, the Fe signal does not change over the entire scan. The absolute concentrations of Fe and Nd+Dy are slightly larger than the stoichiometric composition (82.35 at.% and 11.76 at.%) due to the in chapter 3.2.1 mentioned difficulties regarding overlapping of EDX lines of the HRE and a resulting miscalibration of the EDX. Nevertheless, the Nd content according to the Nd-L_α line in the shell is approximately 1 – 1.5 at.% lower than in the core due to the partial substitution with Dy. The Dy concentration, on the shell on the other hand, is approximately 0.75 – 1.0 at.% according to the Dy-M_α line. Due to the problematics regarding the overlapping of EDX lines and quantification of elements according to their M-lines the Nd deficiency of 1 –1.5 at.% describes the Dy concentration probably more accurate than the Dy-M_α line.

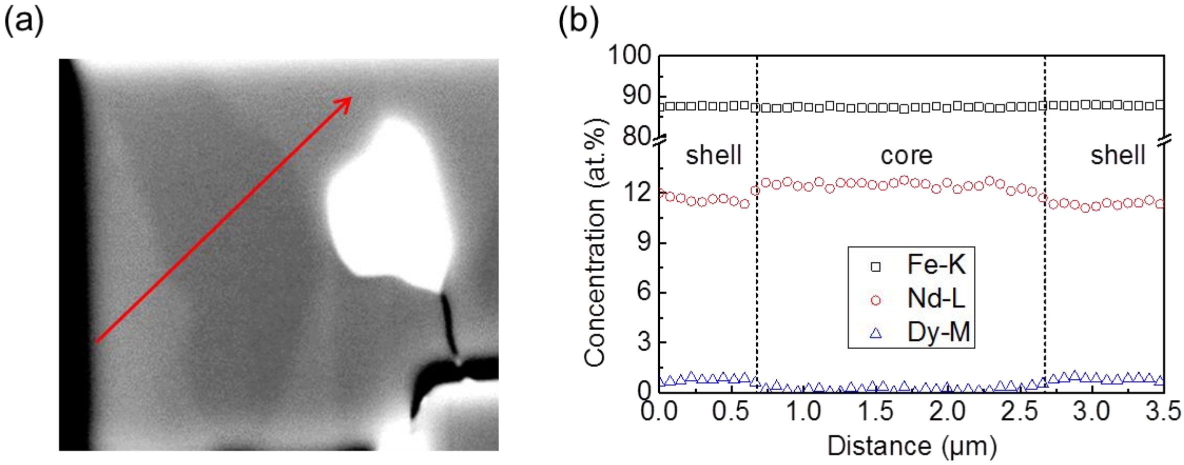

Figure 5.2 STEM-EDX line scan cross a core-shell structured grain. SEM contrast of the scanned line (a) and EDX line profile (b).

Atomic scale images of the same grain were taken from core and shell using Scanning Transmission Electron Microscopy-High Angle Annular Dark Field (STEM-HAADF) imaging mode as shown in Figure 5.3 (b) and (c). The approximate positions of the STEM images are indicated by the arrows in Figure 5.3 (a). The two STEM images display the same crystallographic orientation indicating that core and shell are epitaxially grown on each other. The insets in Figure 5.3 (b) and (c) display nicely the atomic structure of the $Nd_2Fe_{14}B$ phase. The atomic structure is matched with an atomic model of the respective orientation displaying the 2-14-1 characteristic Fe-rings in red as well as Nd in blue and B in green.

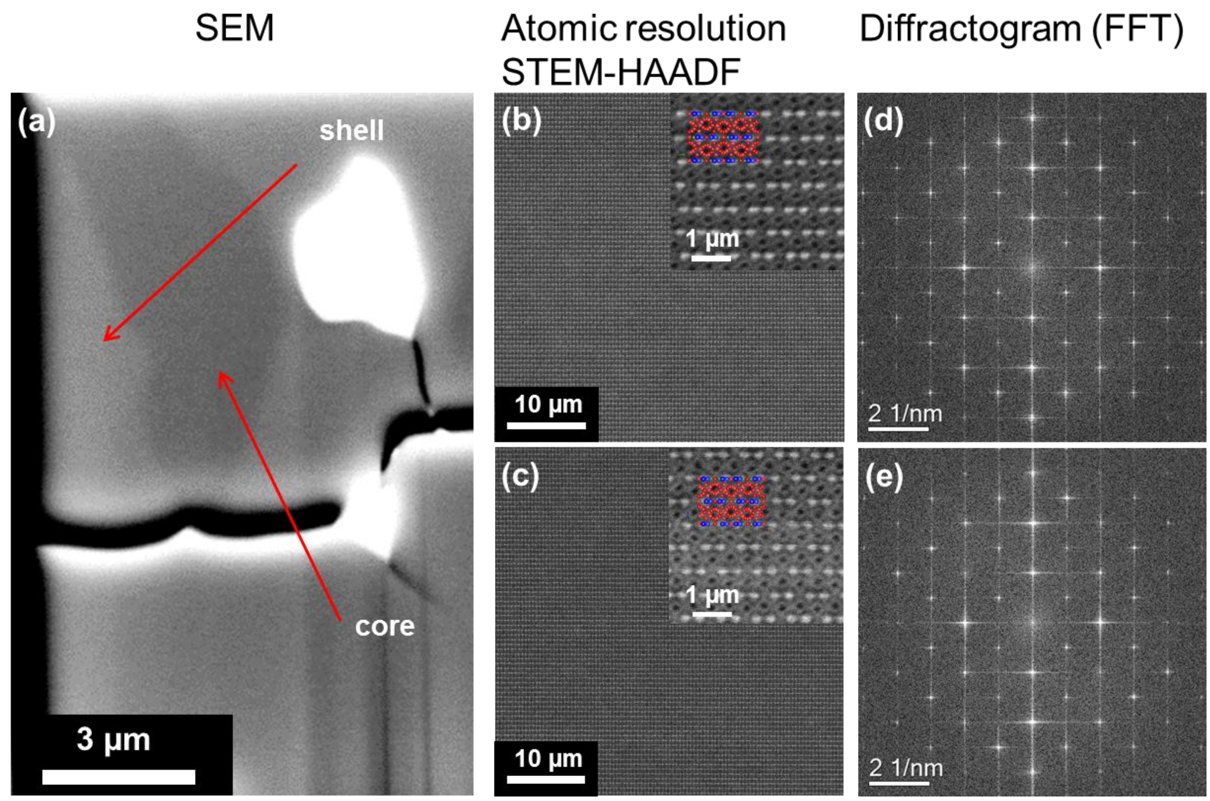

Figure 5.3 Lamella cut by FIB across a core-shell structured grain in SEM (a) and STEM-HAADF of shell (b) and core (c) and respective diffractograms (d,e).

Using a Fourier transformation (FFT) of the atomic position, a diffractogram of core and shell was created shown in Figure 5.3 (d) and (e) to compare the respective lattice constants of core and shell (Figure 5.4). The results show that the lattice constants of core and shell are identical meaning that the partial substitution of Dy for Nd is small enough to not alter the lattice parameters significantly. The implication of this is that at the core-shell interface should be relatively strain free. During the cause of the TEM investigation no signs of lattice defects such as stacking fold were found in the vicinity of the core-shell interface. Nevertheless it cannot be excluded that such defects are present, due to the large size of the grain in comparison to the TEM image size. But the identical lattice constants of core and shell and absence of defects suggest a smooth and defect-less transition from core to shell.

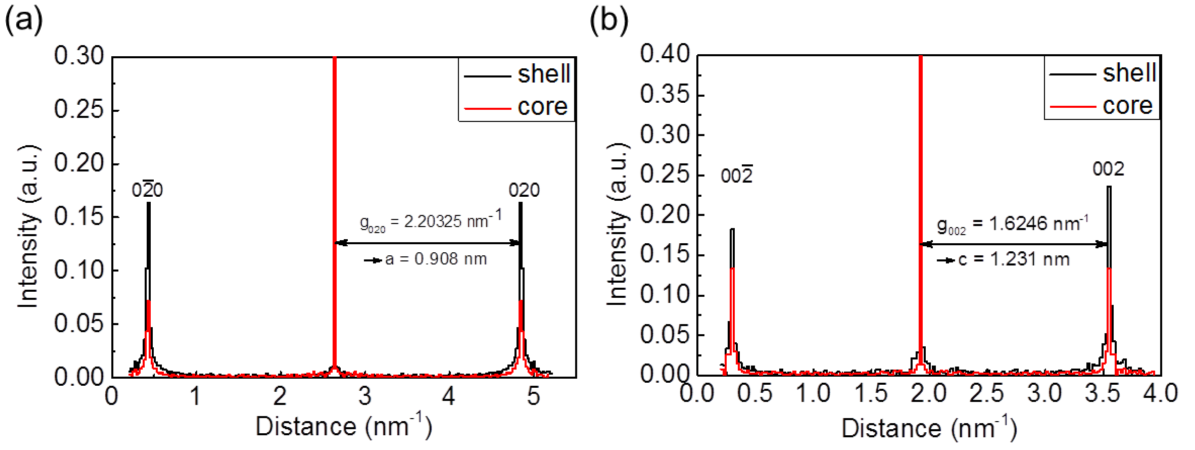

Figure 5.4 Comparison of lattice constants extracted from the diffractogram Figure 5.3 in along the 020 direction (a) and 002 direction (b).

In Figure 5.5 (a) a grain boundary between two core-shell structured grains is shown. In Figure 5.5 (a) a near atomic resolution STEM-HAADF image is depicted showing a grain oriented along its [110] zone axis on the left side of the dark grain boundary. As indicated, the thickness of the grain boundary is approximately 2 nm. While the two grains are quite clearly identifiable by atomic pattern and/or color contrast, the grain boundary shows a different contrast. The respective composition of the grains and grain boundary determined by EDX is depicted in Figure 5.5 (b). As one would expect, the grain boundary is depleted in Fe and enriched in Nd. The Dy concentration according does not show any concentration variation across the grain boundary. This could be due to the overall low Dy concentration and the already discussed difficulty regarding the Dy-M_α line, however it is also likely that Dy does not form a gradient across the grain boundary. Sepehri-Amin *et al.* could show for grain boundary diffused magnets, the grain boundary is not enriched in Dy but shows a uniform contrast extending into the respective grains [Sepehri-Amin2010]. Since the here analyzed magnet has not undergone a GBDP, the situation differs slightly but a uniform Dy contrast is not surprising.

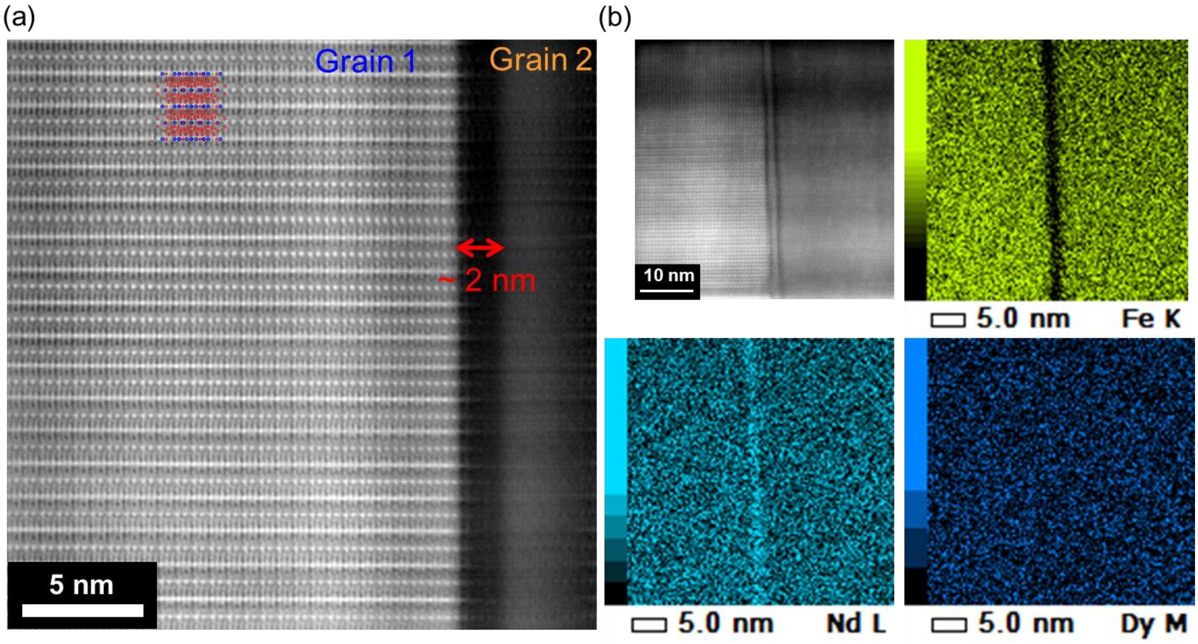

Figure 5.5 STEM-HAADF of the grain boundary and grain 1 oriented along the [110] zone-axis (a) and STEM-EDX mapping of the same grain boundary.

The grains that are indexed by the numbers 1-6 in Figure 5.1 are the same grains that are shown in Figure 5.6 by SEM and MFM. The SEM image on the left hand sight displays the Dy substituted core-shell structure, while the MFM image on the right hand sight shows the same grains in the remanent state. From the MFM images is becomes obvious that the grains marked 1 – 4 are in a SDS, while the grains marked 5 and 6 are in a MDS. Grains in a MDS can be considered demagnetized, since they do not contribute to the magnetization and can easily be manipulated by an external field. The reason, why the remanent state can display MDS grains is the polishing process and self-demagnetization as discussed in chapter 2.3.2

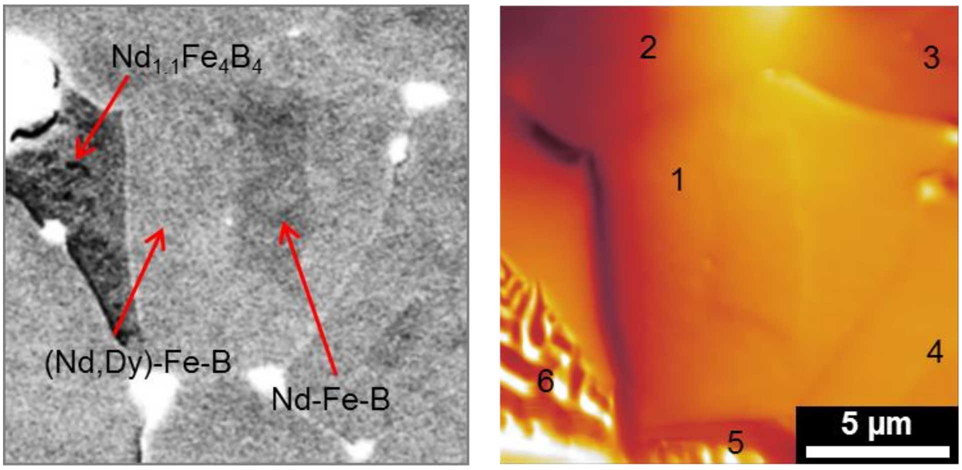

Figure 5.6 Comparison of micro- and domain structure using SEM and MFM showing core-shell structure.

On the left hand MFM image of Figure 5.6 a slight contrast within the grain marked as 1 can be seen. The contrast matches the shape of the core-shell interface in size and position depicted in the SEM image in Figure 5.6. The contrast formation of the MFM arises from the convolution of the magnetic stray field of the MFM tip with the stray field of the sample (see chapter 3.2.5). In the depicted remanent state of the Nd-Fe-B grain, the stray field of the MFM tip can be assumed to be constant meaning that the stray field of the sample has to differ between core and shell. The main difference between core and shell is the Dy content, it is therefore reasonable to assume that the contrast arises from the different magnetic moment of the $(Nd,Dy)_2Fe_{14}B$ shell and the $Nd_2Fe_{14}B$ core [Herbst1991]. The transition from core to shell i.e. its Dy concentration change is sharp enough that the clear distinction can be made from the MFM contrast. Since the magnetic moment changes very abruptly from core to shell it is reasonable to assume that other magnetic properties such as anisotropy field H_a change accordingly.

Starting from the remanent state an external magnetic field is applied in-situ using a PPMS and increased stepwise as described previously in chapter 4. The external field was applied antiparallel to the magnetization of the sample in order to demagnetize it. The domain configuration under an applied field of -0.25 T is depicted in Figure 5.7 (b) showing that the surrounding grains on the top side have collapsed from a SDS to a MDS, while the core-shell grain maintains its SDS. Increasing the external field by 10 mT to -0.26 T, as shown in Figure 5.7 (c), causes the center grain to collapse to a MDS. The previously observed contrast between core and shell can no longer be seen in the MDS, which is an effect of the stray field being far more inhomogeneous in the MDS. It should be noted that no significant difference in the domain structure of core and shell can be observed. Additional MFM images were taken at slightly higher fields (data not shown), however they did not display a significant difference in the domain structure.

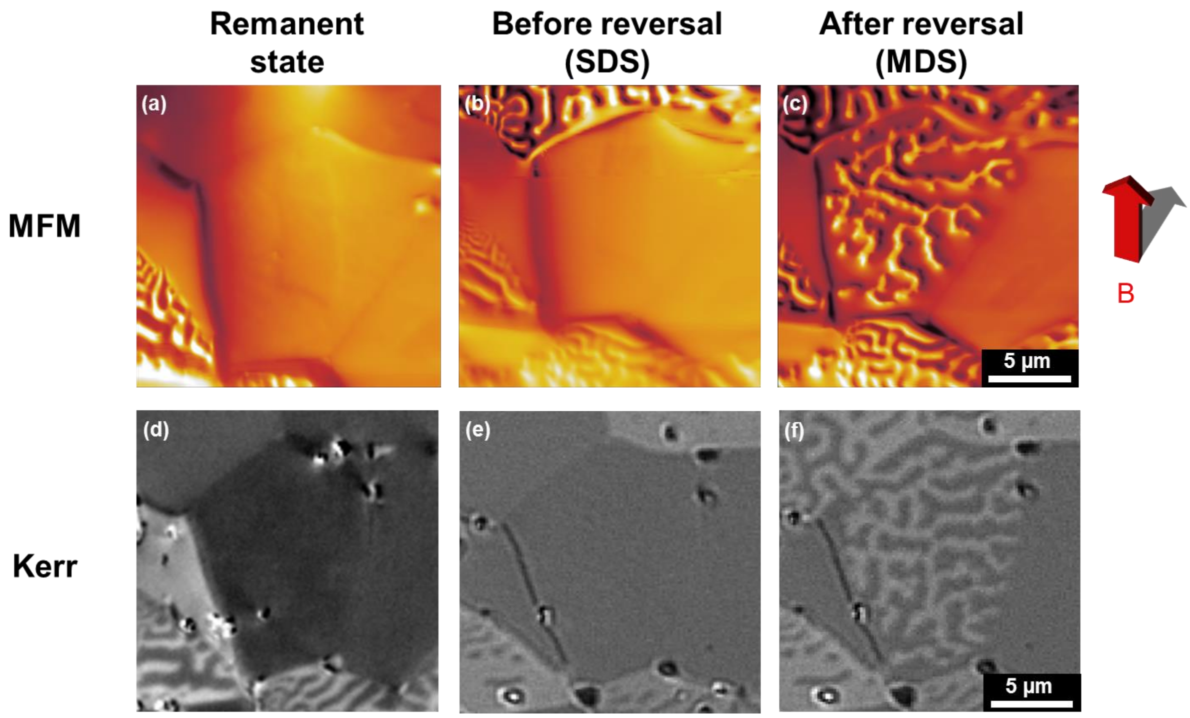

Figure 5.7 Comparison of MFM (top row) and Kerr (bottom row) (a,d) of the sample in remanent state, (b,e) before magnetic reversal in external magnetic field and (c,f) after magnetic reversal in external magnetic field.

While the spatial resolution of the MFM is high enough to image domains in the submicron range (as shown in previous chapters) and the moment resolution is high enough to image the magnetization difference of core and shell, the MFM offers no relevant time resolution. For this reason the same demagnetization experiment was performed using Kerr microscopy to image the domain configuration. Despite Kerr microscopy having a lower spatial and moment resolution, the time resolution in the used setup was 16 and 43 images i.e. frames per second (fps). The Kerr images depicted in Figure 5.7 were recorded with 16 fps, which corresponds to 62.5 ms per image. Prior to the experiment, the sample was re-saturated in an external magnetic field of 7 T. The resulting domain configuration in the remanent state is shown in Figure 5.7 d) depicting the same grain. The same configuration regarding MDS and SDS as in the MFM analysis can be observed, with the distinction that no contrast between core and shell can be observed. The reason why no contrast between core and shell can be observed lies in the sensitivity of the Kerr microscope and imaging technique, since later experiments on the same sample performed by Matic Klug at the University of Kiel using a different setup and imaging technique a slight core-shell contrast was observed. From the remanent state an opposing external magnetic field was applied using an electron magnet. The exact magnetic field strength on the sample surface could not be quantified because of the inhomogeneous nature of the applied field. While the magnetic field was manually ramped up, the domain configuration was constantly observed by Kerr microscopy. The two images in Figure 5.7 e) and f) show the collapse from a SDS to a MDS in two successive frames that are 62.5 ms apart. In the following frames (not shown) where the magnetic field is increased slightly further, no significant change in domain structure can be observed. Neither the MFM not the Kerr microscopy display an intermediate state, meaning that the precise location of the demagnetization cannot be based on the images shown in in Figure 5.7. The depicted domain structures by MFM and Kerr however display some similarities. Neither of the resulting domain configurations in the MDS allows a distinction between core and shell. The transition from SDS to MDS during the demagnetization of the core-shell structured grain does not differ qualitatively from the behavior shown in “regular” Nd-Fe-B sintered magnets depicted in Figure 2.9 or the results observed by Kobayashi *et al.* [Kobayashi2015].

To exclude the external magnetic field as a driving force for the demagnetization, the experiment was repeated using a constant magnetic field. This means that a magnetic field slightly lower than the nucleation field determined of the previous experiment was applied. The demagnetization of the grain is then triggered by the magnetic viscosity, also-called “after effect”, described in chapter 2.1.2. This effect describes the time dependency of magnetization processes under a constant field. In the underlying model by Givord *et al.* [Givord1987b, Givord1987a] the demagnetization is initiated by thermal fluctuations in a critical activation volume, which can be estimated by temperature dependent magnetic viscosity measurements. In this experiment the frame rate was increased to 43 fps i.e. 23.0 ms per image. The transition from SDS to MDS was observed after 1.77 s under constant field, but despite the increased framerate, no intermediate domain configuration was observed.

From the experimental results it can be stated that the demagnetization of the grain occurs in a single step from SDS to MDS across core and shell within the observable time scale of 23 ms even if the external field can be excluded as a driving force. As described previously, the “global-model” by Givord et al. assumes a critical nucleation volume of 200 - 800 nm^3, which corresponds to a nucleation radius of 3.63 – 5.76 nm for a spherical volume. This means that the actual nucleus and nucleation site is not only hard to resolve in time but also in space. The reversed domain that would propagate from the nucleation site through the grain on the other hand would in principle be resolvable and allow an educated guess regarding the approximate location of the nucleation site. Since core and shell in the observed grain/sample are thicker than the nucleation radius/diameter, a fundamental distinction should be possible whether the nucleation occurs in the core or in the shell. This of course requires that it is possible to resolve an intermediate state in which the domain propagation is still in progress but does not cover grain boundary and core at the same time. The time scale on which this process should occur can be estimated by the domain wall velocity i.e. the speed that domain walls can propagate through the magnet, and the size of the grain. To the best of my knowledge the domain wall velocity for $Nd_2Fe_{14}B$ had not been reported in literature at the time this thesis was written. For other systems, which are mostly soft-magnetic, various domain wall velocities have been reported, often for thin films and nanorods, ranging from tens to several hundreds of meter per second [Konishi1971, Hubert and Schäfer1998, Scholz2002, Porter and Donahue2004, Fukumoto2005, Beach2006, Tartaka2007, Heyne2010, Klein2014]. The reported values are partially based on calculations and partially based on experiments. Based on the lateral size of the observed grain and the reported domain wall velocities in other systems, the process of demagnetization should take between 1 µs to about 20 ns in total, which is several orders of magnitude faster than the experimental setup used in this work. One aspect that is not considered in this calculation, however, is the presence of eddy currents that should be more pronounced in bulk samples than in thin films and nanorods, in which most domain wall velocities were measured. Since eddy currents should reduce the domain wall velocity due to Lenz´s law [Hubert and Schäfer1998], the actual domain wall speed could be lower. It is also possible that an intermediate domain state with a local energy minimum exists that might also slow down the domain wall motion with respect to the presented estimation from literature.

Within the framework of the project, a micromagnetic simulation was carried out based on the so far presented experimental results. The simulation was carried out by Dr. Min Yi. The details of the simulation are not included in this thesis but can be found in detail in our joint publication [Helbig2017]. Nevertheless a short summary of the results of the simulations will be given in the following to complement the experimental results:

The simulation was carried out using a similar grain geometry as in the experiment. Due to the limited computational power, the size of the model had to be limited to 3100 x 2420 x 2 nm^3 as depicted in Figure 5.8. Base on the Dy content of the initial powder, estimations for the anisotropy constants K^{NdFeB} and $K^{(Nd,Dy)FeB}$ were made for core and shell. Non-magnetic material and grains that showed a MDS at low fields in the Kerr microscope analysis were assumed to have no magnetic contribution. A 10 nm thick defect layer with the reduced anisotropy constant K^{edge} was included in the model to include the commonly assumed lower anisotropy at the grain boundary [Bance2015b]. Simulations were carried out for different values of K^{edge} showing that for low K^{edge} values the nucleation of the reversed domain occurs at the grain boundary (as shown in Figure 5.8 (c)) making the coercivity proportional to the anisotropy of the defect layer K^{edge}. For higher K^{edge} values of approximately 0.9 $K^{(Nd,Dy)FeB}$ on the other hand, the nucleation occurs in the Dy-free core as shown in Figure 5.8 (d). At this point a further increase of K^{edge} does not result in a higher coercivity since the grain boundary is no longer the *weakest link*.

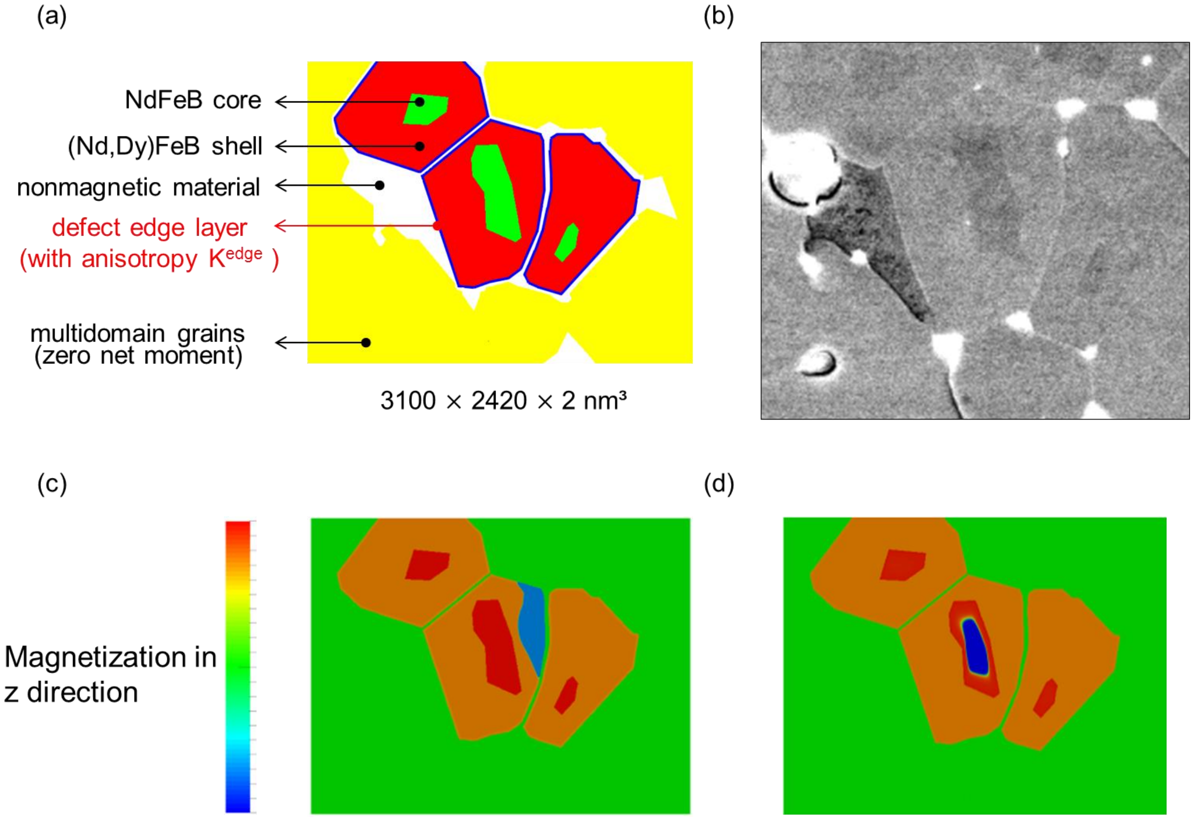

Figure 5.8 (a) Schematic of the micromagnetic model to simulate the magnetization reversal in comparison to the experimental microstructure by SEM (b) Schematic of the micromagnetic model to simulate the magnetization reversal in comparison to the experimental microstructure by SEM (b).

In summary it can be concluded that the analyzed core-shell structures are large enough to allow a clear distinction between core and shell. The resolution regarding magnetic moment of the MFM also allows the distinction of core and shell due to the lower magnetic moment of the Dy substituted shell phase. The demagnetization under external magnetic field occurs as a single step within the experimentally available time resolution of 23 ms. This holds true regardless of whether the demagnetization is caused by a ramping field or occurs due to magnetic viscosity under constant field. Using a micromagnetic model, a dependency of the coercivity on the defect layer could be determined. For sufficiently high anisotropies of the defect layer, the nucleation site of the reversed domain occurs in the core resulting in a maximum coercivity of the grain.

6 Texture dependence of the Grain Boundary Diffusion Process (GBDP) in sintered and hot-deformed Nd-Fe-B magnets

The grain boundary diffusion process (GBDP) that was described and analyzed in previous chapters and has been shown to very effectively increase coercivity using a minimal amount of HRE . Initially this process was applied to sintered Nd-Fe-B magnets using Dy/Tb- oxides, fluorides or in metallic form [Park2000, Hirota2006, Loewe2017], but was later also applied to hot-deformed Nd-Fe-B magnets [Sepehri-Amin2013a, Sawatzki2014b, Woodcock2014b]. In order to suppress grain growth in hot-deformed magnets, the temperatures of the diffusion heat treatment are significantly lower than in sintered magnets. In order to maintain a good wettability at lower temperatures, the procedure usually uses low melting binary or ternary alloys that liquidize during the process [Sawatzki2014b, Woodcock2014b, Tang2015, Seelam2016]. Due to the limited HRE diffusion range of a few millimeters (depending on diffusion time, temperature, HRE element etc. [Loewe2015, Loewe2017]) and the geometry of the respective magnet has to be taken into account meaning that the effectiveness of the process depends on the magnet shape. Since industrially viable magnets are usually textured, one can raise the question, whether the gain boundary diffusion also depends on the texture axis in a given magnet. Strong texture dependence would have to be taken into account for the effective design of grain boundary diffused magnets. The following chapter is therefore dedicated to the evaluation of the texture dependency of the GBDP in different Nd-Fe-B magnets. A large part of the experiments shown in this chapter were conducted by Andreas Abel within the framework of his master thesis.

In order to evaluate the GBDP, or rather the effectiveness of the GBDP, with respect to the texture axis, one has to decide on the criteria to quantify the GBDP. The most straightforward way would be to quantify the HRE concentration at a given diffusion depth and to derive a diffusion profile as used by Loewe *et al*. [Loewe2015]. This method, however, is not easy to realize experimentally: using energy- or wavelength dependent x-ray spectroscopy (EDX/WDX) the HRE concentration can in principle be quantified, however, the measurement is always dependent on the spot size of the used electron beam. Since the HRE containing shells decrease in thickness with increasing diffusion depth, the quantification of the HRE concentration strongly depends on the lateral resolution of the respective electron beam [Samardžija2012]. Sepehri-Amin *et al.* could observe a significantly increased Dy concentration after GBDP as far as 2.7 mm into the magnet using three dimensional atomprobe (3DAP) tomography [Sepehri-Amin2013b]. However, this method is very complex and can hardly be used to obtain a quantitatively accurate diffusion profile. Apart from experimental difficulties, it is also the aim of the GBDP to increase the coercivity beyond a direct proportionality of the HRE concentration. Using the *coercivity* rather than the HRE *concentration* as a function of diffusion depth therefore seems to be a more accurate parameter to evaluate the GBDP. One method used by Loewe *et al.* [Loewe2017] is by determining a coercivity profile by cutting a sample perpendicular to the diffusion direction into thin slices and measuring their coercivity of the slices individually. This approach, however, neglects magnetostatic effects that can occur as a result of the magnet being cut into thin slices. This may be the reason why the authors concluded an overproportional dependence of the overall coercivity on the coercivity of the surface layer of only a few 100 µm. This essentially means that due to magnetostatics, a complete magnet can exhibit different magnetic properties than the sum of its pieces that it was cut from. One could argut, that by cutting a sample into thin slices the geometry and hence the demagnetizing factor are altered and may alter the measured remanent magnetization. The altered Geometry should however not influence the coercivity since the magnetization and hence demagnetization field is zero at the coercivity.

To obtain an insight into the magnetostatic interactions, two different approaches to create a coercivity profile were combined in the following chapter: A single face of a brick shaped sample was brought in contact with a HRE source and subjected to a heat treatment. After the diffusion, thin slices of approximately 0.4 – 0.6 µm thickness were cut, starting from the side opposite to the diffusion source, as depicted in Figure 6.1.

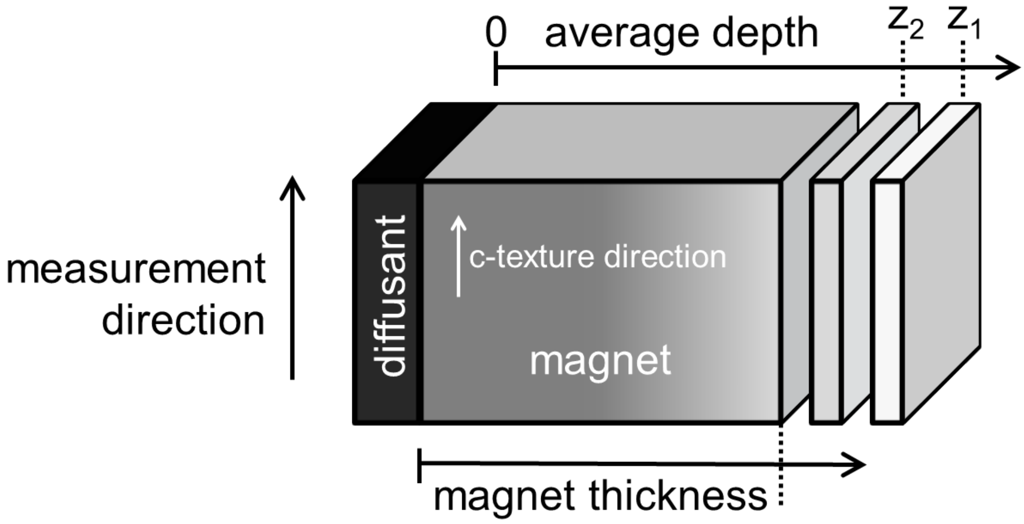

Figure 6.1 Schematic depiction of the experimental procedure to obtain coercivity profiles. Slices of 0.4 - 0.6 mm thickness are cut of the magnet starting with z_1.

Following the cut to obtain a slice z_i, the magnetic properties of each respective slice and the remaining piece of magnet were measured by pulsed field magnetometry. Using this procedure two coercivity profiles can be extracted from one sample: (i) a “local” coercivity profile derived from the individual sample slices as a function of the diffusion depth. And (ii) a “global” coercivity profile derived from the respective remaining piece of magnet as a function of the remaining sample thickness. The two methods allow specific conclusions and hold different advantages and disadvantages: The local coercivity profile obtained by method (i) offers a very precise local coercivity resolution with a high signal to noise ratio with in comparison to the global coercivity profile, where the coercivity is “averaged” over the entire sample piece. This means that unlike the global coercivity profile, the local coercivity profile results in a large absolute coercivity difference between the first and last point. Furthermore, the sample geometry and measurement intervals maintain the same over the course of the measurement. The global diffusion profile derived from method (ii), i.e., from the remaining sample piece as a function of reducing thickness, grands an insight into the overall coercivity profile of the magnet as a whole. The sample piece acts as a single magnet, which is relevant for applications, and also allows conclusions about magnetostatic interactions originating from the heterogeneous coercivity distribution. One also has to keep in mind that, when analyzing the Dy diffusion parallel to the easy axis, only one magnetic pole of the sample is magnetically hardened, which is not entirely comparable to industrial magnets that are diffused from all sides. The diffusion perpendicular to the easy axis on the other hand displays two partially hardened pole surfaces. This particular feature will be discussed later in this chapter.

A different approach to analyze the effect of texture on the GBDP was used by Kim *et al.* by varying the aspect ratio of different grain boundary diffused magnets [Kim2016]. In this method both magnetic poles are hardened, however, this method does not allow a closer resolution of the local coercivity distribution.

6.1 Grain Boundary Diffusion of Dy in Nd-Fe-B sintered magnets

The resulting local and global coercivity profiles for the diffusion directions of elemental Dy in Nd-Fe-B sintered magnets are depicted in Figure 6.2. In the local diffusion profiles, the “Diffusion depth” refers to the distance of the slice center from the Dy source while in the global coercivity profile the “Sample thickness” refers to the thickness of the entire sample. The local coercivity profiles shown in Figure 6.2 (a) display a distinct difference between the perpendicular (⊥ c-axis) and parallel (|| c-axis) diffusion, with respect to the texture axis of the magnet. Unsurprisingly, the slice closest to the Dy source shows the highest coercivity increase for both diffusion directions. In this particular slice the parallel diffusion shows a higher effect, i.e., higher coercivity increase. After the first few 100 µm diffusion depth, however, this ratio reverses and the perpendicular diffusion displays a larger coercivity, with the difference between the two diffusion directions growing with increasing diffusion depths (for the analyzed maximum sample size of approximately 3.5 mm).

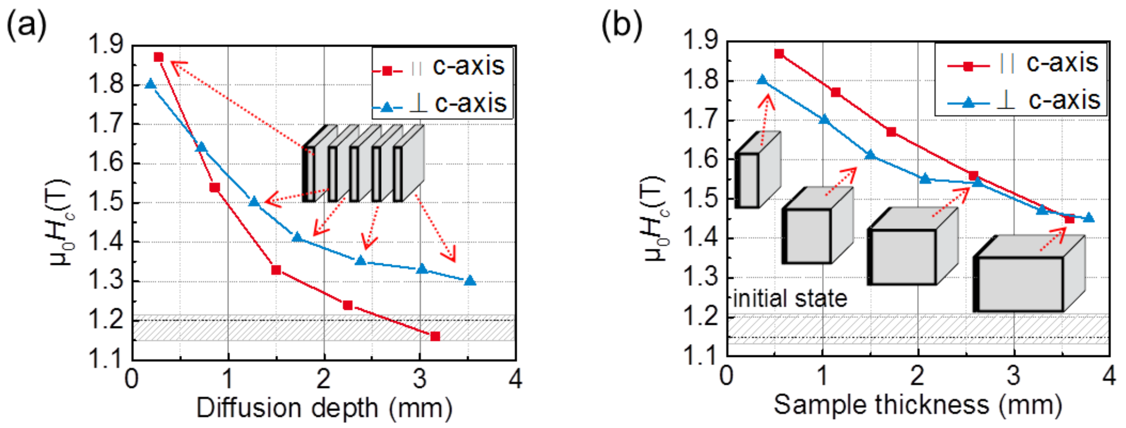

Figure 6.2 (a) Local coercivity profiles in sintered magnets for parallel and perpendicular Dy diffusion indicated by average depth and (b) global coercivity profiles indicated by magnet thickness for parallel and perpendicular Dy diffusion.

The global coercivity profile obtained by method (ii), i.e., by gradually reducing the magnet thickness starting from the not diffused side, is depicted in Figure 6.2 (b). The profiles differ significantly with respect to the the local coercivity profile; the parallel Dy diffusion displays a higher coercivity at lower sample thicknesses and eventually a nearly identical coercivity at larger sample thicknesses. This behavior seems unexpected considering that the local coercivity profile inn Figure 6.2 (a) shows that the coercivity is actually larger for the perpendicular Dy diffusion, the only exception being the first 600 µm close the Dy source. The data suggests that for parallel diffusion, the layer closest to the diffusion source has an overproportional influence on the global coercivity of the sample. Considering the fact that the two data sets, of local and global coercivity were obtained from the same physical sample, the resulting profiles should be consistent with respect to each other. Consequently it should be possible to “reconstruct” the global coercivity profile in Figure 6.2 (b) by averaging the local coercivity profile in Figure 6.2 (a) over the diffusion depth. Under the assumption that no other effects (e.g. magnetostatics) are contributing to the coercivity the average local coercivity profile should match the experimentally obtained global coercivity profile. The local coercivity profiles for each diffusion direction were therefore fitted using an appropriate error function, previously used by Loewe *et al*. [Loewe2017] to obtain the coercivity as a function of diffusion depth $H_c(z)$. Using this function the average local coercivity was derived according to $\overline{H_c}(z) = \frac{1}{z}\int_0^z H_c(z)dz$, as a function of diffusion depth. For of perpendicular diffusion the average local coercivity profile is compared to the global coercivity profile in Figure 6.3 (a). As one might expect, the average local coercivity profile is almost identical to the experimentally obtained global coercivity profile which indicates that all slices of the sample contributes equally to the global coercivity. However, if this procedure is applied to the parallel diffusion profile as displayed in Figure 6.3 (b), the experimentally obtained global coercivity profile is significantly higher than the average local coercivity, indicating that the layers close to the Dy source have an overproportional influence on the global coercivity. This is true for the entire diffusion range with the exception of first approximately 700 µm, which is the thickness of the slice/sample piece used in both methods (i.e. local and global coercivity measurement). In other words, the first points in global and local coercivity profile were obtained from the same sample piece and hence are identical. The difference between the calculated average local coercivity and the experimentally observed global coercivity reaches a maximum of approximately 0.1 T at a diffusion depth of approximately 2.5 mm.

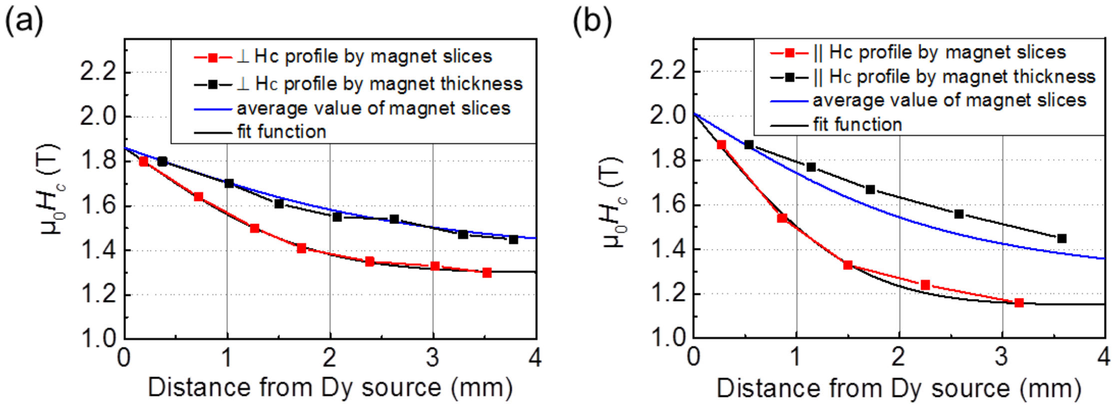

Figure 6.3 Comparison of the average local coercivity with the experimentally obtained global coercivity profile for perpendicular (a) and parallel (b) Dy diffusion.

The fact that the global coercivity differs from the average local coercivity for parallel diffusion, but not for perpendicular diffusion indicates that other effects (e.g. dipole interactions) are involved. One difference between parallel and perpendicular diffusion direction is the different sample shape since the magnetic properties are always measured along the texture axis. Despite starting from approximately cubic samples, the cut slices are measured either parallel or perpendicular to the surface area. Consequently, the respective slices exhibit vastly different demagnetization factors. The demagnetization factor should, however, not influence the measured coercivity since the demagnetization field can be expressed as $H_d = -N \cdot M$ and $M(H_c) = 0$, the coercivity should therefore be independent of the demagnetization factor.

The second difference between the two diffusion directions is that in the case of parallel diffusion, the magnetic pole surface, of north- or south pole, is completely covered with Dy. Consequently, the entire pole surface is magnetically hardened, while in the case of perpendicular diffusion, the magnetically hardened volume stretches from north- to south-pole but does not cover any of the pole surfaces completely as depicted in Figure 6.4. The Dy concentration gradient forming during the diffusion is indicated by the color code, while the dotted lines indicate the cutting direction and respective shape of the slices that are cut from the diffused sample. For parallel diffusion, the global coercivity exceeds the average local coercivity, indicating that one completely magnetically hardened pole surface has an overproportional influence on the global coercivity unlike the partial hardening of two pole surfaces in the case of perpendicular diffusion. From a magnetostatic point of view it appears plausible that the magnetic hardening of *both* pole surfaces might have an overproportional influence on the coercivity. However, the presented results show that this effect is also observable if only *a single* pole surface is magnetically hardened. From an applications point of view this could mean that the HRE consumption during the GBDP could basically be cut in half if the effect is large enough.

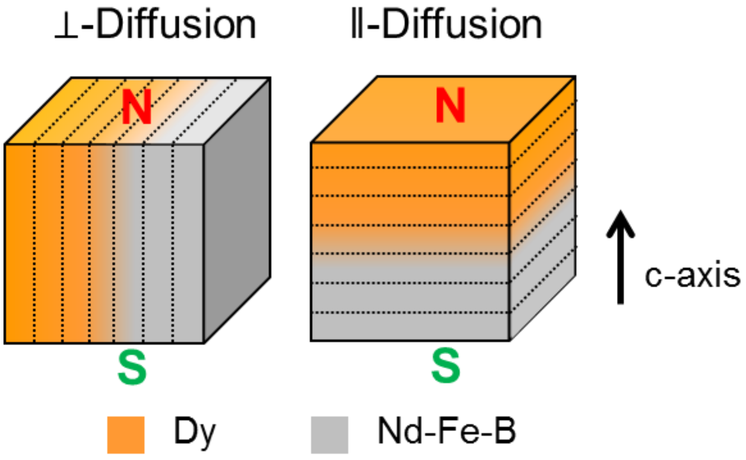

Figure 6.4 Illustration of Dy distribution with respect to the texture axis and cutting direction indicated by the dotted lines.

In order to gain an additional insight into the process, the elemental distribution of Dy was analyzed by EDX by measuring the Dy-M_α line as depicted in Figure 6.5 (a). The respective Dy diffusion source was located on the upper edge for both images, while the texture axis is indicated by the arrows marked “c”. As can be seen, the first 150 µm away from the diffusion source do not show a significant difference between parallel and perpendicular diffusion. Here the Dy is distributed rather homogenously throughout the grains and has penetrated most grains completely. Regarding the concentration, the optical impression is confirmed in Figure 6.5 (b) showing the concentration according to the Dy-M_α line averaged over a 50 µm diffusion depth. Here the Dy concentration of the first 150 µm is identical within the measurement error for both diffusion directions. At higher diffusion depths however the parallel diffusion displays significantly higher Dy concentrations. This is accompanied by the fact that the formation of clearly visible core-shell structured grains in Figure 6.5 (a) reaches a depth of approximately 250 µm or parallel diffusion, in comparison to 190 µm for perpendicular diffusion.

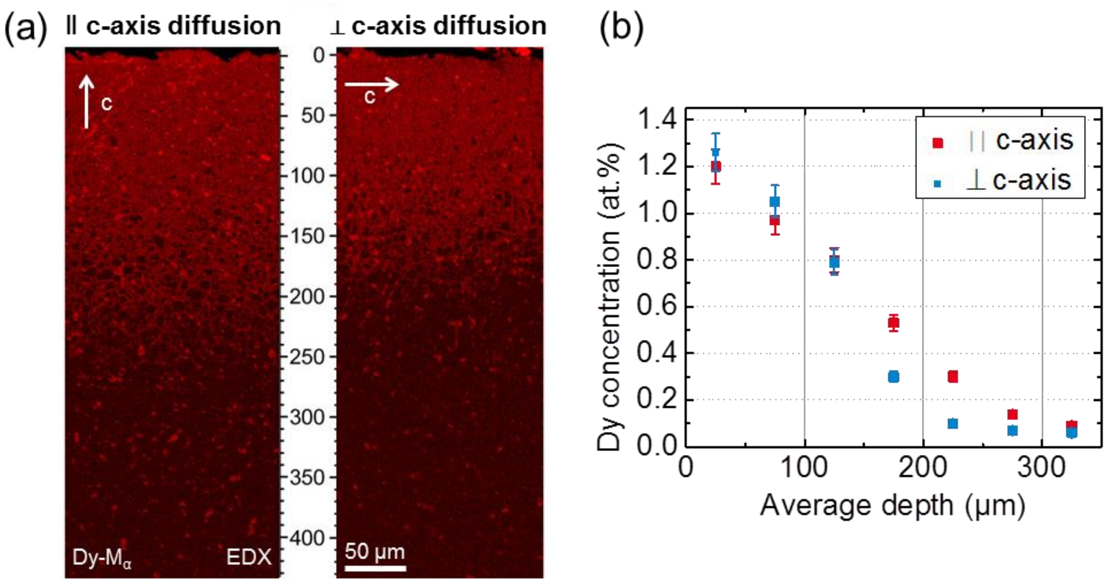

Figure 6.5 (a) EDX map of the Dy-M$_\alpha$ line with the c axis lying in the image plane and the Dy source on the top during the diffusion, (b) concentration profile of Dy by area averaging the Dy-Mα signal obtained by EDX.

At diffusion depths larger than 350 µm the determined Dy concentration for both diffusion directions drops below 1 %, increasing the signal to noise ratio and making it impossible to determine a reliable Dy concentration for either direction. It should be noted that the depth of the EDX profile is only 350 µm, compared to up to 4 mm of the coercivity profiles. The fact that the EDX analysis shows a slightly higher Dy concentration for parallel diffusion is in agreement with the fact that the local coercivity of the first 500 µm is larger for parallel diffusion. From the EDX map in Figure 6.5 (a) it is evident that the detected Dy either located in grains that are homogenously substituted with Dy (as in the first 150 µm) or at triple points. Core-shell structured grains with a Dy rich shell are only distinguishable at a very specific diffusion depth and become undefined at higher diffusion depths. This means that only a fraction of the Dy detected by EDX is actually located at the in core shell structures where it has supposedly the larger effect on coercivity. The “necessary" shell thickness in grain boundary diffused sintered magnets is typically considered to be the range a few nanometer [Bance2015a, Bance2015b]. This matches the observation that the effect of the GBDP on the coercivity is still significant several mm from the diffusion source but the Dy concentration according to EDX is below 0.1 %. This is also due to the fact that the EDX signal is averaged over the EDX beam spot size, which is in the µm range. The fact that the bulk diffusion and the formation of visible core-shell structures reaches deeper for parallel diffusion could be an indication that the bulk diffusion in this case occurs faster and the Dy is no longer available for the GBDP resulting in a lower coercivity had higher diffusion depths.

6.2 Grain Boundary Diffusion of Dy-Nd-Cu in Nd-Fe-B sintered magnets

The same experimental procedure and characterization was also carried out using the low melting Dy alloy $Dy_{20}Nd_{60}Cu_{20}$ instead of pure Dy. Low melting binary or ternary alloys are often used to transfer the GBDP to hot-deformed magnets [Sepehri-Amin2013a, Sepehri-Amin2013c, Akiya2014, Liu2016, Sawatzki2016]. The low melting point allows the GBDP to occur at low temperatures that are high enough to enable the grain boundary diffusion, but low enough to suppress the grain growth during the process. Regarding the use to low melting alloys in sintered magnets, it has been argued that a higher wettability would be achieved by the lower melting point as well as a potentially higher diffusion coefficient [Liang2014, Sawatzki2014a]. In this work, the low melting alloy serves as a reference to the diffusion of pure Dy in sintered magnets as well as for the diffusion of the same low melting alloy in hot-deformed Nd-Fe-B magnets that will be discussed later.

The local and global coercivity profiles for the diffusion of Dy-Nd-Cu in sintered magnets are displayed in Figure 6.6. As can be seen, the differences between parallel and perpendicular diffusion are smaller than for Dy diffusion. Despite the quantitative difference however the results show qualitative the same result: with the exception of the first 500 µm, the local profile shows a slightly higher coercivity, while the global coercivity profile displays slightly higher value for parallel diffusion over the entire diffusion range.

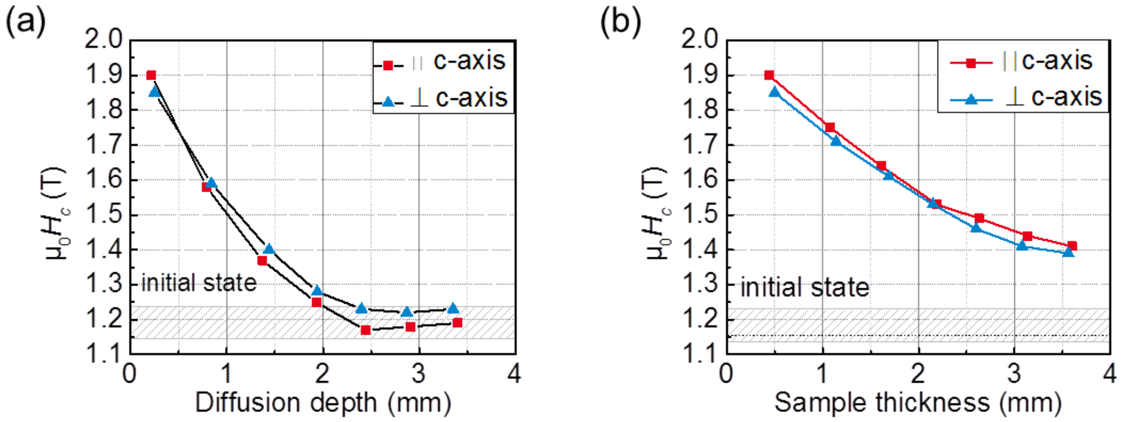

Figure 6.6 (a) Local coercivity profiles of sintered magnets for parallel and perpendicular Dy-Nd-Cu-diffusion, (b) global coercivity profiles of Dy-Nd-Cu diffusion in sintered magnets.

The direct comparison of the diffusion of Dy-Nd-Cu and pure Dy is depicted in Figure 6.7. The local profiles for parallel diffusion depicted in Figure 6.7 (a) show that in the first 1.5 mm from the diffusion source, the coercivity improvement of Dy and Dy-Nd-Cu are almost identical. For higher diffusion depths however pure Dy shows a slightly higher coercivity. The global profiles for parallel diffusion in Figure 6.7 (b) match these results in the sense that pure Dy diffusion displays a higher coercivity at higher magnet thicknesses.

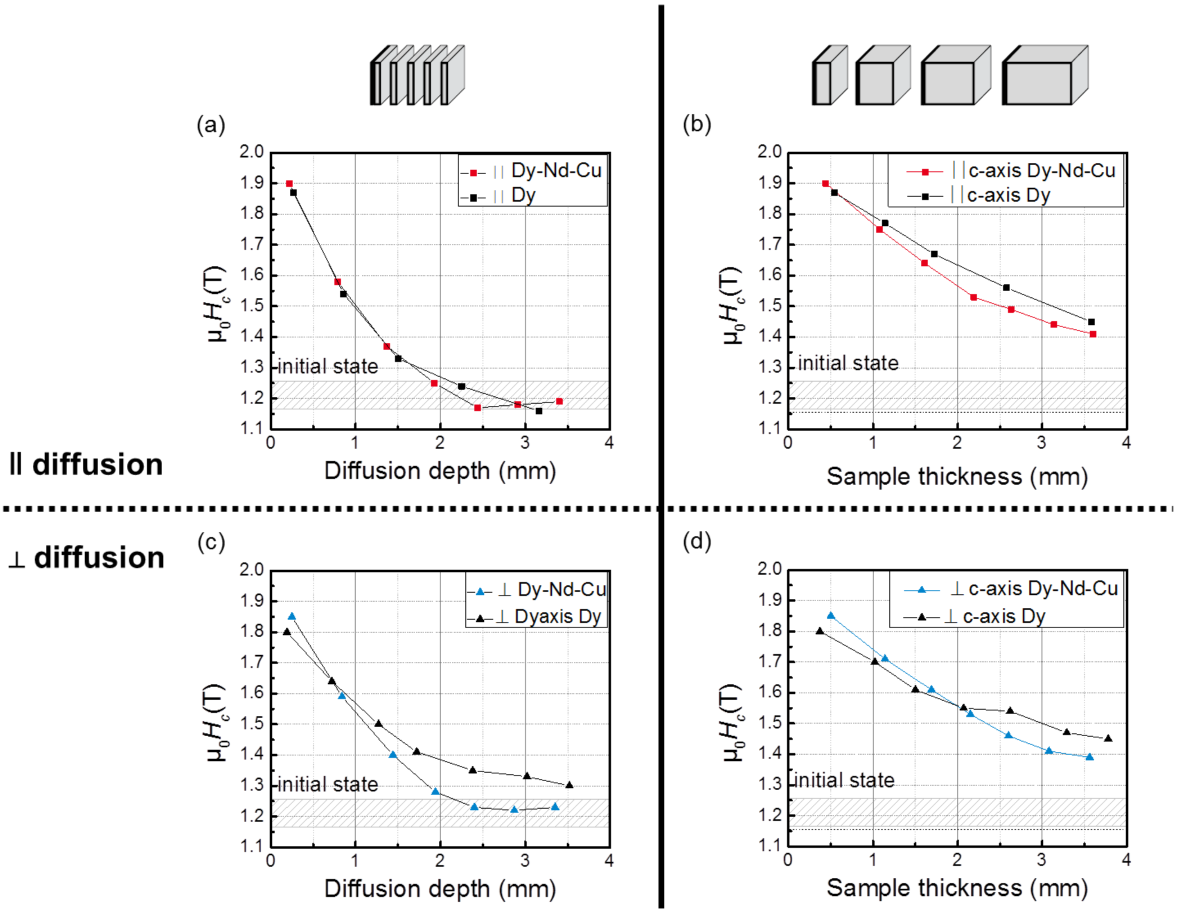

Figure 6.7 Direct comparison of Dy and D-Nd-Cu on sintered magnets (a) comparison of local diffusion profiles for parallel diffusion, (b) comparison global coercivity profiles for parallel diffusion, (c) comparison of local coercivity profiles for perpendicular diffusion and (d) comparison of global diffusion profiles for perpendicular diffusion.

The local coercivity profiles for perpendicular diffusion of Dy and Dy-Nd-Cu are depicted in Figure 6.7 (c). Below approximately 0.7 µm the Dy-Nd-Cu actually displays a higher coercivity than Dy. For larger diffusion depths however the Dy diffusion shows significantly higher values. The same development can be seen for the global profiles in Figure 6.7 (d) where Dy-Nd-Cu display a higher coercivity for magnet thicknesses below approximately 1.7 µm, while for larger thicknesses Dy diffusion results in higher coercivity.
The comparison between Dy and Dy-Nd-Cu indicates that the diffusion of the low melting ternary alloy results in a similar coercivity increase at lower diffusion depths but pure Dy generally causes a higher coercivity improvement at higher diffusion depths. Hence pure Dy results in an overall higher magnetic hardening effect for magnets larger than approximately 2 mm in thickness. The reason for the higher effectiveness of pure Dy at higher diffusion depths might be the fact that the concentration gradient, which is the driving force for the GBDP, is larger if Dy is applied in pure form, rather than being “diluted” by Nd and Cu.

To analyze the effect of pole surface hardening for the diffusion of Dy-Nd-Cu, the same procedure as previously was applied to calculate the average local coercivity profile and compare it to the global coercivity profile. The results are shown in Figure 6.8 (a) for the perpendicular diffusion and (b) for parallel diffusion. The perpendicular diffusion shows that the average local coercivity profile matches the global coercivity profile almost perfectly. Above approximately 2.5 mm the global profile displays a slightly lower coercivity than the average local coercivity. The maximum discrepancy however is in the range of 0.04 T, which is approximately 2.6 % of the total coercivity, and might occur due to statistical fluctuations.

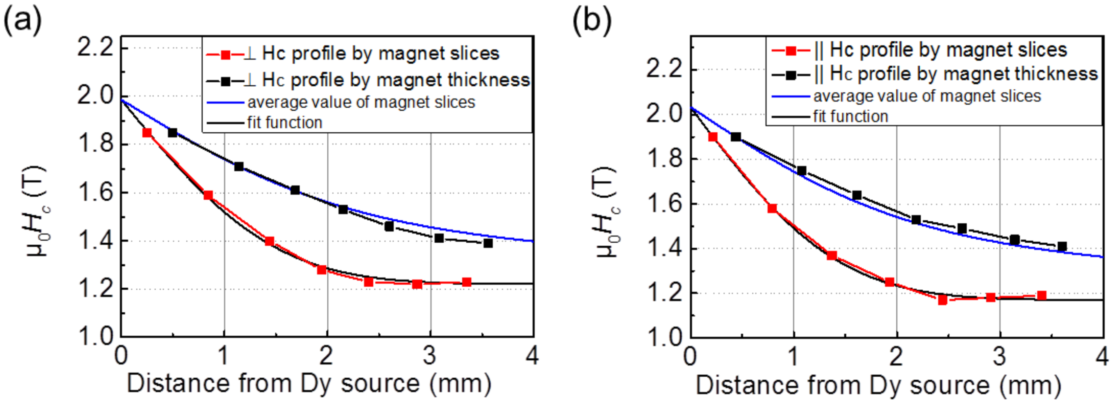

Figure 6.8 Comparison of the average local coercivity with the experimentally obtained global coercivity profile for perpendicular diffusion (a) and parallel diffusion (b) for Dy-Nd-Cu diffusion.

In the case of parallel diffusion in Figure 6.8 (b) on the other hand, the resulting global coercivity profile is slightly larger than the average local coercivity over the entire diffusion length. The difference however is only in the range of 0.03 T, which is approximately a third of the effect observed for Dy in Figure 6.3. The fact that the discrepancy is consistent over the entire diffusion depth suggests that this is not a statistical error and that the pole hardening effect also occurs for the diffusion of Dy-Nd-Cu.

The elemental distribution of the Dy-Nd-Cu diffusion in sintered magnets obtained by EDX is depicted in Figure 6.9.

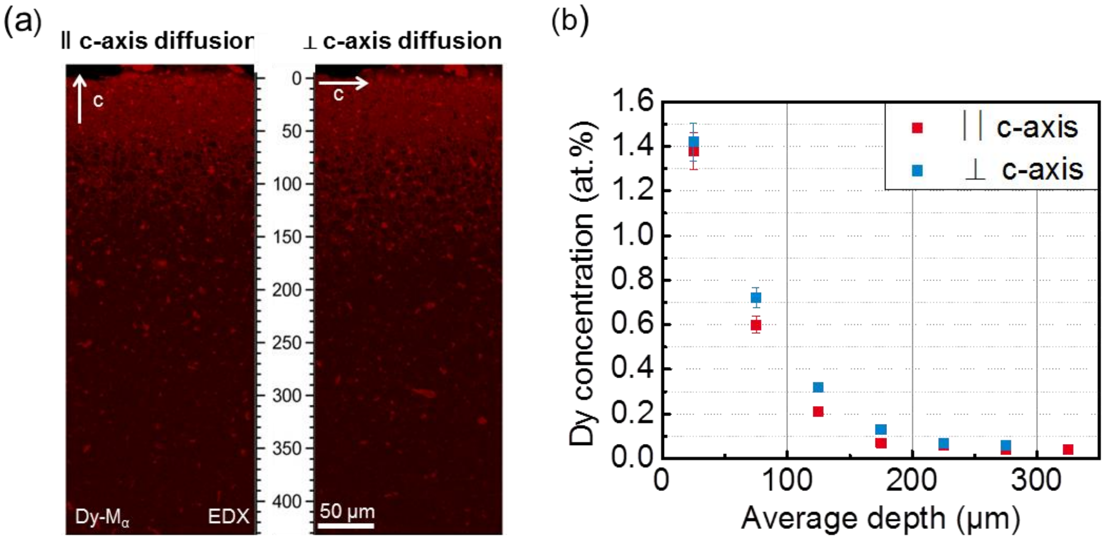

Figure 6.9 EDX map of the Dy-M$_\alpha$ line with the c-axis lying in the image plane and the Dy-Nd-Cu source on the top during the diffusion, b) concentration profile of Dy by area averaging the Dy-Mα signal obtained by EDX.

Within the first 200 µm the detected Dy concentration drops below 0.1 at.% which is a larger concentration drop with diffusion depth than for pure Dy. The formation of visible core-shell structures also does not reach as deep into the magnet as in the case of Dy diffusion. This is not surprising, since the driving force behind the GBDP is the concentration gradient and the Dy concentration in Dy-Nd-Cu is lower than in pure Dy.

Overall it can be concluded that the GBDP of Dy-Nd-Cu largely follows the same trend in terms of anisotropy of the diffusion with respect to the texture axis. A slight pole surface hardening effect can also be observed for Dy-Nd-Cu diffusion, however the effect is weaker than for Dy diffusion.

6.3 Grain Boundary Diffusion of Dy-Nd-Cu in Nd-Fe-B hot- deformed magnets

The Dy-Nd-Cu diffusion was also applied to hot-deformed Nd-Fe-B magnets using the same experimental setup as for sintered Nd-Fe-B magnets. The samples were prepared by hot compaction of commercial MQU-F powder produced by Magnequench® followed by a subsequent deformation step with a degree of deformation of φ=1. A lower diffusion temperature than for sintered magnets of 650°C was used in order to suppress grain growth in the powder, while simultaneously allowing a sufficiently high diffusion. It was confirmed by Differential Scanning Calorimetry (DSC) that at 650°C a sufficiently large amount of liquid phase was present in the Dy-Nd-Cu alloy to ensure sufficient wettability [Sawatzki2015].
The obtained local and global coercivity profiles are shown in Figure 6.10. Due to experimental reasons, the diffusion length for the parallel diffusion had to be limited to 2.25 mm. The difference between the two diffusion directions in hot-deformed magnets is more pronounced than in sintered magnets. Here both coercivity profiles show a significantly higher coercivity for the perpendicular diffusion, the only exception being at very low diffusion depths where the values are almost identical.

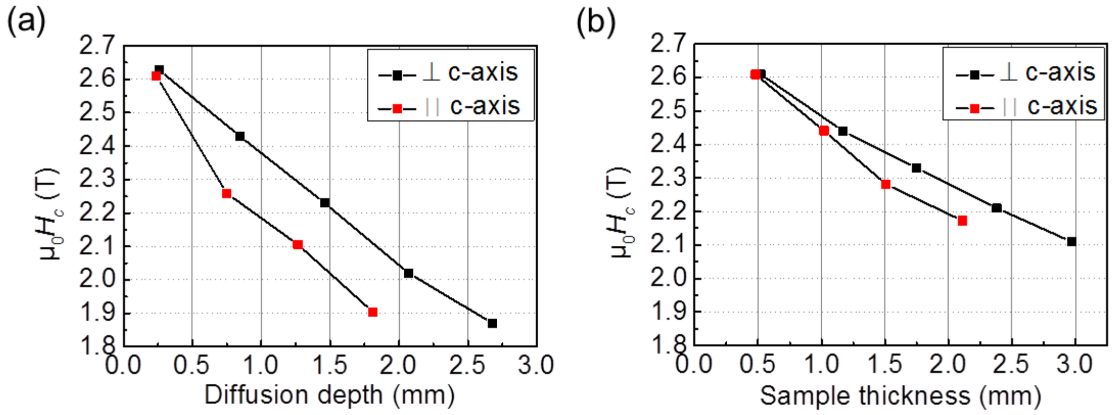

Figure 6.10 Local coercivity profiles of hot-deformed magnets with parallel and perpendicular Dy-Nd-Cu-diffusion, (a) determined by method i) indicated by average depth and (b) determined by method ii) indicated by magnet thickness.

In order to understand the reason why the diffusion differs so drastically with respect to texture direction, one has to consider the microstructure of hot-deformed Nd-Fe-B magnets. In comparison to sintered magnets, the microstructure is a lot more inhomogeneous. The most significant difference is that the grains are platelet shaped and the grain size is in the order of several hundred nanometers. The grain shape and texture forms as a result of the deformation process and can vary over the volume of the sample, meaning that i.e. layer close to the punches can have a lower degree of texture than in the center of the sample.

Figure 6.11 shows the microstructure after the diffusion of Dy-Nd-Cu at different diffusion depths. The comparison of the different diffusion directions shows that in the case of parallel diffusion, texture is very low at the surface and increases gradually within the first 1000 µm eventually forming a brick wall like structure. Even though a lower texture can also be the result of the deformation process, the resulting microstructure in Figure 6.11 is most likely caused by the diffusion process of Dy-Nd-Cu itself according to Tang *et al.* [Tang2018].

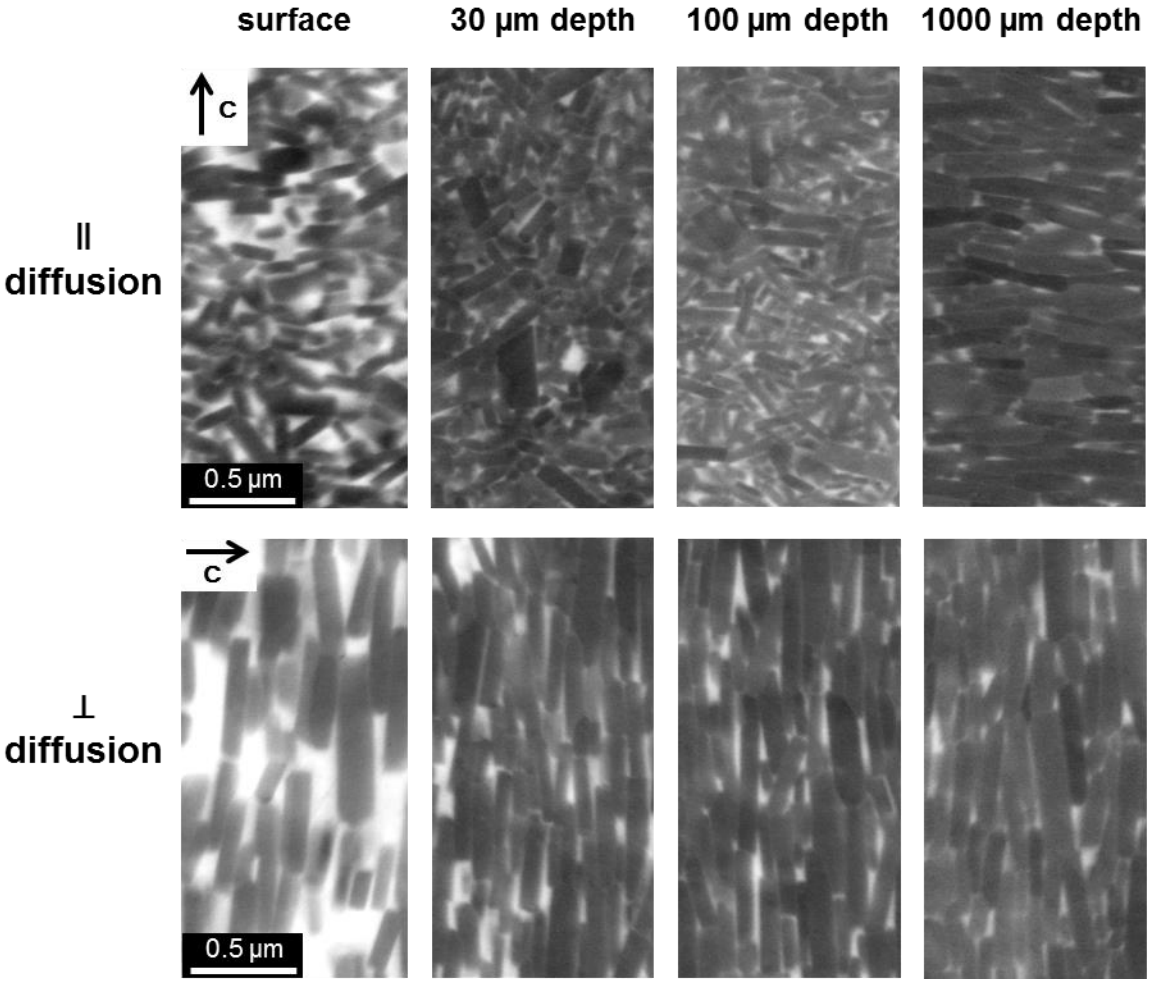

Figure 6.11 Microstructure of the hot-deformed sample depending on the diffusion direction of Dy-Nd-Cu at different distances relative to the diffusion source.

For the perpendicular diffusion on the other hand no reduced texture can be seen in Figure 6.11 for either diffusion depth. In the immediate vicinity of the surface a significant increase of grain boundary phase can be seen. However at diffusion depths of 30 µm to 1000 µm the characteristic brick wall like structure can be seen without significantly increased secondary phase.

Considering the specific brick wall like microstructure of hot-deformed magnets, which actually consists of platelets, it is not surprising that diffusion along the perpendicular direction being the “long side” of the grains would be faster. In this direction the diffusion does not encounter many “obstacles” in form of grains that would hinder the diffusion. To reach a certain diffusion depth, the diffusing species has to diffuse “around” each respective grain as illustrated in Figure 6.12.

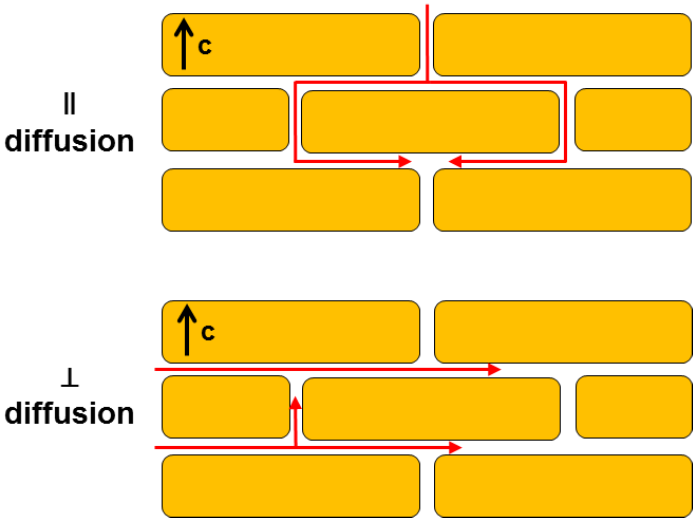

Figure 6.12 Schematic illustration of the GBDP texture dependency in hot-deformed Nd-Fe-B magnets.

Considering the fact that the diffusant i.e. Dy-Nd-Cu and the grain boundary phase is presumed to be liquid (at least partially) at the diffusion temperature of 650°C it is possible to imagine that the parallel diffusion might lead to the observed misalignment of grains by liquefying the GBP and “dissolving” the grains “layer by layer” in the liquid phase. The term “dissolving” refers here not to a chemical dissolving of the 2-14-1 phase but to a “maceration” of the brick-wall like structure and the “floating” of 2-14-1 grains in the liquid phase. In the case of the perpendicular diffusion on the other hand, the “interlinked stacking” of the grains offers a much more robust configuration that does not misalign as easily.
The two described process of grain misalignment and faster diffusion due to fewer “obstacles” overall result in a higher effectiveness of the perpendicular diffusion over the parallel diffusion. This statement holds true for any given diffusion depth as shown in Figure 6.10.

Figure 6.13 shows the comparison of the average local coercivity profile with the obtained global coercivity profile for each diffusion direction. Unlike in sintered magnets, the perpendicular diffusion in Figure 6.13 (a) displays that the average local coercivity profile is actually lower than the experimentally obtained global coercivity profile. In other words, the whole magnet possesses a lower coercivity than the average of its parts. For the perpendicular diffusion in Figure 6.13 on the other hand, the average local coercivity matches quite well the experimentally observed global coercivity. An actual pole hardening effect as in sintered magnets cannot be observed in hot-deformed magnets. In fact the results show a “weakening effect” for the perpendicular diffusion with a lower global coercivity profile than the average local coercivity. This observation might be related to the fact that the grains in hot-deformed magnets are platelet shaped unlike in sintered magnets where the grains are more “cubical” shaped. It is also possible that the interlinked brick wall like structure of the grains shown in Figure 6.11 causes an avalanche effect in terms of demagnetization that propagates differently though the magnet depending on texture direction. A similar demagnetization mechanism was already reported by Thielsch et al. [Thielsch2012]

An EDX analysis of the diffusion in hot-deformed magnets was also performed (data not shown), however the determined intensities were too low to allow any reasonable conclusion.

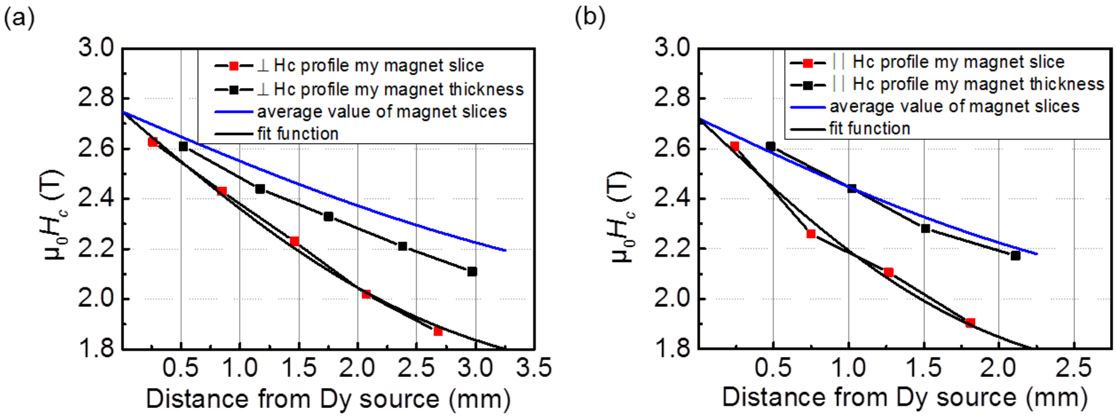

Figure 6.13 Comparison of the average local coercivity in comparison to the global coercivity of perpendicular diffusion (a) and parallel diffusion (b) for Dy-Nd-Cu diffusion in hot-deformed magnets.

The first and last slice of the parallel diffusion that were used to obtain the local coercivity profile were analyzed by MFM. For these slices the magnetic easy axis is normal to the surface and is hence pointing out of the image plane in the MFM image. The topography and domain structure of the slices is depicted in Figure 6.14. The left hand side shows the Dy-rich slice closest to the diffusion source, while the right hand side shows the Dy-lean slice which is the furthest away from the diffusion source. As can be seen in the topography images both images show an area close to a flake boundary.

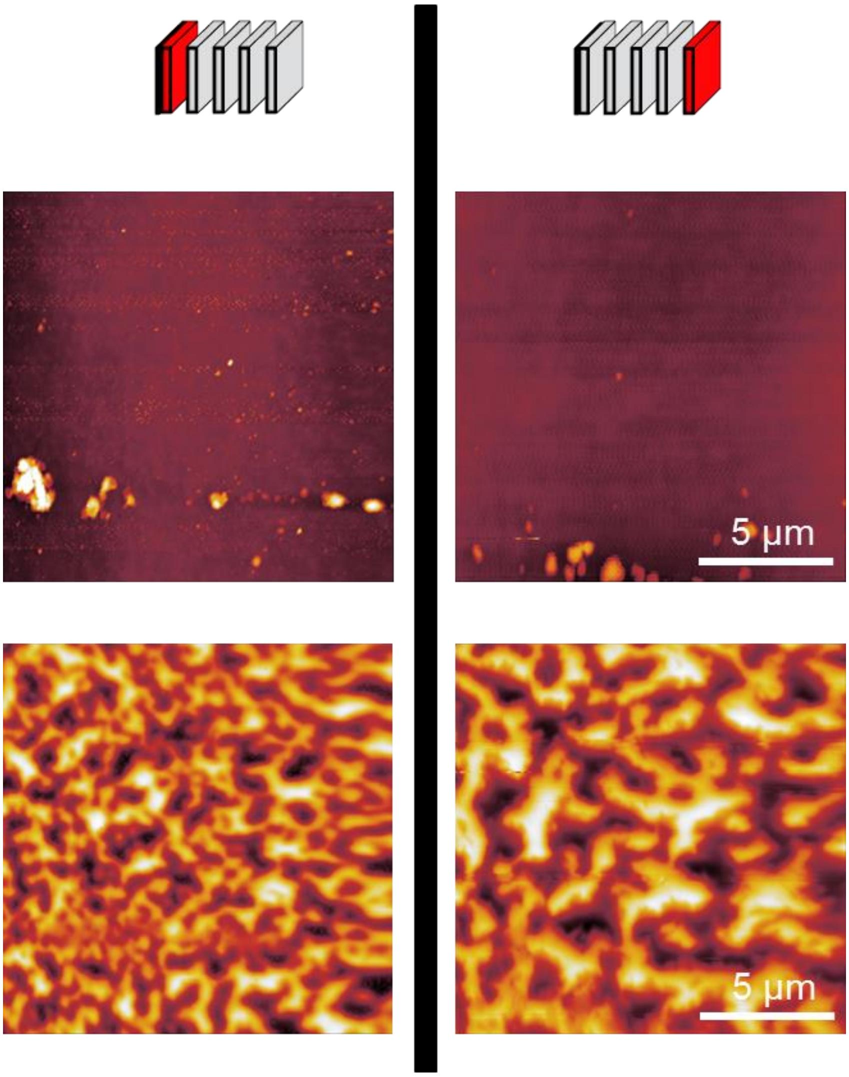

Figure 6.14 Topography and domain structure measured by MFM of the hot deformed Nd-Fe-B slice closest to (left) and furthest away from (right) the diffusion source.

The domain structure, depicted in the bottom row, of the left slice display a far more irregular structure and an on average smaller domain size. This effect was also observed by Kerr microscopy (data not shown), and is presumably caused by the diffusion and subsequent isolation of magnetostatic interactions as also observed by other authors [Sawatzki2018, Tang2018].

The *in-situ* demagnetization observed by MFM of the slides is depicted in Figure 6.14 is displayed in Figure 6.15. In the remanent state both slices are saturated and mostly show dark a red contrast. Low amounts of bright contrast occur mainly at the flake boundary, due to oxide phases. At a low demagnetizing field of -0.3 T the domain structure does not change significantly. If the demagnetizing field is increased to -0.6 T the Dy-lean slice display a reversed interaction domain, which means that the demagnetization starts in this slice, while the Dy-rich slice maintains largely unaffected. The reversed domains in the Dy-lean slice continue to grow at -0.9 T and -1.2 T, whereas the Dy-rich slice maintains its magnetization. Only at the flake boundary a small amount of reversed domains can be seen that coincide with the oxide phase at the flake boundary. At the flake boundary the coercivity is likely to be reduced due to oxidation and decomposition.

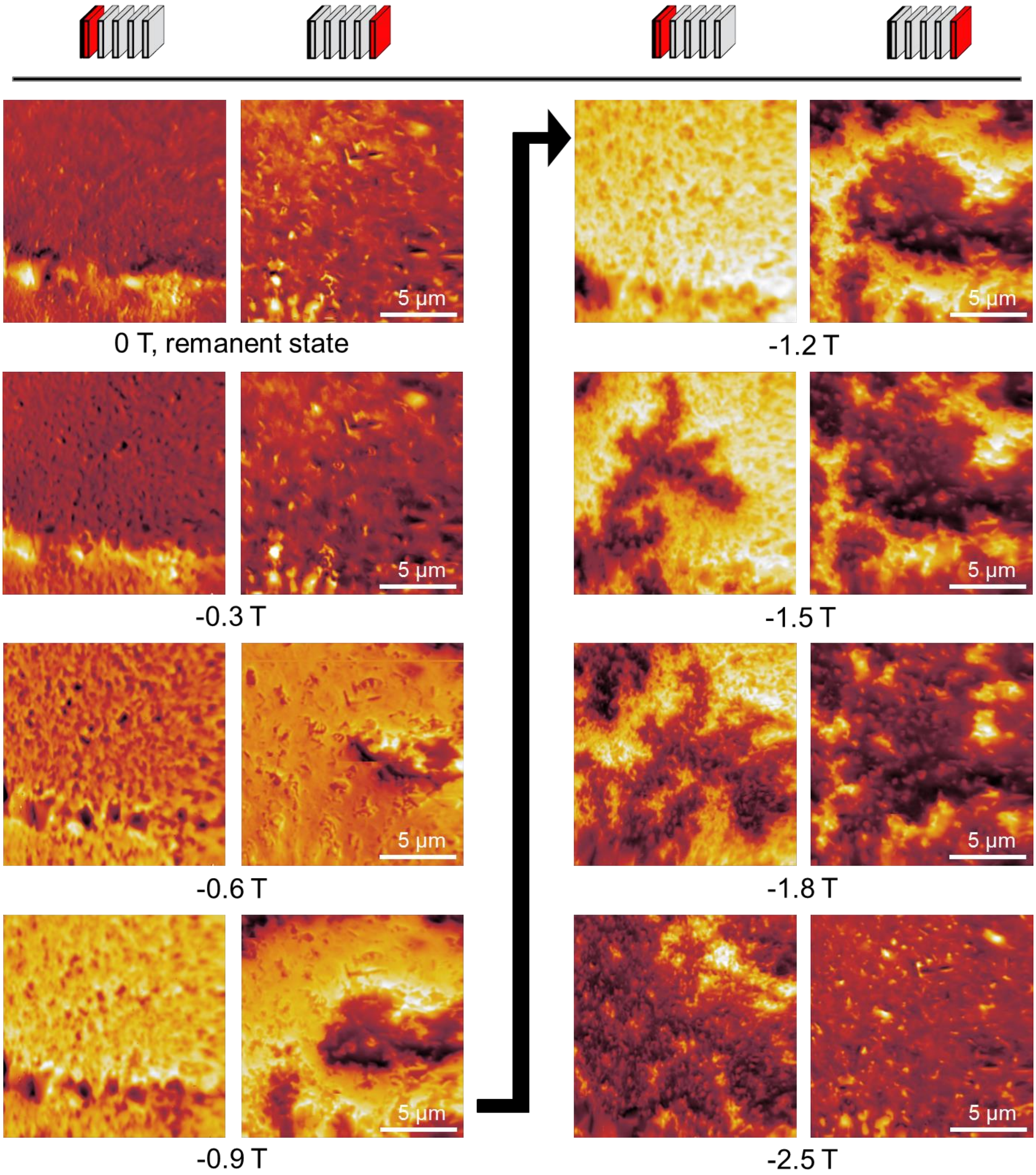

Figure 6.15 Demagnetization observed by MFM under in-situ conditions of a slice close to the diffusion source and far away from the diffusion source.

While the flake center of the Dy-rich slice only starts to demagnetize at a field of -1.5 T, the Dy-lean slice is almost fully demagnetized. The area of dark domain outnumbers the area of bright domains, indicating that the net magnetization of the slice is already reversed with respect to the initial magnetization. At -1.8 T the dark contrasted domain in the Dy-rich slice continues to grow, while the Dy-lean slice has almost completely reversed its magnetization, with only a few bright domains present. The reversal of the Dy-lean slice is complete at -2.5 T, showing a completely reversed domain structure with the only bright contrast originating from non-magnetic phases, such as oxides etc. The reversal of the Dy-rich slice on the other hand is not completed at this field, as s small amount of bright domain are still present.

It can be stated, that the same tendency of the macroscopic behavior can be observed on a magnetic level as well, in the sense, that the Dy-rich slice shows a higher resistance against demagnetization. The results show that the demagnetization process occurs on the nanoscopic level, with the reversed domain proceeding gradually through the magnet after an initial “nucleation”. It can be suspected, that such an initial nucleation of a reversed domain is likely to occur at the flake boundary and is spreading from there into the flake as can be seen for the Dy-rich slice at -1.5 T. However the areal limitation of the MFM makes it impossible to verify or deny such claim, since the entirety of the flake cannot be depicted at once. Furthermore the nucleation process itself is most likely occurring on a time scale far beyond the capabilities of the MFM (see chapter 5). The gradual progression of the reversed domains share similarities with a pinning dominated demagnetization process also reported by other authors [Thielsch2012]. Hence the concept of the core-shell structure hardening mechanism only applies to a certain degree. The suppression of the initial nucleation of a reversed domain is still important to increase coercivity, however due to the pinning-like domain expansion, the initial nucleation is not as detrimental as in sintered magnets. Based on the results the diffusion of Dy-Nd-Cu increases the nucleation field of the initial reversed domain. According to the MFM images of the magnetization process (data not shown), the Dy-lean slice obtained magnetic saturation within approximately 2.4 T, while the Dy-rich slice required more than 2.8 T to be magnetically saturated. Based on this data it can be assumes that the domain expansion also appears to be decreased in the Dy-rich slice. Hence the Dy-rich slice display a higher nucleation field for the reversed domain, as well as a slightly lower domain expansion. The latter is likely to be caused by an improved decoupling of grains caused by the diffusion.

To summarize, the results of this chapter regarding the texture dependency of the GBDP in sintered magnets and hot-deformed magnets, it can be stated that two analysis methods to determine local and global coercivity both hold information that cannot be obtained by one method alone. The local coercivity profiles show that the perpendicular diffusion is slightly more effective in sintered magnets and significantly more effective in hot-deformed magnets. The term “effective” means here that higher coercivities can be obtained at higher diffusion depths. In sintered magnets however this effect is partially compensated in the global coercivity profile by the observed pole hardening effect. This effect is most pronounced for the diffusion of pure Dy.

The “reversed” effect i.e. a weakening effect was observed for the perpendicular diffusion in hot-deformed magnets. For the parallel diffusion neither weakening nor pole hardening effect was observed, meaning that the average local coercivity matches the global coercivity. The preferred diffusion perpendicular to the texture axis in hot-deformed magnets is presumably linked to anisotropic microstructure which consists of platelet shaped grains. A significant texture reduction can be observed by the parallel diffusion within the first few 100 µm, which might be the reason, why no pole hardening effect is observed in hot-deformed magnets.

In hot deformed magnets the microscopic demagnetization observed by MFM shows a gradual pinning-like demagnetization which occurs at higher field for higher Dy concentrations close to the Dy source.

It is noteworthy that the pole hardening effect is observed in sintered magnets even though only one magnetic pole is hardened. From an application point of view this opens up the possibility of a single pole surface GBDP that would reduce the use of HRE.

7 Microstructural and magnetic analysis of commercial Nd-Fe-B sintered magnets

In the following chapter the previously discussed hardening mechanisms in Nd-Fe-B sintered magnets are analyzed using the example of four industrial grade magnets. The focal point is going to be the different microstructural influence factors on the magnetic properties of Nd-Fe-B sintered magnets. The precise design and control of microstructure has been and still is of great importance for permanent magnets to transfer intrinsic to extrinsic properties. The general production procedure of sintered magnets is described in section 2.3.1 and 2.2. Controlling the grain size and grain size distribution is a general challenge when it comes to permanent magnets, however, other microstructural influence factors have to be considered as well.
The four different pilot batch Nd-Fe-B sintered magnets produces by VACUUMSCHMELZE GmbH utilize several different optimization approaches. An improvement of magnetic properties in Nd-Fe-B magnets can either be obtained by an optimization of microstructure i.e. a reduction of grain size or the use of heavy rare earth additives like Dy or Tb (see chapter 2.3.1). Two different substitution methods are used: i) The HRE is already added to the starting alloy, resulting in a homogenous distribution of Dy/Tb in the 2-14-1 phase and thus the entire magnet. Or ii) the HRE is added through the GBDP described in 2.3.4. The substitution in this process is not homogenous but selective i.e. localized at the regions near the grain boundary. Thus resulting in a core-shell structure in each grain consisting of a HRE substituted shell and a “pure” $Nd_2Fe_{14}B$ core [Park2000, Sepehri-Amin2010, Loewe2015, Loewe2017]. For further information also see chapter 2.3.4.

Each of the magnets follows a single or combined approach to increase coercivity and temperature stability. The three different approaches were a reduction of grain size, which will be referred to as “grain refinement” or “grain refined”, a homogenous substitution of Dy and Tb and the grain boundary diffusion of Tb. The specifics for each magnet can be found in Table 3. The goal is a comparison between the different approaches to improve magnetic properties. The magnets were produced under industrial conditions, allowing a realistic property comparison with respect to mass production. The focus point, however, is not only the respective improvement technique as such, but also the amount of HRE elements used to obtain the improvement.

Product	Sample Name	Grain refinement	Dy/Tb substitution (homogeneous)	Tb GBDP
VACODYM® 238TP	VD 1	Yes	No	No
VACODYM® 238DTP	VD 2	Yes	No	Yes
VACODYM® 965TP	VD 3	No	Yes	No
VACODYM® 965DTP	VD 4	No	Yes	Yes

Table 3 Sample overview and respective preparation details of VD 1-4.

As can be seen in Table 3 the sample VD 1 has undergone a grain refinement and is free of HRE elements. Sample VD 2 has undergone the same grain refinement as VD 1 with an additional GBDP of Tb. For the samples VD 3 and VD 4 no grain refinement is used, instead a homogenous substitution of Dy and Tb in the 2-14-1 phase is carried out. In the case of VD 4 an additional GBDP of Tb was applied. All four magnets are designed for high performance applications such as wind turbine generators or electric vehicle engines that justify the use of HRE elements to ensure sufficient coercivity and temperature stability.

The composition of the samples determined by Inductively Coupled Plasma – Optical Emission Spectroscopy (ICP-OES) is depicted in Table 4. Generally elements can be categorized in Nd-Fe-B magnets whether they change intrinsic or extrinsic properties depending on whether they can be substituted into the 2-14-1 phase. Starting with the elements in the 2-14-1 phase, it can be seen that the B content is almost identical in all samples (with a possible exception of VD 1). The Fe content is slightly lower than one would expect because Fe is partially substituted by Co which increased the Curie temperature and saturation magnetization at room temperature (in low concentrations) [Herbst1991].The combined content of Fe and Co is approximately 79 at.% is all samples even though VD 3 and 4 have a slightly higher Co content, and an overall slightly higher Fe + Co content. The slightly lower Fe (+Co) content of VD 1 and 2 can be explained with the higher Al content in these samples, which is also known to substitute Fe in very low concentrations, but also be part on the grain boundary phase [Herbst1991, Löwe2016]. Despite lowering the anisotropy field and Curie temperature, Al is known to improve the coercivity at the expense of saturation magnetization, which can be compensated by Co substitution [Herbst1991]. The Nd content in VD 1 and 2 is approximately 1 at.% higher than VD 3 and 4. The same is true for the combined content of the Light Rare Earth elements (LRE) Nd and Pr combined. A mixture of Nd and Pr is often used in commercial sintered magnets since the two metals occur together as part of the *rare earth basket* and have almost identical intrinsic properties in the 2-14-1 phase [Okada1985, Herbst1991]. The total amount of HRE (Dy + Tb) is VD 1 is approximately 0.1 at.% which is not significant. Interesting is that the Tb content in the grain boundary diffused VD 2 is only 0.2 at.% but has a significantly increased coercivity at 300 K (see Table 5). The total amount of rare earth i.e. LRE + HRE in VD 1 and 2 is with ca. 13.4 at.% slightly lower than in VD 3 and 4 (14.0 at.%). The amount of HRE in VD 3 is with 1.80 at.% almost one order of magnitude larger than the grain boundary diffused VD 2. VD 4, which has also undergone a GBDP even has a slightly higher HRE content of approximately 2 at.% in total.

Elements like Cu and Ga are beneficial in low concentrations at the grain boundaries and are ideally only present in the Nd-rich phase. While the Cu content is identical in all samples, the Ga content in VD 1 and 2 is slightly lower than in VD 3 and 4.

Element	VD 1 (at.%)	VD 2 (at.%)	VD 3 (at.%)	VD 4 (at.%)
B	6.98	6.31	6.21	6.41
Fe	76.19	76.72	75.70	75.56
Co	2.20	2.16	3.53	3.50
Al	1.01	1.01	0.16	0.16
Nd	10.52	10.61	9.68	9.52
Pr	2.70	2.71	2.53	2.49
Dy	>0.03	>0.03	0.90	0.95
Tb	0.08	0.20	0.89	1.03
Cu	0.15	0.13	0.15	0.14
Ga	0.18	0.17	0.23	0.24

Table 4 Composition according to ICP-OES of VD 1-4.

The microstructure of the four samples is shown in Figure 7.1 using the SEM back scattered electron imaging mode with the texture axis (i.e. c-axis) pointing out of the image plane. The Nd-rich grain boundary phase can be seen as bright white contrast mainly at the triple junctions in Figure 7.1, as well as in Figure 7.2, where it is also visible as a thin white line between the 2-14-1 phase grains that are depicted in a darker grey. A slight contrast can also be seen between individual 2-14-1 grains originating from the individual grain orientation.

The comparison between the four VD samples (Figure 7.1) clearly shows the grain size difference between VD 1 and VD 2 with respect to VD 3 and VD 4. All four samples exhibit a similar amount of secondary phases. The grain size and grain size distribution of the 2-14-1 and secondary phase within each sample is quite homogeneous.

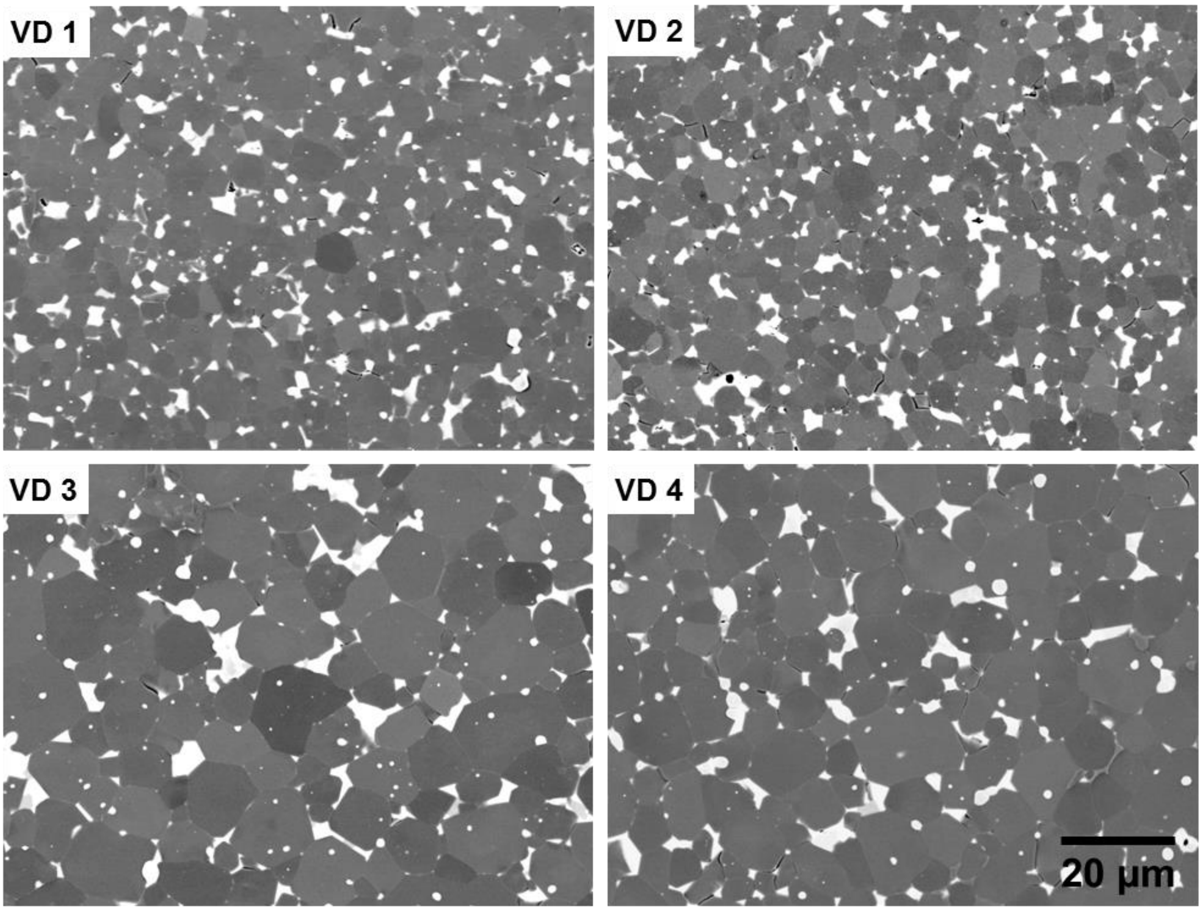

Figure 7.1 SEM-BSE image of VD 1-4 (2000x magnification) with the texture axis (nominal c-axis) pointing out of the image plane.

Depicted in Figure 7.2 is, besides grain boundary phase (GBP) at the triple junctions, also the very thin GBP separating the individual grains. The GBP is contributing strongly to the coercivity mechanism in Nd-Fe-B magnets. By magnetically decoupling the individual 2-14-1 main phase grains from each other, the GBP suppresses the propagation of reversed domains from one grain to the next [Woodcock2012]. The thickness of the grain boundaries in Nd-Fe-B sintered magnets is generally considered to be 1 – 2 nm [Woodcock2012, Kobayashi2015], but has also been reported by Sepehri-Amin *et al.* that the GBDP increases the thickness of the grain boundaries to up to 4.4 nm resulting from the substitution and subsequent rejection of Nd from the $(Nd,Dy)_2Fe_{14}B$ phase [Sepehri-Amin2010].

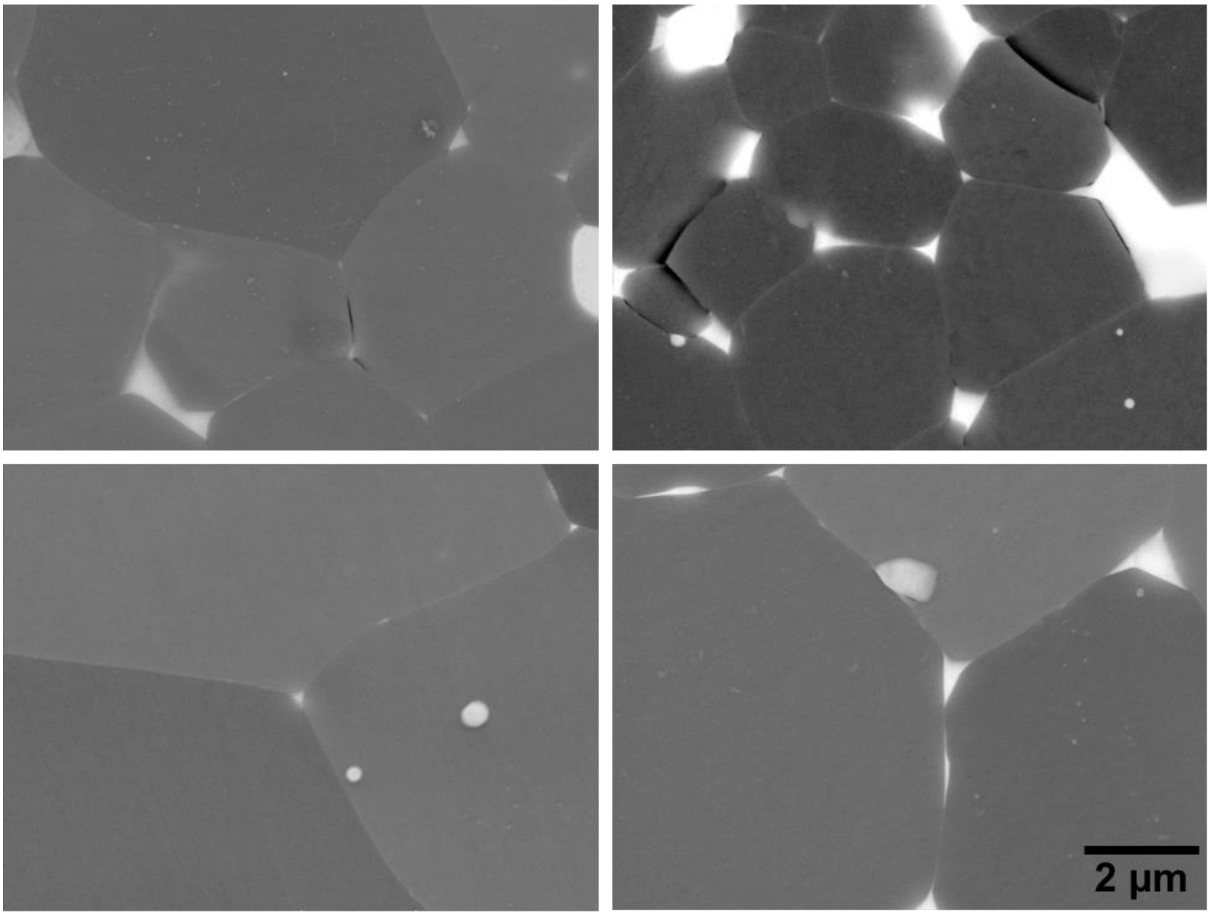

Figure 7.2 SEM-BSE image of VD 1-4 (20,000x magnification) with the texture axis pointing out of the image plane.

An electron back scattered diffraction (EBSD) analysis of the samples was performed to obtain the orientation direction of each individual grain. An exemplary map of VD 1 is shown in Figure 7.3 (a) where the color code represents the individual orientation of the respective grain. The texture axis of magnet is pointing out of the image plane, meaning that the blue contrast corresponds to an ideally oriented grain, while the green/yellow contrast represents the deviation from the ideal orientation. For this analysis only the $Nd_2Fe_{14}B$ phase was considered, excluding secondary phases. A comparison of the corresponding pole figures of the four samples is depicted in Figure 7.3 (b). The pole figures of the [001], [010] and [111] directions indicates that no preferred orientation in the basal plane is present for all samples. This distinction seems to be self-evident, since the orientation in sintered magnets is obtained by aligning the grains along the c-axis in a magnetic field. Nevertheless, if the production process involves some kind of pressing, especially transversal pressing, a preferred orientation could also arise in the basal plane induced from the pressing process.

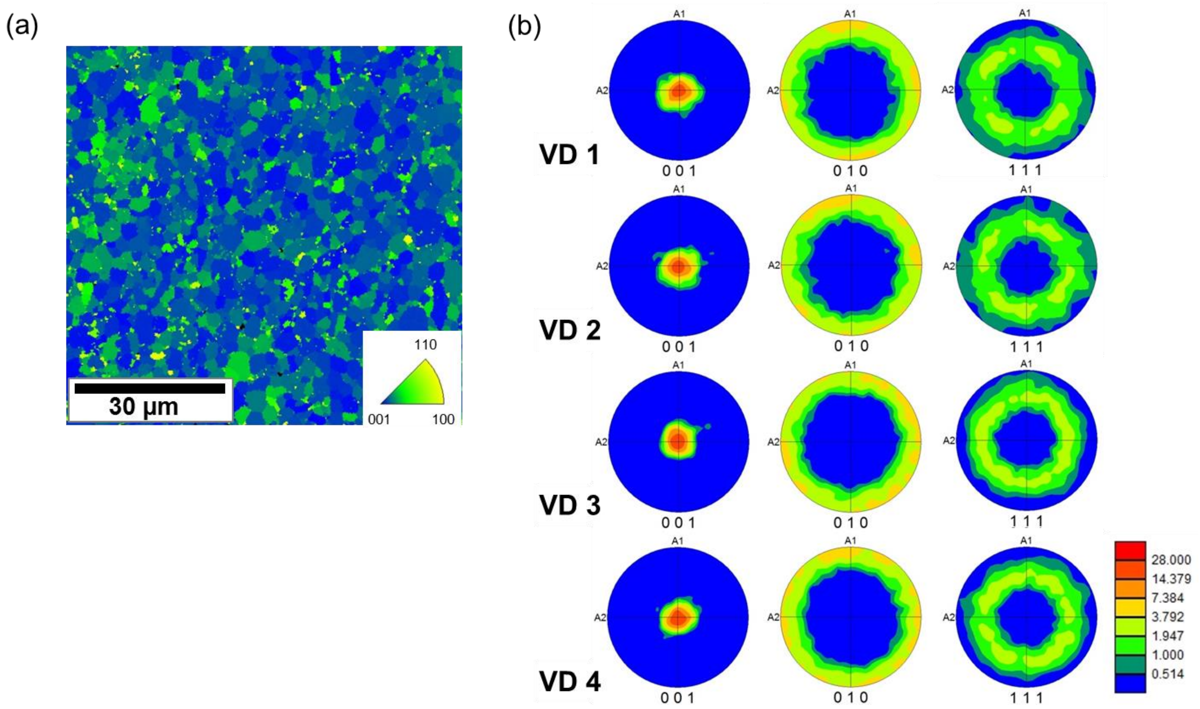

Figure 7.3 (a) EBSD direction map of VD 1 with the texture direction pointing out of the image plane and the blue contrast corresponding to the 001 direction, while any deviation from the 001 orientation is depicted as green/yellow and (b) pole figure plot for VD 1-4 displaying the deviation from the [001], [010] and [111] direction.

In the EBSD analysis, the grains are indexed individually with respect to their orientation. This also allows the extraction of grain size and grain size distribution as well as orientation distribution, the resulting data is shown in Figure 7.4. The direct comparison of the grain size distribution of VD 1 and VD 2 is shown in Figure 7.4 (a), revealing a very similar and narrow distribution. The average grain size for VD 1 is 2.83 µm with a standard deviation (SD) of 1.20 µm, while VD 2 possesses a very similar average grain size of 2.79 µm and a SD of 1.30 µm. The small grain size and narrow distribution show the effectiveness of the grain refinement.

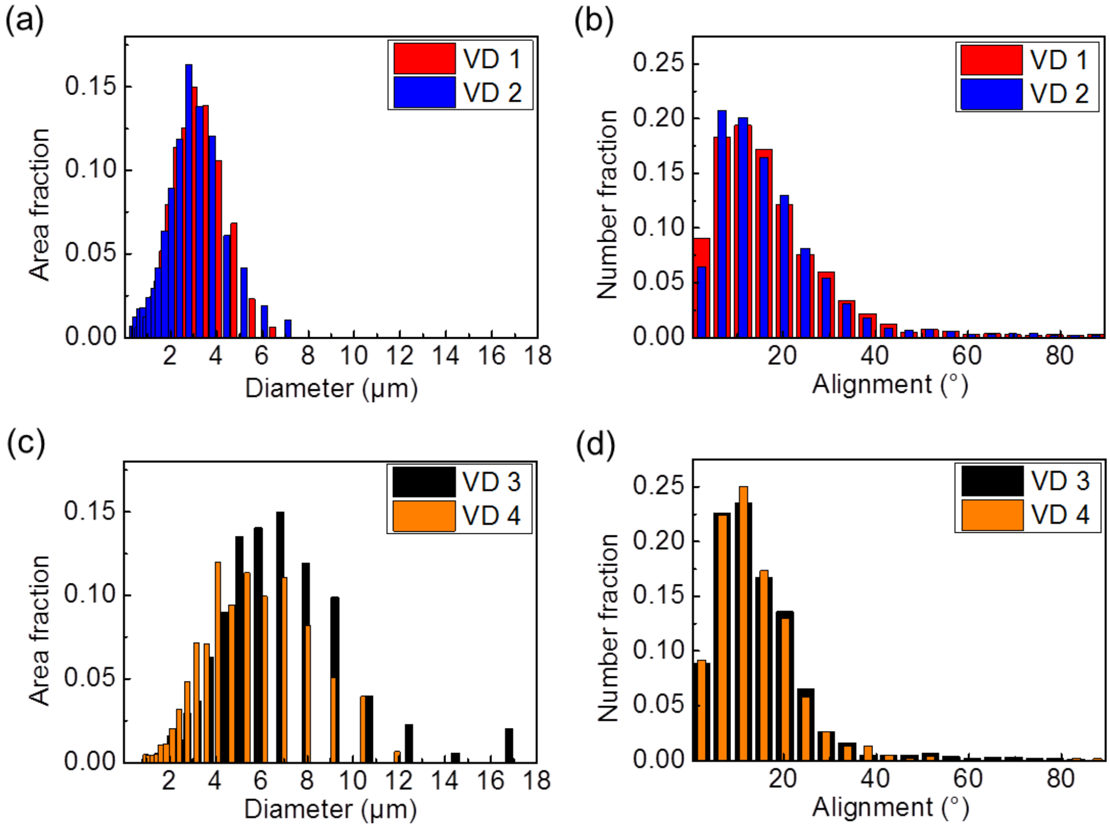

Figure 7.4 Grain size (a, c) and misalignment (b, d) distribution of VD 1-4 data extracted from the EBSD analysis.

As a comparison the grain size distribution of VD 3 and VD 4 (without a grain refinement) are depicted in Figure 7.4 (c). Here the distribution is also quite similar, but the difference between the samples is slightly larger, which is most likely an effect of the limited statistic that the EBSD can provide due to the limited scanned area. The average grain size of VD 3 of 6.43 µm and a SD of 2.90 µm and VD 4 with an average of 5.34 µm and a SD of 2.29 µm is roughly twice as large as VD 1 and VD 2. Also the distribution width of both samples is broader in comparison to VD 1 and VD 2.

The effect of the smaller grain size of VD 1 and VD 2 on the orientation distribution can be seen in Figure 7.4 (b). In comparison to the orientation distribution of VD 3 and VD 4 in Figure 7.4 (d) the distribution of the smaller grained VD 1 and VD 2 is far broader. The orientation distributions of VD 1 and VD 2 are almost identical, as are the average misalignment angles of 17.1° (VD 1) and 17.2° (VD 2). Though the larger grained VD 3 and VD 4 also show a similar distribution with respect to each other, the average misalignment angles of 14.9° (VD 3) and 14.3° (VD 4) are slightly smaller. The effect of a higher misalignment for smaller grains arises from the before mentioned higher difficulty to orient smaller grains in an external magnetic field in the production process. The higher surface of smaller grains leads to more friction between the particles, resulting in a lower alignment during the production process. While perfectly aligned grains display a higher remananece, it has also been reported that perfectly aligned magnets show a lower coercivity than magnets with a certain amount of slightly misaligned grains [Martinek and Kronmüller1990, Elbaz1991, Gao1998]

The magnetic hysteresis curves determined by PPMS-VSM at 300 K of the four VD samples are shown in Figure 7.5 (a). The curves were corrected for demagnetization effects using an appropriate demagnetization factor (ranging from 0.217 to 0.251) calculated using the Metis pulsed field magnetometer software. In terms of remanent magnetization VD 1 and VD 2 are almost identical, as are VD 3 and VD 4. Despite the slightly lower DOT of VD 1 and VD 2 their remanent and saturation magnetization is significantly larger than VD 3 and VD 4. The homogenous HRE substitution in VD 3 and VD 4 and thus the antiferromagnetic coupling with the Fe sub-lattice, reduces the remanent magnetization stronger than the lower DOT of VD 1 and VD 2.

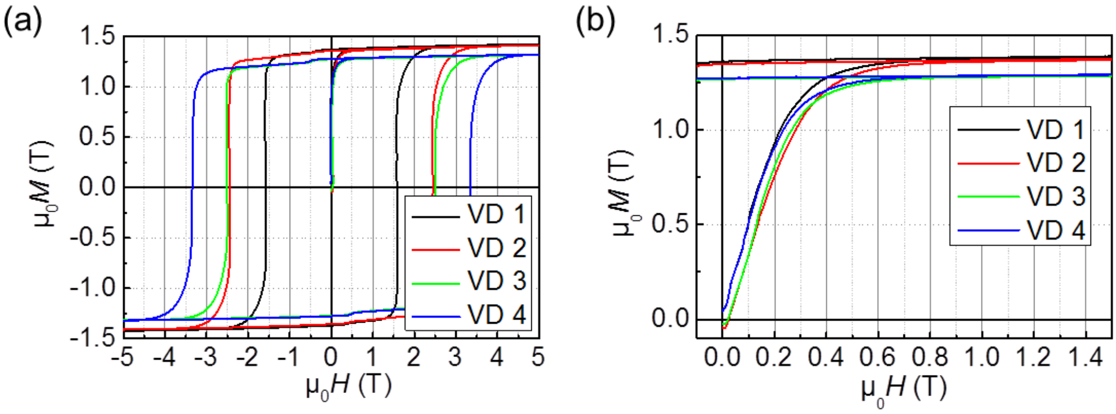

Figure 7.5 (a) Hysteresis loops of VD 1-4 determined by PPMS-VSM, magnetized under 14 T (data not shown) and corrected for demagnetization using an appropriate demagnetization factor (0.217-0.251), (b) initial magnetization curves (not corrected) of VD 1-4.

All four samples show a slight drop in magnetization between -0.3 T and -0.5 T, which is a typical feature of Nd-Fe-B magnets originating from the surface grains of each respective sample. Due to the cutting, grinding and polishing during the sample preparation the surface grains exhibit a strongly reduced coercivity in the range of 0.3 T to 0.6 T (see chapter 2.3.2). The initial magnetization curves of each sample are depicted in Figure 7.5 (b), for these curves no demagnetization correction was employed. Due to the used measuring procedure, the samples had to be exposed to a small magnetic field in order to center them correctly in the PPMS-VSM, thus the initial magnetization curves deviate slightly from the origin in Figure 7.5 (b). The curves show no significant difference with respect to each other, and show the typical feature of a nucleation based magnet [Livingston1987, Coey2010]. This means that in the analyzed magnets no evidence for pinning effects during the initial magnetization process is present, which is generally the case in sintered magnets. However, pinning effects in the initial magnetization curve were reported by Sepehri-Amin *et al.* in sintered magnets with an average grain size of 1 µm [Sepehri-Amin2011], such effects were previously only reported in hot-deformed magnets [Ramesh1988, Thielsch2012, Watanabe2013, Seelam2016] or HDDR processed magnets [Gutfleisch2000b].

A complete overview over the magnetic properties at room temperature (300 K) and the intended operating temperature 150°C (423 K) is depicted in Table 5.

Sample	J_S (T) 300 K	J_r (T) 300 K	$\mu_0 H_c$ (T) 300 K	$(BH)_{max}$ (kJ/m³) 300 K	J_r (T) 423 K	$\mu_0 H_c$ (T) 423 K	$(BH)_{max}$ (kJ/m³) 423 K
VD 1	1.46	1.37	1.58	371	1.27	0.44	210
VD 2	1.44	1.36	2.44	360	1.20	0.90	256
VD 3	1.35	1.27	2.51	335	1.19	0.95	251
VD 4	1.35	1.28	3.34	325	1.13	1.39	231

Table 5 Magnetic properties of VD 1-4 at 300 K and 423 K.

A comparison of the different VD samples at 300 K shows that the grain refined VD 1, without any HRE addition, possesses decent coercivity (0.22 $\mu_0 H_a$) and the highest saturation magnetization and remanence, but also the lowest coercivity. By applying the GDBP to a grain refined sample, the coercivity can be increased by 54.4 % to 2.44 T in VD 2 without any significant losses in saturation or remanent magnetization and a slightly decreased energy product. The homogenous HRE distribution in VD 3 leads to a marginally higher coercivity of 2.51 T, but at the same time also reduces saturation and remanent magnetization by ca. 0.1 T and consequently also lower energy product. Using a combination of homogenous distribution of HRE and GBDP, the coercivity can be increased by 33.1 % to 3.34 T (VD 4) and a slightly reduced remanence and energy product in comparison to VD 3. It is noteworthy here that the combination of the GBDP and grain refinement led to a coercivity increase by 54.4 %, while the application of the GBDP to the homogenously substituted sample only increased coercivity by 33.1 %. There are presumably two factors that are responsible for this: i) Since the grain refined samples (VD 1 and VD 2) exhibit a smaller grain size, they also provide a higher density of grain boundaries that are available for the GBDP. As a result, the HRE can penetrate deeper into the bulk of the magnet and form more chore-shell structured grains. ii) It is widely accepted that the driving force for the GBDP is the concentration gradient of HRE in accordance with Fick´s law. Since the (non-refined) samples VD 3 and 4 already contain homogenously substituted HRE prior to the GBD, the concentration gradient is reduced and consequently the driving force for the GBDP.

To compare the effectiveness of the total amount of HRE the coercivity and HRE content of VD 1 is set as a benchmark and compared to the other samples according to:

$$\eta = \frac{H_{c,VD\,X} - H_{c,VD\,1}}{C_{HRE,VD\,X} - C_{HRE,VD\,1}} \tag{7.22}$$

With $H_{c,VD\,1}$ and $C_{HRE,VD\,1}$ as the coercivity and HRE concentration of VD 1 and $H_{c,VD\,X}$ and $C_{HRE,\,VD\,X}$ as the coercivity and HRE concentration of the respective VD 2 – 4 sample. This calculation neglects the influence of the grain refinement and the other elements in the samples that also influence the coercivity. Furthermore this comparison does not differentiate between Dy and Tb despite Tb being far more potent. Nevertheless it offers a quantitative comparison of the effectiveness of the HRE impact on the coercivity. The resulting values are shown in Table 6:

	η (T/at.%)
VD 1	-
VD 2	7.17
VD 3	0.54
VD 4	0.93

Table 6 Comparison of the coercivity improvement per at.% HRE.

The results show that the Tb introduced by the GBDP (VD 2) is more than one order of magnitude more effective compared to the homogenously distributed Tb and Dy (VD 3). Tb and Dy introduced via the GBDP to a VD 3 can still further increase the effectiveness of the HRE in VD 4 by a factor of 1.7.

At the intended operating temperature of 423 K the difference in remanence between the samples is 0.14 T, which is less than 10 % of the total value. The reason for this is that the Curie temperature of $Dy_2Fe_{14}B$ (598 K) and $Tb_2Fe_{14}B$ (620 K) is higher than the Curie temperature of pure $Nd_2Fe_{14}B$ (585 K) [Herbst1991]. The Curie temperatures of VD 1 – 4 were also measured and will be discussed in the following. At 423 K coercivity is significantly lower, but the loss in coercivity also depends in the amount of HRE in the sample: The coercivity i.e. $\mu_0 H_c$ of VD 1 decreases by 72 % to 0.44 T, $\mu_0 H_c$ of VD 2 decreases by 63 % to 0.90 T, $\mu_0 H_c$ of VD 3 decreases by 62 % to 0.95 T and $\mu_0 H_c$ of VD 4 decreases by 58 % to 1.39 T. The reason for this is also the higher Curie temperature of the HRE substituted phases and the corresponding higher anisotropy field at elevated temperatures. The effectiveness of the GBDP in combination with a grain refinement in terms of coercivity increase is with 104.7 % even larger than at 300 K and results in an increase from 0.44 T (VD 1) to 0.90 T (VD 2). The effectiveness of the GBDP on the homogenously substituted sample (VD 3) without grain refinement increases coercivity by 52.7 % (VD 4) is also larger than at 300 K but nevertheless smaller than between VD 1 and 2, showing the same tendency as at 300 K. At 300 K the energy product of VD 1 and VD 2 are almost identical, and significantly higher than VD 3 and VD 4. At 423 K, on the other hand, the HRE free VD 1 possesses the lowest energy product (210 kJ/m³), while VD 2 possesses the highest (256 kJ/m³). The comparison of magnetic properties shows the effectiveness of the GBDP in combination with a grain refinement, especially at higher operating temperatures.

The comparison of magnetic properties Table 5 displays that the negative impact of the lower saturation magnetization of VD 3 and 4 on magnetic properties at 423 K is far less prominent that at 300 K. As displayed in Table 4 the samples have a slightly different composition of elements that influence the intrinsic properties of the 2-14-1 phase.

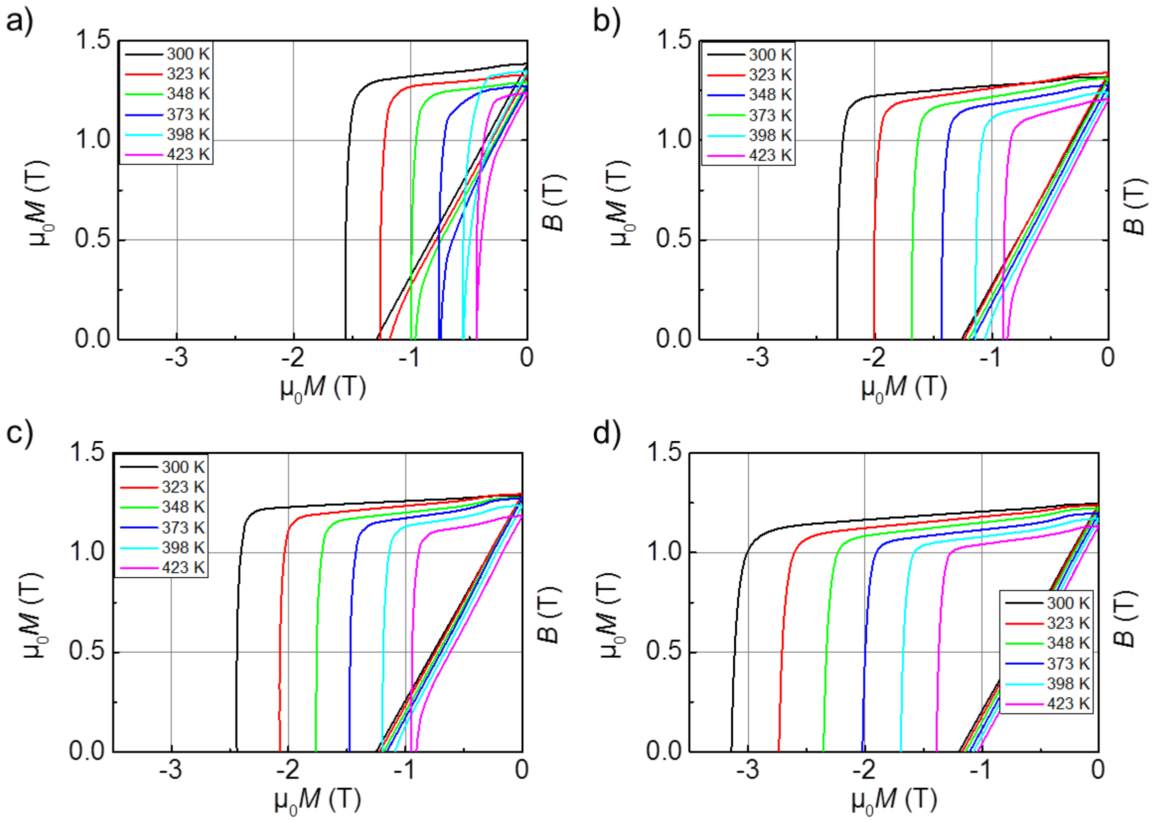

Figure 7.6 Comparison of the temperature dependency of the M(H) and B(H) 1-4 between 300 K and 423 K for VD 1 (a) VD 2 (b), VD 3 (c) and VD 4 (d).

The temperature dependency of the M(H) and B(H) fir VD 1-4 is shown in Figure 7.6 from room temperature up to the intended operating temperature of 423 K. The B(H) curves of VD 1 show a nonlinear behavior and form a “knee” for temperatures as low as 323 K. This indicates magnetic instability, when the magnet is surrounded by a magnetic field e.g. in a motor [Gutfleisch2011]. A magnet should never be operated near a “knee” to avoid permanent magnetization losses. For technical applications a nonlinear B(H) curve also limits the magnet geometries that can be realized, for further details see [Gutfleisch2011]. The fact that the “knee” occurs at rather low temperatures and becomes very pronounced at 423 K indicates that VD is not a viable option to be operated at elevated temperatures. The samples VD 2 and VD 3 show a very similar temperature dependency. A nonlinear B(H) curve only occurs at 423 K indicating that a certain care has to be taken at these operating temperatures. VD 4 shows the highest thermal stability of all samples with a linear B(H) behavior at any given operating temperature between 300 K and 423 K. For VD 4 no restrictions have to be taken at the intended operating temperature of 423 K.

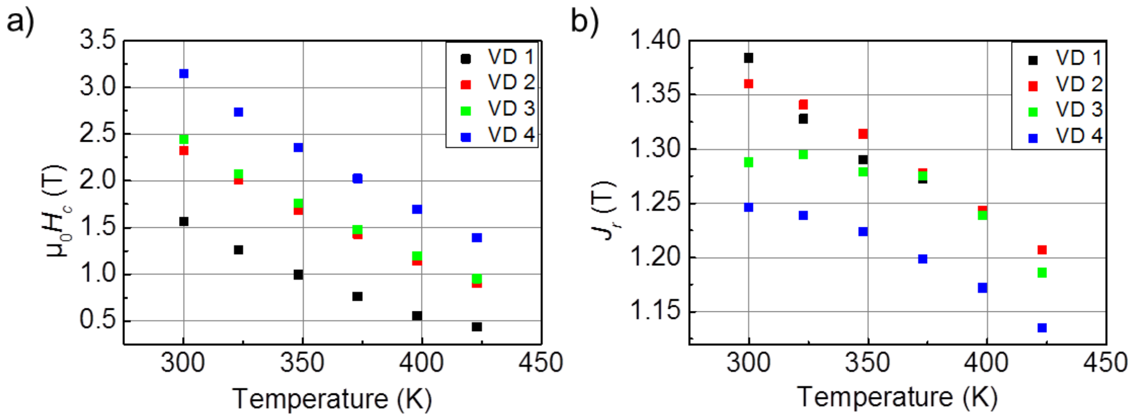

Figure 7.7 Temperature dependency of coercivity (a) and remanent magnetization (b).

The temperature dependency of the coercivity in Figure 6.7 (a) shows a typical slightly concave trend. The respective temperature coefficients β for 300 K to 423 K are shown in Table 7, while VD 1 has the highest temperature dependency, VD 2 and VD 3 display an almost identical behavior and VD 4 has the lowest temperature dependency.

The temperature dependency of the remanence in Figure 7.7 (b) shows a slightly convex shape. The values show a similar trend as the coercivity, but due to the fact that the values were obtained by a pulsed field magnetometer the values are less reliable (see chapter 3.2.8) due to the measuring procedure of the pulsed field magnetometer. The respective coefficients in Table 7 are surprisingly low in comparison to other Nd-Fe-B magnets [Hilzinger and Rodewald2013]. This can presumably be attributed to the low reliability of the remanent magnetization obtained by pulsed field magnetometry.

The Curie temperatures of VD 1 - 4 were estimated by the first derivative of the M vs. T curves measured by VSM in 0.01 T and displayed in Table 7. As expected, the Curie temperatures of VD 1 and VD 2 are almost identical within the precision of the measurement. The value is approximately 12 K higher than the Curie temperature of the pure $Nd_2Fe_{14}B$ phase, which can be attributed to the substitution of Co [Herbst1991]. The GBDP does not change the Curie temperature, which is owed to the fact that only a small volume of the $Nd_2Fe_{14}B$ phase is substituted and the intrinsic properties remain constant.

Sample	Curie Temperature [K]	Temperature coefficient α [%/K] 300 K to 423 K	Temperature coefficient β [%/K] 300 K to 423 K
VD 1	598	-0.065	-0.58
VD 2	596	-0.069	-0.50
VD 3	620	-0.064	-0.50
VD 4	620	-0.072	-0.45

Table 7 Comparison of Curie temperatures of VD 1-4, measured in a field of 0.01 T and temperature coefficients.

The homogenously substituted samples VD 3 and 4 on the other hand show a significantly higher Curie temperature that also does not change due to the GBDP. The value of 620 K happens to be identical with the Curie temperature of the pure $Tb_2Fe_{14}B$ phase despite the samples being only partially substituted. This can be attributed to the higher Co content substituting Fe [Herbst1991].

Since the Curie temperature of the HRE substituted samples VD 3 and 4 are approximately 30 K higher than the VD 1 and 2, there has to be a "break-even point" at which the magnetization of the substituted samples VD 3 and 4 is higher than the HRE "free" samples VD 1 and 2. The determination of this "break-even point", however, is not straightforward. An estimation can be done by determining the magnetization of VD 1 - 4 as a function of temperature by VSM in an external field of 2 T. The resulting curves are displayed in Figure 7.8. Since the exact magnetization is experimentally hard to measure in the VSM due to the dependence on the orientation of the sample in the magnetic field of the VSM, the values have been normalized as $\mu_0 M_{norm}$ using the respective saturation magnetization at 300 K.

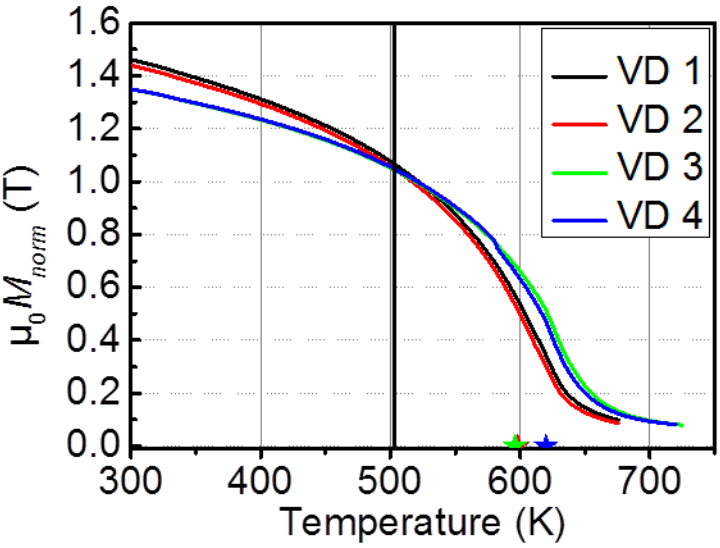

Figure 7.8 Temperature dependence of the normalized magnetization ($\mu_0 M_{norm}$) magnetization of VD 1-4 determined by VSM in 2 T.

The respective curves in Figure 7.8 show that the overall temperature dependence of the magnetization is not affected by the GBDP in either sample, as one would expect based on the Curie temperatures. The "break-even point" where VD 3 and 4 have the same magnetization as VD 1 and 2 is marked by the vertical solid line at approximately 503 K. The problem of this measurement method, however, becomes obvious when comparing the Curie temperatures that were determined in 0.01 T with the $M(T)$ curves in 2 T. The respective values of T_C determined in 0.01 T are indicated in Figure 7.8 by the markings on the temperature axis. Since the measurement of the magnetization was performed in 2 T, a magnetization is still present above the Curie temperature. Therefore this measurement is just an estimation and the actual "break-even point" should also be shifted towards lower temperatures at zero field.

The comparison of microstructural and magnetic properties highlights the role that microstructure plays in the translation of intrinsic to extrinsic properties like remanence and coercivity. Despite the grain refinement resulting in a lower degree of texture, the effect on magnetic properties such as J_r and $(BH)_{max}$ is still less detrimental than the homogenous substitution with HRE especially at room temperature. The compositional analysis displays the effectiveness of the GBDP especially in combination with a grain refinement showing a synergetic effect, improving magnetic properties beyond the direct proportionality to the HRE content. The comparison of Curie temperatures and *M* vs. *T* curves shows that the GBDP also reaches its limits at a certain temperature in comparison to a homogenous HRE substitution.

One parameter that is so taken into consideration in this analysis is the additional energy cost resulting from the grain refinement and powder handling. The same can be said about the mining, extraction etc. of Dy and Tb. A full economic analysis can therefore not be performed within this work.

7.1 Microstructure dependent surface and bulk magnetization in Nd-Fe-B magnets

The different microstructures also influence the formation of surface domain structures in TDS, as depicted by the Kerr microscopy images in Figure 7.9. The texture axis is pointing out of the image plane in all pictures. The top row shows VD 1 and 2 that have a lower grain average size and higher misalignment than VD 3 and 4 shown in the bottom row. As a result, VD 1 and 2 form very few star-like domains (sometimes also referred to as branched or closure-like domains) that are typical for Nd-Fe-B sintered magnets [Khlopkov2004, Goll2014]. Despite a slightly different chemical composition through the GBDP between VD 1 and VD 2 the domain structure in the top row with respect to closure-like domains does not differ significantly. The same is true for VD 3 and VD 4 in the bottom row. The main contributor to the domain pattern here are microstructural properties like grain size and misalignment rather than compositional differences of e.g. Dy and Tb.

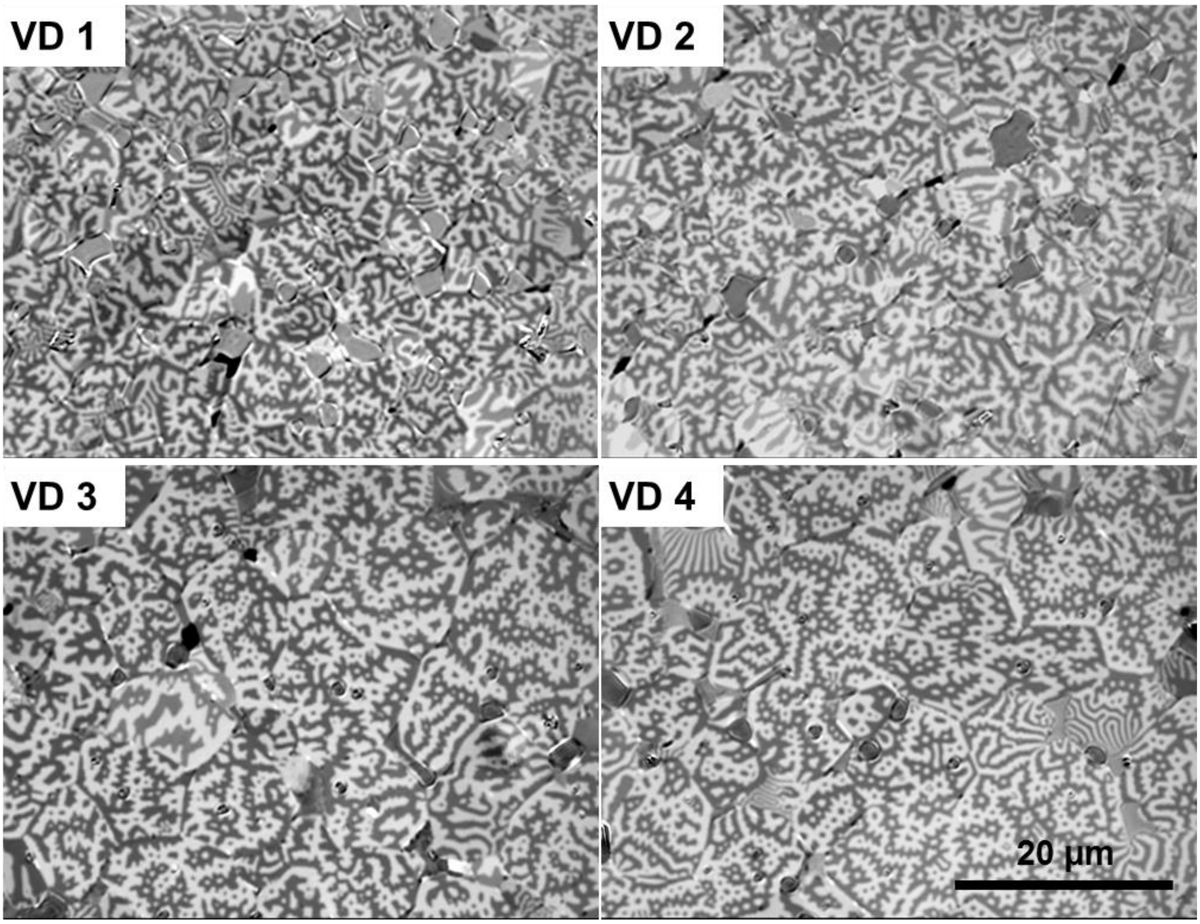

Figure 7.9 Kerr images of VD 1 and VD 2 (top row) as well as VD 3 and VD 4 (bottom row) in the Thermally Demagnetized State (TDS) with the nominal texture axis pointing out of the image plane.

In order to investigate the behavior of bulk domains, the previously applied minor loop method was adapted: In chapter 3, the minor loop method was applied to the re-magnetization from the DCD in order to investigate the role of grains with different sizes, mainly far above and below the critical single domain size, play during the demagnetization. In sintered Nd-Fe-B magnets, as mentioned before, the grain size is far above the critical single domain size and the grain size typically only differs within the same order of magnitude. The minor loop method was therefore modified to apply a demagnetizing field from the remanent state as opposed to a re-magnetizing field from the DCD. This modification was previously applied by Kobayashi *et al.* [Kobayashi2014], Emura *et al.* [Emura2000] and Dospial *et al.* [Dospial2012]. In each minor loop a small demagnetizing field is applied from the remanent state, followed by the removal of the field. For each consecutive loop the demagnetizing field is slightly increased.

A schematic illustration of the sequence is depicted in Figure 7.10: Starting from the remanent state (point A), a small demagnetizing field $\mu_0 H_B$ is applied, resulting in a slightly reduced magnetization J_B (point B). To complete the minor loop, the field is reduced to zero, giving rise to the residual magnetization J_C (point C). In this first example, the magnetization values for J_B and J_C are almost identical, as a result, the difference $\Delta J_{BC}=J_C-J_B$, which is the amount of reversible magnetization, is almost zero.

This in turn means that the involved magnetization change given by $\Delta J_{AC}=J_A-J_C$ is the irreversible magnetization change. In the subsequent minor loop a larger field than H_B is applied, triggering further demagnetization processes as can be seen at point D. In this minor loop, the removal of the field results in an increase in magnetization with respect to J_D. As the magnetization J_E is larger than J_D part of the initial magnetization is recovered and ΔJ_{DE} in this minor loop is larger than zero. This means that reversible magnetization processes (RMP) as well as irreversible magnetization processes (IMP) are contributing to this loop. There are fundamentally two possibilities to change the magnetization of a saturated SDS grain: either by collapsing to a MDS or by single domain like behavior changing from one SDS to the respective reversed SDS. As shown previously, the single domain like coherent spin rotation from SDS to SDS is an irreversible magnetization change within this minor loop method as schematically shown in Figure 7.10 (b).

The collapse from a SDS to a MDS, on the other hand, is split into an irreversible part and a reversible one. The collapse of a single grain to a MDS is schematically illustrated in Figure 7.10 (c). Starting at a fully saturated SDS, grain the application of a field H_B causes the formation of a MDS (point B), which also reduces the magnetization of the grain. When the field is reduced to zero at point C, the domains form the most stable multi domain configuration with respect to the magnetization of the surrounding grains. The driving force behind this process is the minimization of stray field energy. Therefore, as shown in this example, the ratio between “up” and “down” marked domain at point C is approximately 50:50. However, in reality this ratio might differ based on the surrounding micro- and domain structure. The “down” domain at point C corresponds to the amount of irreversible magnetization ΔJ_{irr} that is not recovered at zero field and cannot be recovered without reversing the field direction to re-saturate the grain. The “up” domain represents the maximum possible amount of reversible magnetization in this grain at point C. As can be seen in Figure 7.10 (c), the area marked by the dotted red line indicates the equilibrium state size of the “down” domain. Under an applied field H_B at point B the “down” domain is slightly larger than in the equilibrium state at point C. The difference of “down” domain between point B and point C corresponds to the amount of reversible magnetization ΔJ_{rev} of this loop. At larger fields (i.e. at point D), the domain walls are pushed even further, until they are eventually driven completely out of the grain and the grain becomes re-saturated to a SDS in the “down” direction. At this point the amount of reversible magnetization becomes close to zero, since a low amount of reversible magnetization can occur due to misaligned grains.

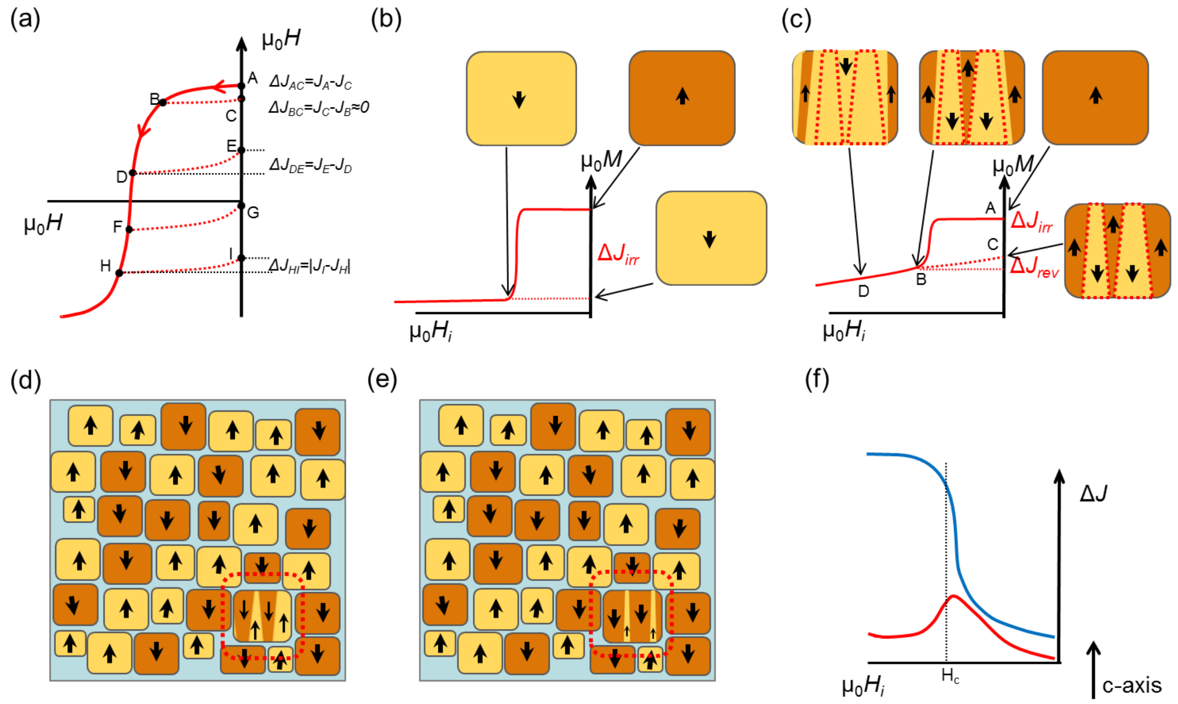

Figure 7.10 (a) Schematic illustration of the performed minor loops from remanent state, (b) schematic domain structure of a single grain forming a Single Domain State during demagnetization, (c) schematic domain structure of a grain forming a Multi Domain State during demagnetization, (d) domain structure after the application of a demagnetizing field close to the coercivity at zero field and (e) demagnetizing field and (f) schematic amount of reversible and irreversible magnetization processes.

As mentioned above, the demagnetizing field of every consecutive loop is slightly increased and the whole demagnetizing process can be "probed" in this way, as indicated by the remaining points F to G in Figure 7.10 (a). From each minor loop a value for the total amount of reversible and irreversible magnetization can be extracted. The values of J_{rev} and J_{irr} can then be plotted as a function of the applied demagnetizing field $\mu_0 H_i$ in the particular loop, as schematically shown in Figure 7.10 (f). The red line corresponds to the amount of reversible magnetization, while the blue line corresponds to the amount if irreversible magnetization. While ΔJ_{irr} displays a sigmoidal curve with the inflection point close to the coercive field, ΔJ_{rev} shows an almost linear increase at low fields and a maximum close to the coercivity and becomes almost linear again at higher fields. The largest change in both curves occurs close to the coercive field since the total magnetization change is also largest close to the coersivity. The amount of IMP (i.e. ΔJ_{irr}) at low fields is typically slightly larger than the amount of RMP (ΔJ_{rev}), as will be shown later. This is an indication that at low fields the demagnetization mainly occurred by single domain grains collapsing to a MDS, since the collapse to a MDS correlates with a certain amount of reversible and irreversible magnetization. Close to the coercivity, where the IMP exceeds the RMP by far, the magnetization change happens mainly by single domain like behavior of grains as shown in Figure 7.10 b). At the same time the amount of RMP decreases above the coercive field, indicating that MDS are re-saturated to stable SDS. In the samples analyzed in this work, the maximum amount of IMP was more than one order of magnitude larger than the RMP. The two parameters are only of comparable size at lower fields. The ratio of IMP to RMP indicates that the magnetization state at zero field after the application of a demagnetization close to H_c should look like Figure 7.10 (d). Here the major part of the grains is in a SDS with only a small portion in a MDS (indicated in red). Under an applied magnetic field, as schematically shown in Figure 7.10 f), the SDS grains maintain unswayed while the domain structure in the MDS grain is driven closer to (re-)saturation.

Another reversible magnetization process that has not been considered yet, is the rotation of magnetic moments in misaligned grains. At low fields this process can be neglected, since the fields are not strong enough to rotate magnetic moments away from the easy axis. On top of that one has to consider that only a few grains are reversed or in a MDS. At larger fields above approximately 1 T, however, when most grains are reversed and in a SDS, this process can contribute to the amount of irreversible magnetization processes. Below the anisotropy field of the respective magnet, this process is proportional to the applied field, since the moments will always return to their equilibrium state at zero field.

The magnets VD 1 - 4, were investigated using the described minor loop method. The minor loop measurement of VD 1 is depicted in Figure 7.11 as an example. As can be seen, the minor loops are all closed, which is important for the application of the minor loop method [Emura2000]. All minor loop measurements discussed in this chapter have not been corrected for demagnetization.

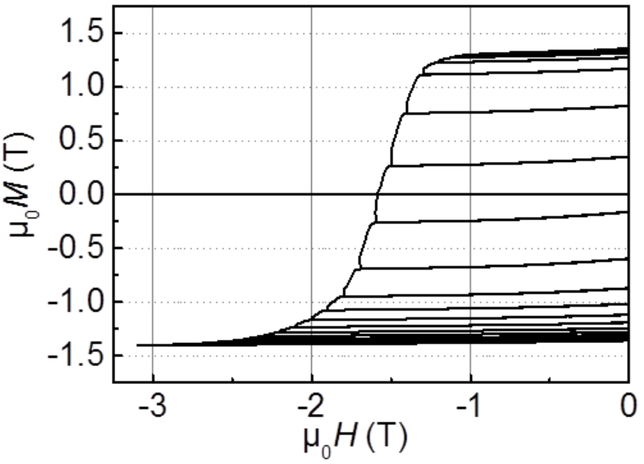

Figure 7.11 Minor loops from the remanent state of VD 1.

The extracted values of RMP and IMP are depicted in Figure 7.12. The IMP, shown in Figure 7.12 (a), displays the same sigmoidal curve form for all VD 1-4 samples. The curves are shifted to larger, i.e. more negative, fields with respect to the coercive field of the respective sample. The amount of IMP increases rapidly if the external demagnetizing field reaches the coercive field. The maximum amount of IMP corresponds to approximately $2J_r$, consequently VD 1 and VD 2 have an almost identical maximum, while VD 3 and VD 4 show a lower maximum, which are also almost identical with respect to each other.

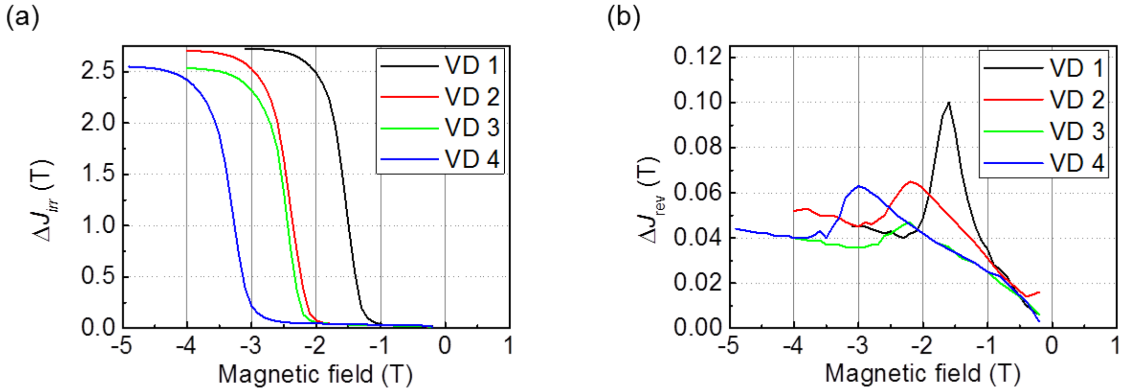

Figure 7.12 (a) Irreversible and (b) reversible magnetization processes extracted from the minor loop analysis for VD 1-4.

In comparison to the IMP, the RMP depicted in Figure 7.12 b) are significantly smaller showing that only a few grains form MDS during the demagnetization. The curve shapes are less similar to each other with respect to the IMP, but all curves show a maximum close to the coercive field. The curves exhibit a respective maximum reversible magnetization of 0.047 - 0.10 T. Considering that the maximum possible reversible magnetization is approximately 2 J_r and assuming that each multi domain grain contributes 50 % of its magnetization to the total amount of RMP, the ratio of grains that form a MDS is 3.7 - 7.3 %. At large fields, the amount of RMP increases linearly with the demagnetizing field. At higher fields the process of rotation of magnetic moments in misaligned grains plays a larger role and can no longer be neglected. The fact that VD 1 and VD 2 show the same slope, as do VD 3 and VD 4, could be attributed to the similar misalignment of grains.
VD 1 displays the highest amount of RMP, reaching a maximum of 0.1 T. In comparison to the rest of the samples, VD 1 does not show a linear increase at low fields. VD 2 displays a lower maximum than VD 1 at a higher field, indicating that the application of the GBDP can reduce the amount of RMP during the demagnetization. The same influence of the GBDP was previously reported by Kobayashi *et al.* [Kobayashi2014]. In VD 3 with a homogenous HRE distribution, the maximum RMP and initial slope at low fields is even lower than in VD 2, indicating that a homogenous distribution of HRE suppressed the formation of MDS even stronger than the GBDP. The maximum RMP of VD 4 is larger, however, this is an effect of the higher coercivity of the sample, since the initial slope at low fields of VD 3 and VD 4 are identical. This essentially means that no additional reduction of MDS can be achieved by the GBDP in the homogenously substituted sample (i.e. VD 3).

To conclude the results of the minor loop analysis in the presented Nd-Fe-B sintered magnets it can be stated that the vast majority of the demagnetization occurs by a single domain like behavior, while a small percentage form MDS in the process. This result does not contradict the Givord model, but it suggests that the nucleation field H_n is either larger or, only slightly lower than the passage and expansion field H_{pass} and H_{expans}. Hence the nucleation, expansion and re-saturation occurs within a very narrow field range. The small amount of grains that form MDS can be further reduced by the HRE content but not suppressed completely. Most effective for the suppression of MDS is the homogenous substitution of HRE but the application of the GBDP also significantly decreases the amount of MDS. Recently, Kobayashi *et al.* have claimed that a complete suppression of MDS can be obtained in very fine grained, HRE free Nd-Fe-B sintered magnets [Kobayashi2018].

8 Summary and outlook

In the Sr-hexaferrite system, three different composite magnets of equal compositions of Al substituted $SrFe_{10}Al_2O_{19}$ with commercial M884 powder were microstructurally and magnetically analyzed. Three specific microstructures were obtained by different sintering temperatures ranging from 1180°C to 1280°C. Under optimal sintering conditions the microstructure consists of grains above and below the critical single domain size ranging from approximately 500 nm to 5 µm with the critical single domain size being approximately 1 µm. A certain tendency for smaller i.e. submicron grains to be Al rich could be observed. By correlating MFM and SEM, 3 different types of microstructure-domain combinations were observed: i) several µm large grains in a MDS, ii) approximately 1 – 2 µm large grains in a SDS and iii) sub-micron sized grains with domains stretching across multiple grains. Through a correlation of surface sensitive MFM and bulk sensitive SQUID magnetometry measurements, the two-step magnetization process could be attributed to the magnetization via domain wall movement in category i) grains and a single domain-like behavior in category ii) and iii) grains. It is noteworthy that a direct comparison of magnetization extracted from the MFM contrast quantitatively matched the magnetization obtained by SQUID magnetometry. However, the accuracy of the magnetization extracted from the MFM contrast decreases if grains that are several µm above the critical single domain size are involved.

Using *in-situ* MFM to analyze the demagnetization by an external field, large grains in the range of few µm were found to reverse their magnetization at lower fields than grains in the range of the critical single domain size or smaller. At the surface, the demagnetization of larger grains was found to occur via a MDS that was typically re-saturated to the reversed SDS within a small field range. Grains close to the critical single domain size or below display a demagnetization via a single step coherent rotation from SDS to the reversed SDS. The conclusions regarding the magnetization and demagnetization processes on the surface (by MFM) were compared to the magnetization/demagnetization processes occurring in the bulk. This was done by comparing MFM measurements with SQUID magnetometry measurements using re-magnetization curves from the DCD as well as the analysis of the amount of reversible magnetization during this process determined by minor loops. The DCD can be considered a “snapshot” of the demagnetization process resulting in a distinctly different domain structure in comparison to the TDS. A comparison of the minor loop analysis and re-magnetization of the different samples leads to the conclusion that MDS are largely absent in the bulk if the sample was sintered at ideal conditions. The presence of MDS at the surface can be attributed to stray fields, which is strongest at the surface but weaker in the bulk.

From the fact that MDS are only present at the surface but absent in the bulk the idea was derived to use high coercivity single domain particles at the magnet surface, especially the pole faces, to suppress the formation of MDS at the surface during the demagnetization. Since large grains possess a lower coercivity and form MDS at the surface that can act as nucleation sites for lower lying grains, their absence at the pole surfaces should increase the overall coercivity of the magnet. Practically this can be obtained by using the same Al substituted $SrFe_{10}Al_2O_{19}$ single domain particles used in the composite. The challenge is to optimize the sintering parameters to make the single domain particles at the pole surfaces sinter to the surface and form a compact layer without over-processing the bulk of the magnet.

In the Nd-Fe-B system, a core-shell structured magnet consisting of a partially Dy substituted shell and a pure Nd-Fe-B core was analyzed using SEM, TEM, MFM and Kerr microscopy. Using SEM in the back scattered electron imaging mode, core and shell can be distinguished according to their contrast, which was also confirmed using STEM-EDX. The crystal orientation and lattice constant of core and shell were determined to be identical by STEM-HAADF. A detailed STEM-EDX analysis of the grain boundary shows the typical grain boundary thickness of approximately 2 nm and elemental distribution with a lower amount of Fe and higher amount of Nd.

By comparing SEM and MFM images, the chemical composition of the core-shell structure can be correlated with the MFM contrast arising from the lower magnetization of the Dy substituted shell. The *in-situ* demagnetization observed by MFM and Kerr microscopy shows a uniform demagnetization of core and shell acting as a unit within the observable time resolution of 43 fps corresponding to 23 ms between two images. Even if the external field can be excluded as a driving force, the time resolution is not high enough to locate a nucleation site in this experiment.

Micromagnetic simulations using a similar grain geometry as experimentally observed, revealed a direct dependency of the grain coercivity on the anisotropy of the defect layer (K^{edge}) near the grain boundary. If the anisotropy of the defect layer (K^{edge}) reaches a specific threshold value the nucleation occurs in the core. At this point a maximum coercivity is obtained, which does not increase further for higher grain boundary anisotropy (K^{edge}).

The main problem with localizing the nucleation site in a core-shell grain *experimentally* is that the realistically obtainable time resolution is orders of magnitudes lower than the time scale on which the actual demagnetization presumably takes place.

The texture dependency of the GBDP was analyzed in sintered and hot-deformed magnets. By cutting the diffused samples into thin slices and measuring the magnetic properties prior and after each cut, a local and a global coercivity profile was obtained. The diffusion experiments were done using pure metallic Dy as well as $Dy_{20}Nd_{60}Cu_{20}$ as diffusant in sintered magnets and $Dy_{20}Nd_{60}Cu_{20}$ in hot-deformed magnets. While the diffusion in sintered magnets was carried out at 900°C followed by a PSA, the diffusion in hot-deformed magnets was carried out at 650°C to minimize the grain growth during the heat treatment. In sintered magnets, the local coercivity profiles lead to the conclusion that grain boundary diffusion perpendicular to the texture axis is more effective for Dy and Dy-Nd-Cu. The diffusion of pure Dy had a slightly higher impact on coercivity than Dy-Nd-Cu. The global coercivity profiles on the other hand show a higher (or similar high) coercivity for parallel diffusion contradicting the results of the local diffusion profiles. To clarify this contradiction of the two measurement methods, the average local coercivities are compared to the global profiles. For perpendicular diffusion, the average local coercivity matches the global coercivity. For parallel diffusion on the other hand the (experimental) global coercivity exceeds the average local coercivity. This effect can presumably be attributed to a pole surface hardening effect. This is especially interesting since only one pole surface was magnetically hardened in this experimental setup. This effect is also interesting from a practical point of view since using a single pole surface coating would reduce the amount of HRE required in the process. This could be especially interesting for applications like motors where the demagnetizing field is rather inhomogeneous and originating from a specific direction, hence the “local hardening” should have significant effect.

In hot-deformed magnets the results of local and global coercivity reveal a faster diffusion (of Dy-Nd-Cu) for perpendicular diffusion (with respect to the texture axis). This can be attributed to the platelet shaped grains that form a brick wall-like structure. For parallel diffusion, the texture within the first few 100 µm is significantly reduced after the diffusion, while the texture for perpendicular diffusion is largely maintained. Unlike in sintered magnets, the comparison between average local coercivity and global coercivity showed that the experimental global coercivity is lower than the average local coercivity for perpendicular diffusion. For parallel diffusion on the other hand, the global coercivity matched the average local coercivity. This means that a pole hardening effect is not observed in hot-deformed magnets but instead a weakening effect is present if the pole surfaces are only partially hardened. The demagnetizing behavior of a HRE rich slice (slice to the Dy-Nd-Cu source) and a HRE lean slice was analyzed using *in-situ* MFM. In the HRE rich slice the demagnetization occurred at higher fields in comparison to the HRE lean slice. The demagnetization in both slices occurred via the “nucleation” of a reversed interaction domain and a subsequent pinning-like domain expansion.

In the last part of the thesis the microstructural properties of Nd-Fe-B sintered magnets were analyzed using the example of four pilot batch magnets by VACUUMSCHMELZE following different approaches to maximize coercivity. Using an EBSD analysis, HRE-lean grain refined samples were found to have a moreover sharper grain size distribution and overall lower grain size. At the same time, the grain refined samples also display a slightly higher misalignment, however, a comparison with magnetic properties shows that the influence of the higher misalignment on remanence is still lower than the magnetization reduction by the homogenous substitution of Dy/Tb. The influence of the grain refinement was also found to alter the domain pattern in the thermally demagnetized state, reducing the amount of star-like domains significantly.

A direct comparison of a grain-refined as well as grain boundary diffused magnet with a homogenously substituted magnet displays almost identical magnetic properties. At the same time the grain boundary diffused magnet only requires a fraction of the HRE of the homogeneously substituted magnet. Due to the higher Curie temperature of homogenously substituted magnets, their performance at higher temperatures increases gradually up to the point where a “break-even point” is reached. A maximum coercivity can be achieved if the GBDP is combined with a homogenous HRE distribution but the most effective use of HRE in this analysis is the combination of grain refinement and inhomogeneous substitution via the GBDP.

Due to the fact that the Nd-rich phase and surface oxidation in Nd-Fe-B plays a dominating role in the coercivity mechanism of surface grains meaning that the polishing process reduces the coercivity, a direct quantitative comparison of surface and bulk magnetization is not possible. The bulk demagnetization processes was therefore analyzed using minor loops and determining the amount of reversible magnetization and hence MDS in the bulk. Using this method, it was determined that the majority of grains display a single domain like behavior. This single domain like behavior can be increased further by the addition of HRE. Through the GBDP and a homogenous HRE distribution both increase the single domain like character, the latter one is more effective than the former.

From this analysis it can be concluded, that the grain refinement in combination with a GBDP results in comparable properties (from an applications point of view) as a homogenous HRE distribution using only a fraction of the HRE content.

References

[Akiya2014] Akiya, T., J. Liu, H. Sepehri-Amin, T. Ohkubo, K. Hioki, A. Hattori and K. Hono. "Low temperature diffusion process using rare earth-Cu eutectic alloys for hot-deformed Nd-Fe-B bulk magnets." Journal of Applied Physics **115** (17), (2014) 17A766.

[Alsmadi2013] Alsmadi, A. M., I. Bsoul, S. H. Mahmood, G. Alnawashi, K. Prokes, K. Siemensmeyer, B. Klemke and H. Nakotte. "Magnetic study of M-type doped barium hexaferrite nanocrystalline particles." Journal of Applied Physics **114** (24), (2013) 243910.

[Bai2002] Bai, Y., J. Zhou, Z. L. Gul and L. T. Li. "Magnetic properties of Cu,Zn-modified Co_2Y hexaferrites." Journal of Magnetism and Magnetic Materials **246** (1-2), (2002) 140-144.

[Bance2015a] Bance, S., J. Fischbacher, A. Kovacs, H. Oezelt, F. Reichel and T. Schrefl. "Thermal Activation in Permanent Magnets." The Journal of The Minerals, Metals & Materials Society **67** (6), (2015) 1350-1356.

[Bance2015b] Bance, S., J. Fischbacher and T. Schrefl. "Thermally activated coercivity in core-shell permanent magnets." Journal of Applied Physics **117** (17), (2015) 17A733.

[Bauer2010] Bauer, D., D. Diamond, J. Li, D. Sandalow, P. Telleen and B. Wanneret. "Critical Materials Strategy, US Department of Energy." (2010).

[Beach2006] Beach, G. S. D., C. Knutson, C. Nistor, M. Tsoi and J. L. Erskine. "Nonlinear domain-wall velocity enhancement by spin-polarized electric current." Physical Review Letters **97** (5), (2006) 4.

[Binnemans2018] Binnemans, K., P. T. Jones, T. Müller and L. Yurramendi. "Rare Earths and the Balance Problem: How to Deal with Changing Markets?" Journal of Sustainable Metallurgy **4** (1), (2018) 126-146.

[Boltich1985] Boltich, E. B., E. Oswald, M. Q. Huang, S. Hirosawa, W. E. Wallace and E. Burzo. "Magnetic characteristics of $R_2Fe_{14}B$ systems prepared with high purity rare earths (R=Ce, Pr, Dy, and Er)." Journal of Applied Physics **57** (8), (1985) 4106-4108.

[Brown2014] Brown, D. N., Z. Wu, F. He, D. J. Miller and J. W. Herchenroeder. "Dysprosium-free melt-spun permanent magnets." Journal of Physics - Condensed Matter **26** (6), (2014) 064202.

[Brown1945] Brown, W. F. "Virtues and Weaknesses of the Domain Concept." Reviews of Modern Physics **17** (1), (1945) 15-19.

[Carey1994] Carey, R., P. A. Gago-Sandoval, D. M. Newman and B. W. J. Thomas. "The magnetic and magneto-optical properties of Co, Cr, Mn, and Ni substituted barium ferrite films." Journal of Applied Physics **75** (10), (1994) 6789-6791.

[Coey2010] Coey, J. M. D. (2010). Magnetism and Magnetic Materials. Published in the United States of America by Cambridge University Press, New York.

[Croat1984] Croat, J. J., J. F. Herbst, R. W. Lee and F. E. Pinkerton. "Pr-Fe and Nd-Fe-based materials: A new class of high-performance permanent magnets (invited)." Journal of Applied Physics **55** (6), (1984) 2078-2082.

[Cullity and Graham2008] Cullity, B. D. and C. D. Graham (2008). Introduction to Magnetic Materials, Wiley.

[Dahal2014] Dahal, J. N., L. Wang, S. R. Mishra, V. V. Nguyen and J. P. Liu. "Synthesis and magnetic properties of $SrFe_{12-x-y}Al_xCoyO_{19}$ nanocomposites prepared via autocombustion technique." Journal of Alloys and Compounds **595**, (2014) 213-220.

[De Groot1998] De Groot, C. H., K. H. J. Buschow, F. R. de Boer and K. de Kort. "Two-powder Nd2Fe14B magnets with DyGa addition." Journal of Applied Physics **83** (1), (1998) 388-393.

[Doser and Keeler1988] Doser, M. and G. Keeler. "LONG-TERM STABILITY OF FE-B-ND-DY ALLOYS MADE BY DY2O3 ADDITIONS." Journal of Applied Physics **64** (10), (1988) 5311-5313.

[Dospial2012] Dospial, M. J., M. G. Nabialek, M. Szota, T. Mydlarz, K. Oźga and S. Lesz. "Influence of heat treatment on structure and reversal magnetization processes of $Sm_{12.5}Co_{66.5}Fe_8Cu_{13}$ alloy." Journal of Alloys and Compounds **536**, (2012) S324-S328.

[Dung1997] Dung, N. K., D. L. Minh, B. T. Cong, N. Chau and N. X. Phuc. "The influence of La2O3 substitution on the structure and properties of Sr hexaferrite." Journal De Physique - iv **7** (C1), (1997) 313-314.

[Elbaz1991] Elbaz, D., D. Givord, S. Hirosawa, F. P. Missell, M. F. Rossignol and V. Villas-Boas. "Angular dependence of coercivity in sintered RFeB magnets." Journal of Applied Physics **69** (8), (1991) 5492-5494.

[Emura2000] Emura, M., D. R. Cornejo and F. P. Missell. "Reversible and irreversible magnetization in hybrid magnets." Journal of Applied Physics **87** (3), (2000) 1387-1394.

[Esper1977] Esper, F. J. "Microstructure of Hard Ferrites and Their Magnetic-Properties." Journal De Physique - Paris **38**, (1977) 69-72.

[EUROPEAN COMMISSION2017] EUROPEAN COMMISSION, t., D. Sustainability, B. Geological, S. B. d. R. G. e. Minières and N. O. f. A. S. Research. Study on the review of the list of Critical Raw Materials, Criticality Assessments, (2017).

[Fahnle1993] Fahnle, M., K. Hummler, M. Liebs and T. Beuerle. "Ab-Initio Electron Theory for Hard-Magnetic Rare-Earth-Transition-Metal Intermetallics." Applied Physics a - Materials Science & Processing **57** (1), (1993) 67-76.

[Fidler and Knoch1989] Fidler, J. and K. G. Knoch. "Electron-Microscopy of Nd-Fe-B Based Magnets." Journal of Magnetism and Magnetic Materials **80** (1), (1989) 48-56.

[Fukagawa and Hirosawa2008] Fukagawa, T. and S. Hirosawa. "Coercivity generation of surface Nd(2)Fe(14)B grains and mechanism of fcc-phase formation at the Nd/Nd(2)Fe(14)B interface in Nd-sputtered Nd-Fe-B sintered magnets." Journal of Applied Physics **104** (1), (2008).

[Fukumoto2005] Fukumoto, K. Magnetization reversal dynamics in magnetically coupled trilayer systems, Freie Universität Berlin, (2005).

[Gabay2011] Gabay, A. M., M. Marinescu, W. F. Li, J. F. Liu and G. C. Hadjipanayis. "Dysprosium-saving improvement of coercivity in Nd-Fe-B sintered magnets by Dy2S3 additions." Journal of Applied Physics **109** (8), (2011).

[Gao1998] Gao, R., W. Li, C. Ji, D. Zhang and J. Zhang. "Effects of the grain alignment on the coercivity and its angular dependence for NdCoFeB permanent magnets." Chinese Science Bulletin **43** (2), (1998) 107-111.

[Ghandehari1986] Ghandehari, M. H. "Reactivity of Dy_2O_3 and Tb_4O_7 With $Nd_{15}Fe_{77}B_8$ Powder and the Coercivity of the Sintered Magnets." Applied Physics Letters **48** (8), (1986) 548-550.

[Givord1987b] Givord, D., A. Lienard, P. Tenaud and T. Viadieu. "Magnetic Viscosity in Nd-Fe-B Sintered Magnets." Journal of Magnetism and Magnetic Materials **67** (3), (1987) L281-L285.

[Givord2003] Givord, D., M. Rossignol and V. M. T. S. Barthem. "The physics of coercivity." Journal of Magnetism and Magnetic Materials **258**, (2003) 1-5.

[Givord1988] Givord, D., P. Tenaud and T. Viadieu. "Coercivity Mechanism in Ferrite and Rare Earth Transition Metal." IEEE Transactions on Magnetics **24** (2), (1988).

[Givord1987a] Givord, D., P. Tenaud, T. Viadieu and G. Hadjipanayis. "Magnetic Viscosity in Different Nd-Fe-B Magnets." Journal of Applied Physics **61** (8), (1987) 3454-3456.

[Goll2014] Goll, D., R. Loeffler, J. Herbst, R. Karimi and G. Schneider. "High-throughput search for new permanent magnet materials." Journal of Physics-Condensed Matter **26** (6), (2014).

[Goto2011] Goto, R., S. Sugimoto, M. Matsuura, N. Tezuka, Y. Une and M. Sagawa. "Nd-Fe-B sintered magnets fabrication by using atomized powders." Journal of Physics: Conference Series **266**, (2011) 012029.

[Graham and Li1989] Graham, C. D. and L. Li (1989). Texture formation in rapidly-quenched Nd- FeB magnets by high-speed hot-deformation. REPM Proc. 10th Int. Workshop on RE Magnets and their Applications, Kyoto, Japan.

[Grand View Research2016] Grand View Research. "Permanent Magnet Market Analysis By Material (Aluminum Nickel Cobalt (AlNiCo), Ferrite, Samarium Cobalt (SaCo), Neodymium Iron Boron (NdFeB)) By Application (Automotive, Electronics, Industrial, Energy, Aerospace, Medical) And Segment Forecasts To 2024." (2016).

[Grieb1997] Grieb, B. "New corrosion resistant materials based on neodym-iron-boron." IEEE Transactions on Magnetics **33** (5), (1997) 3904-3906.

[Grossinger2003] Grossinger, R., C. T. Blanco, M. Kupferling, M. Muller and G. Wiesinger. "Magnetic properties of a new family of rare-earth substituted ferrites." Physica B-Condensed Matter **327** (2-4), (2003) 202-207.

[Grünberger1997] Grünberger, W., D. Hinz, A. Kirchner, K. H. Muller and L. Schultz. "Hot deformation of nanocrystalline Nd-Fe-B alloys." Journal of Alloys and Compounds **257** (1-2), (1997) 293-301.

[Gutfleisch2000a] Gutfleisch, O. "Controlling the properties of high energy density permanent magnetic materials by different processing routes." Journal of Physics D-Applied Physics **33** (17), (2000) R157-R172.

[Gutfleisch2000b] Gutfleisch, O., D. Eckert, R. Schafer, K. H. Muller and V. Panchanathan. "Magnetization processes in two different types of anisotropic, fully dense NdFeB hydrogenation, disproportionation, desorption, and recombination magnets." Journal of Applied Physics **87** (9), (2000) 6119-6121.

[Gutfleisch2013] Gutfleisch, O., K. Guth, T. G. Woodcock and L. Schultz. "Recycling Used Nd-Fe-B Sintered Magnets via a Hydrogen-Based Route to Produce Anisotropic, Resin Bonded Magnets." Advanced Energy Materials **3** (2), (2013) 151-155.

[Gutfleisch1998] Gutfleisch, O., A. Kirchner, W. Grunberger, D. Hinz, H. Nagel, P. Thompson, J. N. Chapman, K. H. Muller, L. Schultz and I. R. Harris. "Textured NdFeB HDDR magnets produced by die-upsetting and backward extrusion." Journal of Physics D-Applied Physics **31** (7), (1998) 807-811.

[Gutfleisch1998b] Gutfleisch, O., A. Kirchner, W. Grunberger, D. Hinz, R. Schafer, L. Schultz and I. R. Harris. "Backward extruded NdFeB HDDR ring magnets." Journal of Magnetism and Magnetic Materials **183** (3), (1998) 359-364.

[Gutfleisch2006] Gutfleisch, O., K. H. Muller, K. Khlopkov, M. Wolf, A. Yan, R. Schafer, T. Gemming and L. Schultz. "Evolution of magnetic domain structures and coercivity in high-performance SmCo 2 : 17-type permanent magnets." Acta Materialia **54** (4), (2006) 997-1008.

[Gutfleisch2011] Gutfleisch, O., M. A. Willard, E. Bruck, C. H. Chen, S. G. Sankar and J. P. Liu. "Magnetic Materials and Devices for the 21st Century: Stronger, Lighter, and More Energy Efficient." Advanced Materials **23** (7), (2011) 821-842.

[Hadjipanayis1983] Hadjipanayis, G. C., R. C. Hazelton and K. R. Lawless. "New iron-rare-earth based permanent magnet materials." Applied Physics Letters **43** (8), (1983) 797-799.

[Harris1985] Harris, I. R., C. Noble and T. Bailey. "The Hydrogen Decrepitation of an $Nd_{15}Fe_{77}B_8$ Magnetic Alloy." Journal of the Less-Common Metals **106** (1), (1985) L1-L4.

[Helbig2017] Helbig, T., K. Loewe, S. Sawatzki, M. Yi, B.-X. Xu and O. Gutfleisch. "Experimental and computational analysis of magnetization reversal in (Nd,Dy)-Fe-B core shell sintered magnets." Acta Materialia **127**, (2017) 498-504.

[Herbst1991] Herbst, J. F. "$R_2Fe_{14}B$ materials: Intrinsic properties and technological aspects." Reviews of Modern Physics **63** (4), (1991) 819-898.

[Heyne2010] Heyne, L., J. Rhensius, A. Bisig, S. Krzyk, P. Punke, M. Klaui, L. J. Heyderman, L. Le Guyader and F. Nolting. "Direct observation of high velocity current induced domain wall motion." Applied Physics Letters **96** (3), (2010).

[Hilzinger and Rodewald2013] Hilzinger, R. and W. Rodewald (2013). Magnetic Materials. Wiley, Publicies Publishing, Erlangen.

[Hirosawa1986] Hirosawa, S., Y. Matsuura, H. Yamamoto, S. Fujimura, M. Sagawa and H. Yamauchi. "Magnetization and Magnetic-Anisotropy of R2fe14b Measured on Single-Crystals." Journal of Applied Physics **59** (3), (1986) 873-879.

[Hirosawa1987] Hirosawa, S., K. Tokuhara and M. Sagawa. "Coercivity of Surface Grains of Nd-Fe-B Sintered Magnet." Japanese Journal of Applied Physics Part 2-Letters & Express Letters **26** (8), (1987) L1359-L1361.

[Hirota2006] Hirota, K., H. Nakamura, T. Minowa and M. Honshima. "Coercivity Enhancement by the Grain Boundary Diffusion Process to Nd-Fe-B Sintered Magnets." IEEE Transactions on Magnetics **42** (10), (2006) 2909-2911.

[Hrkac2014a] Hrkac, G., K. Butler, T. G. Woodcock, L. Saharan, T. Schrefl and O. Gutfleisch. "Modeling of Nd-Oxide Grain Boundary Phases in Nd-Fe-B Sintered Magnets." The Journal of The Minerals, Metals & Materials Society **66** (7), (2014) 1138-1143.

[Hrkac2014b] Hrkac, G., T. G. Woodcock, K. T. Butler, L. Saharan, M. T. Bryan, T. Schrefl and O. Gutfleisch. "Impact of different Nd-rich crystal-phases on the coercivity of Nd-Fe-B grain ensembles." Scripta Materialia **70**, (2014) 35-38.

[Hubert and Schäfer1998] Hubert, A. and R. Schäfer (1998). Magnetic Domains – The Analysis of Magnetic Micrsostructures, Springer.

[Itou1995] Itou, Y., Y. Fukui, T. Kitayama, Y. Iwama, T. Kobayashi and Y. Kato. "Effects of Dy Compound Powder Addition on the Microstructures and the Magnetic-Properties of Nd-Fe-B Sintered Magnets." Journal of the Japan Institute of Metals **59** (1), (1995) 103-107.

[Izatt2016] Izatt, S. R., J. S. McKanzie, N. E. Izatt, R. L. Bruening, K. E. Krakowiak and R. M. Izatt. "Molecular Recognition Technology: A green chemisty process for seperation of indivudual rare earth metals." White paper on separation of Rare Earth Elements **February 20**, (2016).

[Jalli2011] Jalli, J., Y.-K. Hong, G. S. Abo, S. Bae, J.-J. Lee, J.-H. Park, B. C. Choi and S.-G. Kim. "MFM studies of magnetic domain patterns in bulk barium ferrite ($BaFe_{12}O_{19}$) single crystals." Journal of Magnetism and Magnetic Materials **323** (21), (2011) 2627-2631.

[Kanazawa and Kamitani2006] Kanazawa, Y. and M. Kamitani. "Rare earth minerals and resources in the world." Journal of Alloys and Compounds **408-412**, (2006) 1339-1343.

[Kazin2008] Kazin, P. E., L. A. Trusov, D. D. Zaitsev, Y. D. Tretyakov and M. Jansen. "Formation of submicron-sized $SrFe_{12-x}Al_xO_{19}$ with very high coercivity." Journal of Magnetism and Magnetic Materials **320** (6), (2008) 1068-1072.

[Kerr1877] Kerr, J. "On Rotation of the Plane of Polarization by Reflection from the Pole of a Magnet." The London, Edinburgh, and Dublin Philosophical Magazine and Journal of Science **3** (19), (1877) 321-343.

[Khlopkov2006] Khlopkov, K. Mikrotextur und magnetische Mikrostruktur in Hartmagneten aus $(Nd,Pr)_2Fe_{14}B$-Verbindungen, PhD Thesis, TU Dresden, (2006).

[Khlopkov2004] Khlopkov, K., O. Gutfleisch, D. Eckert, D. Hinz, B. Wall, W. Rodewald, K. H. Muller and L. Schultz. "Local texture in Nd-Fe-B sintered magnets with maximised energy density." Journal of Alloys and Compounds **365** (1-2), (2004) 259-265.

[Khlopkov2007] Khlopkov, K., O. Gutfleisch, D. Hinz, K. H. Muller and L. Schultz. "Evolution of interaction domains in textured fine-grained Nd2Fe14B magnets." Journal of Applied Physics **102** (2), (2007).

[Kim2011] Kim, T.-H., S.-R. Lee, D.-H. Kim, S. Nam-Kung and T.-S. Jang. "Microstructural evolution of triple junction and grain boundary phases of a Nd-Fe-B sintered magnet by post-sintering annealing." Journal of Applied Physics **109** (7), (2011) 07A703.

[Kim2016] Kim, T.-H., S.-R. Lee, S. J. Yun, S. H. Lim, H.-J. Kim, M.-W. Lee and T.-S. Jang. "Anisotropic diffusion mechanism in grain boundary diffusion processed Nd–Fe–B sintered magnet." Acta Materialia **112**, (2016) 59-66.

[Kim2012] Kim, T. H., S. R. Lee, S. Namkumg and T. S. Jang. "A study on the Nd-rich phase evolution in the Nd-Fe-B sintered magnet and its mechanism during post-sintering annealing." Journal of Alloys and Compounds **537**, (2012) 261-268.

[Kittel1949] Kittel, C. "Physical Theory of Ferromagnetic Domains." Reviews of Modern Physics **21** (4), (1949) 541-583.

[Klein2014] Klein, P., R. Varga and M. Vazquez. "Enhancing the velocity of the single domain wall by current annealing in nanocrystalline FeCoMoB microwires." Journal of Physics D-Applied Physics **47** (25), (2014) 5.

[Kobayashi2015] Kobayashi, K., M. Nakamura and K. Urushibata. "Magnetic properties of the surface layer and its magnetic interaction with the interior of Nd-Fe-B sintered magnets." Journal of Applied Physics **117** (17), (2015) 10.

[Kobayashi2018] Kobayashi, K., Y.-t. Nimura, K. Urushibata and K. Hayakawa. "Reproduced multi-domain regions during demagnetization in $Nd_2Fe_{14}B$ sintered magnets with different average grain sizes." Journal of Magnetism and Magnetic Materials **451**, (2018) 493-501.

[Kobayashi2014] Kobayashi, K., K. Urushibata, T. Matsushita, S. Sakamoto and S. Suzuki. "Magnetic properties and domain structures in Nd–Fe–B sintered magnets with Tb additive reacted and diffused from the sample surface." Journal of Alloys and Compounds **615**, (2014) 569-575.

[Kobayashi2013] Kobayashi, K., K. Urushibata, Y. Une and M. Sagawa. "The origin of coercivity enhancement in newly prepared high coercivity Dy-free Nd-Fe-B sintered magnets." Journal of Applied Physics **113** (16), (2013) 163910.

[Komuro2010] Komuro, M., Y. Satsu and H. Suzuki. "Increase of Coercivity and Composition Distribution in Fluoride-Diffused NdFeB Sintered Magnets Treated by Fluoride Solutions." IEEE Transactions on Magnetics **46** (11), (2010) 3831-3833.

[Konishi1971] Konishi, S., S. Yamada and T. Kusuda. "Domain-Wall Velocity, Mobility, and Mean-Free-Path in Permalloy Films." IEEE Transactions on Magnetics **Mag7** (3), (1971) 722-&.

[Kools2003] Kools, F. Science and technology of ferrite magnets; Modelling of coercivity and grain growth inhibition, Eindhoven: Technische Universiteit Eindhoven, (2003).

[Kronmüller1985] Kronmüller, H. "The Nucleation Fields of Uniaxial Ferromagnetic Crystals." Physica Status Solidi B-Basic Research **130** (1), (1985) 197-203.

[Kronmüller1987] Kronmüller, H. "Theory of Nucleation Fields in Inhomogeneous Ferromagnets." Physica Status Solidi B-Basic Research **144** (1), (1987) 385-396.

[Kronmüller2007] Kronmüller, H. (2007). Handbook of magnetism and advanced magnetic materials, Wiley Verlag Gmbh.

[Kronmüller1988] Kronmüller, H., K. D. Durst and M. Sagawa. "Analysis of the magnetic hardening mechanism in RE-FeB permanent magnets." Journal of Magnetism and Magnetic Materials **74**, (1988) 291-302.

[Langhof2008] Langhof, N. Phasenbeziehungen und Struktur von substituierten Hexaferriten: Optimierte Dauermagnetwerkstoffe, Friedrich-Alexander-Universität Erlangen-Nürnberg, (2008).

[Lee1985] Lee, R. W. "Hot-Pressed Neodymium-Iron-Boron Magnets." Applied Physics Letters **46** (8), (1985) 790-791.

[Lee1999] Lee, S. K., B. N. Das and V. G. Harris. "Magnetic structure of single crystal $Tb_2Fe_{14}B$." Journal of Magnetism and Magnetic Materials **207** (1-3), (1999) 137-145.

[Li and Graham1990] Li, L. and C. D. Graham. "Mechanism of texture formation by hot deformation in rapidly quenched FeNdB." Journal of Applied Physics **67** (9), (1990) 4756-4758.

[Li2009] Li, W. F., T. Ohkubo, K. Hono and M. Sagawa. "The origin of coercivity decrease in fine grained Nd-Fe-B sintered magnets." Journal of Magnetism and Magnetic Materials **321** (8), (2009) 1100-1105.

[Liang2014] Liang, L., T. Ma, P. Zhang, J. Jin and M. Yan. "Coercivity enhancement of NdFeB sintered magnets by low melting point $Dy_{32.5}Fe_{62}Cu_{5.5}$ alloy modification." Journal of Magnetism and Magnetic Materials **355**, (2014) 131-135.

[Liu2016] Liu, L. H., H. Sepehri-Amin, T. Ohkubo, M. Yano, A. Kato, T. Shoji and K. Hono. "Coercivity enhancement of hot-deformed Nd-Fe-B magnets by the eutectic grain boundary diffusion process." Journal of Alloys and Compounds **666**, (2016) 432-439.

[Livingston1987] Livingston, J. D. "Nucleation Fields of Permanent Magnets." IEEE Transactions on Magnetics **23** (5), (1987) 2109-2113.

[Loewe2017] Loewe, K., D. Benke, C. Kübel, T. Lienig, K. P. Skokov and O. Gutfleisch. "Grain boundary diffusion of different rare earth elements in Nd-Fe-B sintered magnets by experiment and FEM simulation." Acta Materialia **124**, (2017) 421-429.

[Loewe2015] Loewe, K., C. Brombacher, M. Katter and O. Gutfleisch. "Temperature-dependent Dy diffusion processes in Nd-Fe-B permanent magnets." Acta Materialia **83**, (2015) 248-255.

[Loewe2016] Loewe, K., W. Fernengel, K. Skokov and O. Gutfleisch. "Artificial Permanent Magnet and Manufacturing Procedure of the Artificial Permanent Magnet" (2016), PCT/EP2016/060633,

[Löwe2016] Löwe, K. Grain Boundary Engineering in Sintered Nd -Fe -B Permanent Magnets for Efficient Utilization of Heavy Rare Earth Elements, PhD Thesis, TU Darmstadt, (2016).

[Maki1989] Maki, K., A. Forkl, T. Dragon and H. Kronmuller. "Investigation of the Domain-Structure of Sintered Fendb-Al Magnets." Physica Status Solidi a-Applied Research **116** (2), (1989) 803-812.

[Malfliet2008] Malfliet, A., G. Cacciamani, N. Lebrun and P. Rogl (2008). Boron – Iron – Neodymium. Landolt-Börnstein - Ternary Alloy Systems, Springer. **11-D1:** 482-511.

[Martinek and Kronmüller1990] Martinek, G. and H. Kronmüller. "Influence of grain orientation on the coercivity field in Fe-Nd-B permanent magnets." Journal of Magnetism and Magnetic Materials **86**, (1990) 177-183.

[Mishra and Lee1986] Mishra, R. K. and R. W. Lee. "Microstructure, domain walls, and magnetization reversal in hot-pressed Nd-Fe-B magnets." Applied Physics Letters **48** (11), (1986) 733-735.

[Mo2008] Mo, W. J., L. T. Zhang, Q. Z. Liu, A. D. Shan, J. S. Wu and M. Komuro. "Dependence of the crystal structure of the Nd-rich phase on oxygen content in an Nd-Fe-B sintered magnet." Scripta Materialia **59** (2), (2008) 179-182.

[Moitra2014] Moitra, A., S. Kim, S.-G. Kim, S. C. Erwin, Y.-K. Hong and J. Park. "Defect formation energy and magnetic properties of aluminum-substituted M-type barium hexaferrite." Computational Condensed Matter **1** (Supplement C), (2014) 45-50.

[Nakamura2011] Nakamura, H., K. Hirota, T. Ohashi and T. Minowa. "Coercivity distributions in Nd-Fe-B sintered magnets produced by the grain boundary diffusion process." Journal of Physics D-Applied Physics **44** (6), (2011).

[Nakamura2012] Nakamura, M., K. Urushibata, K. Kobayashi and S. Sugimoto (2012). Effects of mechanical polishing of defferent crystal planes on coercivity of Nd–Fe–B sintered magnets. Proc. of the 22nd Workshop on Rare-Earth Permanent Magnets and Their Applications, Nagasaki, Japan.

[Nga2012] Nga, T. T. V., N. P. Duong and T. D. Hien. "Composition and magnetic studies of ultrafine Al-substituted Sr hexaferrite particles prepared by citrate sol-gel method." Journal of Magnetism and Magnetic Materials **324** (6), (2012) 1141-1146.

[Nishio2009] Nishio, H., Y. Minachi and H. Yamamoto. "Effect of Factors on Coercivity in Sr-La-Co Sintered Ferrite Magnets." IEEE Transactions on Magnetics **45** (12), (2009) 5281-5288.

[Nothnagel1991] Nothnagel, P., K. H. Müller, D. Eckert and A. Handstein. "The influence of particle size on the coercivity of sintered NdFeB magnets." Journal of Magnetism and Magnetic Materials **101**, (1991) 379-381.

[Okada1985] Okada, M., S. Sugimoto, C. Ishizaka, T. Tanaka and M. Homma. "Didymium-Fe-B sintered permanent magnets." Journal of Applied Physics **57** (8), (1985) 4146-4148.

[Oono2011] Oono, N., M. Sagawa, R. Kasada, H. Matsui and A. Kimura. "Production of thick high-performance sintered neodymium magnets by grain boundary diffusion treatment with dysprosium–nickel–aluminum alloy." Journal of Magnetism and Magnetic Materials **323** (3-4), (2011) 297-300.

[Pang2010] Pang, Z., X. Zhang, B. Ding, D. Bao and B. Han. "Microstructure and magnetic microstructure of La+Co doped strontium hexaferrites." Journal of Alloys and Compounds **492** (1-2), (2010) 691-694.

[Park2000] Park, K. T., K. Hiraga and M. Sagawa. "Effect of Metal-Coating and Consecutive Heat Treatment on Coercivity of Thin Nd-Fe-B Sintered Magnets." Proceedings of the Sixteenth International Workshop on Rare-Earth Magnets and Their Applications, (2000) 257-264.

[Pastushenkov1994] Pastushenkov, Y. G., L. E. Afanasieva and R. M. Grechishkin. "Surface domain structure and local demagnetizing field in Nd-Fe-B permanent magnets." physica status solidi (a) **142** (1), (1994) K41-K45.

[Porter and Donahue2004] Porter, D. G. and M. J. Donahue. "Velocity of transverse domain wall motion along thin, narrow strips." Journal of Applied Physics **95** (11), (2004) 6729-6731.

[Pullar2012] Pullar, R. C. "Hexagonal ferrites: A review of the synthesis, properties and applications of hexaferrite ceramics." Progress in Materials Science **57** (7), (2012) 1191-1334.

[Ramesh1988] Ramesh, R., G. Thomas and B. M. Ma. "Al2o3 Additions to Fe-Nd-B Magnets - Can Pinning Be Achieved." Journal of Applied Physics **63** (8), (1988) 3333-3333.

[Rhein2018] Rhein, F. Nanoskalige Magnete und Magnetkomposite auf Ferritbasis, PhD Thesis, TU Darmstadt, (2018).

[Rhein2018] Rhein, F., T. Helbig, V. Neu, M. Krispin and O. Gutfleisch. "In-situ magnetic force microscopy analysis of magnetization and demagnetization behavior in Al 3+ substituted Sr-hexaferrite." Acta Materialia **146**, (2018) 85-96.

[Rhein2017] Rhein, F., R. Karmazin, M. Krispin, T. Reimann and O. Gutfleisch. "Enhancement of coercivity and saturation magnetization of Al3+ substituted M-type Sr-hexaferrites." Journal of Alloys and Compounds **690**, (2017) 979-985.

[Rodewald2002] Rodewald, W., M. Katter and G. Reppel. "Fortschritte bei pulvermetallurgisch hergestellten Neodym-Eisen-Bor Magneten." Hagener Symposium Pulvremetallurgie **18**, (2002) 225-245

[Sagawa1984] Sagawa, M., S. Fujimura, N. Togawa, H. Yamamoto and Y. Matsuura. "New material for permanent magnets on a base of Nd and Fe (invited)." Journal of Applied Physics **55** (6), (1984) 2083.

[Sagawa1987] Sagawa, M., S. Hirosawa, H. Yamamoto, S. Fujimura and Y. Matsuura. "Nd-Fe-B Permanent-Magnet Materials." Japanese Journal of Applied Physics Part 1-Regular Papers Brief Communications & Review Papers **26** (6), (1987) 785-800.

[Samardžija2012] Samardžija, Z., P. McGuiness, M. Soderžnik, S. Kobe and M. Sagawa. "Microstructural and compositional characterization of terbium-doped Nd–Fe–B sintered magnets." Materials Characterization **67**, (2012) 27-33.

[Sasaki2016] Sasaki, T. T., T. Ohkubo and K. Hono. "Structure and chemical composition of the grain boundary phase in Nd-Fe-B sintered magnets." Acta Materialia **115**, (2016) 269-277.

[Sasaki2015] Sasaki, T. T., T. Ohkubo, Y. Une, H. Kubo, M. Sagawa and K. Hono. "Effect of carbon on the coercivity and microstructure in fine-grained Nd-Fe-B sintered magnet." Acta Materialia **84**, (2015) 506-514.

[Sawatzki2015] Sawatzki, S. Der Korngrenzendiffusionsprozess in nanokristallinen Nd-Fe-B Permanentmagneten, PhD Thesis, TU Darmstadt, (2015).

[Sawatzki2014a] Sawatzki, S., I. Dirba, H. Wendrock, L. Schultz and O. Gutfleisch. "Diffusion processes in hot-deformed Nd–Fe–B magnets with DyF_3 additions." Journal of Magnetism and Magnetic Materials **358-359**, (2014) 163-169.

[Sawatzki2014b] Sawatzki, S., A. Dirks, B. Frincu, K. Löwe and O. Gutfleisch. "Coercivity enhancement in hot-pressed Nd-Fe-B permanent magnets with low melting eutectics." Journal of Applied Physics **115** (17), (2014).

[Sawatzki2016] Sawatzki, S., C. Kübel, S. Ener and O. Gutfleisch. "Grain boundary diffusion in nanocrystalline Nd-Fe-B permanent magnets with low-melting eutectics." Acta Materialia **115**, (2016) 354-363.

[Sawatzki2018] Sawatzki, S., T. Schneider, M. Yi, E. Bruder, S. Ener, M. Schonfeldt, K. Guth, B. X. Xu and O. Gutfleisch. "Anisotropic local hardening in hot-deformed Nd-Fe-B permanent magnets." Acta Materialia **147**, (2018) 176-183.

[Schneider1990] Schneider, G., E. T. Henig, F. P. Missell and G. Petzow. "Microstructure of Sintered Fe-Nd-B Magnets." Zeitschrift Fur Metallkunde **81** (5), (1990) 322-329.

[Schneider1986] Schneider, G., E. T. Henig, G. Petzow and H. H. Stadelmaier. "Phase-Relations in the System Fe-Nd-B." Zeitschrift Fur Metallkunde **77** (11), (1986) 755-761.

[Scholz2002] Scholz, W., H. Forster, D. Suess, T. Schrefl and J. Fidler. "Micromagnetic simulation of domain wall pinning and domain wall motion." Computational Materials Science **25** (4), (2002) 540-546.

[Schrefl1993] Schrefl, T., H. F. Schmidts, J. Fidler and H. Kronmuller. "Nucleation of Reversed Domains at Grain-Boundaries." Journal of Applied Physics **73** (10), (1993) 6510-6512.

[Schultz1987] Schultz, L., J. Wecker and E. Hellstern. "Formation and properties of NdFeB prepared by mechanical alloying and solid-state reaction." Journal of Applied Physics **61** (8), (1987) 3583-3585.

[Seelam2016] Seelam, U. M. R., L. H. Liu, T. Akiya, H. Sepehri-Amin, T. Ohkubo, N. Sakuma, M. Yano, A. Kato and K. Hono. "Coercivity of the Nd-Fe-B hot-deformed magnets diffusion-processed with low melting temperature glass forming alloys." Journal of Magnetism and Magnetic Materials **412**, (2016) 234-242.

[Seelam2014] Seelam, U. M. R., T. Ohkubo, T. Abe, S. Hirosawa and K. Hono. "Faceted shell structure in grain boundary diffusion-processed sintered Nd–Fe–B magnets." Journal of Alloys and Compounds **617**, (2014) 884-892.

[Sepehri-Amin2013a] Sepehri-Amin, H., J. Liu, T. Ohkubo, K. Hioki, A. Hattori and K. Hono. "Enhancement of coercivity of hot-deformed Nd-Fe-B anisotropic magnet by low-temperature grain boundary diffusion of Nd60Dy20Cu20 eutectic alloy." Scripta Materialia **69** (9), (2013) 647-650.

[Sepehri-Amin2010] Sepehri-Amin, H., T. Ohkubo and K. Hono. "Grain boundary structure and chemistry of Dy-diffusion processed Nd-Fe-B sintered magnets." Journal of Applied Physics **107** (9), (2010).

[Sepehri-Amin2013b] Sepehri-Amin, H., T. Ohkubo and K. Hono. "The mechanism of coercivity enhancement by the grain boundary diffusion process of Nd–Fe–B sintered magnets." Acta Materialia **61** (6), (2013) 1982-1990.

[Sepehri-Amin2016] Sepehri-Amin, H., T. Ohkubo and K. Hono. "Micromagnetic Simulations of Magnetization Reversals in Nd-Fe-B Based Permanent Magnets." Materials Transactions **57** (8), (2016) 1221-1229.

[Sepehri-Amin2013c] Sepehri-Amin, H., T. Ohkubo, S. Nagashima, M. Yano, T. Shoji, A. Kato, T. Schrefl and K. Hono. "High-coercivity ultrafine-grained anisotropic Nd-Fe-B magnets processed by hot deformation and the Nd-Cu grain boundary diffusion process." Acta Materialia **61** (17), (2013) 6622-6634.

[Sepehri-Amin2012] Sepehri-Amin, H., T. Ohkubo, T. Shima and K. Hono. "Grain boundary and interface chemistry of an Nd-Fe-B-based sintered magnet." Acta Materialia **60** (3), (2012) 819-830.

[Sepehri-Amin2011] Sepehri-Amin, H., Y. Une, T. Ohkubo, K. Hono and M. Sagawa. "Microstructure of fine-grained Nd-Fe-B sintered magnets with high coercivity." Scripta Materialia **65** (5), (2011) 396-399.

[Shinba2005] Shinba, Y., T. J. Konno, K. Ishikawa, K. Hiraga and M. Sagawa. "Transmission electron microscopy study on Nd-rich phase and grain boundary structure of Nd-Fe-B sintered magnets." Journal of Applied Physics **97** (5), (2005).

[Soderžnik2017] Soderžnik, M., H. Sepehri-Amin, T. T. Sasaki, T. Ohkubo, Y. Takada, T. Sato, Y. Kaneko, A. Kato, T. Schrefl and K. Hono. "Magnetization reversal of exchange-coupled and exchange-decoupled Nd-Fe-B magnets observed by magneto-optical Kerr effect microscopy." Acta Materialia **135**, (2017) 68-76.

[Street and Woolley1949] Street, R. and J. C. Woolley. "A Study of Magnetic Viscosity." Proceedings of the Physical Society of London Section A **62** (357), (1949) 562-572.

[Szymura1999] Szymura, S., A. A. Lukin, A. A. Zhuravlyev, M. C. Margaryan, Y. M. Rabinovich and H. Bala. "Peculiarities of forming of magnetic hardening in sintered Nd15Fe76.2Ti1.0Al0.8B7 permanent magnet by ageing." Physica Status Solidi a-Applied Research **174** (2), (1999) 513-519.

[Tabatabaie2009] Tabatabaie, F., M. H. Fathi, A. Saatchi and A. Ghasemi. "Microwave absorption properties of Mn- and Ti-doped strontium hexaferrite." Journal of Alloys and Compounds **470** (1-2), (2009) 332-335.

[Taguchi1998] Taguchi, H. "High Performance Ferrite Magnets – From the Perspective of Powder Technology –." KONA Powder and Particle Journal **16**, (1998) 116-124.

[Tang2018] Tang, X., R. Chen, M. Li, C. Jin, W. Yin, D. Lee and A. Yan. "Grain boundary diffusion behaviors in hot-deformed $Nd_2Fe_{14}B$ magnets by PrNd-Cu low eutectic alloys." Journal of Magnetism and Magnetic Materials **445**, (2018) 66-70.

[Tang2015] Tang, X., R. J. Chen, W. Z. Yin, C. X. Jin, D. Lee and A. Yan. "The magnetization behavior and open recoil loops of hot-deformed Nd-Fe-B magnets infiltrated by low melting point PrNd-Cu alloys." Applied Physics Letters **107** (20), (2015).

[Tartaka2007] Tartaka, H., T. Yamada, Y. Takemura, S. Abe, S. Kohn and H. Nakamura. "Constant velocity of domain wall propagation independent of applied field strength in vicalloy wire." IEEE Transactions on Magnetics **43** (6), (2007) 2397-2399.

[Tenaud1987] Tenaud, P., A. Chamberod and F. Vanoni. "Texture in Nd-Fe-Bmagnets analysed on the basis of the determination of Nd2Fe14B single crystals easy growth axis." Solid State Communications **63** (4), (1987) 303-305.

[Thielsch2012] Thielsch, J., H. Stopfel, U. Wolff, V. Neu, T. G. Woodcock, K. Güth, L. Schultz and O. Gutfleisch. "In situ magnetic force microscope studies of magnetization reversal of interaction domains in hot deformed Nd-Fe-B magnets." Journal of Applied Physics **111** (10), (2012) 103901.

[Töpfer2005] Töpfer, J., S. Schwarzer, S. Senz and D. Hesse. "Influence of SiO2 and CaO additions on the microstructure and magnetic properties of sintered Sr-hexaferrite." Journal of the European Ceramic Society **25** (9), (2005) 1681-1688.

[Uestuener2006] Uestuener, K., M. Katter and L. W. Rodewald. "Dependence of the Mean Grain Size and Coercivity of Sintered Nd-Fe-B Magnets on the Initial Powder Particle Size." IEEE Trans. Magn. **42**, (2006) 2897.

[Velicescu1995] Velicescu, M., P. Schrey and W. Rodewald. "Dy-Distribution in the Grains of High-Energy (Nd,Dy)-Fe-B Magnets." IEEE Transactions on Magnetics **31** (6), (1995) 3623-3625.

[Vock2014] Vock, S. Resolving Local Magnetization Structures by Quantitative Magnetic Force Microscopy, PhD Thesis, TU Dresden, (2014).

[Wang2004] Wang, J. F., C. B. Ponton, R. Grossinger and I. R. Harris. "A study of La-substituted strontium hexaferrite by hydrothermal synthesis." Journal of Alloys and Compounds **369** (1-2), (2004) 170-177.

[Watanabe2013] Watanabe, N., M. Itakura and M. Nishida. "Microstructure of high coercivity Nd–Fe–Co–Ga–B hot-deformed magnet improved by the Dy diffusion treatment." Journal of Alloys and Compounds **557**, (2013) 1-4.

[Welte Mahltechnik1995] Welte Mahltechnik, G. "Verfahren zur Herstellung von Dauermagneten" (1995), DE4330197 A1, https://encrypted.google.com/patents/DE4330197A1?cl=de (14.02.18)

[Widmer2015] Widmer, J. D., R. Martin and M. Kimiabeigi. "Electric vehicle traction motors without rare earth magnets." Sustainable Materials and Technologies **3**, (2015) 7-13.

[Woodcock2014a] Woodcock, T. G., F. Bittner, T. Mix, K. H. Muller, S. Sawatzki and O. Gutfleisch. "On the reversible and fully repeatable increase in coercive field of sintered Nd-Fe-B magnets following post sinter annealing." Journal of Magnetism and Magnetic Materials **360**, (2014) 157-164.

[Woodcock and Gutfleisch2011] Woodcock, T. G. and O. Gutfleisch. "Multi-phase EBSD mapping and local texture analysis in NdFeB sintered magnets." Acta Materialia **59** (3), (2011) 1026-1036.

[Woodcock2014b] Woodcock, T. G., Q. M. Ramasse, G. Hrkac, T. Shoji, M. Yano, A. Kato and O. Gutileisch. "Atomic-scale features of phase boundaries in hot deformed Nd-Fe-Co-B-Ga magnets infiltrated with a Nd-Cu eutectic liquid." Acta Materialia **77**, (2014) 111-124.

[Woodcock2012] Woodcock, T. G., Y. Zhang, G. Hrkac, G. Ciuta, N. M. Dempsey, T. Schrefl, O. Gutfleisch and D. Givord. "Understanding the microstructure and coercivity of high performance NdFeB-based magnets." Scripta Materialia **67** (6), (2012) 536-541.

[Xu2011] Xu, F., L. T. Zhang, X. P. Dong, Q. Z. Liu and M. Komuro. "Effect of DyF3 additions on the coercivity and grain boundary structure in sintered Nd-Fe-B magnets." Scripta Materialia **64** (12), (2011) 1137-1140.

[Yan2010] Yan, G. L., P. J. McGuiness, J. P. G. Farr and I. R. Harris. "Optimisation of the processing of Nd-Fe-B with dysprosium addition." Journal of Alloys and Compounds **491** (1-2), (2010) L20-L24.

[Yan2006] Yan, M., L. Q. Yu, W. Luo, W. Wang, W. Y. Zhang and Y. H. Wen. "Change of microstructure and magnetic properties of sintered Nd-Fe-B induced by annealing." Journal of Magnetism and Magnetic Materials **301** (1), (2006) 1-5.

Acknowledgement

First and foremost I would like to thank Prof. Dr. Oliver Gutfleisch for the opportunity to write my PhD thesis in his group Functional Materials at the TU Darmstadt. From start to finish he offered me guidance, while simultaneously giving me all the freedom in terms of research direction.

I would also like to thank Prof. Dr. Thomas Schrefl for kindly being the co-referee for my thesis and participating in my PhD defense.

My gratitude also extends to the rest of the Functional Materials group for their constant support throughout the 4 years. The amount of fruitful discussions, help and useful tips I received from the group during this time, greatly contributed to this work. I am especially grateful to Dr. Konrad Löwe for sharing his extensive knowledge of Nd-Fe-B sintered magnets with me as well as Dr. Simon Sawatzki for a constant stream of ideas and for teaching me hot-deformation of Nd-Fe-B.

I would also like to express my gratitude to my project partners Thorsten Gröb and Michael Dürrschnabel for extensive SEM and TEM characterization, as well as Urban Rohrmann for the TEM sample preparation at the Fraunhofer IWKS Alzenau.

Furthermore I would like to thank the federal state of Hessen for funding the project RESPONSE through its LOEWE initiative and the VACUUMSCHMELZE GmbH for providing me with sample material.

Last but not least, I thank Dr. Fabian Rhein, Dr. Min Yi and Andreas Abel for the great collaboration, hours of discussion and good company along the way.